621.38
YUT

T350

Study of Integrated Optic Sensor for rapid detection of adulteration of petroleum products and blood glucose concentration

A thesis submitted in part fulfillment of the requirements for award of the degree of Doctor of Philosophy

ARADHANA DUTTA
Regn. No: 010/2009

School of Engineering
Department of Electronics & Communication Engineering
Tezpur University

"Study of Integrated Optic Sensor for rapid detection of adulteration of petroleum products and blood glucose concentration"

Ph.D. thesis by Aradhana Dutta, dedicated

To,

My deceased parents, late Robin Dutta and late Lilima Dutta, who raised me to be the lady that I am today and also who were always supportive of me in all my endeavors; thank you for your words of spiritual and emotional support. You are my blessings from God and I thank God for you;

and

My brother Ajoy Rajkhowa and husband for their care and patience during the course of this research work. Their encouragement has meant me so much during the pursuit of my doctorate degree. There is no doubt in my mind that without their noble support and counsel I could not have completed this process.

Abstract

The demand for optical sensors has been on the rise in the recent years. This is due to their widespread applications in industries and clinical instrumentation. Tremendous investigations have been made in the development of wide range of optical techniques to simplify accurate sensing procedure. This paves the way for development of highly sensitive planar waveguide optical sensors based on evanescent wave. Optical planar waveguide sensors have many advantages such as high sensitivity, low detection limit, immunity to electromagnetic interference, increased sensitivity over existing sensing detection techniques and also inherent compatibility with fiber optic network. Applications of such optical sensors include medical diagnostics, petroleum adulteration, food quality and environmental monitoring. The purpose of optical sensor is to measure the concentration of some specific chemical compound or to detect that its concentration is above some critical limit. The detection in general is based on the change of the effective refractive index of the propagating mode. From the relevant literature survey, we find that some authors demonstrate the development of an optical sensor for enhancement of sensitivity, whereas others present different sensing applications. Hence, in this Ph. D. thesis, a systematic and comprehensive study on planar waveguide optical sensor has been done that include design and development of a theoretical model using Simple Effective Index Method (SEIM) for the sensor structure and its application using evanescent wave sensing method. The notion behind this study has been mainly driven by the prospect that very few promising results on optical waveguide sensor have been reported. The proposed optical sensor with high waveguide sensitivity of ~0.95 requires very minimal sample for its sensing applications, such as detection of glucose concentration in blood plasma and also detect adulteration in petroleum products such as petrol, diesel and kerosene. Since medical diagnostics has received most of the attention to date, in this direction a consistent effort has been given in an attempt to integrate a planar waveguide based optical sensor system with LOC device platform to develop a sensor system that can be used for rapid testing of glucose concentration in blood plasma.

Abstract

The proposed technique can be very useful for management of diabetes, as this can separate plasma from whole blood directly with the use of LOC and then detect glucose concentration in blood plasma. It has been observed that the technique can be extended for applying as a low cost online diagnostic technique for detection of diabetes in clinical test. Further, we find that extensive studies have been made for implementation of integrated optical waveguide sensor that made use of materials such as Lithium Niobate, polymers, III-V semiconductors and silicon based materials. Among these materials it is found that Silicon (Si) based materials such as Silicon-On-Insulator (SOI) (silicon core), SiO_2/SiO_2-GeO_2 (Core) and $SiO_2/Silicon$ Oxynitride (SiON) core provides moderately low propagation losses, low material cost and compatibility with well known conventional silicon based Integrated Circuit (IC) technology.

With respect to sensors, we find that the important challenge for its applications is performance. This is in general categorized in terms of sensitivity, specificity and reusability. In this Ph. D. work, all these three aspects for designing a consistent, accurate sensor have been thoroughly studied without affecting their input parameters like sensitivity, specificity and reusability. And hence, the prime objectives of this thesis are considered as follows:

(i)   Design and development of integrated optic waveguide sensor using silicon based materials.

(ii) Implementation of the fabricated integrated optic sensor for detecting adulteration in petroleum based products.

(iii) Use of this sensor for detection of glucose level in diabetes.

✳✳✳✳✳

AUTHOR'S DECLARATION

I certify that this thesis entitled, "**Study of Integrated Optic Sensor for rapid detection of adulteration of petroleum products and blood glucose concentration**" which I now submit for examination of the award of Doctor of Philosophy at the Tezpur University under the supervision of Dr. Partha Pratim Sahu, Tezpur University, Assam, is entirely my own work and has not been taken from the work of others, save and to the extent that such work has been cited and acknowledged within the text of my work.

This thesis is prepared according to the regulations for doctoral research by Tezpur University and has not been submitted in whole or in part for another award in any other third level institution.

The work reported on in this thesis conforms to the principles and requirements of the Tezpur University guidelines in research.

I further declare that:

The Copyright of this thesis rests with the author, and no quotation from it or information derived from it may be published without the prior written consent of the author.

Date:..27/06/2014............

Signed:...Aradhana Dutta.........................

TEZPUR UNIVERSITY

Certificate

This is to certify that the thesis entitled **Study of Integrated Optic Sensor for rapid detection of adulteration of petroleum products and blood glucose concentration** submitted to the School of ___ **Engineering** ___, Tezpur University in part fulfillment for the award of the degree of Doctor of Philosophy in ___ **Electronics & Communication Engineering** ___ is a record of research work carried out by **Ms. Aradhana Dutta** under my supervision and guidance.

All help received by him/her from various sources have been duly acknowledged.

No part of this thesis has been submitted elsewhere for award of any other degree.

(Dr. Partha Pratim Sahu)
Ph. D. Supervisor

Professor,
Department of Electronics & Communication Engineering
School of Engineering
Tezpur University

TEZPUR UNIVERSITY
(A Central University established by an Act of Parliament)
Napaam, Tezpur- 784028
DISTRICT: SONITPUR::ASSAM:: INDIA

Certificate of the External Examiner and ODEC

This is to certify that the thesis entitled **"Study of Integrated Optic Sensor for Rapid Detection of Adulteration of Petroleum Products and Blood Glucose Concentration"** submitted by **Aradhana Dutta, Department of Electronics & Communication Engineering, School of Engineering** to **Tezpur University** in partial fulfillment for the award of the degree of **Doctor of Philosophy** in **Electronics and Communication Engineering** has been examined by us on _20.4.2015_ and found to be satisfactory.

The committee recommends for the award of the degree of Doctor of Philosophy.

Supervisor

(Prof. Partha Pratim Sahu)

Date: 20/04/2015

External Examiner

(RAJIB BANDYOPADHYAY)

Date: 20.4.2015

Acknowledgement

The work presented in this thesis would not have been possible without the guidance and encouragement of several individuals both from engineering and non-engineering domain. Hence, I would like to take this opportunity to express my sincere gratitude to all of them who have always been with me and for me, although sometimes they are hidden in the shadows throughout this wonderful journey.

First and foremost, I must thank God for blessing and guidance throughout this research period.

I feel great pleasure and honor to express my profound sense of reverence to my supervisor Dr. Partha Pratim Sahu for his venerable guidance, persistent help and providing me an excellent atmosphere during the course of this research. I am extremely grateful to him for the massive effort he put into the completion of my Ph. D. research work. I endorse special thanks to him for his extraordinary efforts in helping me in solving the trickiest problems faced during my research work.

I would like to thank Prof. Manabendra Bhuyan (Sir) and Prof. Nityananda Sarmah (Sir) for their valuable insights and suggestions as my Ph. D. committee members to better my thesis work.

I am grateful to Prof. Jiten Ch. Dutta (Sir) for providing me much inspiration to perform better in this research work and be successful.

I cannot visualize my current position without the love, care and support from my only loving brother, Ajoy Rajkhowa. I owe my gratitude to him for striving hard and because of whom my research has been the one that I will cherish forever. It is impossible to describe his support in words. If I have to mention one thing about him, among many, then I would proudly declare that while struggling for completion of this doctoral research work during this entire period, he has taught me to lead a life by standing alone.

I express my heartfelt gratefulness to my husband Bidyut Deka for affording his countless hours in providing me the guidance, support and courage over the years during this research period. My life has been changed into a better direction in a way that I could not have dreamed of two years before. Without you, this thesis would have never been completed. Your positive attitude at all levels of my life has given me the strength to carry on. Thank you so much.

I owe my deep gratitude to my mother-in-law Mrs. Makani Deka and father-in-law Mr. Barun Ch. Deka. Their prayers and words of encouragement meant to me so much. It is impossible to describe their support in words. A special sensation of gratitude to my sisters-in-law Archana Deka for her endless love and support towards the completion of my doctoral research. Thanks to my brother-in-law Pranjal Deka and sister-in-law Daijee Talukdar Deka for their best wishes.

I am beholden to a very precious group of people for their constant support throughout my stay at Department of Electronics & Communication Engineering. I would like to express my heartiest acknowledgment to the following:

Mr. Anukul Baishya (Sir), for boosting my morale throughout the course of research and also for his parent-like support and the home feeling whenever I was in need during my stay in Tezpur.

All the faculty members, Department of Electronics & Communication Engineering, Tezpur University for the support and advice during the course of my research period.

The office staff, Department of Electronics & Communication Engineering, Tezpur University for their hospitality.

All the technicians, Department of Electronics & Communication Engineering, Tezpur University, who helped to make my work possible.

Contents

A

List of Tables

Chapter-2

Table 2.1: Fiber optical sensor classifications based on three characteristics.

Table 2.2: Classification of waveguides based on dimension of light confinement.

Table-2.3: Waveguide materials and its properties and fabrication steps.

Table-2.4: Characteristics of optical sensors as reported by different authors.

Table 2.5: Petroleum Fractions.

Table-2.6: Different adulteration detection techniques as reported by previous authors.

Chapter-3

Table-3.1: List of available etchants for wet etching.

Chapter-4

Table 4.1 Design parameters.

Table 4.2 Performance comparison with other existing system.

Chapter-5

Table 5.1 Design parameters used for the proposed planar waveguide optical sensor.

Table 5.2 Effect of Alloxan on glucose level of rats for different days.

Table 5.3 Detection performance comparison for different blood glucose concentration measurement system.

B

List of Figures

Chapter-1

Chapter-2

B

List of Figures

B

List of Figures

B

List of Figures

B

List of Figures

B

List of Figures

B

List of Figures

B

List of Figures

Chapter-5

B

List of Figures

Glossary of Abbreviations

A

AOD	Assam Oil Division
ARROW	Anti Resonant Reflecting Optical Waveguides
ATR	Attenuated Total Reflection

B

BPM	Beam Propagation Method

C

CAE	Computer-aided-engineering
CE	Cylindrical Enclosure

D

DI	Deionized

E

E.I	Electromagnetic Interference
EIM	Effective Index Method
EPCA	Environment Pollution Control Authority
EW	Evanescent Wave

F

FBG	Fiber Bragg grating
FDTD	Finite Difference Time Domain
FEM	Finite Element Method
FD-BPM	Finite Difference–Beam Propagation method
FD-SVBPM	Finite Difference Semi-Vector Beam Propagation
FDVBPM	Finite Vector Beam Propagation method
FOS	Fiber Optic sensors
FTIR	Fourier Transform Infrared

H

HSD	High Speed Diesel

I

IC	Integrated Circuit
IO	Integrated Optical
IOCL	Indian Oil Corporation Limited

L

LED	Light Emitting Diode
LOC	Lab-on-a-Chip
LOOM	Low Optical Overlap Mode

Glossary of Abbreviations

LOD	Limit of Detection
LOQ	Limit of Quantization

M

MBE	Molecular Beam Epitaxial
MEMS	Microelectro-mechanical Systems
MIO	Multilayer Integrated Optical Sensor
MZI	Mach-Zehnder Interferometer

N

NA	Numerical Aperture

P

PA	Photoacoustic
PCE	Plastic Cylindrical Enclosure
PDS	Public Distribution System
PECVD	Plasma Enhanced Chemical Vapour Deposition
PEG	Poly (ethylene glycol)
PID	Photonic Integrated Device
PCS	Plastic-clad-silica
PQQ	Pyrroloquinolone Quinone
PTFE	Polytetrafluoro ethylene

R

RCA	Radio Corporation of America
RF	Radio Frequency
RIE	Reactive Ion Etching
RI	Refractive Index

S

SAIF	Sophisticated Analytical Instrumentation Facility
SEIM	Simple Effective Index Method
SOI	Silicon-On-Insulator
SPR	Surface Plasmon Resonance

T

TE	Tranverse Electric
TEL	Tetra Ethyl Lead
TM	Tranverse Magnetic
TIR	Total Internal Reflection

U

UV	Ultraviolet

D

List of Symbols

α	alpha
β	beta
γ	gamma
Γ	gamma (capital)
δ	delta
Δ	delta (capital)
ε	epsilon
ζ	zeta
η	eta
θ	theta
Θ	theta (capital)
λ	lambda
Λ	lambda (capital)
μ	mu
ν	nu
ξ	xi
π	pi
Π	pi (capital)
ρ	rho
σ	sigma
τ	tau
φ	phi
Φ	phi (capital)
χ	chi
ψ	psi
Ψ	psi (capital)
ω	omega
Ω	omega (capital)

List of Publications

Journal papers

(i) **Aradhana Dutta**, Bidyut Deka and Partha Pratim Sahu, "Modeling and fabrication of evanescent waveguide based optical sensor for sensitivity enhancement using SiON technology," *J. of Optical Engineering*, **52**(7), 077101, 2013.

(ii) **Aradhana Dutta**, Bidyut Deka, Partha P. Sahu, "Design and fabrication of silicon oxynitride based evanescent optical waveguide sensor for rapid detection of adulteration in petrol," *J. of Procedia Engineering*, **64**, 195-204, 2013.

(iii) **Aradhana Dutta**, Partha P. Sahu, "Monitoring glucose in blood plasma with optical waveguide sensor," *PNAS* (Communicated).

Conference/Workshop contributions

(i) **Aradhana Dutta**, Bidyut Deka, Partha Pratim Sahu, "Sensitivity enhancement of evanescent waveguide optical sensor for detecting adulterant traces in petroleum products using SiON technology," Proc. of SPIE (*to be online in Nov'13*), *8th Ibero American Optics Meeting/11th Latin American Meeting on Optics, Lasers, and Applications*, (RIAO OPTILAS 2013), July 22-26, 2013, Porto, Portugal.

(ii) **Aradhana Dutta**, Bidyut Deka, Partha Pratim Sahu, "Study on highly sensitive asymmetric waveguide optical sensor for detection of sucrose concentration based on leaky quasi-modes," Proc. of SPIE (*to be online in Nov'13*), *8th Ibero American Optics Meeting/11th Latin American Meeting on Optics, Lasers, and Applications*, (RIAO OPTILAS 2013), July 22-26, 2013, Porto, Portugal.

(iii) Bidyut Deka, **Aradhana Dutta**, Partha Pratim Sahu, "Comparative study on compact planar waveguide based photonic integrated couplers using simple effective index method," Proc. of SPIE (*to be online in Nov'13*), *8th Ibero American Optics Meeting/11th Latin American Meeting on Optics, Lasers, and Applications*, (RIAO OPTILAS 2013), July 22-26, 2013, Porto, Portugal.

(iv) Bidyut Deka, **Aradhana Dutta**, Partha Pratim Sahu, "Study on compactness of planar waveguide based integrated optic couplers using tooth shaped grating assisted geometry," Proc. of SPIE (*to be online in Nov'13*), *8th Ibero American Optics Meeting/11th Latin American Meeting on Optics, Lasers, and Applications*, (RIAO OPTILAS 2013), Porto, Portugal, July 22-26, 2013.

E

List of Publications

(v) **Aradhana Dutta**, Bidyut Deka and Partha P. Sahu, "Integrating optical glucose sensing into a planar waveguide sensor structure, *Proc. of American Institute of Physics (AIP)*- 1536, pp. 1256-57 (2013); doi: 10.1063/1.4810697, International conference on Recent Trends in Applied Physics & Material Science (RAM 2013), Bikaner, India, Feb 01-02, 2013.

(vi) Bidyut Deka, **Aradhana Dutta** and Partha P. Sahu, Design and Fabrication of Compact Integrated Optic Waveguide Coupler using SiON/SiO2 Material, *Proc. of American Institute of Physics (AIP)*-1536, pp. 1231-32 (2013); doi: 10.1063/1.4810685, International conference on Recent Trends in Applied Physics & Material Science (RAM 2013), Bikaner, India, Feb 01-02, 2013.

(vii) B. Deka, **A. Dutta**, G. Hegde, P. Sahu, "Fabrication and comprehensive study of silicon oxynitride based compact directional coupler and multimode interference coupler," *Proc. of SPIE*, vol. 8760, pp. 876024-5, International Conference on Communication and Electronics System Design (ICCESD), Jaipur, India, January 28-30, 2013,.

(viii) B. Deka, **A. Dutta**, N. Gogoi, P. P. Sahu, "Comparative Study of Directional Coupler and Two-Mode Interference Coupler Based on Tooth Shaped Grating Assisted Structure", *Proc. of Frontier in Optics and Photonics 2011 XXXVI OSI Symposium*, pp. 149-152, Indian Institute of Technology, NewDelhi, December 3-5, 2011.

Before anything else, preparation is the key to success.

-Alexander Graham Bell

Chapter 1

General Introduction

Outline of the Chapter:

1.1 General perspective

1.2 Motivation

1.3 Present State-of-Art

1.4 Aims and Objectives

1.5 Original contribution made by thesis

1.6 Outline and scope of the thesis

1.7 List of References

Chapter 1

1.1 General perspective

Day by day, the research effort in optical sensing has increased for their challenging applications that include clinical diagnostics, adulteration with their accuracy and selectivity. Their precise sensitivity to online detection and identification has fueled the development of compact optical sensors. An optical sensor can measure the concentration or the change in concentration of some specific chemical compound or just merely to detect that its concentration is above some decisive limit. This chemical compound or the measurand as it will be referred to henceforth, can for example be the concentration of glucose in water or the concentration of glucose in blood plasma. In order to convert the concentration of the measurand into a physical parameter that can be directly measured, there is in general need of a transduction layer, or sensing layer. For a sensor to be called an optical sensor, the optical properties of this transduction layer/sensing layer need to be dependent on the concentration of the measurand. An additional read-out system is necessary to translate the chemically induced changes of optical properties into an electrical output signal. We call a sensor 'integrated optical' if at least the sensing region consists of an integrated optical waveguiding system in which a sensing medium is placed close to the wave guide core as cladding for the use in chemical sensing [1]-[5], biochemical sensing [6]-[10] and other medical applications [11]-[13]. In comparison to other optical sensors, planar integrated waveguide optical sensors provide good compactness, robustness, immunity to electromagnetic interferences, high sensitivity, low cost and very short response time. This is because the depth of penetration of evanescent field of the planar waveguide into the medium of lower refractive index region is in the order of magnitude of a fraction of a wavelength. As a result, it is not detected by the guided light and has no influence on the measuring signal generated as a result and hence requires very short response time. It is very

important to stress out that also such integrated optic planar waveguide sensing platform exhibits the inherent capability of integrating with fiber-optic network. In integrated optical sensor structures, the precise sensing requires accurate modeling of these structures in which one has to consider the surrounding sensing region of the waveguide sensor accurately for enhancement of sensitivity. As this thesis deals with integrated optical planar waveguide sensors, in this context in Fig. 1.1, some considerations have been shown that lead towards the use of planar waveguide technology for the physical implementation of the sensor in different domains such as chemical, optical etc.

Chemical domain

Optical domain

Optical interrogation signals

- No electromagnetic interference
- A higher sensitivity to many measurands
- Specific optical sensing mechanisms

Bulk optics

Guided wave optics

Guided Wave Optics

- A better control over the optical light path
- Possibility of evanescent wave sensing
- Reduced size and weight

Planar waveguide technology

- Compact optical circuitry
- Ease of access to the optical path using evanescent field sensing

Fiber optics

Planar waveguide optics

Fig-1.1: Some considerations leading towards integrated optical planar waveguide sensors

In the refractive Integrated Optical (IO) sensors the change of Refractive Index (RI) of the sensing layer is converted into a change of properties of the guided modes and generally, the detection is based on the change of the effective refractive index of the guided mode propagating light beam. Using evanescent field sensing, a change in refractive index in the sensing layer used e.g. on top of the core layer of the waveguide will be translated into a change in power of the guided mode coming out of the sensing region.

1.2 Motivation

The motivation behind this study on this Ph. D. thesis work is as follows:

(i)   Integrated optical (IO) sensors based on planar waveguide platform offers the doable advantage of the better control of light path by the use of the optical waveguides, and a reduced size with high sensitivity.

(ii) Such sensors can perform sensitive measurements also on biological systems.

(iii) Additionally, IO sensors can be integrated with Lab-On-a-Chip (LOC) that preserves the miniature dimension, and is capable of doing measurements in clinical diagnostics at low cost.

(iv) Because IO sensors are small, furthermore they offer the possibility to realize sensor for a cheap mass production similar to the way electronic chips are produced now a days.

1.3 Present State-of-Art

Extensive studies have been made for implementation of integrated optical waveguide sensor that made use of materials such as Lithium Niobate [14]-[16], polymers [17]-[19], III-V semiconductors [20][21] and silicon based materials [22]-[25]. But we find that out of these materials Silicon (Si) based materials such as Silicon-On-Insulator (SOI) (silicon core), SiO_2/SiO_2-GeO_2 (Core) and SiO_2/Silicon Oxynitride (SiON) core provides moderately low propagation losses, low material cost and compatibility with well known conventional silicon based Integrated Circuit (IC) technology. In fact, SiO_2/SiON is considered as a promising material for development of planar waveguide based optical sensors. SiO_2/SiON materials offers the wide range of refractive index in

between 1.45 (SiO_2) - 2.0 (Si_3N_4) providing the auxiliary advantage for high index contrast designs and due to the property of optical transparence from 210 nm to beyond 2000 nm [26][27]. Apart from the materials, we find that although tremendous progress has been made in the field of integrated optical waveguide sensor, very few studies have been reported for development of integrated planar waveguide optical sensor with enhanced sensitivity and requirement of minimal sample volume for its sensing applications. Previous authors on the existing literature has reported on metal-clad planar waveguide sensor [28], using metamaterial with negative permittivity and permeability [29], Si_3N_4/SiO_2 slot waveguide microring resonator [30], slot-waveguides [31], silicon-on-insulator (SOI) photonic wire waveguides [32], sol–gel SiO_2:TiO_2 film/ion–exchange glass optical waveguides [33] for sensing applications.

From the relevant literature [28]-[39], we find that some authors demonstrate the development of an optical sensor for enhancement of sensitivity, whereas others present different sensing applications. The proposed study in this Ph. D. thesis is aimed at both design and development of a highly sensitive optical sensor based on planar waveguide sensing technology. The sensors make use of very minimal sample volume for its sensing applications such as detection of glucose concentration in blood plasma and also detect adulteration in petroleum products such as petrol, diesel and kerosene. In our studies, a consistent effort has been given in an endeavor to integrate a planar waveguide based optical sensor system with LOC device platform to develop a sensor system that can be used for rapid testing of glucose concentration in blood plasma. The proposed technique can be very useful for management of diabetes, as this can separate plasma from whole blood directly with the use of LOC and then detect glucose concentration in blood plasma. The conclusion in this work is supported by the significant finding, that the sensing approach developed preserves the miniature dimensions of the sensor and simplifies the instrumental design requiring only minimal sample volume of ~0.141 ml for its sensing purpose, which is very small compared to the available work in the existing literature as reported by previous authors.

1.4 Aims and Objectives

As discussed in detail in the preceding chapter 2 (Literature survey), we find that the most important challenge for the sensor applications is its performance and this is in general categorized in terms of three components: Sensitivity, Specificity and Reusability. In this doctoral research work, all these aspect for designing a precise high sensitive sensor have been studied without affecting the input parameters like sensitivity, specificity and reusability and the main objectives of this Ph. D. thesis are considered as follows:

    I. Design and development of the integrated optic waveguide based sensor using silicon based materials.

   II. Implementation of the fabricated integrated optic sensor for detecting adulteration in petroleum based products.

  III. Use of this sensor for detection of glucose level in diabetes.

1.5 Original contribution made by thesis

The contributions are stated below:

1. Design and development of an evanescent planar waveguide optical sensor using Silicon Oxynitride (SiON) as the core layer on silica-silicon wafer and its implementation for sensing glucose concentration in aqueous solution incorporating composite planar waveguide geometry. Using Simple Effective Index Method (SEIM), the theoretical predictions and experimental results at wavelength 632.8 nm are analyzed and presented. The dispersion relation from the wave equation of the optical waveguide structure has been derived for estimating the propagation constants of the modes propagated in the planar waveguide structure. Further, the sensor response to the change of the sensing layer refractive index has also been discussed.

2. Implementation of the integrated optical sensor with the embedded planar waveguide geometry for detecting adulterant traces in petroleum products using SiON planar waveguide technology. The planar waveguide of length ~90,000 μm and core width ~50 μm with high sensitivity can detect adulteration within a very short time ~0.25 second without involving the use of chemicals.

---

3. A rapid diabetic detection technique with waveguide based optical sensing technology using Lab-On-a-Chip (LOC) device platform has been developed, using the principle of Newtonian motion of viscous flow and light propagation through the optical waveguide. The technique developed has been implemented for detection of glucose level in blood plasma of alloxan-induced diabetic rat.

1.6 Outline and scope of the thesis

This Ph. D. thesis comprises of six chapters. It is arranged such that chapter-3 focus on the design and development of a theoretical model for optical sensor using composite planar waveguide geometry, whereas chapter-4 presents its implementation for adulteration sensing application. Chapter-5 deals with integration of planar waveguide sensor structure that was housed within a Cylindrical Enclosure (CE) and interfaced with microfluidic controlled Lab-on-a-Chip (LOC) device for detection of blood glucose concentration in diabetes management. In this thesis, all the chapters including the chapters (3-5) having our works is described as follows:

Chapter 1 gives a preface of the Integrated Optic (IO) sensors as background information with some key terms frequently used in the field of sensors and a brief outline of works presented along with the scope of this thesis. The motivation for the development of an IO sensor based on the platform of Silicon technology is reported in this chapter.

Chapter 2 contains an overview of optical sensor as reported by previous authors. Since, the sensor effect is caused by the interaction of evanescent wave of the guided mode with the sample; the phenomenon of evanescent wave sensing scheme has also been discussed. It has been shown how sensitivity is related to the limit of detection (LOD), which is defined as the minimum amount of concentration or mass of the biochemical substance that can be detected by the sensor over the background signal. In order to explain evanescent wave sensing principle, a mathematical description of wave propagation in planar waveguide using Maxwell's equation has been mentioned. The wave propagations are represented by Simple Effective Index Method (SEIM), Finite

Element Method (FEM), Finite Difference Time Domain (FDTD) method and Beam Propagation Method (BPM) for finding the propagation constant. Since, $SiO_2/SiON$ has been used as the waveguide material for fabricating the optical sensor, in this context an introduction of the silicon material based fabrication platform, that was used to develop the sensor reported in this thesis is given, as well as the motivation for the use of Silicon Oxynitride (SiON) as the waveguide material. A comparative study also has been done with other waveguide material such as SOI, SiO_2/SiO_2-GeO_2, Ti: $LiNbO_3$, GaAsInP/InP and polymeric materials.

Chapter 3 presents the design and development of the proposed planar waveguide structure. Using Maxwell's equation, a theoretical analysis has been carried out for wave propagation in planar waveguide sensor with silicon oxynitride (SiON) as the waveguide material. Using boundary condition of this proposed structure on the solution of wave equation, the dispersion relation from the wave equation of the structure has been derived for estimating the propagation constants of the modes propagated in the planar waveguide structure. The modal analysis of the three dimensional (3D) planar waveguide has been made by using Simple Effective Index method (SEIM) [36]. From the simulation results, it is found that the measured normalized power reduces with increase in length (L) of the waveguide and this decrease slowly with length (L) for L > 100,000 μm. The variation of normalized power with change of refractive index of the sensing region (n_s), ranging from 1.33363 to 1.33453 has also been observed. The sensitivity of the proposed waveguide sensor remains almost constant with core refractive index (n_c) upto n_c=1.46, corresponding to waveguide core of width 50 μm for better coupling of laser light power with wavelength (λ)=632.8 nm. The designed waveguide structure of length~100,000 μm and core width~50 μm has been fabricated using the Silicon Oxynitride (SiON) technology and then adapted for sensing glucose concentration in aqueous solution with high waveguide sensitivity ~0.95. The waveguide sensor having core without top cladding was housed within a Cylindrical Enclosure (CE) with the sample solution inside. The Helium Neon (He-Ne) laser power of wavelength (λ)~632.8 nm was launched into the waveguide sensor using butt coupling through input optical fiber and then output power of the

sensor was coupled to optical fiber with the help of a germanium pin detector. The variation of power with variation of glucose concentration in distilled water has been measured by optical power meter. It has been found that the power decreases with increase of glucose concentration because refractive index (RI) increases with glucose concentration. This variation agrees with theoretical results obtained by using a mathematical model based on SEIM. So, the waveguide sensor can be used for different application such as adulteration of petroleum products and glucose level detection in blood plasma which are discussed in chapter-4 and chapter-5 respectively.

Chapter 4 describes the detection of adulteration of petroleum based products such as petrol, kerosene and diesel with the embedded planar waveguide sensor (as described in chapter 3). The sensor sensitivity has been analyzed for detecting the adulterant traces in pure petroleum products, procured from Indian Oil Corporation Limited (IOCL), Assam Oil Division (AOD) Digboi, Assam. For detecting the petroleum adulteration, adulterated petroleum product was used as a sensing material which acted as a cladding layer of the planar waveguide sensor and was put inside the cylindrical enclosure (CE). The light power obtained from a He-Ne laser of wavelength 632.8 nm was focused into the optical fiber to launch the power into the SiON based waveguide sensor, of length ~90,000 µm and core width ~50 µm with efficient Butt coupling and the output signal from the waveguide sensor was coupled by an optical fiber for detection of the same to the optical detector placed at the other end of the sensor. The sample volume has been estimated and it was found the proposed sensor requires very minimal sample ~ 0.25 ml for its sensing purpose which is 160 times less than that required for fiber optic sensor, as reported in the existing literature. Based on the flow rate of the sample (~1 ml/sec), the detection time has also been estimated and we found that the sensor takes only ~0.25 second for its detection. The variation of the detected power with change of adulterant concentration in petrol has been measured using an optical power meter. The variation of the refractive indices with adulterant (diesel and kerosene) concentration in petrol has also been measured by using an Abbe refractometer. The measured power decreases with increase of kerosene concentration and same variation is obtained with· increase of diesel concentration. This is because the refractive index increases with

increase of adulterant concentration. The waveguide sensitivity is obtained as ~4.1 which is ~40 times more than that of the existing planar waveguide sensors [40] and ~20 times more than that of asymmetric waveguide structure [41]. The technique allows spot determination of adulteration in pure petroleum products without involving the use of chemicals. Further the sensor requires very minimal sample for adulteration detection.

Chapter 5 reports the development of a rapid diabetic detection method using planar waveguide fabricated by us as described in chapter-3. In the proposed method, Lab-on-a-Chip was used for fast separation of plasma and the separated blood plasma was passed from LOC to the cylindrical enclosure (CE) through the interfacing capillary tube. The interfacing tube was designed by considering the Poisselle's equation of viscous flow so that without any micro pump the blood plasma can move into the CE. The length of CE has also been designed by using the same principle so that the viscous force pushes the blood plasma to get the CE filled with it. The LOC device is a commercially available microfluidic chip (*Product code: 15-1503-0168-02, microfluidic ChipShop GmbH, Stockholmer Str.20D-07747 Jena, Germany, dated: 05-03-2013*) of size 75.5 mm x 25.5 mm x 1.5 mm). From the theoretical results, we find that for different waveguide core thickness the measured normalized power decreases with increase of the waveguide length and this becomes almost constant at length (L) ~50,000 μm. Further, we observe that this value has almost been the same as that obtained for the interfacing capillary tube design. So the waveguide of core width 50 μm and length ~50, 000 μm have been fabricated for the use in detection of glucose level in blood plasma as discussed in chapter-3. The fabricated waveguide sensor was housed in the CE which is interfaced with LOC using interfacing capillary tube as mentioned earlier. For our experiment of glucose level detection, diabetes has been induced in the rat with different doses of Alloxan monohydrate injected intraperitoneally. The blood glucose estimation has also been done orally in the pathological laboratory for comparison. It has been observed that the measured normalized power remained invariable as glucose level of rats with alloxan dose 60 mg/kg body weight has almost remain constant (95 mg/dl to 117 mg/dl) which indicated the normal range of glucose level from zero day to 9 days. In case of the rats with

alloxan dose 90 mg/kg body weight, the measured power decreases from zero day to 11 days as glucose level increases with number of days from normal glucose level (110 mg/dl) in zero days to 420 mg/dl, due to over activation of T-cell causing death of insulin secreting β-cells. In case of the rats with dose 110 mg/kg body weight, the glucose level has increased from 108 mg/dl to 823 mg/dl (which is severe diabetic) within 3 days and because of that the measured power is reduced to 40 % with respect to input power. It has been observed that when the rats with alloxan dose 110 mg/kg body weight was administered; they have died after 3 days. The proposed experimental set up (as described in Chapter-3) has been calibrated with the known results (measured orally) obtained from the rats with alloxan dose 90 mg/kg body weight. It has been found that the measured power obtained from the sensor decreases with increase of glucose level. This is because the refractive index (RI) (as measured using Abbe Refractometer) increases with increase of glucose level in blood plasma. After calibration, the glucose level was measured with respect to time (days). It has been found that the variation of glucose level obtained from our set up is close to that obtained orally in the pathological laboratory. Further, it is seen that the signal at the output of the sensor is independent of RI of the SR for $n_s \geq n_c$, as the signal will no longer be confined in the core region. So, the limit of detection (LOD) of our sensor will be restricted up to core RI and for our experimental setup, Limit of Detection (LOD) is ~1.333-1.46 which is found to be more than the earlier reported works.

Finally, in **chapter 6,** the conclusions of the thesis are drawn with key contributions of this Ph. D. research work, as stated earlier in this chapter.

The application of fabricated integrated optical planar waveguide sensor for online monitoring of adulterated petroleum products in refinery during the fractional distillation process can be one of the future prospects. Such a sensor which requires very minimal sample for its adulteration detection without involving any other chemicals would help to ensure the purity of the product yielding better accuracy and high sensitivity compared to the existing optical sensors within a very short time. From the proposed rapid diabetes detection method, it has been observed that this technique can be very easily extended for development of a low cost online diagnostic tool for detecting blood glucose level for diabetic patients in the near future. This planar

waveguide sensor which requires very minimal sample ~0.141 ml is less than the work found in the recent reported literature [32]. Finally, this sensor can also be used for different applications such as rapid testing of bacteria colony detection, arsenic content in water due to its high sensitivity and accuracy.

1.7 List of References

1.   Vijayan, M. V., et al. Fuke, R. N. Karekar, and R. C. Aiyer, Planar Optical Waveguide CO_2 Evanescent Wave Sensor Based on a Clad of Alstonia Scholaris Leaf Extract, *IEEE Sensors Journal* **9** (1), 13-19, 2009.

2.   Abulaiti, H., et al. Highly Sensitive and Selective NiO Film/K+ -Exchanged Glass Composite Optical Waveguide Sensor for Chlorobenzene Vapor Detection, *Journal of Physics: Conference Series* **307**, 1-6, 2011.

3.   Ansari, Z. A., et al. Influence of chlorine on planar optical guide cladded with RbCl and AgCl, *Appl. Surf. Sci.* **125** (2), 149-156, 1998.

4.   DeGrandpre, M. D., et al. Thin film planar waveguide sensor for liquid phase absorbance measurements, *Anal. Chem.* **62** (18), 2012-2017, 1990.

5.   Kuhn, K. J. & Burgess, L. W. Chemometric evaluation of the multimode response of an ion-diffused planar optical waveguide to liquid phase analytes, *Anal. Chem.* **65** (10), 1390-1398, 1993.

6.   Barrios, C. A. Optical Slot-Waveguide Based Biochemical Sensors, *Sensors*, **9** (6), 4751-4765, 2009.

7.   Mukundan, H., et al. Waveguide-Based Biosensors for Pathogen Detection, *Sensors*, **9** (7), 5783-5809, 2009.

8.   Singh, V. & Kumar, D. Theoretical Modeling of a Metal-Clad Planar waveguide based biosensors for the detection of pseudomonas-like bacteria, *Progress in Electromagnetics Research M* **6**, 167–184, 2009.

9.   Barrios, C. A. Label-free optical biosensing with slot-waveguides, *Optics Letters* **33** (7), 708-710, 2008.

10.   Horvath, R., et al. Optical waveguide sensor for on-line monitoring of bacteria, *Optics letters* **28** (14), 1233-1235, 2003.

11. Liu, Y., et al. An Integrated Optical Sensor for Measuring Glucose Concentration, *Appl. Phys. B* **54**, 18-23, 1992.

12. Hulme, J. P., et al. Simple leaky-waveguide devices for the detection of bacterial spores, *Sensors and Actuators B* **160** (1), 1508-1513, 2011.

13. Mukundan, H., et al. Planar optical waveguide-based biosensor for the quantitative detection of tumor markers, *Sensors and Actuators B* **138** (2), 453-460, 2009.

14. Runde, D., et al. Mode-selective coupler for wavelength multiplexing using LiNbO$_3$:Ti optical waveguides, *Cent. Eur. J. Phys.* **6** (3), 588-592, 2008.

15. Rottmann, F., et al. Integrated-optic wavelength multiplerxers on lithium niobate based on two-mode interference, *J. of Lightwave Tech.* **6** (6), 946-952, 1988.

16. Lin, J. P., et al. Four-channel wavelength division multiplexer on Ti: LiNbO$_3$ *Electronics Lett.* **25** (23), 1608-1609, 1989.

17. Mule, A.V., et al. Photopolymer-based diffractive and MMI waveguide couplers, *IEEE Photonic Tech. Lett.* **16** (11), 2490-2492, 2004.

18. Ibrahim, M. H., et al. A novel 1x2 multimode interference optical wavelength filter based on photodefinable benzocyclobuene polymer, *J. of Microwave and Optical Tech. Lett.* **49** (5), 1024-1028, 2007.

19. Chan, H. P., et al. A wide angle X-junction polymeric thermo optic digital switch with low crosstalk, *IEEE Photonic Tech. Lett.* **15** (9), 1210-1212, 2003.

20. Chin, M. K., et al. High-index-contrast waveguides and devices, *Appl. Opt.* **44** (15), 3077-3086, 2005.

21. Nishihara, H., Haruna, M., & Suhara, T. *Optical Integrated Circuits*, McGraw-Hill, New York, 1989.

22. Miya, T. Silica-based planar lightwave circuits: passive and thermally active devices, *IEEE J. Sel. Topics Quantum Electron.* **6** (1), 38-45, 2000.

23. Yamada, H., et al. Si photonic wire waveguide devices, *IEEE J. of Selected Topics in Quant. Electr.* **12** (6), 1371-1379, 2006.

24. Kashahara, R., et al. New structures of silica-based planar light wave circuits for low power thermooptic switch and its application to 8x8 optical matrix switch, *J. Lightwave Tech.* **20** (6), 993-1000, 2002.

25. Worhoff, K., et al. Design, tolerance analysis and fabrication of silicon oxynitride based planar optical waveguides for communication devices, *J. of Lightwave Tech.* **17** (8), 1401-1407, 1999.

26. Bona, G. L., et al. SiON high refractive-index waveguide and planar lightwave circuit, *IBM J. Res. & Dev.* **47** (2.3), 239-249, 2003.

27. Chen, K., & Chan, H. P. Silicon oxynitride optical waveguide ring resonator utilizing a two-mode interference structure, *Int. J. Photoenergy*, **2012**, 1-5, 2012, doi:10.1155/2012/496267.

28. Kumar, D., & Singh, V. Theoretical modeling of a nonlinear asymmetric metal-clad planar waveguide based sensors, *Optik* **122** (20), 1872-1875, 2011.

29. Taya, S. A., et al. Enhancement of sensitivity in optical waveguide sensors using left-handed materials, *Optik* **120** (10), 504-508, 2009.

30. Karasinski, P. Planar Optical Waveguide Sensor Structures with Grating Couplers, *Acta Physica Polonica A* **116**, 30-32, 2009.

31. Carlos, A. B. Optical Slot-Waveguide Based Biochemical Sensors, *Sensors* **9** (6), 4751-4765, 2009.

32. Densmore, A., et al. A Silicon-on-Insulator Photonic Wire Based Evanescent Field Sensor, *IEEE Photonic Tech. Lett.* **18** (23), 2520-2522, 2006.

33. Karasinski, P. Optical uniform/gradient waveguide sensor structure characterization, *Opto-Electronics Review* **19** (1), 01-09, 2011.

34. Parriaux, O., & Dierauer, P. Normalized expressions for the optical sensitivity of evanescent wave sensors: erratum, *Optics Lett.* **19** (20), 1665-1665, 1994.

35. Taya, S.A., et al. Enhancement of sensitivity in optical waveguide sensors using left-handed materials, *Optik* **120** (10), 504-508, 2009.

36. Renling, Z., et al. The Sensing Structure Optimization of Planer Optical Waveguide with Fermi Refractive Index, *J. of Lightwave Tech.* **28** (23), 3439-3443, 2010.

37. Yimit, A., et al. Thin film composite optical waveguides for sensor applications: a review, *Talanta* **65** (25), 1102-1109, 2005.

38. Airoudj, A., et al. Design and Sensing Properties of an Integrated Optical Gas Sensor Based on a Multilayer Structure, *J. Anal. Chem.* **80** (23), 9188-9194, 2008.

39. Veldhuis, G.J., et al. Sensitivity Enhancement in Evanescent Optical Waveguide Sensors, *J. of Lightwave Tech.* **18** (5), 677-682, 2000.

40. Passaro, V.M.N., & Dell''olio, F. Guided-wave optical biosensors, *Sensors* **7** (4), 508-536, 2007.

41. Taya, S. A., et al. Theoretical Analysis of TM nonlinear asymmetrical waveguide optical sensors, *Sensors and Actuators A: Phys.* **147**, 137-141, 2008.

✳ ✳ ✳ ✳ ✳

My scientific studies have afforded me great gratification; and I am convinced that it will not be long before the whole world acknowledges the results of my work.

-Gregor Mendel

Integrated Planar Waveguide Optical Sensor – A Review Study

Outline of the Chapter:

2.1 Introduction
2.2 Fundamentals of optical waveguide
    2.2.1 Wave equation in symmetric slab waveguide
    2.2.2 Planar waveguides and the modes
        2.2.2.1 Guided modes
        2.2.2.2 Radiation and leaky modes
    2.2.3 Introduction to Numerical methods for approximate modal analysis
        2.2.3.1 Effective Index Method (EIM)
        2.2.3.2 Finite Element Method (FEM)
        2.2.3.3 Finite Difference Time Domain (FDTD) Method
        2.2.3.4 Beam Propagation Method (BPM)
2.3 Optical sensor and its Classification
    2.3.1 Fiber Optic (FO) sensors and classification
        2.3.1.1 Intensity Based Fiber Optic Sensor
        2.3.1.2 Wavelength Modulated Fiber Optic Sensors
        2.3.1.3 Phase Modulated Fiber Optics Sensors
        2.3.1.4 Polarization Modulated Fiber Optic Sensors
    2.3.2 Integrated Optical Waveguide Sensors
        2.3.2.1 Integrated Optical Interferometers
        2.3.2.2 Grating-Coupler Sensors
        2.3.2.3 Evanescent-Wave and Surface Plasmon Resonance Sensors
    2.3.3 Basic Principle: Optical Planar Waveguide Sensors
        2.3.3.1 Integrated Optic Planar Waveguide Sensor Effect
    2.3.4 Comparison between fiber optic sensor and integrated optical planar waveguide sensor
    2.3.5 Requirement of IO planar waveguide sensors
2.4 Performance parameters of optical sensors
    2.4.1 Sensor Sensitivity
    2.4.2 Limit of Detection (LOD)
    2.4.3 Limit of Quantization (LOQ)
    2.4.4 Selectivity or Specificity
    2.4.5 Sample Volume
2.5 Review on planar waveguide materials and fabrication technologies
2.6 Optical planar waveguide sensor and applications-a review study
    2.6.1 Refractometric optical sensing and petroleum fuel adulteration
        2.6.1.1 Causes of petroleum adulteration
        2.6.1.2 Impacts due to petroleum adulteration
        2.6.1.3 Petroleum adulteration detection as reported by earlier authors
        2.6.1.4 Status of petroleum adulteration in Indian context
    2.6.2 Integrated optical waveguide sensor as detection element for
    Lab-on-a-Chip sensing application
        2.6.2.1 Non-invasive sensing approach for measurement of glucose concentration
        2.6.2.2 Significance of sensing glucose

Chapter 2

2.1 Introduction

Recently, optical techniques have been demonstrated for sensing applications due to its high sensitivity, selectivity and low detection time. Such sensing that make use of change of light energy through bio/chemical/mechanical processes into a detectable signal adds to intrinsic advantages because of its accuracy. As compared to other existing sensing technologies, the strength and versatility of optical sensors lie in the wide range of optical properties that serve to generate the sensing signal. These properties include, but are not limited to refractive index, optical absorption, fluorescence, polarization, and even nonlinear optical processes such as lasing, Raman scattering, and multi-photon absorption and emission. When used alone or in combination, the sensing signals can provide vast amount of information regarding the presence and interaction of bio/chemical molecules. As a result, optical sensors have broad applications in clinical diagnostics, biotechnology industry, pharmaceuticals, and petroleum adulteration. In this direction, waveguide optics has become attractive for sensing application which can be summarized as follows:

- o High sensitivity/specificity.
- o Immunity to any kind of electromagnetic interference (E.I).
- o Small size, light weight and great flexibility, that allow access to otherwise restricted areas.
- o Capability of resisting to chemically aggressive and ionizing environments.
- o Easy interface with fiber optic network.
- o Low detection time

There are three basic characteristics for performance evaluation of an optical sensor.

- ▪ Light–analyte interaction: Stronger light-matter interaction usually results in a higher sensitivity and better (e.g., lower) detection limit.

- Sensor miniaturization: These are directly related to sample consumption, device portability, detection time, and detection cost.

- Integration of fluidics with optical sensing elements: Effective and efficient fluidics not only reduces the sample consumption and hence the cost, but also enhances light–analyte interaction and expedites the detection processes.

In this chapter, initially we have started with fundamentals of optical waveguide, as its principle forms the basis for optical sensing mechanism. We have described different types of optical sensors such as fiber optic sensor and planar waveguide sensors. Since the proposed sensor has been used for detecting adulteration in chapter-4 of this doctoral research, in this regards, a review has also been done on sensors used for detection of adulteration using waveguide sensors. Finally, we have described works on sensors used for detection of glucose level in blood, as reported by earlier authors from the existing literature as the proposed sensor have been used for detection of glucose level in blood as described in chapter–5 of this Ph. D. thesis.

2.2 Fundamentals of optical waveguide

Planar waveguides are optical structures that confine optical radiation along the direction of propagation [1]. Considering the refractive index distribution in the planar waveguide structure, these can be classified as step-index waveguides or graded index waveguides. The step-index planar waveguide is the simplest structure for light confinement, and is formed by a uniform planar film with a constant refractive index (homogeneous film, n_f =constant), surrounded by two dielectric media of lower refractive indices [2]. The homogeneous upper medium, or cover, has a refractive index of n_c, and the lower medium, with refractive index n_s, is often called substrate. Usually, it is assumed that the refractive index of the cover is less than or equal to the refractive index of the substrate, $n_c \leq n_s$, and in this way we have $n_f > n_s \geq n_c$.

If the upper and the lower media are the same (equal optical constants), the structure forms a symmetric planar waveguide. On the other hand, in integrated optics if the upper and lower media are different, then it is known as an asymmetric planar waveguide (Fig. 2.1). If the high index film is not homogeneous, but its refractive index

is depth (thickness of the waveguide) dependent (along the x-axis in Fig. 2.2), the structure is called a graded index planar waveguide [3]. Usually the refractive index is maximum at the top surface, and its value decreases with thickness until it reaches the value corresponding to the refractive index of the substrate (Fig. 2.2).
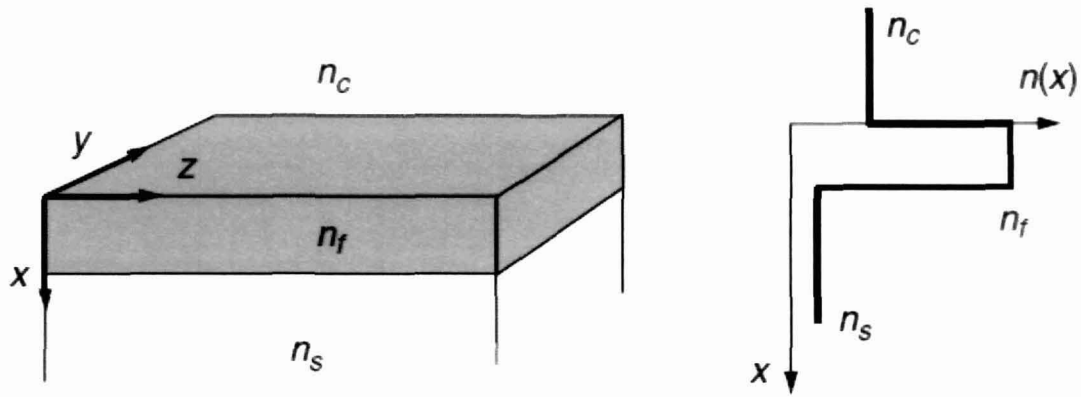
Fig-2.1: Asymmetric step index planar waveguide. Right: refractive index profile, where $n_f > n_s \geq n_c$ [1].
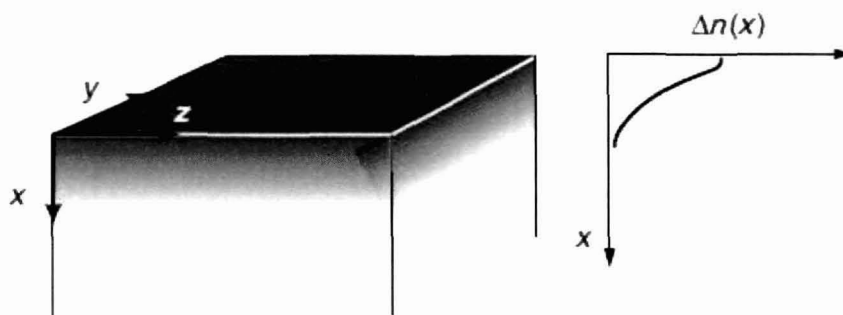
Fig-2.2: Graded index planar waveguide [1].

Asymmetric step-index planar waveguides are fabricated by depositing a high-index film on top of a lower index substrate, by means of physical methods (thermal evaporation, molecular beam epitaxy, sputtering, etc.) or chemical methods (chemical vapour deposition, metal-organic chemical vapour deposition etc.).

The more accurate description of light propagation within a waveguide is obtained by means of Maxwell's equations. When the geometric boundary conditions at media

interfaces are introduced, only discrete solutions of the wave equations are permitted. This means that only discrete waves can propagate, namely 'modes', characterized by discrete amplitudes and discrete velocities [4] [5]. Waveguides can be single-mode or multimode according to whether a single or a multiplicity of modes can propagate. Once the materials constituting the waveguide are set for a given wavelength, the number of supported modes depends on waveguide dimension, namely on the fiber core radius or the planar waveguide thickness. A characteristic of a guided mode which is particularly important for sensing devices is its spatial amplitude distribution. Often, in fact, the interaction between the propagating mode and the quantity to be measured (the measurand) occurs through the evanescent field of the mode itself, namely its exponentially-decreasing tail.

2.2.1 Wave equation in symmetric slab waveguide
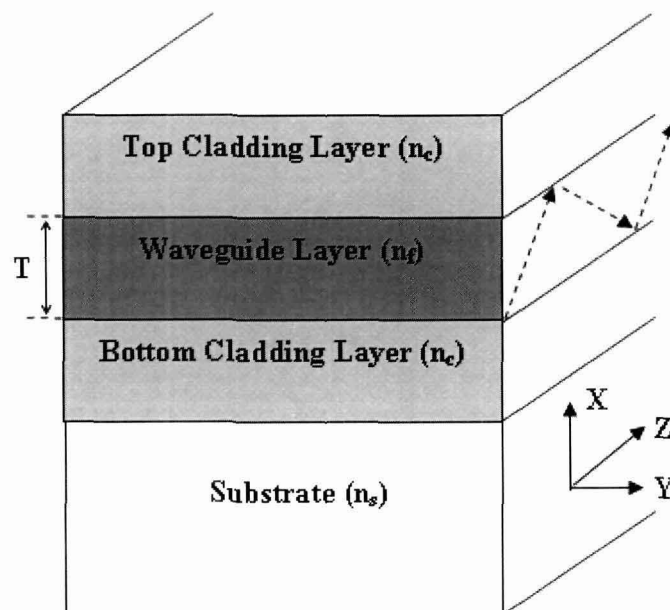
Fig-2.3: Schematic view of Integrated Optic waveguide sensor structure

Fig-2.3 shows the schematic view of a symmetric waveguide consisting of a waveguide layer of refractive index n_f having lightwave confined, top and bottom cladding layers

each having of refractive indices n_c respectively. The wave propagation of the waveguide (Fig. 2.3) can be analysis considering the Maxwell equation [4-5] as follows,

$$\nabla \times E = -\mu_0 \frac{\partial H}{\partial t} \tag{2.1}$$

and $\quad \nabla \times H = \varepsilon_0 n^2 \frac{\partial E}{\partial t} \tag{2.2}$

where n is the refractive index. Also the plane-wave propagation can be define as

$$E = E(x, y) e^{j(\omega t - \beta z)} \tag{2.3}$$

$$H = H(x, y) e^{j(\omega t - \beta z)} \tag{2.4}$$

Substituting Eqs. (2.3) and (2.4) into Eqs. (2.1) and (2.2) respectively, we obtain the following two set of equations for the electromagnetic field components:

$$\begin{cases} \dfrac{\partial E_z}{\partial y} + j\beta E_y = -j\omega\mu_0 H_x \\[2mm] -j\beta E_x - \dfrac{\partial E_z}{\partial x} = -j\omega\mu_0 H_y \\[2mm] \dfrac{\partial E_y}{\partial x} - \dfrac{\partial E_x}{\partial y} = -j\omega\mu_0 H_z \end{cases} \tag{2.5}$$

$$\begin{cases} \dfrac{\partial H_z}{\partial y} + j\beta H_y = j\omega\varepsilon_0 n^2 E_x \\[2mm] -j\beta H_y - \dfrac{\partial H_z}{\partial x} = j\omega\varepsilon_0 n^2 E_y \\[2mm] \dfrac{\partial H_y}{\partial x} - \dfrac{\partial H_x}{\partial y} = j\omega\varepsilon_0 n^2 E_z \end{cases} \tag{2.6}$$

From the Fig. 2.3, it is observed that both the electromagnetic fields: electric field (E) and magnetic field (H) are y-axis independent i.e. $\dfrac{\partial E}{\partial y} = 0$ and $\dfrac{\partial H}{\partial y} = 0$. Substituting these relations into Eqs. (2.5) and (2.6), two independent electromagnetic modes are obtained, which are denoted as TE mode and TM mode respectively. The TE mode satisfies the following wave equation:

$$\frac{d^2 E_y}{dx^2} + \left(k^2 n^2 - \beta^2\right) E_y = 0 \tag{2.7}$$

where
$$H_x = \frac{-\beta}{\omega\mu_0} E_y$$
(2.8)

$$H_z = \frac{j}{\omega\mu_0} \frac{dE_y}{dx}$$
(2.9)

and $E_x = E_z = H_y = 0$
(2.10)

From the equations (2.8)-(2.10), it is seen that the tangential components E_y and H_z should be continuous at the boundaries of two different media and the electric field component along the z-axis is zero (i.e. $E_z = 0$). Since the electric field lies in the plane that is perpendicular to the z-axis, this electromagnetic field distribution is called Transverse Electric (TE) mode.

The equation (2.6) can be written by considering y independency for TM mode which satisfies the following wave equation:

$$\frac{d}{dx}\left(\frac{1}{n^2}\frac{dH_y}{dx}\right) + \left(k^2 - \frac{\beta^2}{n^2}\right)H_y = 0$$
(2.11)

where $E_x = \frac{\beta}{\omega\varepsilon_0 n^2} H_y$
(2.12)

$$E_z = -\frac{j}{\omega\varepsilon_0 n^2}\frac{dH_y}{dx}$$
(2.13)

$$E_y = H_x = H_z = 0$$
(2.14)

Thus the Eq. (2.14) gives the magnetic field component along the z-axis is zero (i. e. $H_z=0$). Since the magnetic field lies in the plane that is perpendicular to the z-axis, this electromagnetic field distribution is called Transverse Magnetic (TM) mode. The solution in the case of light propagation with TM polarization is basically the same for the TE polarization, with the exception that the boundary conditions are slightly different, because of the factor $(1/n^2)$ in the continuity of the magnetic field component derivative.

2.2.2 Planar waveguides and the modes

Light propagation in the optical waveguide has been analyzed by examining the case of an asymmetric planar waveguide from the point of view of ray optics.

We consider the planar waveguide depicted in Fig. 2.3, where we have assumed that the refractive index of the film n_f is higher than the refractive index corresponding to the substrate n_s and the upper cover n_c. In addition, we assume the usual situation in which the relation $n_s > n_c$ is fulfilled. In this way, the critical angles that define Total Internal Reflection (TIR) for the cover–film interface (θ_{1C}) and the film–substrate boundary (θ_{2C}) are determined by:

$$\theta_{1c} = \sin^{-1}\left(\frac{n_c}{n_f}\right)$$ (2.15)

$$\theta_{2c} = \sin^{-1}\left(\frac{n_s}{n_f}\right)$$ (2.16)
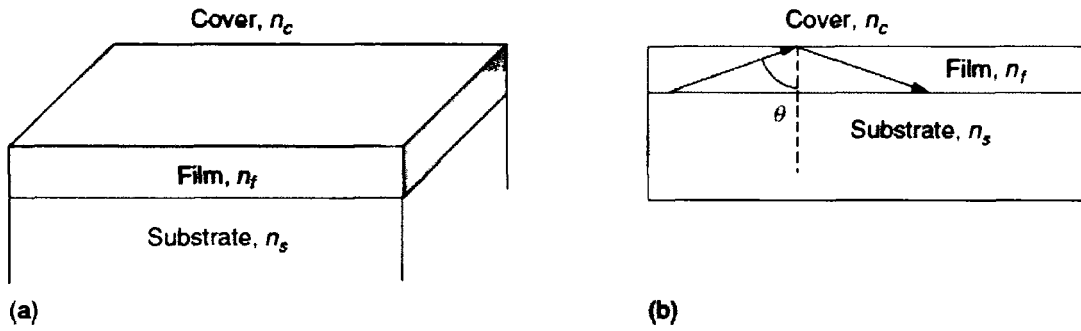
Fig-2.4: (a) Asymmetric planar waveguide and (b) Zig-zag trajectory of a ray inside the film [1].

In addition, as we have $n_f > n_s \geq n_c$, it follows that the critical angles fulfill the relation $\theta_{2c} > \theta_{1c}$. If now we fix our attention to the propagating angle θ of the light inside the film [Fig. 2.4], three situations can be distinguished:

(i) $\theta < \theta_{1C}$. In this case, if the ray propagates with internal angles θ lower than the critical angle corresponding to the film–cover interface θ_{1C}, the light penetrates the cover, as well as the substrate, because $\theta_{2C} > \theta_{1C}$. Thus, the radiation is not confined to the film, but travels in the three regions. This situation corresponds to radiation modes, because the light radiates to the cover layer and the substrate (Fig. 2.5).
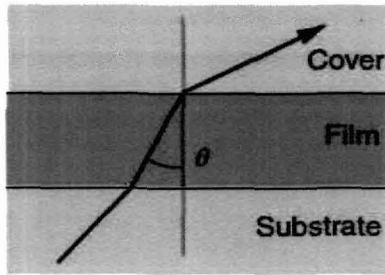
Fig-2.5: Radiation mode in an asymmetric step-index planar waveguide [1].

(ii) $\theta_{1c} < \theta < \theta_{2c}$. Light travelling in these circumstances is totally reflected at the film-cover interface, thus it cannot penetrate the cover region. Nevertheless, the radiation can still penetrate the substrate, and therefore it corresponds to substrate radiation modes, or in short, substrate modes (Fig. 2.6).
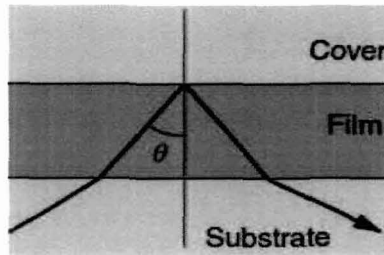
Fig-2.6: Ray path followed by a substrate radiation mode [1].

(iii) $\theta_{2c} < \theta < \dfrac{\pi}{2}$. In this situation, the ray will suffer total internal reflection (TIR) at the upper and lower interfaces, and thus the radiation is totally confined and cannot escape the film. This corresponds to a guided mode (Fig. 2.7).
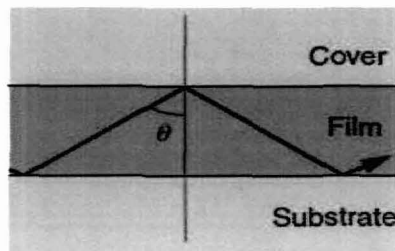
Fig-2.7: Guided mode in an asymmetric planar waveguide, showing the ray path [1].

The optical ray approach for the guided modes in planar optical waveguides, considering a ray of light inside the film moving on a zig-zag path. The first condition which a ray of light must fulfill in order to be confined in the film region is that the angle of incidence at the upper and lower interfaces must be higher that the critical angles at the cover–film and film–substrate boundaries (Fig. 2.8).
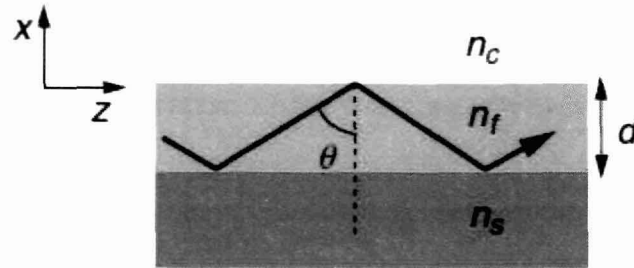
Fig-2.8: Ray tracing a zig-zag path in an asymmetric step-index planar waveguide [1].

The general solution of the wave equation discussed in the previous section have been applied to the case of guided modes supported by asymmetric step-index planar waveguides, considering the geometry as shown in Fig. 2.9.

2.2.2.1 Guided modes

The general solution discussed in the previous section 2.2.1 can easily be applied to the case of guided modes supported by asymmetric step-index planar waveguides, considering the geometry as shown in Fig. 2.9.
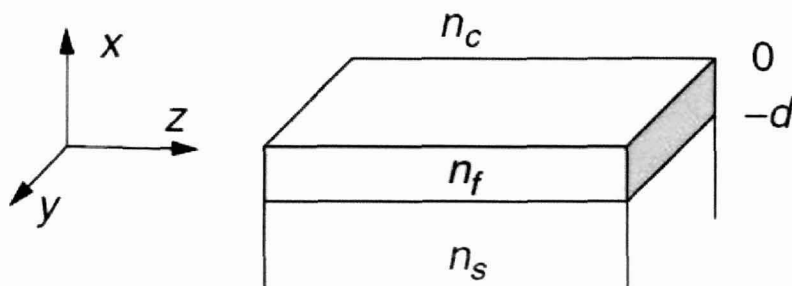
Fig-2.9: Geometry used for the analysis of propagating modes in an asymmetric step-index planar waveguide [1].

The three media have refractive indices n_c (cover), n_f (film) and n_s (substrate), and are separated by planar boundaries perpendicular to the x-axis, the light propagation being along the z-axis. We further assume that $n_f > n_s \geq n_c$ and that the plane $x=0$ corresponds to the cover–film boundary. Therefore, if the film thickness is d, the film–substrate interface is located at the plane $x= -d$ respectively.

Guided TE-modes

Although step-index planar waveguides are the structures inherently inhomogeneous, within each of the three regions the refractive indices are constant. Thus, considering each region separately, the wave equation for TE modes is expressed as shown in Eq. (2.7).
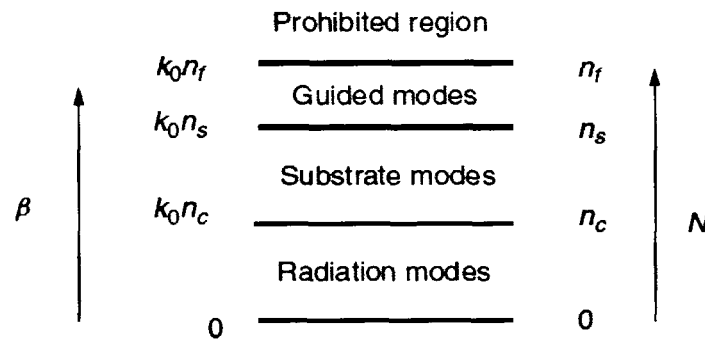
Fig-2.10: Range of values for the propagation constant β and the effective refractive index N for guided modes, substrate modes and radiation modes [1].

Fig. 2.10 shows the range of values for the propagation constant β and the effective refractive index N for guided modes, substrate modes and radiation modes. The propagation constant β associated with a particular mode must fulfill the condition:

$$k_0 n_s < \beta < k_0 n_f \qquad (2.17)$$

Further, the effective refractive index, N of the guided mode must lie in between the refractive index of the film n_f and the refractive of the substrate n_s (reference to Fig. 2.9).

$$n_s < N < n_f \qquad (2.18)$$

The wave equation (2.7) in each homogeneous region can be written as:

$$\frac{d^2E_y}{dx^2} - \gamma_c^2 E_y = 0 \quad x \geq 0 \qquad \text{(Cover)} \qquad (2.19)$$

$$\frac{d^2E_y}{dx^2} + K_f^2 E_y = 0 \quad 0 > x > -d \qquad \text{(Film)} \qquad (2.20)$$

$$\frac{d^2E_y}{dx^2} - \gamma_s^2 E_y = 0 \quad x \leq -d \qquad \text{(Substrate)} \qquad (2.21)$$

where the three parameters γ_c, K_f and γ_s are given by:

$$\gamma_c^2 = \beta^2 - k_0^2 n_c^2 \qquad (2.22)$$

$$K_f^2 = k_0^2 n_f^2 - \beta^2 \qquad (2.23)$$

$$\gamma_s^2 = \beta^2 - k_0^2 n_s^2 \qquad (2.24)$$

By solving the differential equations (2.22)–(2.24), the electric fields in the cover, film and substrate regions can be expressed as:

$$E_y = \begin{cases} Ae^{-\gamma_c x} & x \geq 0 \\ Be^{iK_f x} + Ce^{iK_f x} & -d < x < 0 \\ De^{\gamma_s x} & x \leq -d \end{cases} \qquad (2.25)$$

The boundary conditions require that E_y and dE_y/dx must be continuous at the cover–film interface ($x=0$) and at the film–substrate frontier ($x=-d$), giving place to four equations that relate the constant parameters A, B, C and D and the propagation constant β. Therefore, we have five unknown quantities to be determined from only a set of four equations. Indeed, one of the constant parameters cannot be determined and should remain free (for instance, the parameter A), and it will be determined once the energy carried by the propagating mode is settled. By solving this set of equations, and after cumbersome calculation, the following equation is obtained:

$$\tan(K_f d + m\pi) = \frac{\dfrac{\gamma_c}{K_f} + \dfrac{\gamma_s}{K_f}}{1 - \left(\dfrac{\gamma_c}{K_f}\right)\left(\dfrac{\gamma_s}{K_f}\right)} \quad ; \text{ where m=0, 1, 2, 3 ...} \qquad (2.26)$$

This relation is considered as the dispersion relation for the asymmetric step index planar waveguide, and is a transcendental equation involving the parameters that define the waveguide structure (n_c, n_f, n_s and d), the working wavelength (λ) and the propagation constant β of the guided mode, and from which one can calculate numerically the propagation constant β. In general, there exist several solutions for the propagation constant β depending on the integer number m. This integer number m is called the mode order, and the associated propagation constant is referred as β_m.

It is convenient to define a set of parameters, called *normalized parameters*, in such a way that the transcendental equation (2.26) can be universalized for any asymmetric step-index waveguide. These parameters are defined as:

$$b = \left(N^2 - n_s^2\right) \Big/ \left(n_f^2 - n_s^2\right) \tag{2.27}$$

$$V = k_0 d \left(n_f^2 - n_s^2\right)^{1/2} \tag{2.28}$$

$$a = \left(n_s^2 - n_c^2\right) \Big/ \left(n_f^2 - n_s^2\right) \tag{2.29}$$

$$\tan\left[V\sqrt{1-b}\right] = \frac{\sqrt{\dfrac{b}{1-b}} + \sqrt{\dfrac{b+a}{1-b}}}{1 - \dfrac{\sqrt{b(b+a)}}{1-b}} \tag{2.30}$$

In general, Eq. (2.26) or (2.30) admit a finite number of solutions for a finite number of the integer, m and thus the waveguide will support a finite number of guided modes. In this case, we refer to it as a multi-mode waveguide. In the particular case in which the dispersion equation only admits a solution for m=0, the waveguide is called a monomode or single mode waveguide.

Guided TM modes

In this case we are interested in the determination of the electromagnetic field structure within the planar waveguide based on the magnetic field, because in TM polarization the magnetic field has a single component (H_y). The wave equation for TM propagation in a homogeneous region can be expressed as:

$$\frac{d^2 H_y}{dx^2} + [k^2 n^2 - \beta^2] H_y = 0 \tag{2.31}$$

Following a similar procedure to that performed for TE modes in section 2.2.2.1, a transcendental equation for confined TM waveguide modes in terms of the normalized parameters is obtained as:

$$\tan[V\sqrt{1-b}] = \frac{\dfrac{1}{\gamma_1}\sqrt{\dfrac{b}{1-b}} + \dfrac{1}{\gamma_2}\sqrt{\dfrac{b+a}{1-b}}}{1 - \dfrac{1}{\gamma_1\gamma_2}\dfrac{\sqrt{b(b+a)}}{(1-b)}} \tag{2.32}$$

This is the dispersion relation for TM guided modes of an asymmetric step-index planar waveguides. In this equation we have defined, (say, for simplicity) the parameters as

$$\gamma_1 \equiv \left(\frac{n_s}{n_f}\right)^2, \ \gamma_2 \equiv \left(\frac{n_c}{n_f}\right)^2 = \gamma_1 - a(1-\gamma_1)$$

Cut-off

An important aspect concerning waveguides is to know what should be the minimum film width necessary for the waveguide support of a specific mode of order m, at a given wavelength. In this situation, the effective refractive index of this particular mode N should be very close to the substrate refractive index n_s, as it is shown schematically in Fig. 2.11.
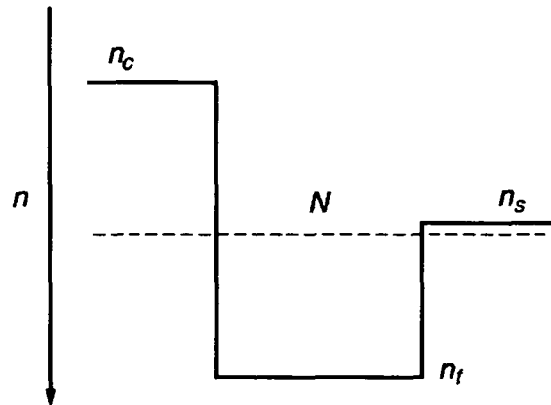
Fig-2.11: Position of the effective refractive index N, relative to the refractive indices of the waveguide structure, for a mode close to the cut-off [1].

In this case, it yields:

$$N \approx n_s \Rightarrow b = \frac{\left(N^2 - n_s^2\right)}{\left(n_f^2 - n_s^2\right)} \approx 0 \qquad (2.33)$$

The normalized film thickness V for TE and TM modes at the cut-off is given by,

$$V_C^{TE} = \tan^{-1}\left(a^{1/2}\right) + m\pi \qquad ; \text{TE modes} \qquad (2.34)$$

$$V_C^{TM} = \tan^{-1}\left(\frac{a^{1/2}}{\gamma_2}\right) + m\pi \qquad ; \text{TM modes} \qquad (2.35)$$

From these relations, two important conclusions can be deduced:

(i) As n_c must be lower than n_f, it follows that $\gamma_2 = \left(\frac{n_c}{n_f}\right)^2 < 1$, and consequently it holds that $V_C^{TM} > V_C^{TE}$. This inequality implies that if a waveguide supports a TM mode of m-th order, the waveguide also supports a TE mode of the same order. The reciprocal situation does not apply in general.

(ii) For a symmetric waveguide (a=0), Eq. (2.30) and Eq. (2.32) yield $V_C^{TM} = V_C^{TE} = m\pi$. This indicates that a symmetric planar waveguide always supports at least the fundamental mode m=0, both TE and TM polarized modes, regardless of the size (film thickness) or refractive indices of the guiding structure.

2.2.2.2 Radiation and leaky modes

Up to now we have examined the solution of the wave equation for planar waveguides in terms of guided modes, where the radiation is mainly confined only within the film, in the form of evanescent waves. In this case, the mode effective index was restricted between the refractive index of the film and that of the substrate. Nevertheless, the wave equation, for both TE and TM polarization light also admits solutions for effective indices lower than n_s. In this case, we are dealing with radiation modes, where the light is no longer confined to the film, but can "leak" to adjacent regions, losing the light power inside the film core as the wave propagates along the waveguide. For this reason, these types of solutions are often called leaky modes.

For effective refractive index values lower than n_s and higher than n_c (i.e. $n_c \langle N \langle n_s$ or $k_0 n_c \langle \beta \langle k_0 n_s$), the solutions in the film and substrate regions are in the

form of oscillatory functions, while the behavior of the fields in the cover region is in the form of exponential decay. This condition $\beta \langle k_0 n_s$ corresponds to substrate radiation modes, where the light is not confined to the film region, but also spreads out to the substrate, as can be seen in Fig. 2.12. In addition, the solutions for these leaky substrate modes are not discrete, but instead the wave equation for substrate modes admits an infinite number of solutions for continuous propagation constant values β (or effective refractive index N).
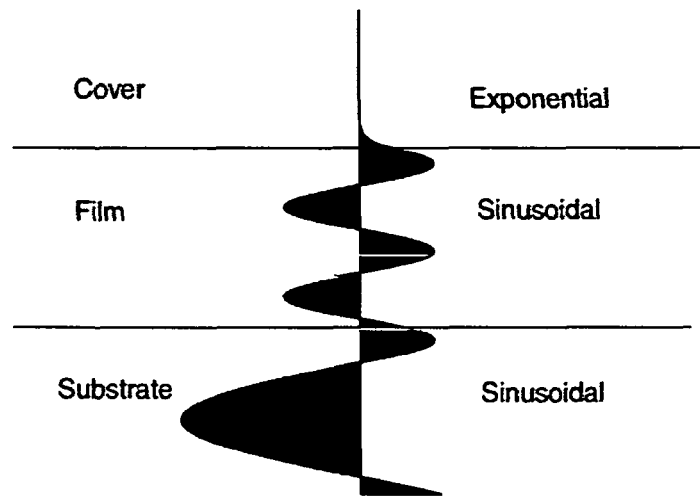
Fig-2.12: Substrate radiation mode in an asymmetric step-index planar waveguide [1].
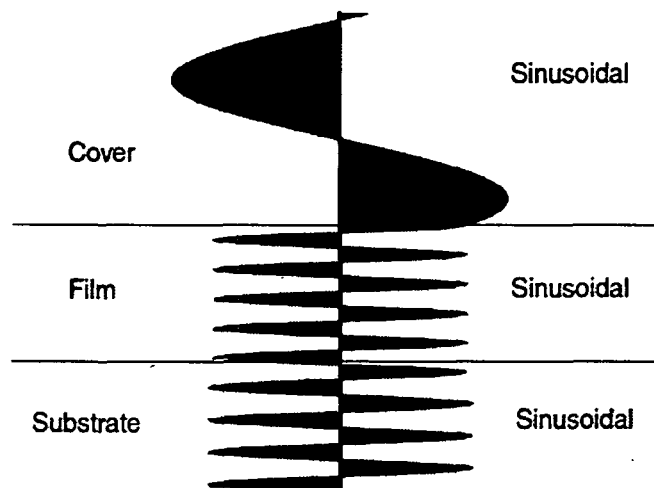
Fig-2.13: Radiation mode in an asymmetric step-index planar waveguide [1]

Finally, if the modal effective refractive index N is lower than n_c ($N < n_c \Rightarrow \beta < k_0 n_c$) the solution for the modal fields in the three regions is in the form of sinusoidal functions. In this case the field pattern corresponds to a radiation mode, where the light cannot be confined in the film but leaks to the cover and substrate regions, as can be seen in Fig. 2.13. Also, as in the case of substrate modes, there exist a continuous and infinite number of values for the propagation constant of radiation modes, with an infinite number of solutions for the electromagnetic field distribution.

2.2.3 Introduction to Numerical methods for approximate modal analysis

There are several numerical methods for modal characterization in optical waveguides which yield good results in general. However, we will describe here four widely used methods:

2.2.3.1 Effective Index Method (EIM)

Marcatili's method (Marcatili, 1969) [6] was extended by Knox and Toulios (1970) [7] who proposed the Effective Index Method (EIM), which soon after became one of the most popular methods for the analysis of optical waveguides. Unlike numerical methods, EIM is considered as semi-analytical methods, which make certain approximation to the structure under consideration and then solve the resulting simplified problem analytically. The popularity of the EI method is due to its simplicity, which comes from the fact that it reduces the three dimensional wave guide structures into an equivalent two-dimensional structure.

This method is one of the simplest approximate methods for obtaining the modal fields and the propagation constant analysis for calculating the propagation modes of channel waveguides. It applies the tools developed for planar waveguides to solve the problem of two-dimensional (2D) structures in channel waveguides having arbitrary geometry and index profiles. It consists of solving the problem in one dimension, described by the x coordinate, in such a way that the other coordinate (the y-coordinate) acts as a parameter. In this way, one obtains a y-dependent effective index profile; this generated index profile is treated once again as a one-dimensional problem from which the effective index of the propagating mode is finally obtained. The propagation

constants supported by a 2D channel waveguide having a refractive index profile which depends on two coordinates n=n(x, y) are then calculated by solving the propagation modes for two 1D planar waveguides. The EIM treats the channel waveguide as the superimposition of two 1D waveguides: planar waveguide-I confines light in the x-direction, while planar waveguide-II traps light in the y-direction [as shown in Fig.-2.14]. For propagating modes polarized mainly along the x-direction $\left(E_x^{pq}\right)$, where that the major field components are E_x, H_y and E_z. The propagation of these polarized modes is similar to the TM modes in a 1D planar waveguide, and their solutions will correspond to the effective indices N_I. Further, the second planar waveguide (waveguide-II) is considered to be built from a guiding film of refractive index N_I, which has previously been calculated. The modes for the second planar waveguide are TE polarized, with E_x, H_y and H_z as non-vanishing components, because the light is mainly polarized along the x-direction.

(a) 3D Waveguide-I

(b) 2D Waveguide-I
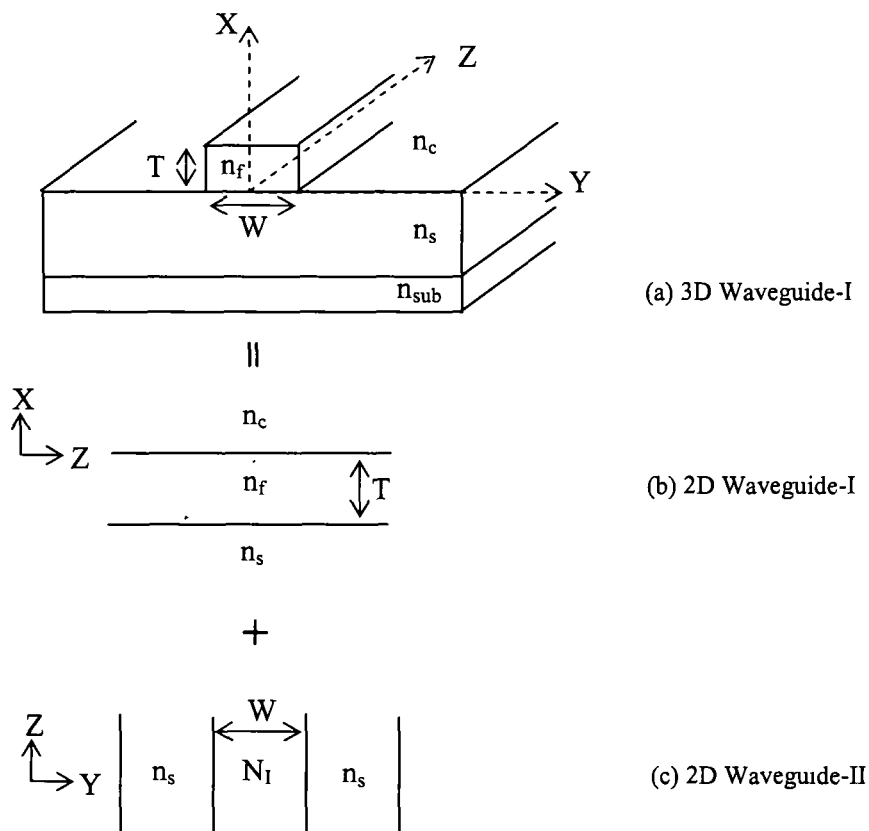
(c) 2D Waveguide-II

Fig-2.14: Analytical model of effective index method for 3D waveguide geometry [8].

In the Fig-2.14, an analytical model of simple effective index method (SEIM) for three dimensional (3D) waveguide geometry has been shown, where

N_l = Effective refractive index of 2D waveguide-I

n_s =n_c =Refractive index of upper cladding and lower cladding

n_{sub} =Refractive index of substrate

T = Thickness of 2D waveguide-I and

W =Width of 2D waveguide-II

The procedure for calculation of effective refractive index for 3D waveguide geometry can be summed up as follows [8],

(i) The two dimensional optical waveguide is replaced with a combination of two one dimensional optical waveguides.

(ii) For each one dimensional waveguide, the effective is calculated index along y-axis.

(iii) The waveguide is modeled by using the effective index calculated in step (2) along x-axis.

(iv) The effective index is to be obtained by solving the model in step-3 along x-axis.

In the analysis of optical waveguides, analytical methods such as Effective Index Method (EIM), Marcatili's methods etc. are slightly less accurate than Finite Difference Time Domain (FDTD) and Beam Propagation Method (BPM) [9]. In spite of the lower accuracy, these methods have become popular waveguide design tools because of their simplicity, easier to use, requires lesser numerical calculations. The ability to convert a three dimensional problem in two dimensional one is the main feature and advantage of this method [8]. So we have tried to use this method in the study of mode propagation of our proposed planar waveguide based optical sensor in the proceeding chapters of the thesis.

2.2.3.2 Finite Element Method (FEM)

The finite-element method (FEM) uses a variational formulation for the solution of waveguide problems [9]. For dielectric waveguides, the usual approach is to use all three components of the H or the E vector. The advantage of using the three

components of the field is that no boundary conditions need to be set except at the exterior boundary. From Maxwell's equations,

$$\nabla \times \varepsilon_r^{-1}(\nabla \times H) = k_0^2 H \qquad (2.36)$$

Taking the inner product of this equation with H^* leads to a functional of the form

$$F = \int_S \left[(\nabla \times H)^* . \varepsilon_r^{-1}(\nabla \times H) - k_0^2 H..H^*\right] dxdy \qquad (2.37)$$

If the trial function coefficients are a_i, then requiring $\partial F/\partial a_i = 0$ provides the equations for the matrix eigen value problem. The trial functions must span the whole domain and satisfy the exterior boundary conditions, and this becomes difficult for arbitrary shapes. Thus, the finite-element method discretizes the domain into a set of adjoining triangles, and the trial functions are defined within each triangle with unknown coefficients. In the nodal element scheme, the trial functions are expressed in the non-orthogonal area coordinates ζ_I, and linear higher order trial functions in terms of the ζ_I can be used. Further, the integrations of the functional can be performed for each triangle before the matrix equation is assembled. The problem with the functional in (2.37) is that, spurious eigen value modal solutions occur. Furthermore, the formulation requires that β be specified, and the corresponding frequency ω in k_0 is obtained. Since the divergence equation has not been specifically set in this functional, inclusion of this equation in the functional with a summation parameter α mitigates this. While this approach does not eliminate the spurious modes, it pushes them to the higher order modes depending on the choice of α. Some check needs to be made to ensure that the spurious modes are eliminated from the solutions by running the code with different values of α. Using this technique, Rahman and Davies [10] have obtained results on a ridge guide that remain the benchmark against which all other methods are compared. This method has also been used by other groups [11] for modal solutions. An improvement on the three component field method was suggested by Cendes [12], in which the transverse fields are defined by edge elements and the longitudinal field is defined by the usual nodal elements. An edge element between the triangle vertices is defined by,

$$W_{ij} = \left(\zeta_i \nabla \zeta_j - \zeta_j \nabla \zeta_i\right) l_{ij} \qquad (2.38)$$

where ζ_I is the area coordinate defined above and l_{ij} is the length of the edge between these vertices.

The result of this definition is that the edge element is a trial function that is along the edge ij. The functional used here is given in (2.38), and the preferred field set is the components of E. With this choice of trial functions, the spurious modes are eliminated. Use of second-order edge elements has given excellent results. Recent work in the finite-element area has focused on the use of edge elements.

2.2.3.3 Finite Difference Time Domain (FDTD) Method

The FDTD technique represents a widely used propagation solution technique in integrated optics, especially in photonic band gap device computations where the beam propagation solutions are inadequate, or cannot cope with the geometry. The major limitation is that the three-dimensional version requires large storage and extremely long computation times. The basic technique has been outlined in several papers and books devoted to the technique, for example, [13] and [14]. The solution of the wave propagation is by direct integration in the time domain of the Maxwell curl equations in discretized form. For example, the component of the curl equation is given by,

$$\frac{\partial H_y}{\partial x} - \frac{\partial H_x}{\partial y} = \frac{\partial D_z}{\partial t} \tag{2.39}$$

Discretizing via central differences in time and space gives,

$$\varepsilon\left[\frac{E_z^{t+\Delta t}(x,y,z) - E_z^t(x,y,z)}{\Delta t}\right]$$

$$= \left[\frac{H_y^{t+\Delta t/2}(x+\Delta x/2,y,z) - H_y^{t+\Delta t/2}(x-\Delta x/2,y,z)}{\Delta x}\right] \tag{2.40}$$

$$- \left[\frac{H_x^{t+\Delta t/2}(x,y+\Delta y/2,z) - H_x^{t+\Delta t/2}(x,y-\Delta y/2,z)}{\Delta y}\right]$$

The grid is staggered in time and space (the so-called Yee mesh following [15], and the equations for the other field components follow this form. With a given excitation at the

input either in CW or pulsed form, the excitation may be propagated through the structure by time stepping through the entire grid repeatedly. This first-order difference formulation is second-order accurate. In the interest of time and computational speed, most of the computations in the integrated optics area are in two dimensions. Higher order formulations are also available but the overhead that is carried slows down the marching algorithm, while improving accuracy for a specific grid size. The integrated form of the curl equations leads to a finite volume formulation. Again, a marching algorithm is developed on a split grid, as above. A recent two-dimensional alternative to the above first-order formulation, as applied to optical guides, is the higher order compact algorithm based on the split operator technique of Strang [16] and Shang [17]. In this approach, two fields, for example E_z and B_x are combined to define a Riemann time invariant variable, and the propagation of this variable uses the piecewise parabolic approximation suggested by Woodward and Colella [18]. Since the algorithm is two-dimensional the run times are smaller, and because of the parabolic approximation, higher order accuracy is obtained without the overhead of the higher order formulation.

2.2.3.4 Beam Propagation Method (BPM)

One of the fundamental aspects in integrated optics is the analysis and simulation of electromagnetic wave propagation in photonics devices based on waveguide geometries, including optical waveguides. The problem is to be solved such as for a given arbitrary distribution of refractive index n (x, y, z), and for a given wave field distribution at the input plane at z=0, E (x, y, z = 0), the spatial distribution of light E (x, y, z) at a generic point z must to be found. In this case, the distribution of the refractive index is known, which defines the optical circuit. When a light beam is injected at z=0, the problem is to determine the light intensity distribution at the exit, and in particular, what will be the output light intensity in each of the output branches.

The *Beam Propagation Method (BPM)* is useful to the study of light propagation in integrated photonics devices based on optical waveguides with the help of a paraxial form of the Helmholtz relation, known as the Fresnel equation. This relation is valid for paraxial propagation in slowly varying optical structures, which is the starting point to develop BPM algorithms.

The solution to the Helmholtz equation or the Fresnel equation applied to optical propagation in waveguides is known as the Beam Propagation Method (BPM) [19]. Two numerical schemes have been used to solve the Fresnel equation. In one numerical scheme, optical propagation is modeled as a plane wave spectrum in the spatial frequency domain, and the effect of the medium in homogeneity is interpreted as a correction of the phase in the spatial domain at each propagation step. The use of the fast Fourier techniques connects the spatial and spectral domains, and this method is therefore called Fast Fourier transform BPM (FFT-BPM). The propagation of EM waves in inhomogeneous media can also be described directly in the spatial domain by a finite difference (FD) scheme [19]. This technique allows the simulation of strong guiding structures, and also of structures that vary in the propagation direction. The beam propagation method which solves the paraxial form of the scalar wave equation in an inhomogeneous medium using the finite difference method is called finite difference BPM (FD-BPM). Also methods based on finite differences which solve the vector wave equation, called finite difference vector wave BPM (FDVBPM) have been developed. There is an intermediate approximation, which starts from the wave equation but ignores coupling terms between the transversal components of the fields, and for that reason this method is usually referred to as finite difference semi-vector BPM (FD-SVBPM).

The BPM is one of the commonly used numerical tools for modelling structures that are non uniform in propagation direction for time harmonic optical signals. Since the optical carrier frequency is usually very large compared to the signal bandwidth modelling with a monochromatic wave is sufficiently accurate for many devices. Commercialized computer aided design software (e.g. OptiWave, RSoft, BBV) based on this technique is available and their capabilities concerning wide angle problems, bidirectional propagation and anisotropy are steadily improved.

In this reported work, beam propagation method has been used for mode propagation in planar waveguide sensor and using optiBPM software (version 9.0) we have prepared the layout of the proposed waveguide sensor which is discussed in Chapter-3.

2.3 Optical sensor and its Classification

Since our proposed studies are related to optical sensor, it is essential to discuss the basic characteristics of optical sensor. The following characteristics of optical sensor make them advantageous over other types of sensors:

(i) Optical sensors are highly sensitive and accurate. Such sensors use an add-layer which has the ability to attract the analytes more effectively. This increases the sensitivity of a sensor to a particular analyte. Although other type of sensors such as electronic based sensors could also employ this technique, they traditionally suffer from a major problem of electromagnetic noise [20].

(ii) Fabricating an optical sensor is more cost-effective feasible than that of other existing optical sensors such as waveguide sensor which can be easily integrated on to a chip [21].

(iii) Multichannel sensing can be done by optical sensors due to its compactness [22] [23]. Microfluidic channels are also one of the current developments in the industry where analytes can be flown in the fluids and due to the shift in the resonant wavelength of the analytes, sensing becomes a possibility [24].

(iv) Another attractive application of optical sensor is its compatibility with fiber optic technology. This integration helps in the reduction of problems dealt with optical inputs and outputs by not integrating them as separate light sources [22]-[25].

(v) The response time in an optical sensor is much shorter compared to that of other existing sensors [26].

(vi) Optical sensors are highly immune to electromagnetic disturbances.

Optical sensors can be classified based on their sensing mechanisms and architectures. Fluorescence, Surface Plasmon Resonance (SPR), Raman scattering, absorption change, photon migration spectroscopy and change in effective index are a few of the sensing mechanisms that optical sensors follow [20]. Interferometer, Anti Resonant Reflecting Optical Waveguides (ARROW), hollow waveguides, Bragg gratings, slot waveguides, ring resonator, photonic crystals, meta materials and Low Optical Overlap Mode (LOOM) structures are examples of the various architectures that

optical waveguides employ [20]-[26]. There are mainly two types of optical sensor-optical fiber sensor and planar waveguide sensors as shown in the following Fig. 2.15.
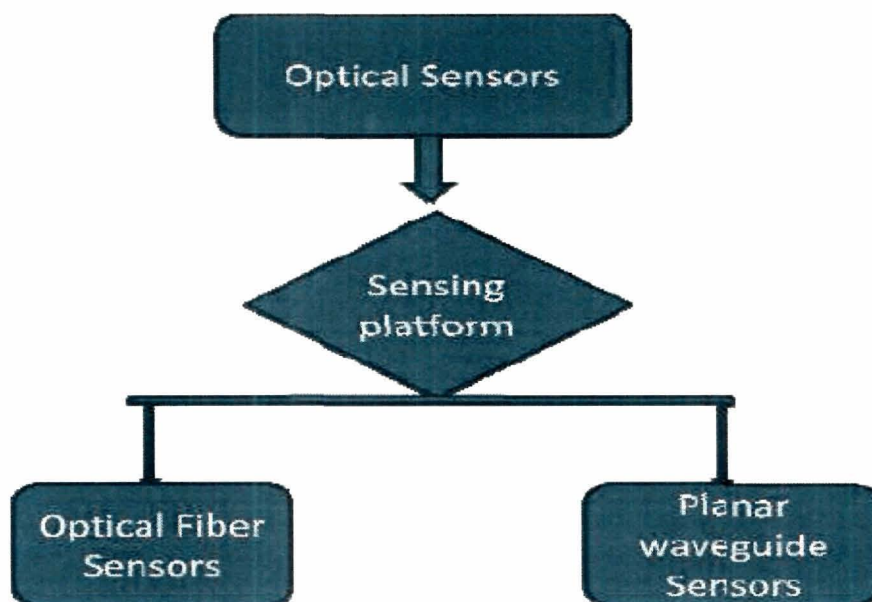
Fig-2.15: Classification of optical sensors

Recently, optical waveguide sensors are preferred for different applications due to higher sensing region in its compact size in comparison to optical fiber sensors.

2.3.1 Fiber Optic (FO) sensors and classification

Fiber optic sensors are excellent candidates for monitoring environmental changes and they offer many advantages over conventional electronic sensors as listed below:

  o Easy integration into a wide variety of structures, including composite materials, with little interference due to their small size and cylindrical geometry.
  o Inability to conduct electric current.
  o Immune to Electromagnetic Interference (E.I) and Radio Frequency (R.F) interference.
  o Lightweight.
  o High sensitivity.

o Multifunctional sensing capabilities such as strain, pressure, corrosion, temperature and acoustic signals.

To date, fiber optic sensors have been widely used to monitor a wide range of environmental parameters such as position, vibration, strain, temperature, humidity, viscosity, chemicals, pressure, current, electric field and several other environmental factors [27] [28]. The basic structure of optical fiber is shown in Fig. 2.16, whereas the general block diagram of fiber optics sensor is shown in Fig. 2.17.
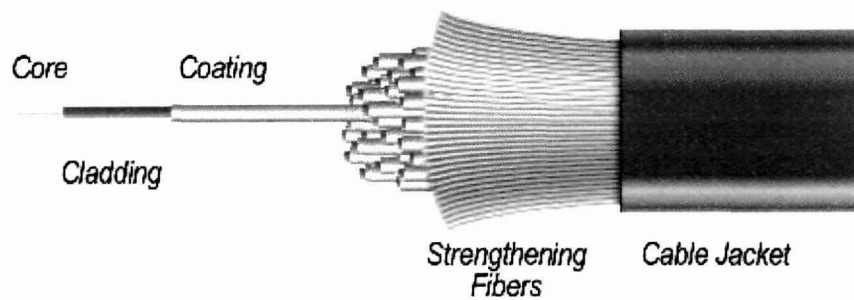
Fig-2.16: Basic structure of an optical fiber [29]

Fig. 2.17 shows a schematic diagram of a fiber-optical sensor system consist of an optical source (laser, LED, laser diode, *etc.*), optical fiber, sensing or modulator element transducing the measurand to an optical signal, an optical detector and processing electronics (oscilloscope, optical spectrum analyzer, *etc.*) [30].
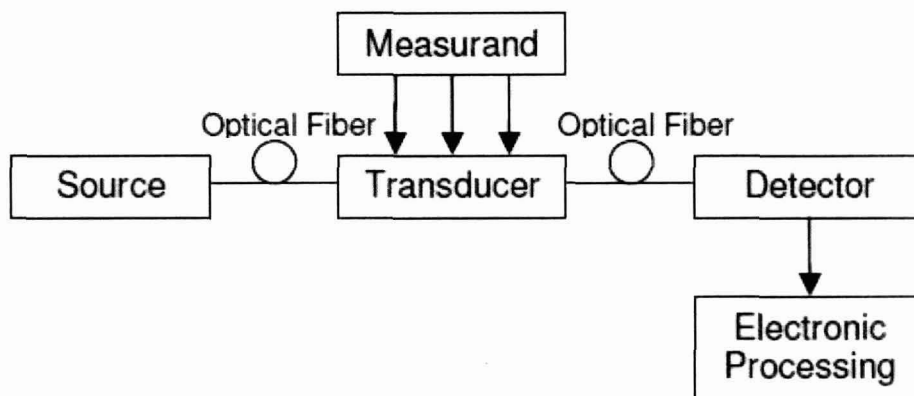
Fig-2.17: Basic components of an optical fiber sensor system [29]

Fiber-optical sensors are divided into two basic classes referred to as intrinsic, or all-fiber and extrinsic, or hybrid sensors. The intrinsic fiber-optical sensor has a sensing region within the fiber and light never goes out of the fiber. In extrinsic sensors, light has to leave the fiber and reach the sensing region outside, and then comes back to the fiber [31]. Furthermore, fiber-optical sensors can also be classified under three categories [30]: the sensing location, the operating principle and the application, as shown in Table 2.1.

Table 2.1: Fiber optical sensor classifications based on three characteristics

Category	Class	Trait
Sensing location	Point sensors	With a sensitized tip in the measurand field
	Distributed Sensors	To measure along the length of the fiber itself
	Quasi-distributed Sensors	"in between" point and distributed sensors
Operating Principle	Intensity sensors	-
	Phase sensors	-
	Frequency sensors	-
	Polarization sensors	-
Application	Physical sensors	For temperature, stress, velocity etc.
	Chemical sensors	For pH, gas analysis, spectroscopic studies, etc
	Biomedical sensors	For blood flow, glucose content etc

On the basis of sensing location, there are three types of fiber optical sensor- point sensor, distributed sensor and quasi-distributed sensors in which both point and distributed sensing location are used for the measurement. Based on the operating principal and demodulation technique, a fiber optic sensor can be further divided into intensity, phase, frequency or polarization sensor. Based on the application, a fiber optic sensor can be classified as follows:

- Physical sensors: Used to measure physical properties like temperature, stress, etc.

- Chemical sensors: Used for pH measurement, gas analysis, spectroscopic studies, etc.

- Bio-medical sensors: Used in bio-medical applications like measurement of blood flow, glucose content etc.

2.3.1.1 Intensity Based Fiber Optic Sensor

Intensity-based fiber optic sensors rely on signal undergoing some loss. They are made by using an apparatus to convert what is being measured into a force that bends the fiber and causes attenuation of the signal. Other ways to attenuate the signal is through absorption or scattering of a target. The intensity-based sensor requires more light and therefore usually uses multimode large core fibers [32]. The advantages of these sensors are: simplicity of implementation, low cost, possibility of being multiplexed, and ability to perform as real distributed sensors. The disadvantages are: relative measurements and variations in the intensity of the light source may lead to false readings, unless a referencing system is used [33].

One of the intensity-based sensors is the micro-bend sensor, which is based on the principle that mechanical periodic micro bends can cause the energy of the guided modes to be coupled to the radiation modes and consequently resulting in attenuation of the transmitted light. As seen in Fig. 2.18, the sensor is comprised of two grooved plates and between them an optical fiber passes. The upper plate can move in response to pressure. When the bend radius of the fiber exceeds the critical angle necessary to confine the light to the core area, light starts leaking into the cladding resulting in an intensity modulation [34].
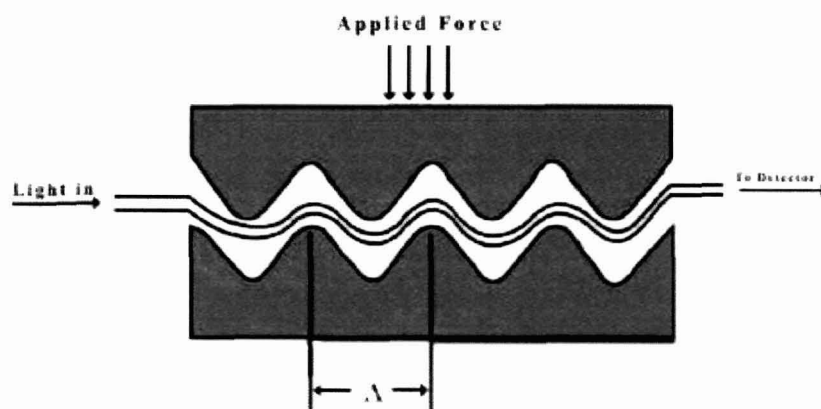
Fig-2.18: Intrinsic fiber optic sensor [29].
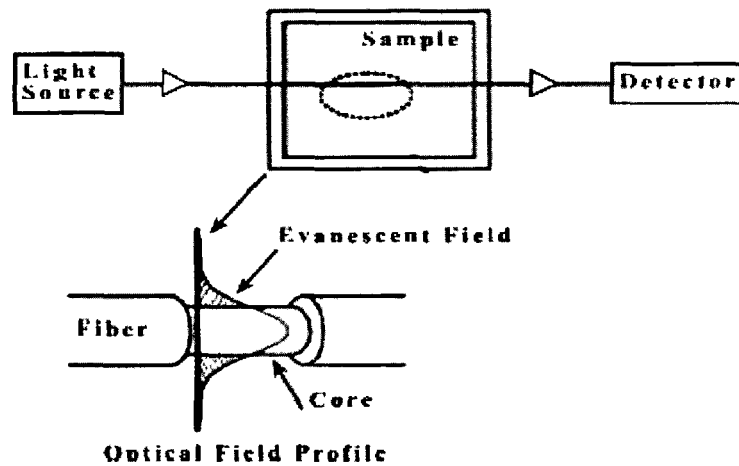
Fig-2.19: Evanescent wave fiber optic chemical sensor [29].

Another type of intensity based fiber optic sensor is the evanescent wave sensor (see Fig. 2.19) that utilizes the light energy which leaks from the core into the cladding. These sensors are widely used as chemical sensors. The sensing is accomplished by stripping the cladding from a section of the fiber and using a light source having a wavelength that can be absorbed by the chemical that is to be detected. The resulting change in light intensity is a measure of the chemical concentration. Measurements can also be performed in a similar method by replacing the cladding with a material such as an organic dye whose optical properties can be changed by the chemical under investigation [35].

2.3.1.2 Wavelength Modulated Fiber Optic Sensors

Wavelength modulated sensors use changes in the wavelength of light for detection. Fluorescence sensors, black body sensors, and the Bragg grating sensor are examples of wavelength-modulated sensors. Fluorescent based fiber sensors are being widely used for medical applications, chemical sensing and physical parameter measurements such as temperature, viscosity and humidity. Different configurations are used for these sensors where two of the most common ones are shown in Fig. 2.20. In the case of the end tip sensor, light propagates down the fiber to a probe of fluorescent material. The

resultant fluorescent signal is captured by the same fiber and directed back to an output demodulator [36].

End Tip

Fluorescent material
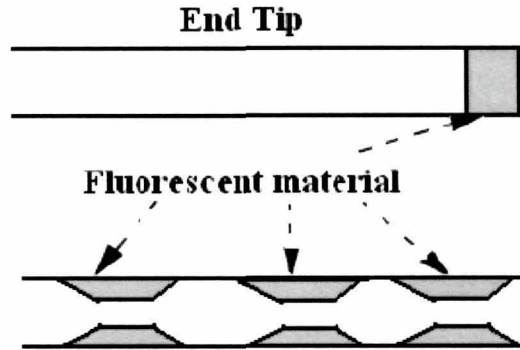
Fig-2.20: Fluorescent fiber optic sensor probe [29].

The most widely used wavelength based sensor is the Bragg grating sensor. Fiber Bragg gratings (FBGs) are formed by constructing periodic changes in index of refraction in the core of a single mode optical fiber. This periodic change in index of refraction is normally created by exposing the fiber core to an intense interference pattern of UV energy. The variation in refractive index so produced, forms an interference pattern which acts as a grating.

Fiber Core   Photo-Imprinted Grating

Input Signal

Reflected Signal

Transmitted Signal

$\lambda_B = 2n \Lambda$

Input Spectrum   Transmitted Spectrum   Reflected Spectrum

strain-induced shift

λ_B
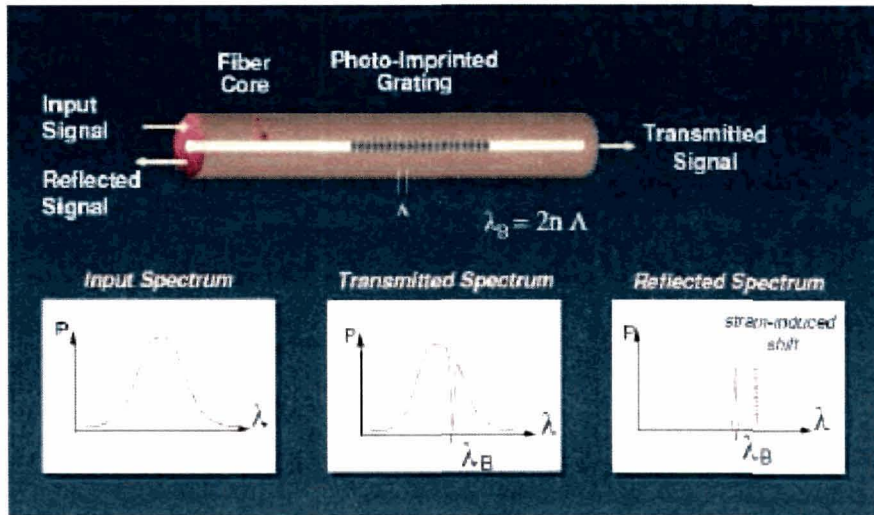
Fig-2.21: Bragg grating response [29], where λ_B =Bragg wavelength and Λ =grating period respectively.

The Bragg grating sensor operation is shown in Fig. 2.21 where light from a broadband source (LED) whose center wavelength is close to the Bragg wavelength is launched into the fiber. The light propagates through the grating, and part of the signal is reflected at the Bragg wavelength. The complimentary part of the process shows a small sliver of signal removed from the transmitted signal. This obviously shows the Bragg grating to be an effective optical filter [32].

2.3.1.3 Phase Modulated Fiber Optics Sensors

Phase modulated sensors use changes in the phase of light for detection. The optical phase of the light passing through the fiber is modulated by the field to be detected. This phase modulation is then detected interferometrically, by comparing the phase of the light in the signal fiber to that in a reference fiber. In an interferometer, the light is split into two beams, where one beam is exposed to the sensing environment and undergoes a phase shift and the other is isolated from the sensing environment and is used for as a reference. Once the beams are recombined, they interfere with each other [37]. Mach-Zehnder, Michelson, Fabry-Perot, Sagnac, polarimetric, and grating interferometers are the most commonly used intereferometers. The Michelson and Mach-Zehnder interferometers are shown in Fig. 2.22 (a) and Fig. 2.22 (b) respectively.
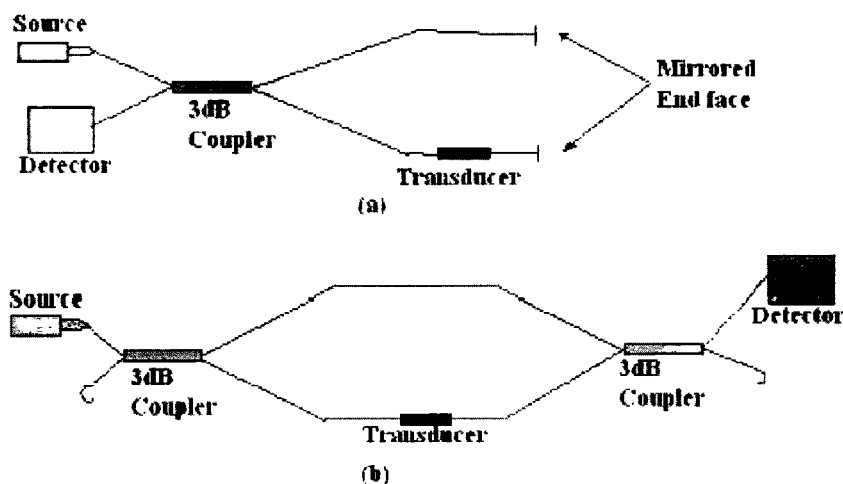
Fig-2.22: Schematic diagrams of (a) Michelson interferometer and (b) Mach-Zehnder interferometer [29].

There are similarities and differences between the Michelson and Mach–Zehnder interferometers. In terms of similarities, the Michelson is often considered to be folded Mach–Zehnder, and vice versa. Michelson configuration requires only one optical fiber coupler. Because the light passes both through the sensing and reference fibers twice, the optical phase shift per unit length of fiber is doubled. Thus, the Michelson can intrinsically have better sensitivity. Another clear advantage of the Michelson is that the sensor can be interrogated with only a single fiber between the source-detector module and the sensor. However, a good-quality reflection mirror is required for the Michelson interferometer [27].

2.3.1.4 Polarization Modulated Fiber Optic Sensors

The direction of the polarization of the electric filed of the light field is defined as the polarization state of the light field. There are different polarization states of the light field- linear, elliptical, and circular polarization states. For the linear polarization state, the direction of the electric field always keeps in the same line during the light propagation.
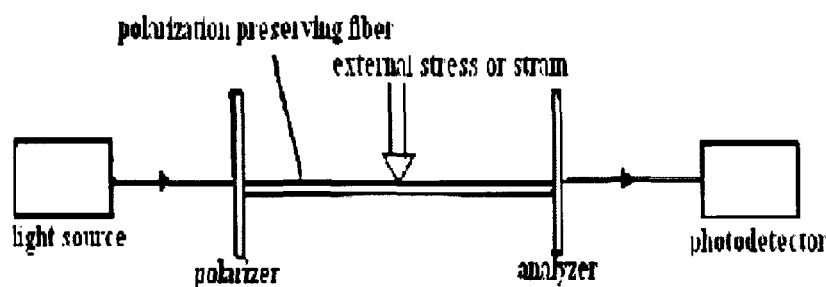
Fig-2.23: Polarization-based fiber optic sensor [29].

For the elliptical polarization state, the direction of the electric field changes during the light propagation. The end of the electric field vector forms an elliptical shape; hence, it is called "elliptical polarized light". The refractive index of a fiber changes when it undergoes stress or strain. Thus, there is an induced phase difference between different polarization directions. This phenomenon is called photoelastic effect.

Moreover, the refractive index of a fiber undergoing a certain stress or strain is called induced refractive index. The induced refractive index changes with the direction of applied stress or strain. Thus, there is an induced phase difference between different polarization directions. In other words, under the external perturbation, such as stress or strain, the optical fiber works like a linear retarder. Therefore, by detecting the change in the output polarization state, the external perturbation can be sensed [27].

Fig. 2.23 shows the optical setup for the polarization based fiber optic sensor. It is formed by polarizing the light from a light source via a polarizer that could be a length of polarization-preserving fiber. The polarized light is launched at 45 degrees to the preferred axes of a length of bi-refrigent polarization-preserving fiber. This section of fiber is served as sensing fiber. Under external perturbation such as stress or strain, the phase difference between two polarization states is changed. Then, the output polarization state is changed according to the perturbation. Hence, by analyzing the output polarization state at the exit end of the fiber, the external perturbation can be detected [27].

2.3.2 Integrated Optic Waveguide Sensors

The basic principles of planar waveguide sensors are same as that for the fiber optic sensors. The two fields have been developed at different paces and with slight different targets. Fibers have the unique capability of operating over extended gauge lengths (even km!) in either point sensing or distributed sensing format. In the former case, the FOS is configured in such a way that monitoring of the measurand occurs at a specified location along the fiber; in the latter case, light is guided by confining it in optical structures known as waveguides by utilizing the Total Internal Reflection principle.

Table 2.2: Classification of waveguides based on dimension of light confinement

Light confinement dimensions	Type of waveguide
1D	Planar waveguides
2D	Channel waveguides
3D	Photonic crystals

Light is confined within the waveguide along the dimensions of 1D, 2D or 3D. So planar waveguide can be classify based on the dimensions of the light that is confined as- planar waveguides (1-D), channel waveguides (2-D) and photonic crystals (3-D) respectively as shown in the Table 2.2.

Channel waveguides known as 2D waveguides are those which have a higher refractive index in the core when compared to substrate and cover. In this type of structure, the Total Internal Reflection (TIR) takes place at the interfaces and also at the lateral boundaries. The refractive index of the core region is always maintained more than the refractive indices of surrounding regions. The channel waveguides can be classified in a similar manner to planar waveguides in terms of step index or graded index or symmetric/asymmetric except that we have to consider the addition of one extra dimension. Three main types of channel waveguides have been in use namely stripe waveguide, ridge waveguide and buried waveguide respectively.

Integrated Optic (IO) planar waveguides can be fabricated with a variety of materials such as $SiON/SiO_2$, GeO_2-SiO_2/SiO_2, GaAsInP/InP, Ti: $LiNbO_3$, SOI and polymers. Its greater advantage is that it permits flexibility both in design and manufacturing by exploiting the combination of thin films technology with other planar waveguide technologies, such as surface acousto-optic interaction, laser writing, silicon micromachining, microelectro-mechanical systems (MEMS), optoelectronic integration on a semiconductor substrate etc. Since IOSs as a temperature and a displacement sensor, were first reported in 1982 [38][39], afterwards many other integrated optical devices for sensing application have been proposed and demonstrated [40]-[42]. The detail of integrated optic planar waveguide sensor is discussed in the subsequent section 2.3.2.1. In the following sections, some examples of IOSs are very briefly presented and discussed.

2.3.2.1 Integrated Optical Interferometers

Mach-Zehnder Interferometers (MZI) based on integrated optics are easily fabricated, by means of standard integrated circuit (IC) technologies and are one of the most common structures exploited for the detection of the phase shift induced by a measurand. The schematic structure of an integrated optical MZI is shown in Fig.-

2.24(a), and the field distribution in the waveguide (and the interacting evanescent field) is sketched in Fig. 2.24(b). Several sensing devices have been demonstrated, e.g. for the detection of displacement, for refractometry and for bio-sensing [43] [44].
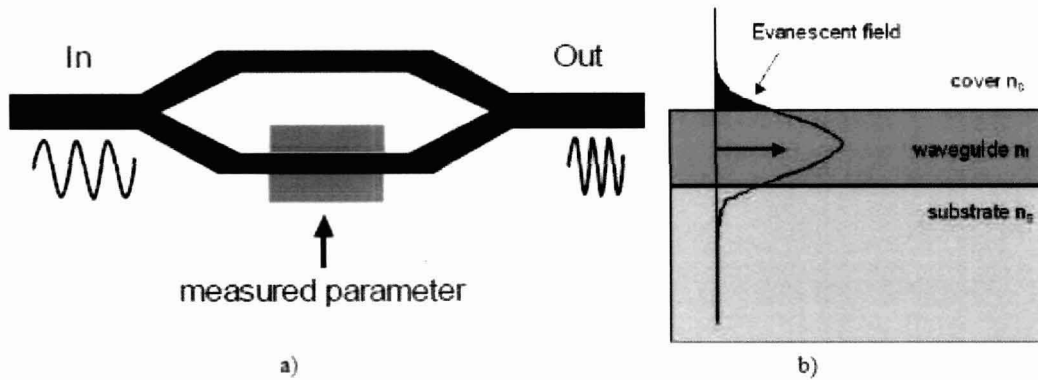
Fig-2.24: a) Top-view of an IO MZI structure and b) Behavior of the modal field distribution in the waveguide structure [44].

2.3.2.2 Grating-Coupler Sensors

In integrated optics, the light is launched into the thin-film waveguide by prism coupling, grating coupling, or fiber-to-waveguide butt-coupling [45]. The prism-coupling is the most common technique in the laboratory, whereas grating couplers can be fabricated directly on top or inside the waveguide itself, offers a more robust mechanism for practical application. Grating couplers, however, are not simply another way of performing the access function to/from an optical waveguide. As their operation depends critically on the refractive indices of the guiding film and of surrounding media (once the wavelength is fixed), the precise measurement of the in-coupling angle constitutes a sensitive tool to detect changes in refractive index or wavelength induced by a measurand [46]. Commercial grating coupler sensor chips are available. The cladding layer modifies the optical, chemical or biochemical properties of the surface of the chip. A wide choice of coatings, from thin films of SiO_2, TiO_2, TaO_2, ITO (Indium Tin Oxide), ZrO_2, to thick films of PTFE, silicone etc., are used. The biosensing application of grating coupler sensors include adsorption of protein at surface, immunosensing, drug screening, analysis of association and dissociation kinetics, and

many more. Typical size of the chip is 48 mm (length) x 16 mm (width) x 0.55 mm (thickness), and the guiding sol-gel layer has thickness in the range 170 to 220 nm; grating area is 2 mm (L)×16 mm (W), its depth (the grating is a surface relief structure) is about 20 nm, and its pitch is ≈ 0.4 μm.

2.3.2.3 Evanescent-Wave and Surface Plasmon Resonance Sensors

The origin of the evanescent wave may be explained as follows: When light propagates in an optical fiber or waveguide, a fraction of the radiation extends a short distance from the guiding region into the medium of lower refractive index which surrounds it. This evanescent wave which decays exponentially with distance from the waveguide interface, defines a short sensing volume within which the evanescent energy may interact with molecular species. Recently, optical waveguide sensors based on such evanescent wave (EW) interactions have attracted significant research interest [47][48].

The motivation for adopting the EW approach derives from a number of advantages offered by the technique in particular applications:

(i) Because the interrogating light remains guided, no coupling optics is required in the sensing region and an all fiber approach is feasible. Furthermore, considerable miniaturization is possible for which EW interactions are predominant sensing mechanisms.

(ii) The technique can provide enhanced sensitivity over conventional bulk optics approaches.

(iii) In contrast to other sensing methods, EW approach affords the sensor designer greater control over interaction parameters such as interaction length, sensing volume and response time.

The control over the degree of penetration of the EW into the low index medium is characterized by the penetration depth d_p, which is the perpendicular distance from the interface at which the electric field amplitude, E has fallen to $1/e$ of its value, E_0 at the interface i.e.

$$E = E_0 \exp(-z/d_p)$$ (2.41)

The magnitude of the penetration depth is given by:

$$d_p = \frac{\lambda}{2\pi n_1 \left[\sin^2 \theta - \left(\frac{n_2}{n_1} \right)^2 \right]^{1/2}}$$

(2.42)

where λ is the vacuum length, θ is the angle of incidence to the normal at the interface and n_1, n_2 are the refractive index values of the dense and rare media, respectively. Although d_P is less than λ, it is clear from Eq. (2.42) that its value rises sharply as the angle of incidence approaches the critical angle, $\theta_c = \sin^{-1}\left(\frac{n_2}{n_1} \right)$. This eq. (2.42) highlights the importance of the interface angle θ in the design of EW sensors.
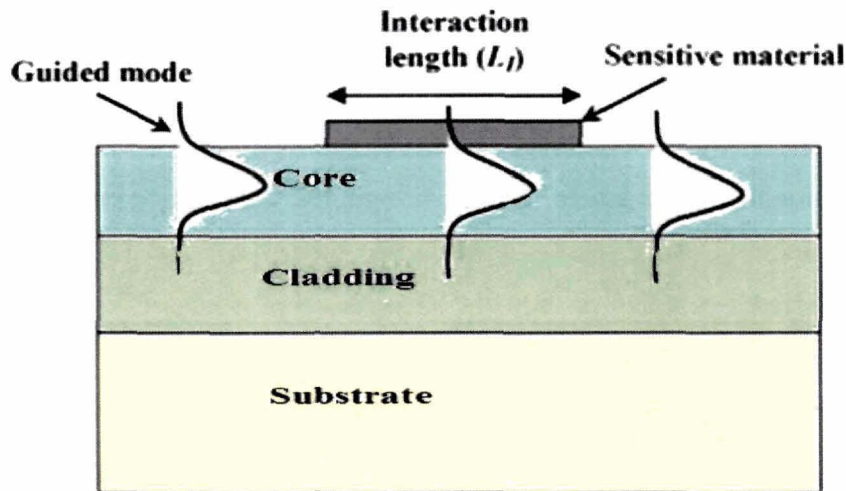
Fig-2.25: Evanescent wave sensor [49].

Fig. 2.25 depicts a typical sensor which employs the evanescent sensing technique. When the total internal reflection occurs at an angle bigger than the critical angle, the evanescent field decays exponentially. In the structure, Silicon is used as the substrate material. A sensitive material is used on top of the waveguide material called as an ad-layer to help attract analytes easily and effectively. This increases the sensitivity.

Fig. 2.26(a) depicts the angle of the incident light being less than the critical angle. Fig. 2.26(b) depicts the incident angle equal to the critical angle. For total internal

reflection, the angle of the incident ray must be greater than the critical angle, which is depicted by Fig. 2.26(c).
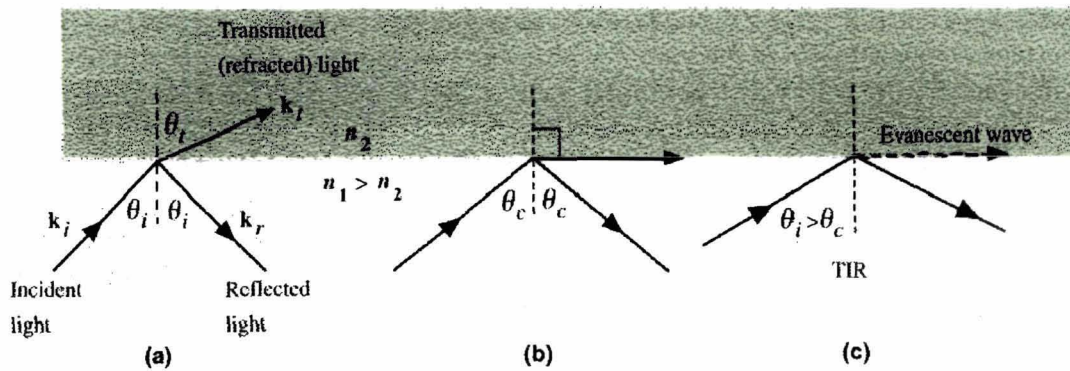
Fig-2.26: Formation of evanescent wave (based on [50])

Thus, the evanescent wave is formed and it penetrates into the region of lower refractive index. The species to be detected are made to interact with the evanescent field that penetrates into the cladding region. Strong evanescent wave absorption occurs when the peak absorbance wavelength of the analytes equals the wavelength of the light that is propagated [50]-[52]. Further criteria about the material selection are discussed later in this chapter.
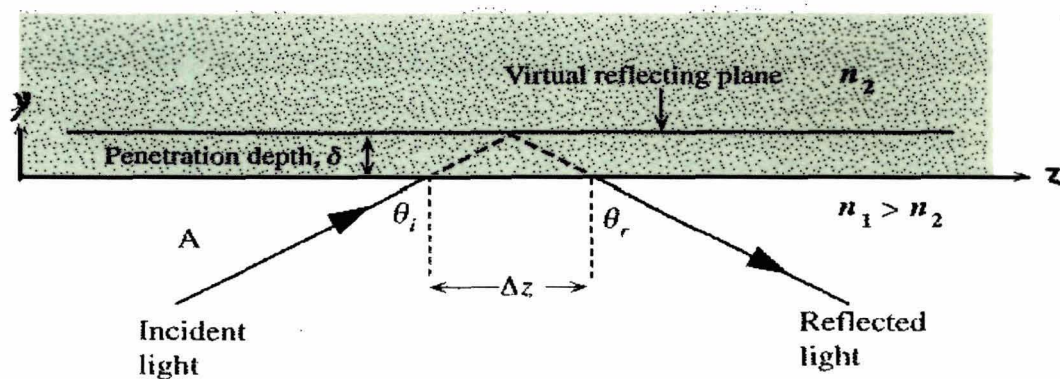
Fig-2.27: Penetration depth (based on [50])

Fig. 2.27 shows the phenomenon of evanescent wave sensing along with the determination of the penetration depth. A ray of light is incident upon the reflecting

plane with an angle θ_i whereas n_2 is the refractive index of the cladding which is air. n_1 is the refractive index of the core region. According to the principle of total internal reflection, n_1 is greater than n_2. This penetration depth can be measured using Eq. (2.43) if we have the knowledge of operating wavelength and refractive indices of core and cladding regions.

The penetration depth of electric field in the region can also be determined as [53][54],

$$\delta = \left(\frac{\lambda}{2\pi}\right)\left[N^2 - n_c^2\right]^{-1/2} \tag{2.43}$$

where δ– penetration depth which determines the exponential decay of the electric field

λ– wavelength of operation

N– effective refractive index of the core and

n_c–refractive index of the cladding region

Fig. 2.25 shows the basic principle of an evanescent wave sensor. In the sensing region, the testing sample (measurand) acts as cladding region and hence the evanescent light wave propagation depends on measurand which interact with evanescent waves. The change in a chemical or physical parameter of the cladding or sensing region (usually constituted by a fluid or an ultra-thin transducer film) is converted into an optically measurable quantity by means of a change in absorption of the guided wave or in its effective index [47]. Such sensing structure relies on measurand induced changes of the field profile of the guided mode; this is in contrast to the the refractive IO-sensors in which the changes of the effective refractive index n_{eff} are exploited [55].

The technique which is becoming a key tool for characterizing biomolecular interaction is that based on Surface Plasmon Resonance (SPR) [56]. The optical excitation of surface Plasmon by the method of Attenuated Total Reflection (ATR) was demonstrated in the late Sixties, and very soon it was applied for characterization of metal thin films [57]. In early Eighties the use of SPR for gas sensing and biosensing was demonstrated [59][60] and since then SPR sensor technology has continued to grow up [61] and it is now commercialized.

2.3.3 Basic Principle: Optical Planar Waveguide Sensors

Although trapped within the dielectric medium of the optical waveguide, the radiation that propagates inside the waveguide can be perturbed by the external environment, and this perturbation can be used to draw useful information for sensing purposes. In fact, the interaction of the parameter of interest that is the measurand with the waveguide produces a modulation in the propagation constants of the guided light beam. That modulation represents the sensitive function of the measurand of interest.
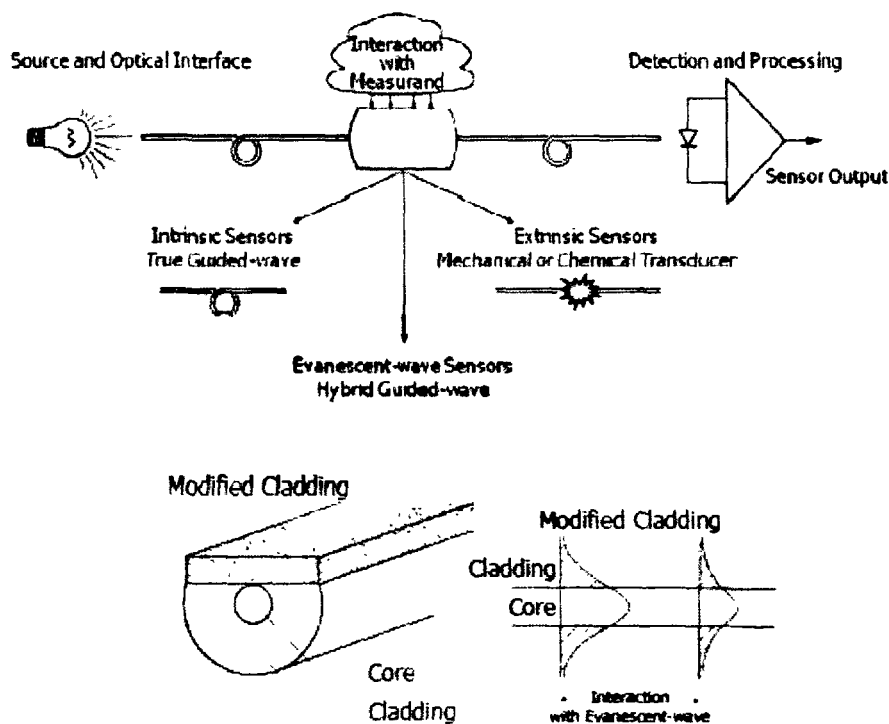
Fig-2.28: The waveguide sensor: general working principle [44].

As shown in Fig.2.28, the basic elements constituting a guided wave sensor are: an optical source, an optical interface for source-to-waveguide light coupling, the waveguide itself where the measurand induced light modulation occurs, a photo detector and the electronics for amplification, signal processing and data display. In accordance to the optical parameter, which is modulated by the measurand, waveguide sensors can be divided into four basic categories:

- Phase-modulated,
- Polarisation-modulated,
- Wavelength-modulated,
- Intensity-modulated.

Waveguide sensors are further subdivided as intrinsic, extrinsic, or evanescent-wave sensors. Intrinsic sensors are true waveguide sensors in which the sensing element is the waveguide itself. Extrinsic sensors make use of an optical transducer coupled to waveguide, the optical constants of which are modulated by the measurand. Evanescent-wave sensors are hybrid intrinsic/extrinsic sensors, since measurand-induced modulation occurs in the waveguide itself, in most cases because of the presence of a measurand-sensitive cladding section.

2.3.3.1 Integrated Optic Planar Waveguide Sensor Effect

The integrated optic planar waveguide sensors make use of guided waves or modes in optical waveguides; in particular of the orthogonally polarized TE_0 and TM_0 modes of high refractive index. The modes in planar optical waveguides are TE_m (transverse electric or s-polarized) modes and TM_m (transverse magnetic or p-polarized) modes, where m =0, 1 . . . . is the mode number. In sensor applications, it is seen that the effective refractive index N is the most important physical quantity of the guided modes. The modes propagate down the waveguide with the phase velocity v_p, = c/N, where c is the velocity of light in vacuum and N is the effective refractive index of the mode; N depends on polarization (TE or TM), mode number m, wavelength λ, the properties of the wave guiding film F, i.e., its thickness dF/λ in units of λ and its refractive index n_F, and on the refractive indices n_s and n_c respectively, of the substrate S and of the medium C covering the waveguide (as shown in Fig.2.29). The field of a guided wave penetrates as an evanescent wave traverses a small distance Δz_c into the medium C, which in sensor applications is the sample covering the waveguide. More precisely, the evanescent field decays exponentially proportional to exp (- $z/\Delta z_c$) with distance z from the waveguide surface, where

$$\Delta z_c \equiv \left(\frac{\lambda}{2\pi}\right) \left[N^2 - n_c^2\right]^{1/2} \tag{2.44}$$

is the penetration depth. The basic IO sensor effect is caused by interaction of the evanescent wave of the guided mode with the sample. The evanescent field 'senses' changes in the refractive-index distribution near the waveguide surface. Thus changes ΔN in the effective refractive indices of the guided modes are induced. This is the basic or primary IO sensor effect on which all IO sensors are based.
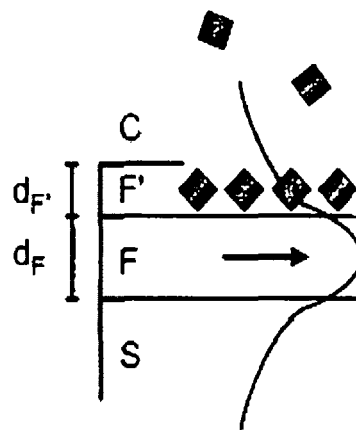
Fig-2.29: Basic IO sensor effect. Changes ΔN of the effective refractive index N of a guided mode are induced by changes of the refractive-index distribution n(z) in the vicinity of the waveguide surface, i.e., within the penetration depth Δz_c of the evanescent field in the sample C. Sensor effect (1): molecules transported by convection or diffusion adsorb on the surface forming an adlayer F' of thickness $d_{F'}$ and refractive index $n_{F'}$. Sensor effect (2): homogeneous change Δn_c of refractive index of (liquid) sample C [54].

The effective refractive-index changes (ΔN) can be induced by two different effects as follows:

i. the formation of an adlayer F' of adsorbed or bound molecules, which are transported by convection or diffusion from the bulk of the gaseous or liquid sample C to the waveguide surface. This adlayer is modeled as a homogeneous layer F' of thickness d_F and refractive index n_F.

ii. changes Δn_c of the refractive index n_c of the homogeneous (liquid) sample C covering the waveguide surface. Only in the case of microporous waveguides,

iii. a third sensor effect can occur, namely the adsorption or desorption of molecules in pores of the wave guiding film F itself, which primarily changes its refractive index n_F by Δn_F and in turn leads to an effective refractive-index change ΔN.

The field distribution inside the waveguide F itself, and not the evanescent field in C, is responsible for effect (iii). If all the effects (1)-(3) are simultaneously present, the resulting effective refractive-index changes are:

$$\Delta N = \left(\frac{\partial N}{\partial D_F}\right) d_F + \left(\frac{\partial N}{\partial n_c}\right) \Delta n_c + \left(\frac{\partial N}{\partial n_F}\right) \Delta n_F \qquad (2.45)$$

How the sensitivity constants $\left(\frac{\partial N}{\partial D_F}\right)$, $\left(\frac{\partial N}{\partial n_c}\right)$ and $\left(\frac{\partial N}{\partial n_F}\right)$ depend on the optical parameters of the waveguide F, substrate S and sample C. Effect (1) makes it possible to monitor in real time the adsorption of molecules on the waveguide surface or their desorption from the surface, respectively. Effect (ii) is the basis for the application of IO sensors as differential refractometer. Effects (i) and (ii) are also the basis of (bio) chemical sensors. Effect (3) can be exploited in relative-humidity sensing and in gas sensing. In other cases, such as in refractometry and in affinity sensing, effect (3) can be rather disturbing and compact waveguides with very low microporosity are preferable. As expressed in Eq. (2.45), the effects (i)-(iii) contribute additively to the effective refractive-index changes ΔN. In order to differentiate between the two or three different effects, it is therefore necessary to measure the effective refractive-index changes of the corresponding number of guided modes at the same wavelength λ. The optical sensitivity constants: $\left(\frac{\partial N}{\partial d_F}\right)$, $\left(\frac{\partial N}{\partial n_C}\right)$, and $\left(\frac{\partial N}{\partial d_F}\right)$ introduced in Eq. (2.45) are the differential changes in effective refractive index of a guided mode for a small change in:

(i) the thickness dF, of an adsorbed or bound adlayer F';

(ii) the refractive index n_c of the (liquid) sample;

(iii) the refractive index n_v of the microporous waveguide film F.

The optical sensitivity constants have been calculated using two independent methods. The first method [62] [63] starts from the exact mode guiding condition for a planar two-layer waveguide consisting of the wave guiding film F (of thickness d_F and refractive index n_F) with an adsorbed or bound adlayer F' (of arbitrary thickness $d_{F'}$ and refractive index $n_{F'}$) sandwiched between the substrate S and the sample C of refractive indices n_s and n_c, respectively. The limit of very thin adlayers F' considers as $d_{F'} \ll \lambda$. The second method [64] is a perturbation theoretical approach applied to a planar waveguide with any transverse refractive-index distribution. Both methods gave the same results for single-layer step-index waveguides. However, the perturbational approach gives more physical insight, in that the basic formula shows the relation between the effective refractive-index changes ΔN of the guided mode and the changes in refractive index in the vicinity of the waveguide surface (within a layer of the order of the penetration depth Δz_c) that are 'probed' by the evanescent field of the guided mode. For the TE modes, we have

$$\left(\Delta N^2\right) = \frac{\int\limits_{-\infty}^{+\infty} \Delta\varepsilon(z)[u(z)]^2\, dz}{\int\limits_{-\infty}^{+\infty} [u(z)]^2\, dz} \qquad\qquad (2.46)$$

where u(z) is the transverse electric-field distribution of the unperturbed guided mode as a function of the coordinate z perpendicular to the planar waveguide. $\Delta\varepsilon(z) = 2n(z)\Delta n(z)$ is the change in dielectric permittivity, $\varepsilon(z)$ and the change in refractive-index distribution $\Delta n(z)$. For TM modes, for the corresponding formula also can be derived [54]. The main results are:

(i) The optical sensitivity constants depend on the polarization (TE or TM) of the mode, the mode number m (m = 0, 1 . . .), the waveguide thickness df/λ in units of λ, and on the refractive indices n_s, n_F and n_c.

(ii) From Eq.(2.46) we conclude that a high field strength of the 'probing' evanescent field (in the numerator of Eq. (2.46)) for a given power of the guided wave (which is proportional to the denominator in Eq. (2.46)) or in other words, a

strong confinement of the transverse field distribution of the guided wave yields

high sensitivity constants $\left(\dfrac{\partial n}{\partial d_F}\right)$ and $\left(\dfrac{\partial n}{\partial n_c}\right)$.

Both constants are inversely proportional to the so-called effective waveguide thickness d_{eff}, which for TE waves is the sum of the waveguide thickness d_F and the penetration depths Δz_c and Δz_s of the evanescent fields into sample C and substrate S.

i. e. $d_{eff} = d_F + \Delta z_c + \Delta z_s$

Therefore, to obtain high sensitivities $\left(\dfrac{\partial n}{\partial d_F}\right)$ and $\left(\dfrac{\partial n}{\partial n_c}\right)$, very thin waveguide films F

have to be used. But for a mode to be guided in a planar waveguide, the waveguide film F must have a thickness d_F somewhat larger than the minimum or cut-off thickness

$$\left(d_F\right)_m^\rho = \frac{1}{2}\lambda\left(n_F^2 - n_s^2\right)^{-\frac{1}{2}} \times \left[m + \pi^{-1}\arctan\left\{\left(\frac{n_F}{n_c}\right)^{2\rho}\left[\frac{n_s^2 - n_c^2}{n_F^2 - n_s^2}\right]^{\frac{1}{2}}\right\}\right]$$ (2.47)

which depends on the mode number m= 0, 1 . . . and on the polarization with p=0 and 1 for TE mode and TM mode respectively. From Eq.(2.47) we learn that waveguides with cut-off thicknesses $\left(d_F\right)_0^\rho$ of the TE$_0$ and TM$_0$ modes much smaller than the wavelength λ can only be realized if the difference $(n_F\text{-}n_s)$ between the refractive indices of the waveguide film F and the substrate S is large, e.g., $(n_F\text{-}n_s)\geq 0.3$. The consequence is that with very thin high-refractive-index films F on glass or silica substrates high optical

sensitivity constants $\left(\dfrac{\partial N}{\partial d_F}\right)$ can be obtained. Such very thin waveguides were

originally of no importance in the past, because IO components were only of interest for optical communication purposes and for fibre sensors, and therefore, they had to be compatible with monomode fibers. In order to achieve low coupling losses between IO components and fibers, the waveguide thicknesses or mode diameters have to be matched to the core diameter (typically about 5-10 μm) of monomode fibers. (Planar) waveguides satisfying these requirements, such as waveguides fabricated by diffusion processes just below the surfaces of either glasses or electro-optic crystals such as

LiNbO$_3$, have very low optical sensor sensitivities; the sensitivity constant $\left(\dfrac{\partial N}{\partial d_F}\right)$ is

one to two orders lower than for very thin high-refractive-index films. This dependence of the optical sensitivity constants on waveguide parameters has some bearing on the history of the basic IO sensor effect. This effect was discovered, by serendipity. The original object of the work [65] was actually to find out whether or not grating couplers could be fabricated on dip-coated SiO$_2$-TiO$_2$ waveguides (produced by a sol-gel process) on glass substrates by embossing at room temperature a surface relief grating with submicron grating constant A into the gel films, which were subsequently 'fired' at temperatures of about 500 °C to become hard amorphous films. Since sol-gel films shrink considerably in depth (by a factor of typically three to four) [66], the eventual success of this new method to fabricate surface relief gratings with 1/A = 1200-3600 lines per mm was not guaranteed from the outset. But very shallow surface relief gratings (with a modulation depth of several to a few tens of nanometer) are fortunately well suited as grating couplers, having coupling lengths of the order of millimeters.

When these SiO$_2$-TiO$_2$ waveguides provided with surface relief gratings were used for in-coupling experiments with red He-Ne laser light, the unexpected and surprising finding was that the intensity of the light coupled into the waveguide at a constant angle of incidence α was not constant in time as is to be expected from the incoupling condition but varied erratically; expressed differently, the optimum incoupling angle $\alpha_l(t)$ varied, which corresponds to a time-dependent effective refractive-index change $\Delta N(t)$. Soon it was found that the effect was caused by variations of the relative humidity in the environment of the coupler grating on the waveguide. This first IO sensor experiment was reported at the European Conference on Integrated Optics held in Florence in 1983 [67]. Nowadays, this experiment is routinely performed to demonstrate the basic IO sensor effect. (The sensitivity of the SiO$_2$-TiO$_2$ waveguides with respect to relative-humidity changes is greatly enhanced by their microporosity; in highly porous waveguides, the sensor effect (3) can even be predominant [68]-[70]. In Fig. 2.26 we present optical sensitivity constants versus waveguide thickness d_F calculated for two different high-index wave guiding films F, i.e., waveguides of type (a) with n_F=1.8 and n$_s$=1.47 and waveguides of types (b) with n_F=2.01 and n$_s$=1.46.

Waveguides of type (a) correspond to the SiO_2-TiO_2 films, while waveguides of type (b) can be realized with films of higher TiO_2 contents or of Si_3N_4. The substrates S are glass, silica or oxidized silicon wafers (Si/SiO_2).
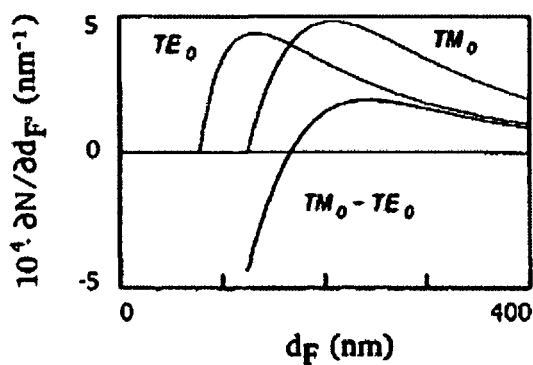
(a)
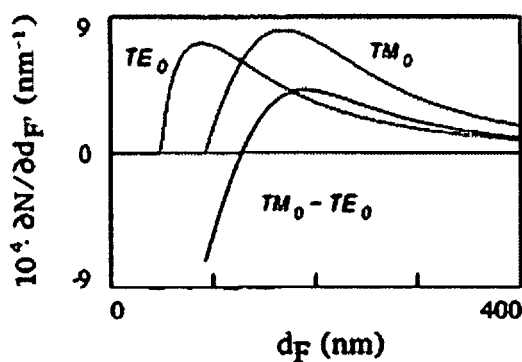
(b)

Fig-2.30: Calculated sensitivities $\dfrac{\partial N}{\partial d_F}, \dfrac{\partial N_{TM_0}}{\partial d_F}$ for TE_0 and TM_0 modes, and sensitivity

$\dfrac{-\partial \tilde{N}}{\partial d_F}$ of difference interferometer vs. waveguide thickness d_F for adsorption of H_2O

molecules from a gaseous sample, where $\tilde{N} = N_{TE_0} - N_{TM_0}$, n_c=1, n_F=1.33, λ=633 nm.

Top, waveguide of type (a) with parameters n_F= 1.80 and n_s= 1.47; bottom, waveguide of type (b) with parameters n_F= 2.01 and n_s = 1.46 [54].

Fig. 2.30 shows the sensitivity constant $\left(\dfrac{\partial N}{\partial d_F}\right)$, for the adsorption of water on the

waveguide surface. For waveguides of type (a) the thickness range $d_F \approx 130 - 200 \ nm$

yields the highest sensitivities. Adsorption of one H_2O monolayer of thickness, $d_F = 0.3$

nm on these waveguides induces maximum effective refractive-index changes $\Delta N \sim$

$(1.2\text{-}1.5) \times 10^{-4}$ for TE_0 and TM_0 modes.

(a)   (b)
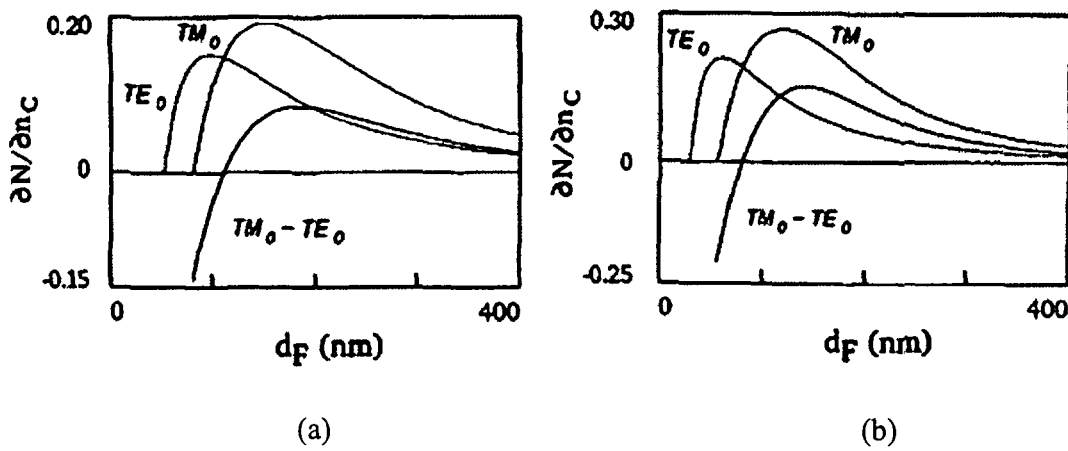
Fig-2.31: Calculated sensitivities $\dfrac{\partial N_{TE_0}}{\partial n_c}, \dfrac{\partial N_{TM_0}}{\partial n_c}$ for TE_0 and T_0M modes, and sensitivity

$\dfrac{-\partial \tilde{N}}{n_c}$ of difference interferometer as a differential refractometer for aqueous solutions

vs. waveguide thickness d_F, $n_c = 1.33$, $\lambda = 633$ nm. Top waveguide of type (a); bottom, waveguide of type (b) as in Fig. 2.30 [54].

Fig. 2.31 shows the sensitivity constants $\dfrac{\partial N}{\partial n_c}$ for IO sensors working as

refractometers for samples C having a refractive index near $n_c = 1.33$, such as aqueous solutions.

In microporous wave guiding films F the sensor effect (iii) can occur, i.e., an adsorption of analyte molecules inside the pores. This leads to a change $\Delta n_F = (1 - q)\Delta n_p$ of the film's refractive index, where q is the packing density of the

solid material, (1-q) the relative pore volume and Δn_p, the change in refractive index inside the pores.
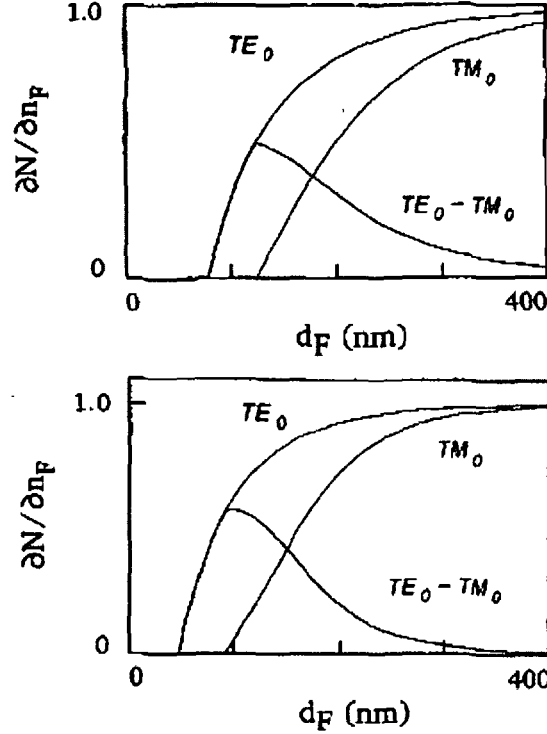
Fig-2.32: Calculated sensitivities $\dfrac{\partial N_{TE_0}}{\partial n_F}, \dfrac{\partial N_{TM_0}}{\partial n_F}$ for TE_0 and TM_0 modes, and sensitivity

$\dfrac{\partial \tilde{N}}{n_c}$ of difference interferometer related to adsorption of molecules from a gaseous

sample C inside the microporous wave guiding film F vs. its thickness d_F, $n_c=1$ and

$\lambda=633$ nm respectively [54].

The optical sensitivities $\left(\dfrac{\partial N}{\partial n_F} \right)$ for adsorption from a gaseous medium such as air are

shown in Fig. 2.32. For both the TEo and TMo modes, the sensitivities $\left(\dfrac{\partial N}{\partial n_F} \right)$ versus

d_F monotonically approach the value one for large waveguide thicknesses. For the sensor effect (iii), the field inside the wave guiding film F is responsible, not the evanescent field as in sensor effects (i) and (ii). Therefore, it is not necessary to use very

thin high-index wave guiding films F in grating coupler and interferometric IO sensors.

But with the difference interferometer high optical sensitivities $\dfrac{\partial \widetilde{N}}{\partial n_F}$ are only obtained

with thin waveguides. An additional advantage of very thin waveguides is that the sensors' response times due to in- and out-diffusion of the analyte are small.

2.3.4 Comparison between Fiber optic sensor and integrated optical planar waveguide sensor

Even after a number of years of development, fiber-optic sensors have still not enjoyed great commercial success, since it is difficult to replace already well-established technologies, even if they exhibit certain limitations. Fiber optic sensors have attracted considerable attention, especially in the application of biochemical species detection having excellent advantages such as good compactness and high sensitivity, shorter response time, low cost, and high compatibility with fiber optic networks. However, optical fiber-based systems do not seem promising with respect to fabrication, efficiency and miniaturization. However, planar waveguide-based platforms employing evanescent wave sensing techniques have shown tremendous improvement [71] and evanescent wave sensors have proven to be highly sensitive [72]-[74].

2.3.5 Requirement of IO planar waveguide sensors

Much of the reported work today has focused on miniaturization of sensors for the purpose of improving performance and throughput. The benefits of miniaturization, such as smaller sample requirements, reduced reagent consumption, decreased analysis time, and higher levels of throughput and automation can be very easily achieved with integrated optic sensing technology. In clinical diagnostics and in environmental monitoring there is need for these extreme sensitivities. Because IO sensors are small, they also offer the possibility to realize multi-purpose sensor arrays and the way is open for a cheap mass production similar to the way electronic chips are produced nowadays. It is not necessary for the sensor industry to bear all the cost of the research and development of IO devices and systems by itself. So we can conclude that there are

ample reasons why IO sensors should have our interest: IO sensors, to our opinion, can be expected to play a very important role in future.

2.4 Performance parameters of optical sensors

Optical sensor performance is determined by a number of parameters [75][76] such as Sensitivity, Limit of Detection (LOD), Limit of Quantization (LOQ) and Specificity/Selectivity that are summarized as follows:

2.4.1 Sensor sensitivity

Sensitivity is the change of the sensor output signal in response to a change in a property of the sensor (e.g., the concentration of an analyte deposited on the sensor surface). It is a parameter that defines the ability of a sensor to transduce an input signal, (which is the variation of a sensor property) to an output one. Different definitions of sensitivity such as waveguide sensitivity etc. can be found in literature in relation to the parameter representing the changing property, i.e. the input signal. If the sensor interacts with an analyte in contact with its surface, the mass/sensor surface unit ratio can be assumed as input variable. In case of sensors sensitive to an analyte bound to the surface; the input signal is the concentration of the analyte. In this case, the parameter takes also into account some aspects such as the total exposed area and the kinetics of the binding between the sensor and the analyte.

2.4.2 Limit of Detection (LOD)

Limit of Detection (LOD) is defined as the minimum amount of concentration or mass of the biochemical substance that can be detected by the sensor over the background signal. Limit of detection depends on the resolution of the sensor. Resolution is the smallest change that can be observed in the output signal. It is a critical performance parameter for detecting analytes at low concentration or molecules at low weight and depends on transducer, read-out technique, overall noise level and data processing.

2.4.3 Limit of Quantization (LOQ)

An additive figure used to describe the smallest concentration of a measurand that can be measured by an analytical procedure is the Limit of Quantization (LOQ). It is defined as the lowest concentration at which not only the analyte can be reliably detected, but also at which some predefined goals concerning measurement errors, i.e. bias and imprecision, are met. The dynamic range is the range of the measured values detectable by the sensor. It is lower limited by the LOD and upper-limited by saturation of the sensing signal sensor or by physical limitation such as sensor breakage or unpredictable changes of the sensitivity.

2.4.4 Selectivity or Specificity

In addition to being able of producing an output signal related to the presence of an analyte, a sensor must also be able to distinguish between the analyte and any other substance. This capability is named selectivity or specificity, which is difficult to be measured due to the very large number of possible substances that do not generate an output signal. In fact, the sensor selectivity becomes particularly important when trying to detect an analyte at low concentration in an environment containing a high concentration of other materials, many of which cannot specifically bind to the sensor and therefore can produce an anomalous signal. Many biosensors exploit complex, specific binding interactions provided by nature, such as antibody-antigen, nucleic acid hybridization, biotin-streptavidin, and enzyme-substrate interactions. Other substances such as aptamers have been artificially developed for the same purpose.

2.4.5 Sample Volume

The sample volume is the smallest requested volume to make a reliable measurement. Other aspects, such as portability and cost, can have a significant impact on the commercial success of a sensing technique. Portability refers to the possibility to easily carry the biosensors. It is important for real-time detection when time and location are critical aspects, such as in case of difficult transportation of the sample to the laboratory (as an example in case of environmental pollution control and patients at bed). Cost is determined by the disposable and by the instrumentation. Although the optical

technologies are in principle more advantageous in terms of cost for performing an individual assay because they do not use tag reagents, the cost of the transducer has to be low enough. This can be achieved, as an example, by designing a sensor, even using an expensive technology that can be regenerated and used for several successive analyses.

2.5 Review on planar waveguide materials and fabrication technologies

The research described in this thesis is partly motivated by the desire to explore the interesting possibility to fabricate state-of-the-art SiON based planar waveguide sensor with potentially low cost and by applying the standardized processes using $SiO_2/SiON$ as a Waveguide Material.

Table-2.3 shows the optical properties and fabrication steps of different waveguide materials used for fabrication of PID's [77]. It is found from the table that the fabrication steps of waveguide devices used for silicon based materials are as same as those used for conventional IC technology but those are not the same for other waveguide materials as mentioned in the table-2.3. The fabrication steps of silicon based materials can easily be adapted in mass production which is commercially viable. Since InP/GaAsInP waveguide materials uses Molecular Beam Epitaxial (MBE) growth technique, the fabrication cost of InP/GaAsInP waveguide is more than other materials. The basic fabrication steps for polymeric waveguide materials is LASER writing which is cheaper therefore, it is difficult to use the same technology for mass production. Moreover LASER writing technique is time consuming.

Table-2.3 also shows that high index contrast are available in $SiO_2/SiON$, InP/GaAsInP, SOI and Polymeric waveguide materials to compact waveguide device components, compared to Ti:LiNbO_3 and SiO_2/SiO_2-GeO_2 materials having lower index contrast. In addition, these materials show polarization insensitive property in comparison to Ti:LiNbO_3 material because of crystal structure. Actually, polymeric and silicon based materials show thermo optic properties. Although, polymeric materials have higher thermo optic coefficient and easy processing of devices, but silicon based materials are highly stable and compatible to conventional IC processing technology.

Although SOI has higher index contrast of fixed value~2, but wide variation of the index contrast (maximum up to 0.53) can be achieved by varying nitrogen and oxygen content in SiON material. In case of SOI waveguide device, the reported propagation losses of SOI waveguides is 0.1 dB/cm [78] and the fiber to chip coupling loss are of the order of 2-5 dB/facet, whereas in case of SiO_2/SiON, the propagation losses are same as SOI materials but fiber to chip coupling loss (order of 1 dB per facet) is lower than that of SOI material. The SiO_2/SiON material also shows more chemical inertness property than SOI material. More over, the processing system of SiO_2/SiON waveguide device is available with us for fabrication of waveguide devices. Because of the above reasons, we have chosen SiO_2/SiON as waveguide material in which SiON material is used for core fabrication of the planar waveguide as mentioned in detail in the Chapter-3 respectively.

Table-2.3: Waveguide materials and its properties and fabrication steps

Materials with range of refractive index	Δn (max)	Δn taken by previous authors	Properties				Basic Steps of fabrication	Material cost/ processing cost	Reported sensing application
			Thermo-optic coefficient $\alpha = \dfrac{dn}{dT}$	Electro-optic coefficient (r_{33})	Stability	Polarization sensitivity/ Birefringence			
SiO_2/SiON Index range~ (1.45 – 1.98)	~ 0.53	0.033 [79] 0.103 [80]	10^{-5} / ^{0}C [81]	-----	High [81]	Polarization Insensitive [81] /10^{-6}	i) Formation of SiO_2 lower cladding layer on Si-Substrate ii)Formation of SiON layer on SiO_2 layer iii) Fabrication of SiON core with photolithography iv) Formation of Top cladding SiO_2 layer	Mode-rate/ High	
GeO_2-SiO_2/ SiO_2 Index range~ (1.45 – 1.47)	~ 0.02	0.0075 [82] 0.0025 [83]	10^{-5} / ^{0}C [81]	-----	High [81]	Polarization Insensitive [81]/10^{-5}	i) Formation of SiO_2 lower cladding layer on Si-Substrate ii)Formation of SiO_2-GeO_2 layer on SiO_2 layer iii) Fabrication of SiO_2-GeO_2 core with photolithography and RIE iv) Formation of Top cladding SiO_2 layer	Moderate/ High	

Table-2.3: Waveguide materials and its properties and fabrication steps (**continue..**)

Materials with range of refractive index	Δn (max)	Δn taken by previous authors	Properties				Basic Steps of fabrication	Material cost/ processing cost	Reported sensing application
			Thermo-optic coefficient $\alpha = \dfrac{dn}{dT}$	Electro-optic coefficient (r_{33})	Stability	Polarization sensitivity/ Birefringence			
Silicon on insulator (SOI) (3.4767)	2.026	---	1.84×10^{-4} / ^{0}C [81]	----	High [81]	Polarization insensitive /10^{-4}	i) Formation of SOI wafer by using Bond and etch back method or Separated by implanted oxygen method ii) Fabrication of Si core with photolithography and RIE ii) Formation of Top cladding SiO_2 layer	Mode-rate/ High	
Ti: LiNbO$_3$ Index range~ (2.15- 2.21)	~0.06	0.006 [84] 0.01 [85]	---	30.8 pm/V [8]	High [8]	Polarization sensitive [8] /10^{-2}	i) Formation of Ti: LiNbO$_3$ using thermal Ti diffusion ii) Fabrication of waveguide core with photolithography and etching	High/high	

Table-2.3: Waveguide materials and its properties and fabrication steps (**continue..**)

Materials with range of refractive index	Δn (max)	Δn taken by previous authors	Properties				Basic Steps of fabrication	Material cost/ processing cost	Reported sensing application
			Thermo-optic coefficient $\alpha = \dfrac{dn}{dT}$	Electro-optic coefficient (r_{33})	Stability	Polarization sensitivity/ Birefringence			
InP/GaAsInP Index range~ (3.13 - 3.5)	~0.33	0.13 [86] 0.167 [87] 0.15 [88] [89]	----	-----	Stable [86]	Polarization Insensitive [86] / 2.5×10^{-4}	i) Formation of GaAsInP layer by using molecular beam epitaxial growth (MBE) ii) Formation of InP layer by using MBE iii) Fabrication of waveguide core with photolithography and etching	High/ High	-
Polymer Index range~ (1.44 -1.65)	~0.21	0.03 - 0.1 [90]	10^{-4} /^{0}C [90]	10 – 200 pm/V	Low	Polarization Insensitive / 10^{-2}- 10^{-6}	i) Fabrication of polymer layers by using chemical processing polymerization ii) Fabrication of polymeric waveguide by using LASER writing	Low/low	-

2.6 Optical planar waveguide sensor and applications-a review study

Table 2.4 shows different optical planar waveguide sensors reported by previous author. Very few studies have been reported for integrated planar waveguide optical sensor. D. Kumar and V. Singh [91] reported the analysis of the sensitivity of a five-layer metal-clad planar waveguide based sensor having nonlinear material in the cover media. It has been shown that the introduction of the nonlinear material in the waveguide not only improves the sensitivity but also provides additional parameters to increase the sensitivity. Fig 2.33 shows the schematic of a metal-clad planar waveguide based sensor having five layers structure with 1 mm thick glass plate as a substrate [n_S= 1.48534(FK51A)], a metal cladding of 30 nm silver (n_M = 0.065 + i4.0) a 500 nm thick polystyrene (PS) film (n_F=1.59); the affinity layer is approximately 30–60 nm thick and coated with carbon source or hydrophobic plastic as demonstrated by V. Singh and D. Kumar. Since the number of layers is more, fabrication cost of this type of sensor is high.
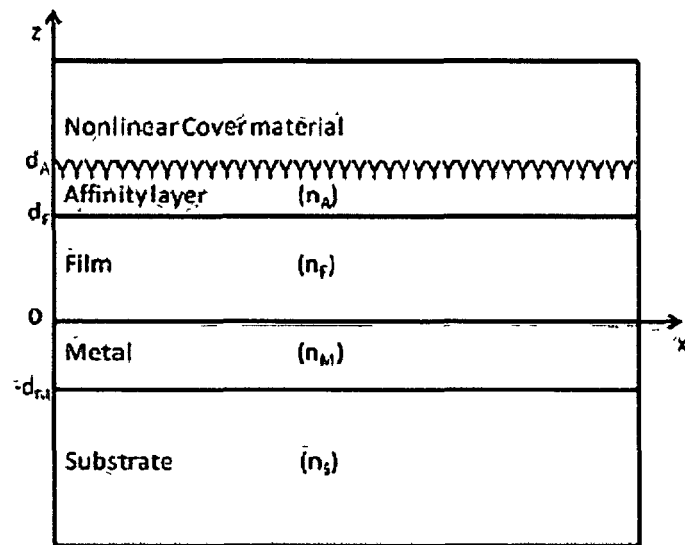
Fig-2.33: Schematic diagram of a five-layer nonlinear asymmetric metal-clad planar waveguide with their refractive indices.

Parriaux et al. [92] presented an extensive theoretical analysis for the design of evanescent linear waveguide sensors and derived the conditions for the maximum achievable sensitivity for both TE and TM polarizations as shown in Fig. 2.34.
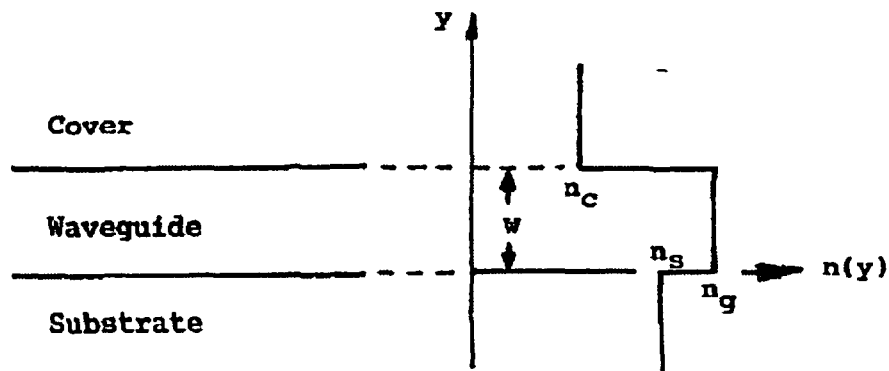
Fig-2.34: Step-index slab waveguide of width w and substrate, guide, and cover refractive indices n_s, n_g, and n_c.

In this case, the asymmetry parameter is $a = \dfrac{n_g^2 - n_c^2}{n_g^2 - n_s^2}$. But sensing area of this type of waveguide is small and hence sensing is reduced.
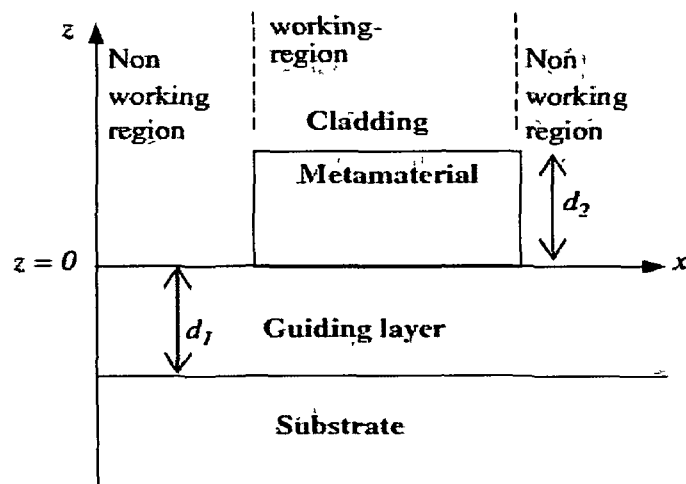
Fig-2.35: Schematic structure of integrated waveguide sensor with a metamaterial layer.

Taya et al. [93] has shown that the sensitivity of an optical waveguide sensor can be dramatically enhanced by using a metamaterial with negative permittivity and permeability, as shown in Fig. 2.35. In the figure, a guiding layer with permittivity ε_f,

permeability μ_f and thickness d_1 is sandwiched between a semi-infinite substrate with permittivity ε_s and permeability μ_s and a semi-infinite cladding with permittivity ε_c and permeability μ_c. In the working region, there is a layer of metamaterial with negative permittivity ε_m, negative permeability μ_m, and thickness d_2 between the cladding and the guiding layer. In this sensor, the number of layers is more and hence fabrication cost is also high.
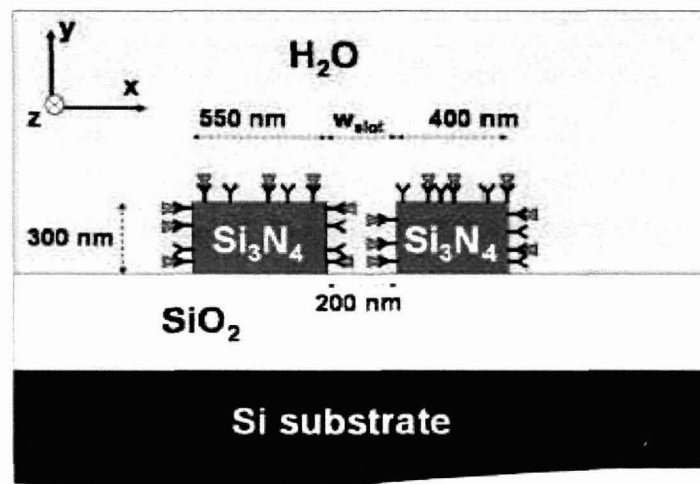
(a)

Fig-2.36: (a) Schematic cross section of the Si_3N_4/SiO_2 ring slot-waveguide used for optical sensing of biomolecules. Triangles and Y-shaped symbols represent antigen and antibody molecules, respectively.

Carlos et al. [94] has demonstrated label-free molecule detection by using an integrated biosensor based on a Si_3N_4/SiO_2 slot waveguide micro ring resonator as shown in Fig. 2.36(a). The device consists of a 70 μm radius slot waveguide ring resonator made of Si_3N_4 on SiO_2. The Si_3N_4 rails of the slot-waveguide ring are separated by 200 nm (w_{slot}), and their widths are 400 and 550 nm for the outer and inner rails, respectively, as shown in Fig. 2.36(b). Although this type of sensor structure has number of layers, the slot type sensing structure is slightly complex.

TE-like mode
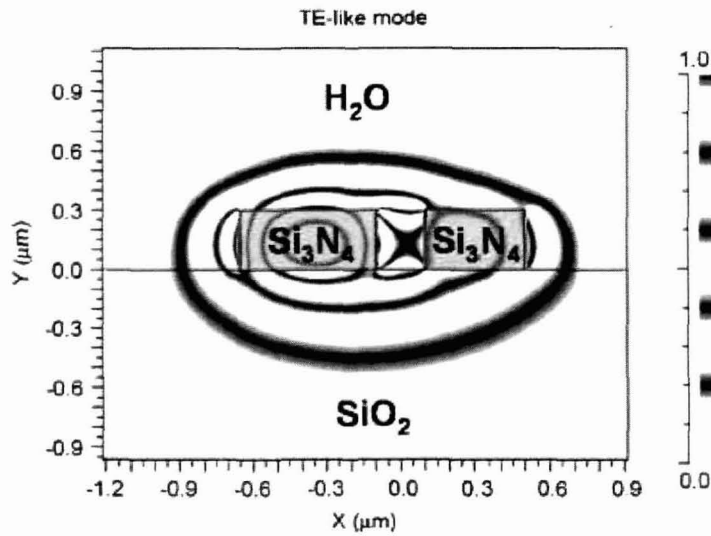
(b)

Fig-2.36: (b) Calculated quasi-TE mode of the ring slot-waveguide turning to the left (−x axis) with a radius of curvature of 70 μm and an operation wavelength of 1.3 μm.

P. Karasinski [95], presented planar waveguide sensor structures with grating couplers for the application in evanescent field spectroscopy as shown in Fig. 2.37.
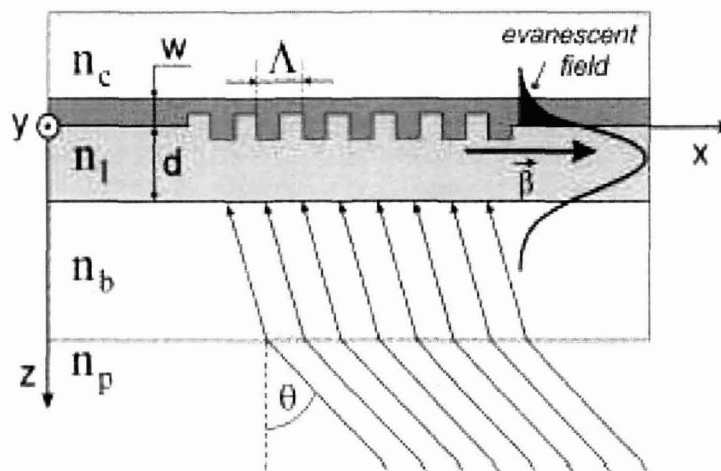
Fig-2.37: Planar sensor structure

Planar slab waveguides of high refractive index ($n \approx 1.8$) were produced in sol-gel technology. The layers SiO_2:TiO_2 were coated on BK7 glass substrate using dip-coating method. Since the structure is fabricated by sol-gel technology but not by conventional IC technology, it can not have mass production.
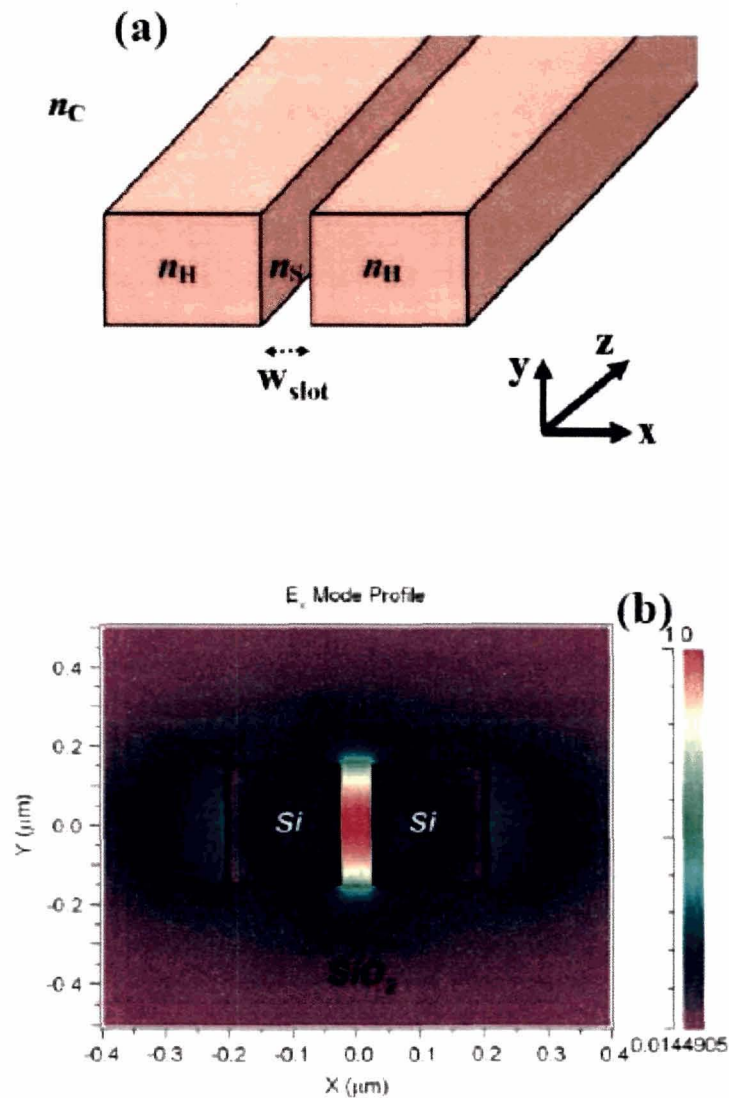
Fig-2.38: (a) Schematic view of a slot-waveguide. (b) Calculated E_x profile of the quasi-TE eigen mode in a Si ($n_H = 3.45$)/SiO_2 ($n_S=n_C=1.44$) slot-waveguide at a wavelength of 1.55 μm. E-field is enhanced in the nano scale slot-region of refractive index n_S.

Carlos Angulo Barrios [96] has shown in Fig. 2.38 that, the use of slot-waveguides has proven to be advantageous over conventional waveguides in terms of sensitivity and potential use in applications requiring the fusion of nano-photonics and nano-fluidics.

Densmore et al. [97] demonstrated a new highly sensitive evanescent field sensor using silicon-on-insulator (SOI) photonic wire waveguides. P. Karasinski [98] presented the results of theoretical analysis and the results of experimental research of composite sol−gel SiO2:TiO2 film/ion−exchange glass optical waveguides, as shown in Fig. 2.39. The theoretical part of the work presented modal characteristics and the influence of the parameters of the uniform waveguide film on homogeneous sensitivity. The fabrication cost is high.
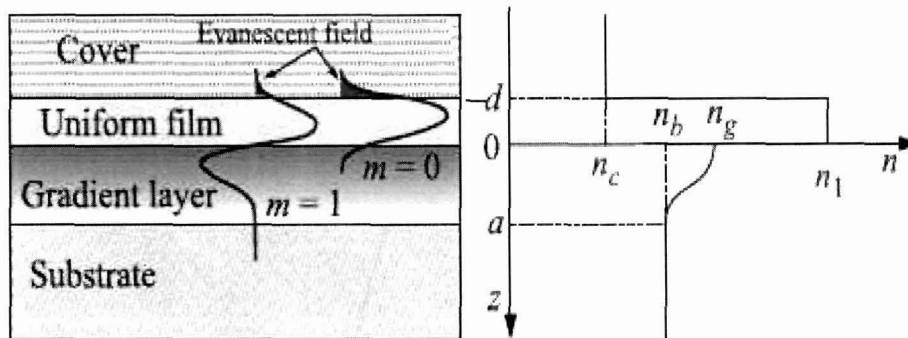
Fig-2.39: Diagram of a composite optical waveguide structure.

Very recently, S. A. Taya and Taher M El-Agez [99], presented an extensive theoretical treatment of an optical waveguide sensor consisting of thin dielectric film surrounded by an aqueous cladding and an ideal non-absorbing plasma substrate. They have considered the case when the frequency of the guided light is greater than the plasma frequency so that the refractive index of the substrate is less than unity. Fig. 2.40 shows the structure that provides a reverse symmetry configuration in which the refractive index of the substrate is less than that of the cladding. Although the sensor structure is simple, the device is costly as the fabrication is done on the costly plasma substrate.

Cladding n_c

————————————————— X=h

                          x
                          ↑
Guiding layer n_f |
                      y ○——→ z

————————————————— X=0

Plasma layer n_p
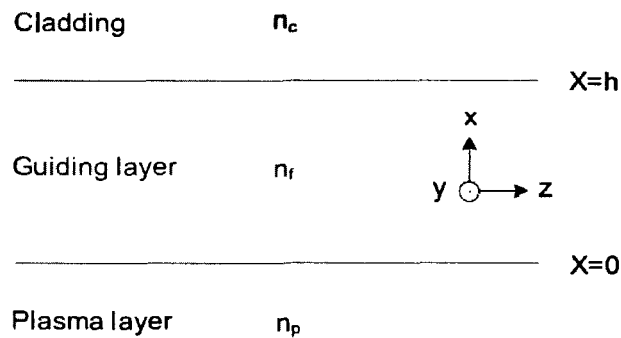
Fig-2.40: A schematic diagram of the slab waveguide sensor under consideration

Zou et al. [100], presented planar waveguides with Fermi graded refractive index variation were examined as sensors for the measurement of solution concentrations. The waveguides were fabricated on B270 optical glass by an ion exchange method using the composite salt $0.004AgNO_3$-$0.996NaNO_3$. The experimental device for sensing solution concentrations is shown in Fig. 2.41. This type of sensor requires very good alignment system which can be made portable.
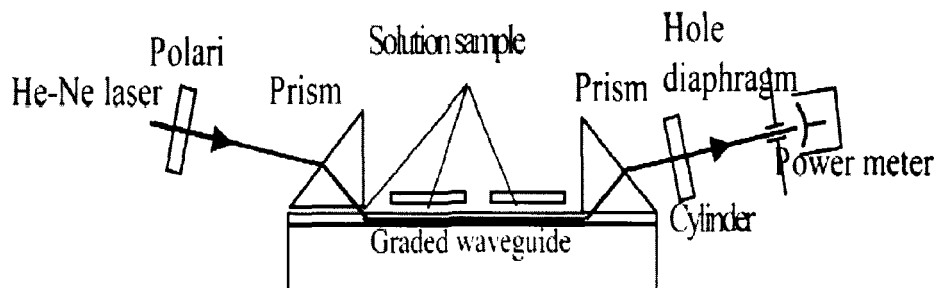
Fig-2.41: Experimental set up for solution concentration sensing

Yimit et al. [101], presented the design and fabrication of highly sensitive thin-film composite optical waveguides (OWG) sensor device with high refractive index for sensor applications as shown in Fig. 2.42(a) and Fig. 2.42(b) respectively.
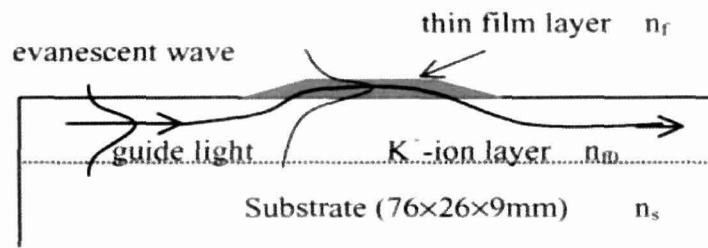
(a)
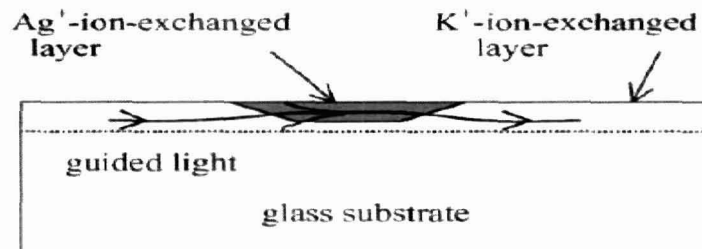
(b)

Fig-2.42: (a) Structure of the composite OWG and the principle of operation. n_s, n_{f0}, and n_f are respectively, refractive index of the substrate (1.515), the K+-ion-exchanged layer (1.5195), and of the thin film. **(b)** Structure of the ion-exchanged composite OWG. The arrow shows how the guided light is transferred from one part of the OWG to another part via adiabatic transition.

Airoudj et al. [102] presented a new Multilayer Integrated Optical sensor (MIO) for ammonia detection at room temperature as shown in Fig. 2.43(a) and Fig. 2.43(b) respectively. The sensor is based on the interaction of the evanescent wave of the guided mode (orthogonally polarized TE_0 and TM_0 modes) with the sensitive material. Then, the penetration depth of the evanescent field must be higher than the passive layer thickness. Since sensing area is less, sensitivity is less than the other sensors.
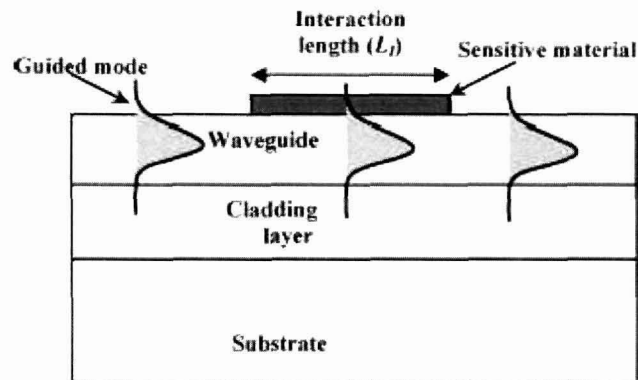
(a)
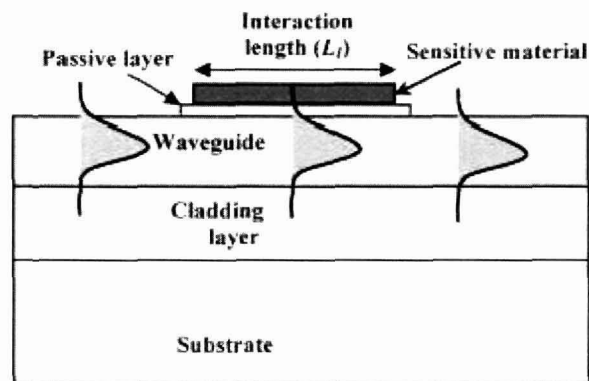
(b)

Fig-2.43: Schematic structures of the two types of waveguide sensors: **(a)** conventional waveguide sensor; **(b)** multilayer integrated waveguide sensor.

Veldhuis et al. [103], has shown that the sensitivity of the effective refractive index on the cladding index in evanescent optical waveguide sensors, can be larger than unity. It has been shown that in the case of homogeneous sensing with a three-layer slab waveguide the sensitivity of the effective refractive index to variations of the cladding index can be larger than unity for TM polarization and strong guidance. The Schematic representation of the slab waveguide is shown in Fig. 2.44.
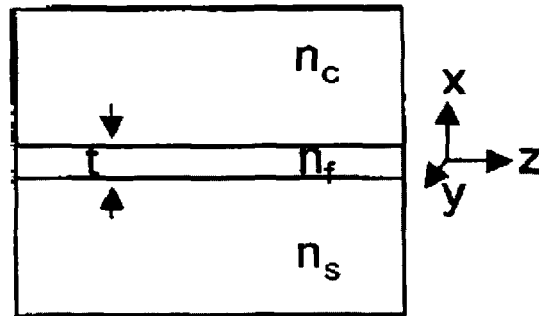
Fig-2.44: Schematic representation of the slab waveguide under study. The grey area indicates the normal electric field component of the TM mode in a large-guidance waveguide.

From the above studies, it is evident that very good planar waveguide sensor requires the following characteristics:

(i)   Simple structure having less number of layers for reducing cost of fabrication.

(ii)   More sensing area for enhancement of sensitivity.

(iii)   Use of low cost material for reduction of fabrication cost.

(iv)   High selectivity

(v)   Use of conventional IC processing technology for mass production

(vi)   Simple alignment set-up for making it portable

From the reported sensors as mentioned in Table-2.4, it is seen that no planar waveguide sensors show all the above characteristics together. So it is required to propose and develop simple planar waveguide based sensor structure having bigger sensing area and less number of layers using low cost materials. The use of conventional IC technology can provide its production for reduction of fabrication cost. In this thesis, we have tried to propose and develop the same sensors which are reported in chapter-3, 4 and 5 respectively.

Table-2.4: Characteristics of optical sensors as reported by different authors.

Author's Name/ material used	Type of waveguide Structure	Core size and cladding width (μm)	Sensitivity	Wavelength of light source	Application	Fabrication cost
Kumar, D., & Singh, V. [91] Glass/Silver	Planar waveguide	0.5x0.03 $(\mu m)^2$	5.36×10^{-4} nm	0.6328 μm	-	High
Parriaux et al. [92]	Planar waveguide	-	-	-		Moderate
Taya, S.A., et al. [93] Si_3N_4	Planar waveguide	-	-	-	-	High
Carlos, A. B., et al. [94] Si_3N_4 /SiO_2	Slot waveguide	-	1.8 and 3.2 nm/ (ng/mm2)	1.3 μm	detection of Bovine Serum Albumin and anti-BSA, respectively.	Moderate
Karasinski, P. [95] SiO_2:TiO2	Planar waveguide	-	0.113 and 0.147	677 nm	Chemical and biochemical measurements	Moderate
Carlos, A.B. [96] SiO_2/Si_3N_4 and Si/SiO_2	Slot waveguide	-	212 nm/RIU	1.55 μm	Biochemical sensing	Moderate
Densmore, A., et. al. [97] SOI	Planar waveguide	-	0.31	1550 nm	bio-chip applications	High
Karasinski, P. [98] SiO_2:TiO_2	Planar waveguide	-	3×10^{-3} (TM1) 1.4×10^{-3} (TE1)	677 nm	Chemical and biochemical measurements of water solutions.	High
Sofyan, A.T., & Taher, M.E. [99] water/ZeSe/ideal plasma	Planar waveguide	-	-	1550 nm	Characterization of plasma media	High

Table-2.4: Characteristics of optical sensors as reported by different authors (**continue..**)

Author's Name/ material used	Type of waveguide Structure	Core size and cladding width (µm)	Sensitivity	Wavelength of light source	Application	Fabrication cost
Renling, Z., et al. [100] B270 optical glass/ composite salt 0.004AgNO₃-0.996NaNO	Planar waveguide	-	-	632.8 nm	-	High
Yimit, A., et al. [101] potassium-ion-exchanged (K+) glass	Planar waveguide	-	10^{-4}	633 nm	(bio-) chemical sensing	High
Airoudj, A., et al. [102] polyaniline (PANI)/ polymethyl metha- crylate (PMMA)	Planar waveguide	-	17% for LI = 5 mm and 6% for LI = 2 mm	632.8 nm and 980 nm	ammonia detection	Moderate
Veldhuis, G.J., et al. [103] InP/GaAsInP	Planar waveguide	-	1.35	1550 nm		High

2.6.1 Refractometric optical sensing and petroleum fuel adulteration

Since the proposed work consists of sensing of adulteration of petroleum products, we have tried to report previous studies on adulteration of petroleum products.

The Motor Spirit and High Speed Diesel (Regulation of Supply and Distribution and Prevention of Malpractices) Order, 1998, defines adulteration as the introduction of a foreign substance into motor spirit/high speed diesel, illegally or unauthorized with the result that the product does not conform to the requirements and specifications of the product. The foreign substances are called adulterants, which when introduced alter and degrade the quality of the base transport fuels. Adulteration is financially unattractive when less than (10%) while more than 30% [104] without doubt is likely to be detected by the user from the degradation of the performance of the engine caused by the adulterated fuel. In addition, we see that the oil companies add antiknock compounds like Tetra Ethyl Lead (TEL), $(CH_3CH_2)_4Pb$ to raise the antiknocking property.

$$4CH_3CH_2Cl + 4NaPb \rightarrow (CH_3CH_2)_4 Pb + 4NaCl + 3Pb \qquad (2.48)$$
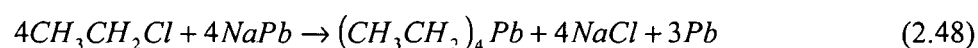
To check the adulteration effectively, it is necessary to monitor the fuel quality at the distribution point itself. The equipment for this purpose should be portable and the measurement method should be quick, capable of providing test result within a very short time. The measuring equipment should also be preferably inexpensive (as a large number of such units would need be simultaneously deployed) and easy to use. It is found that the earlier techniques available for detecting adulteration [105]-[111] require taking out the sample for measurement and thus they are time consuming and are unable to sense adulteration level below 20 % [112]. So in our work, we try to detect adulteration of petroleum products (specially petrol with diesel, diesel with kerosene and petrol with both kerosene and diesel) below 20% level with accuracy, enhanced sensitivity and minimal sample volume by using optical waveguide sensor (mentioned in chapter 3). This technique is immunity to electromagnetic interferences, avoiding chemical hazardous. Besides all these above advantages, planar waveguide based optical sensors offer an important key feature that the sensor is very sensitive to variation in refractive index of sensing material surrounding the core (as cladding). Before detection of adulteration, we like to mention chemical composition of petroleum.

Petroleum is a mixture of Hydrogen and Carbon starting number of carbon atoms from C_1 to C_{70} and more. The ultimate analysis of petroleum indicates that in addition to hydrocarbons (83-87% of Carbon (C) and 11-15% of Hydrogen (H)) small quantities of nitrogen (N), sulphur (S) and oxygen (O) are also present. Sulphur is present generally as alkylsulphides, hydrosulphides and hydrogen sulphide, and thiophine and less frequently, combined oxygen is present as carboxylic acids (napthalenic acids) (COOH group), ketones (C=O) and phenols (C_6H_5OH). The disagreeable odour of petroleum is due to the sulphur compounds present in it. The hydrocarbon present in the crude petroleum may be divided into two main classes.

Open chain or aliphatic compounds: comprising of

- n-paraffins series (C_nH_{2n-2}),
- isoparaffin series (C_nH_{2n+2}) and,
- olefin series (C_nH_{2n}).

Ring compounds: comprising of

- naphthalene series (C_nH_{2n}) (derivative of cyclopentane and cyclohexane)
- aromatic series or benzene series.

In petroleum gaseous paraffins (hydrocarbons), methane (CH_4) to butane (C_4H_{10}) are present in the dissolved state. The napthenic hydrocarbons present in petroleum are mainly the derivatives of cyclopentane and cyclohexane. As Fig. 2.45 indicates, aromatic compounds have higher carbon-to-hydrogen (C/H) ratios than naphthenes, which in turn have higher C/H ratios than paraffins. The heavier (more dense) the crude oil, the higher its C/H ratio. Due to the chemistry of oil refining, the higher the C/H ratio of a crude oil, the more intense and costly the refinery processing required to produce given volumes of petrol/gasoline and distillate fuels. The proportions of the various hydrocarbon classes, their carbon number distribution, and the concentration of hetero-elements in a given crude oil determine the yields and qualities of the refined products. The petroleum fraction for petrol, kerosene and diesel is shown in Table 2.5.

Table 2.5: Petroleum Fractions

Sl. No	Petroleum Fraction	Boiling Range ^0C	Approximate No. of Carbon atoms
1	Petroleum Ether	30-70	C_5-C_7
2	Petrol	40-140	C_5-C_9
3	Naptha	140-180	C_9-C_{10}
4	Kerosene	180-250	C_{10}-C_{16}
5	Diesel	250-320	C_{10}-C_{18}

Fig. 2.46 shows the step wise process of fractional distillation for obtaining the petroleum products such as petrol, kerosene and diesel.
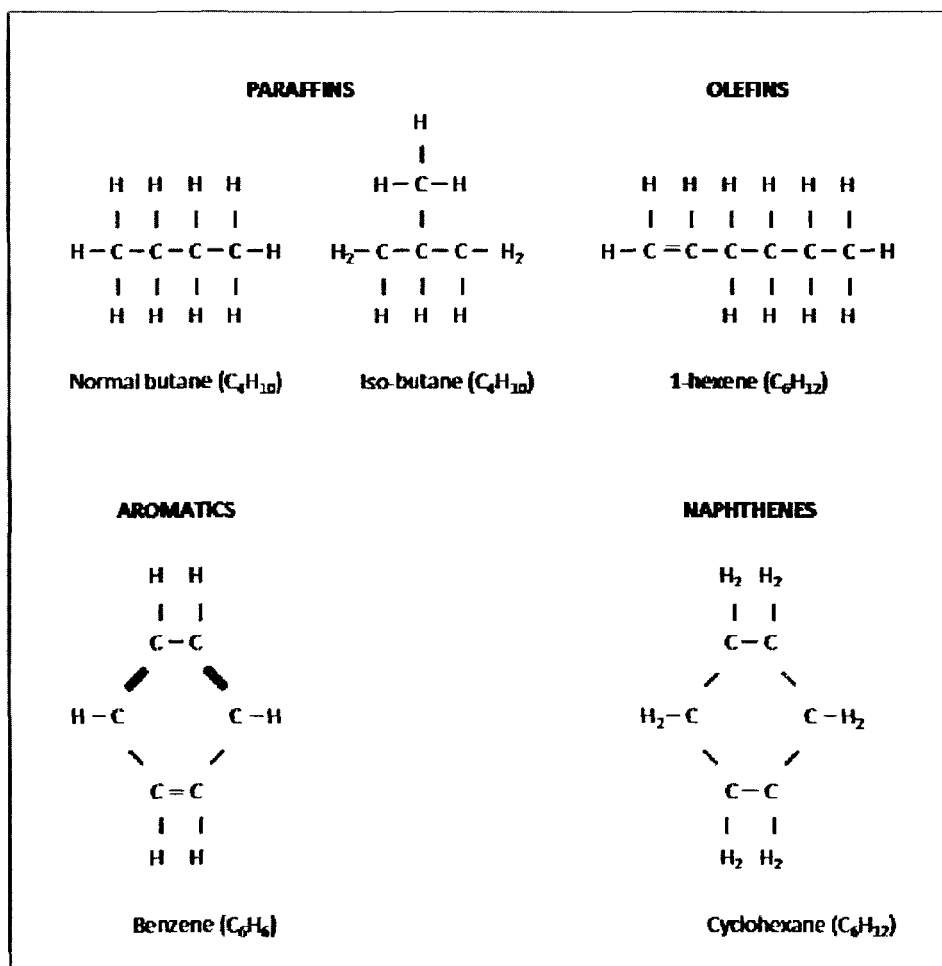
Fig-2.45: Important Classes of Hydrocarbon Compounds in Crude Petroleum
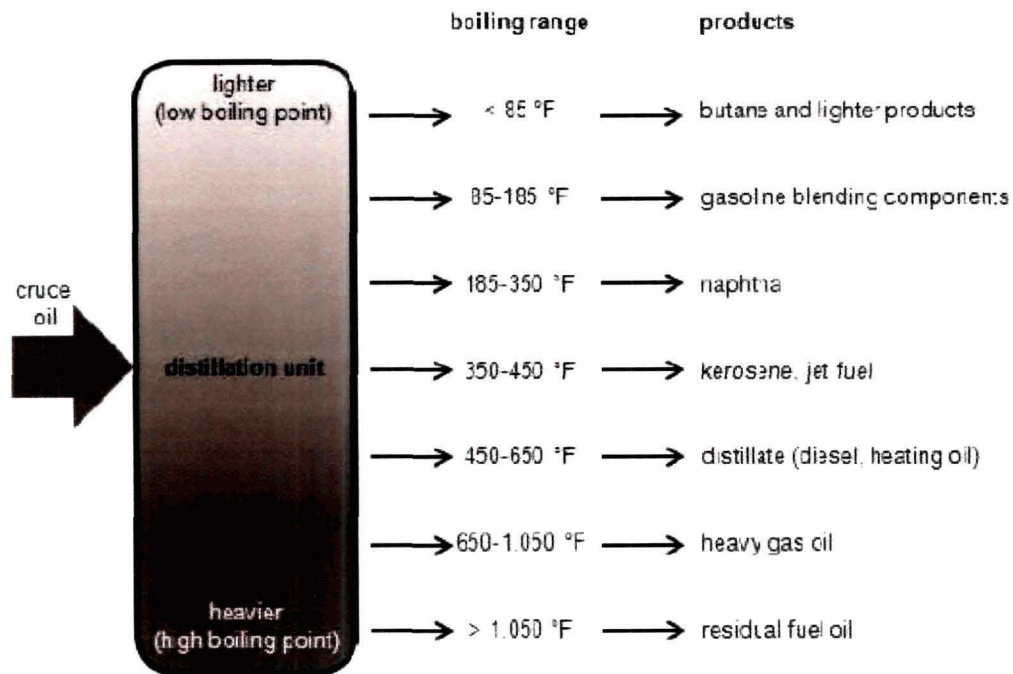
Fig-2.46: Fractional Distillation Process: Step-by-Step

2.6.1.1 Causes of petroleum adulteration

Most developing country governments have not yet established a system of fines that can act as a strong deterrent to fuel adulteration. There are number of reasons for this, including poor governance, shortage or absence of technical staff and paraphernalia for designing and conducting monitoring. Given these limitations, identifying and dealing with this abuse will require addressing problems on multiple fronts. The primary factors that encourage the practice of adulteration are the following –

❖ Existence of differential tax levels amongst the base fuels, intermediate products and byproducts. The adulterants being taxed lower than the base fuels give monetary benefits when mixed with replacing a proportion of the base fuels.

❖ Differential pricing mechanism of fuels and adulterants and easy availability of adulterants in the market.

❖ Lack of monitoring and consumers awareness.

❖ Lack of transparency and uncontrolled regulations in the production-supply and marketing chain for intermediates and byproducts of refineries.

❖ Non-availability of mechanism and instruments for spot-checking the quality of fuels.

2.6.1.2 Impacts due to petroleum adulteration

High sulphur contents of the kerosene can deactivate the catalyst and lower conversion of engine out pollutants. Kerosene addition may also cause fall in octane quality, which can lead to engine knocking. When petrol is adulterated with diesel fuels, the same effect occurs but usually at lower levels of added diesel fuel. Both diesel and kerosene added to petrol increases engine deposit formation. Petrol may also be adulterated with petrol boiling range solvent like toluene, xylene and other aromatics. With the 'judicious" adulteration, the petrol would not exhibit drivability problems in motor vehicles. Larger amounts of toluene and /or mixed with xylene cause some increase in HC, CO, NOx emissions, and significant increase in the level of air toxins -especially benzene - in the tailpipe exhaust. The adulterated petrol itself could have increased potential human toxicity if frequent skin contact is allowed. Extremely high levels of toluene (45 % or higher) could cause premature failure of neoprene, styrene butadiene rubber and butyl rubber components in the fuel system [112]. This has caused vehicle fires in some cases, especially in older vehicles. Adulteration of gasoline by waste industrial solvents is especially problematic as the adulterants are so varied in composition. They causes increased emissions, may even cause vehicle breakdown. Even low levels of these adulterants can be injurious and costly to vehicle operation. For petrol, any adulterant that changes its volatility can affect drivability. High volatility (resulting from addition of light hydrocarbons) in hot weathers can cause vapour lock and stalling. Low volatility in cold weather can cause starting problems and poor warm-up [113].

The amalgamation of kerosene with automotive diesel is generally practiced by oil industry worldwide as a means of adjusting the low temperature operability of the fuel. This practice is not harmful or detrimental to tailpipe emissions, provided the resulting fuel continues to meet engine manufacturer's specifications (especially for viscosity and cetane number). However, high-level adulteration of low sulphur diesel fuel with higher level sulphur kerosene can cause the fuel to exceed the sulphur

maximum. The addition of heavier fuel oils to diesel is usually easy to detect because the resultant fuel will be darker than normal. Depending on the nature of these heavier fuel oils and the possible presence of additional PAHs, there could be some increase in both exhaust PM and PAH emissions.

2.6.1.3 Petroleum adulteration detection as reported by earlier authors

As mentioned earlier, adulteration of transport fuels at the point of sale and during transportation is a routine problem in India. There are several petroleum products available in our country, which are close substitute of petrol and diesel, but are available at considerable lower prices. The price differential is usually in the range of Rs. 70-80 in case of petrol and Rs. 50-60 in case of diesel. Since kerosene is usually considered as poor man's fuel, Govt. of India has been subsidizing it for public distribution for several years. It is common knowledge that significant portion of this subsidized kerosene is being diverted for adulterating petrol. Several studies/survey carried out recently, have simultaneously pointed out alarming rise in the cases of fuel adulteration in our country and some of them are as below –

❖ Tata Consultancy has conducted an extensive survey on the kerosene distribution pattern within the country [114]. They arrived at the conclusion that more than 30% of Kerosene distribution intended for household consumption through PDS outlets flowed back to industry in one form or the other. This was a clear indication towards the flourishing business of adulteration in our country.

❖ According to Anti Adulteration Cell of India, Naphtha is a commonly used adulterant for petrol. The modus operandi is to import the product in huge quantity and divert it for adulteration. In a major seizure, recently the Cell detected import of naphtha through the Mangalore port allegedly for adulteration of auto fuels in Kerala, Andhra Pradesh, Karnataka, W. Bengal and M.P [114]. The intention was to import and move the products to a factory in Pondicherry, where it got blended with other adulterant chemicals. Following the investigation, the Cell sealed 82 kL of naphtha, 31 kL of other products along with plant and machinery allegedly used for adulteration.

❖ Similarly a case of adulteration has also been reported from Uttar Pradesh in the city of Meerut, where an authorized transport company was caught with adulterated stock. This transport agency had the authority to transport both petrol & diesel to retail outlets and solvents for industrial use. The agency was supposedly using its workplace for adulterating diesel with kerosene.

❖ According to news in "The Times of India", the State Government of Maharashtra loses a whopping Rs. 81 lakh and Rs. 75.6 lakh every month on account of combined sales & excise tax revenue against petrol and diesel adulteration in Mumbai city alone. This is believed to be 10 percent of the genuine sale, industry source reveal [114].

❖ Various estimates have been made of the extent of financial loss to the national exchequer as well as the oil companies as a result of diversion of PDS kerosene, use of off-spec, low value, hydrocarbons mixed with petrol and diesel, evasion of sales tax etc. Although these estimates vary over a wide range, it is safe to assume that the nation is losing at least Rs. 10,000 crores annually as a result of adulteration of fuel. If too this is added the social costs as a result of environmental pollution, damage to vehicles and other engines, etc., the loss could be substantially higher [114].

❖ With the plethora of foreign car manufacturers making a beeline to set up manufacturing facilities in the country, their first and immediate concern is the quality of petrol that gets supplied to the users' cars. They have uniformly found that supplies are heavily adulterated and particularly the Octane content is much lower than the specification value of 87%.

❖ Recently under the direction of the Supreme Court, Environment Pollution Control Authority (EPCA) through a local NGO (CSE) carried out tests of fuel samples from retails outlets and other points. The results of the study reveal 8.3% sample failure of the sample tested against 1-2 percent reported by oil companies in the past. The study further reveals that adulterated fuel in intelligent mix allowed retail outlets to reap a huge profit of more than Rs. 25, 000 a day [114].

2.6.1.4 Status of petroleum adulteration in Indian context

Studies on petrol adulteration started in 1966 with the use of semi-micro chromatography to deal with the problem of adulteration [115]. It has the objective of providing an alternative experimental procedure for a modified phase-titration method [116][117] which shows major improvements over currently available approaches and has considerable potential as the basis of an "in the field" method of analysis. Table-2.6 shows the previous reported studies on petroleum adulteration detection. Of the range of optical fiber sensors reported in the literature, it is found that the intensity based optical fiber sensors represent one of the most basic types of optical fiber sensor [118]. But the main drawback of these types of sensors is that the source fluctuations will affect the output intensity which can be overcome using a reference signal. Languease [119] presented an optical fiber refractometer for liquids which eliminates the influence of attenuation due to the liquids. L.S.M. Wiedemann et al. [120] proposes a method to detect adulteration by using physico-chemical properties of gasoline samples and performing statistical analysis. Sukhdev Roy [119] proposes a method of changing the refractive index of cladding of fiber for detecting adulteration of fuel which is based on the modulation of intensity of light guided in the fiber due to change in the refractive index of the cladding formed by adulterated fuel and the phenomenon of evanescent wave absorption. L. M. Bali [121] et al has developed an optical sensor for determining the proportional composition of two liquids in a mixture. It is based on changes in the reflected light intensity at the glass-mixture interface brought about by the changes in the proportion of one liquid over that of the other in the mixture. It uses a simple configuration consisting of the end separated fibers where T-R coupling is decided by medium filled in the gap. This configuration however is difficult to handle because of precision needed for alignment so as to get maximum sensitivity.

From the studies mentioned in Table-2.6, it is evident that the optical sensors used in these structures have lesser sensitivity, because of having less sensing area. Moreover these sensors require more sample volumes for testing. So these sensors are not suitable for online testing. The planar waveguide sensors proposed in this thesis (as mentioned in Chapter-3) has more sensitivity requiring less sample volumes for its adulteration detection. In Chapter-4, we have tried to mention how our proposed

sensors were used for adulteration sensing with high sensitivity and minimal sample volumes.

Table-2.5: Different adulteration detection techniques as reported by previous authors (**continue..**)

Author's Name/ material or instrument used	Type of sensor	Length of the sensor	Core size (μm) and cladding width (μm)	Numerical Aperture (NA)/ microscope objective	Sensitivity	Wave length of light source	Application	Room Tempe-rature	Noticeable advantage
Mishra, V., et al. [124]/ Single mode fiber (SMF-28, Corning) with a UV written long period fiber grating (LPFG)	Fiber optic sensor	-	-	-	0.12 nm		hydrocarbon contamination study	-	Detect presence of 10 % contaminant in petrol and diesel.
Patil, S. S., et al. [125]/ microcontroller	Fiber optic sensor	-	488 μm x 612 μm	0.47	-	-	Adulteration detection applications	-	-

Table-2.6: Different adulteration detection techniques as reported by previous authors

Author's Name/ material or instrument used	Type of sensor	Length of the sensor	Core size (μm) and cladding width (μm)	Numerical Aperture (NA)/ microscope objective	Sensitivity	Wave length of light source	Application	Room Tempe-rature	Noticeable advantage
Kishor, K., et al. [122]/ Optical time-domain reflectometer	Optical-fiber based	-	-	-	-	Pulsed laser diode at 1550 nm	Determination of adulteration in petrol	25^{0}C	-
Roy, S. [119]/plastic-clad-silica (PCS)	Fiber optic sensor		600 (μm)	0.4/20x	-	He-Ne laser at 632.8 nm	Determining adulteration of petrol and diesel by kerosene	30^{0}C	-
Bahari, M. S., et al. [123]/ spectro-photometer	-	-	-	-	-	Spectroph otometer set at 600 nm.	Determination of the adulteration of petrol with kerosene	-	Reduction of titration volume difference in batch variations

2.6.2 Integrated optical waveguide sensor as detection element for lab on a chip sensing application

Since our proposed work contain sensing of glucose concentration in blood, in this context we have tried to report previous works as reported by earlier authors on diagnose/detection of glucose concentration in blood. While significant advances have been made in the incorporation of light sources and detectors into chip-based optical platforms, this section primarily focus on integrated optical detection with microfluidic lab-on-a-chip (LOC) device platform. For separation and concentration of the different components in whole blood, we have seen that microfluidics based LOC devices use numerous techniques such as, acoustophoresis [126], cross-flow filtration [127], centrifugal forces [128], or gravitational sedimentation [129]. It is seen that LOC offer great possibilities in such applications as clinical point-of-care diagnostics, such as detection of blood glucose concentration, largely due to the fact that they do not involve any complexity. Great advantages include reduction of the analytical testing cost and time and also reduced consumption of sample and reagents. An accurate and fast detection is achievable with LOC, because detection is carried out off-chip which can manipulate small volumes of liquid in microfluidic channels of tens to hundreds of micrometers. This entails the miniaturization of analytical systems and reduction of required sample and reagent volumes onto a small microchip. Although several detection methods are being investigated including optical, magnetic, capacitive, and electrochemical, among these methods, integrated waveguide based technique using LOC is incredibly advantageous compared to the existing techniques. In such techniques, it is seen that since the governing physics of waveguide operation and the concept of their utility as an analytical device are quite simple, light is guided through the device on account of Frustrated Total Internal Reflection (FTIR), which generates an evanescent optical field that decays exponentially from the sensor surface. The present survey in this section through the relevant literature serves to highlight the most recent progress in applying chip-integrated waveguides for lab-on-a-chip (LOC) sensing applications, with special emphasis on detection of glucose level concentration in diabetes.

Development of the LOC technologies offers other indispensable benefits including better process control and lower manufacturing cost [130]-[132]. It is observed optical sensors using LOC offer compact alternatives to classical instrumentation while delivering comparable performance and disposable formats and makes LOC a superior candidate to support sensing applications. The two main factors that play a character in the choice of detection method for an LOC application are sensitivity and scalability to smaller dimensions. Moreover, devices incorporating LOC do not require a large amount of peripheral equipment for acquisition of detector signal. This makes the development of portable instrumentation based on LOC devices a realistic possibility.

The most important benefits of such an integrated waveguide based LOC platform include:

- Disposability
- Rapid prototyping and a final product with the same tools and materials
- High process repeatability
- Integrated functionality
- Enabling fabrication of multiple chips simultaneously.

2.6.2.1 Non-invasive sensing approach for measurement of glucose concentration

The development of ultra-compact and sensitive sensing structures with minimal sample requirement for accurate sensing has been of great recent interest. Waveguide-based optical sensing technology appears to be exceptionally amenable to chip integration and miniaturization. One of the main advantages of such technology is the possibility to integrate all the functions (chemical, optical, microfludics and electronics) in one single platform offering an ideal solution for the implementation of true lab-on-a-chip devices. Fig. 2.47 summarizes the vast field of glucose measurement techniques and distinguishes three different categories: invasive, minimal invasive and non-invasive approaches. Optical techniques like polarimetry [133][134], Raman spectroscopy [135][136], diffuse reflection spectroscopy [137][138]], absorption spectroscopy [139]-[141], thermal emission spectroscopy [142][143], fluorescence spectroscopy [144][145] and photoacoustic (PA) spectroscopy [146]-[148] have been

used to sense glucose with respect to non-invasive monitoring. As we see that most current devices are simple planar devices that do not incorporate the detection and after the reaction has taken place, the readout must be done with complex instrumentation in laboratory settings. That is the main reason why we have incorporated "on-chip" detection by using optical waveguide based sensors. By using this advanced technology, diagnosis in developing countries for detection of glucose concentration of diabetes patient could become an important achievement for the near future.
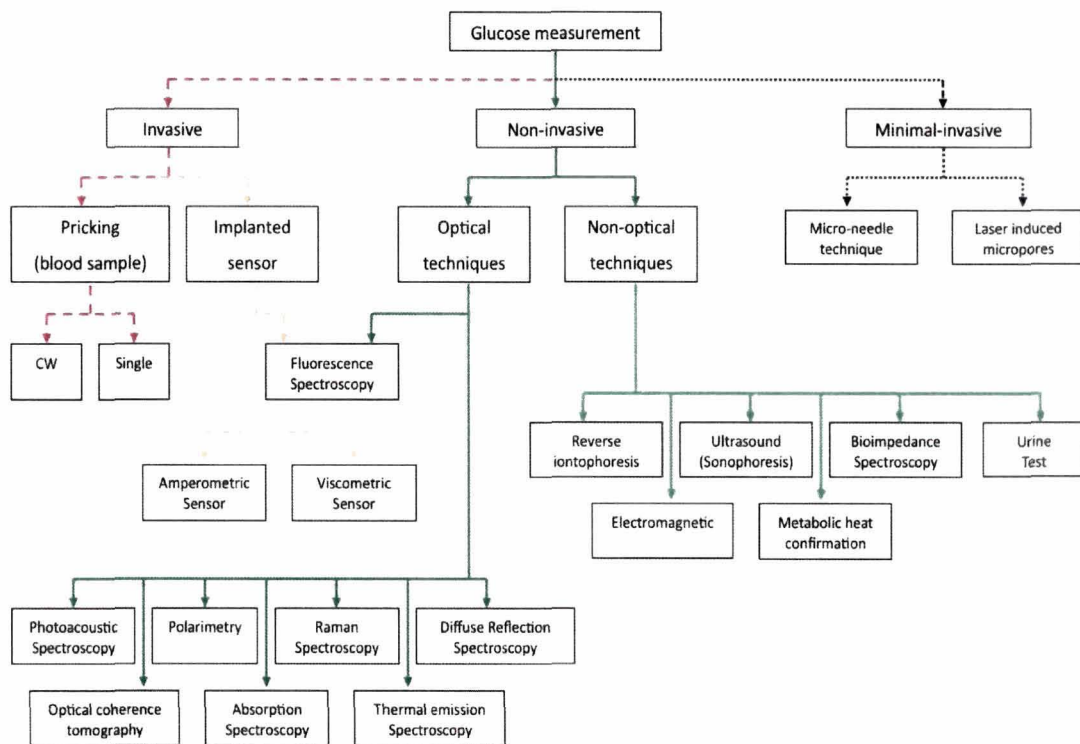
Fig. 2.47: Overview of possible techniques and active research areas for in-vivo glucose measurements.

2.6.2.2 Significance of sensing glucose

Although numerous schemes have been developed for the determination of glucose, optical sensors for sensing of glucose are a matter of highly active research. The first sensing schemes for true on-line sensing (both electrochemical and optical) have been reported several decades ago. One is based on the measurement of the quantity of oxygen consumed according to Eq. (2.46) that is catalyzed by GOx. Alternatively, the

H_2O_2 formed according to Eq. (2.46) may be determined by electrochemical or optical means. A third option consists in the determination of the quantity of protons formed (i.e. the decrease in pH) (Eq. (2.47)).

$$D - glucono - 1,5 - lactone + H_2O \rightarrow gluconate + H^+ \quad (2.46)$$

$$\beta - D - glu\cos e + O_2 \rightarrow D - glucono - 1,5 - lactone + H_2O_2 \quad (2.47)$$
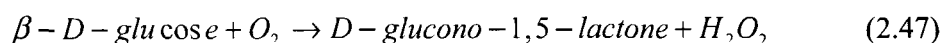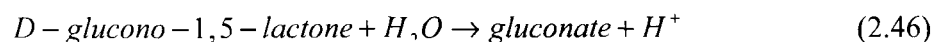
The enzyme glucose dehydrogenase also has been used to sense glucose. It catalyzes the conversion of glucose to form a gluconolactone according to Eq. (2.48):

$$\beta - D - glu\cos e + NAD^+ \rightarrow D - glucono - 1,5 - lactone + NADH \quad (2.48)$$
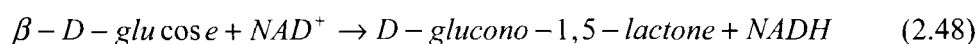
The amount of NADH formed according to Eq. (2.48) may be measured, for example, by photometry at 345 nm or via its fluorescence peaking at 455 nm, but this reaction cannot be easily reversed and comes to an end once all NAD+ is consumed. Hence, it is less suited (and less elegant) in terms of continuous sensing. The electrons transferred in Eq. (2.46) can be directly shuttled onto an electrode by so-called direct enzyme wiring (a direct electron transfer from an electrode to the reaction center, either by mediators or by incorporating nano wires directly into the enzyme) [149][150]. Sensors employing mediators are in widespread use ever since the 1990s, and sensors based on nano wires since the year 2000.

All present-day commercial optical sensors rely on the use of GOx. Respresentative (larger) manufacturers include OptiMedical Inc., Idexx Inc. Becton-Dickinson Comp. Teruma Inc.

2.6.2.3 Glucose concentration in human physiological fluids –blood

Monitoring of glucose concentrations (GC) in blood or interstitial fluid is crucial towards understanding the physiological state.

In the quest to demonstrate the benefits of glucose monitoring, several sensors have recently been developed which allow continuous glucose monitoring for several days [151]. The most advanced sensors include the Medtronic Minimed CGMS® Gold System® from Medtronic Diabetes (Northridge, CA), the STS® sensor from DexCom (San Diego, CA) and the FreeStyle Navigator® Continuous Glucose Monitor by Therasense/Abbott Diabetes Care (Alameda, CA). These commercially-available implantable sensors are based on electroenzymatic sensing platforms, which exhibit

excellent analytical performance in vitro. However, they also require a permanent connection from the implanted sensor to an instrument outside the body, providing a potential infection pathway [152], and have drawbacks of instability of the enzyme [153] electrochemical system, inaccuracy, low precision, extended warm-up period and frequent calibration requirements that make them more cumbersome for in vivo use [154]-[157]. Therefore, most diabetes patients still prefer to measure their blood glucose using a glucometer [158], which involves pain. In fact, the poor patient compliance with recommended testing regimens due to the invasive nature of "finger-pricking," has further fueled the research for noninvasive and minimally-invasive technologies.

Several embodiments of potentially-implantable probes have been demonstrated in the past, including enzymatic assays [159]-[164]. The design and implementation of enzymatic sensors for long-term in vivo application is complicated due to the consumption of glucose and oxygen, generation of potentially toxic byproducts (gluconic acid, hydrogen peroxide), enzyme degradation, and the strong dependence of the glucose response on local tissue oxygen. Therefore, an alternative mechanism based on affinity binding is being investigated by many groups [165]-[171]. The first affinity based sensor proposed for monitoring glucose levels within the interstitial fluid was reported by Schultz et al [166]. Since that pioneering effort, a number of advancements toward in vivo use have been reported, including poly (ethylene glycol) (PEG) hydrogel microspheres [172] and fuzzy microshells [171]. Follow up work has extended the optical interactions into the near infrared by labeling Con A and dextran with NIR dyes [170],[173],[174]. However, the true potential for use in vivo remains a question because of lingering concerns about Con A toxicity, aggregation and irreversible binding [175]. For this reason, alternative receptors have been studied for "smart tattoo" formats, including boronic acid derivatives [176]-[178], apo-enzymes [179]-[183] and genetically engineered glucose-binding proteins [184][185]. So, it is found that measurement of glucose concentration in human physiological fluids is of great importance. In clinical diagnosis of metabolic disorders like diabetes this is characterized by high levels of glucose in human physiological fluids.
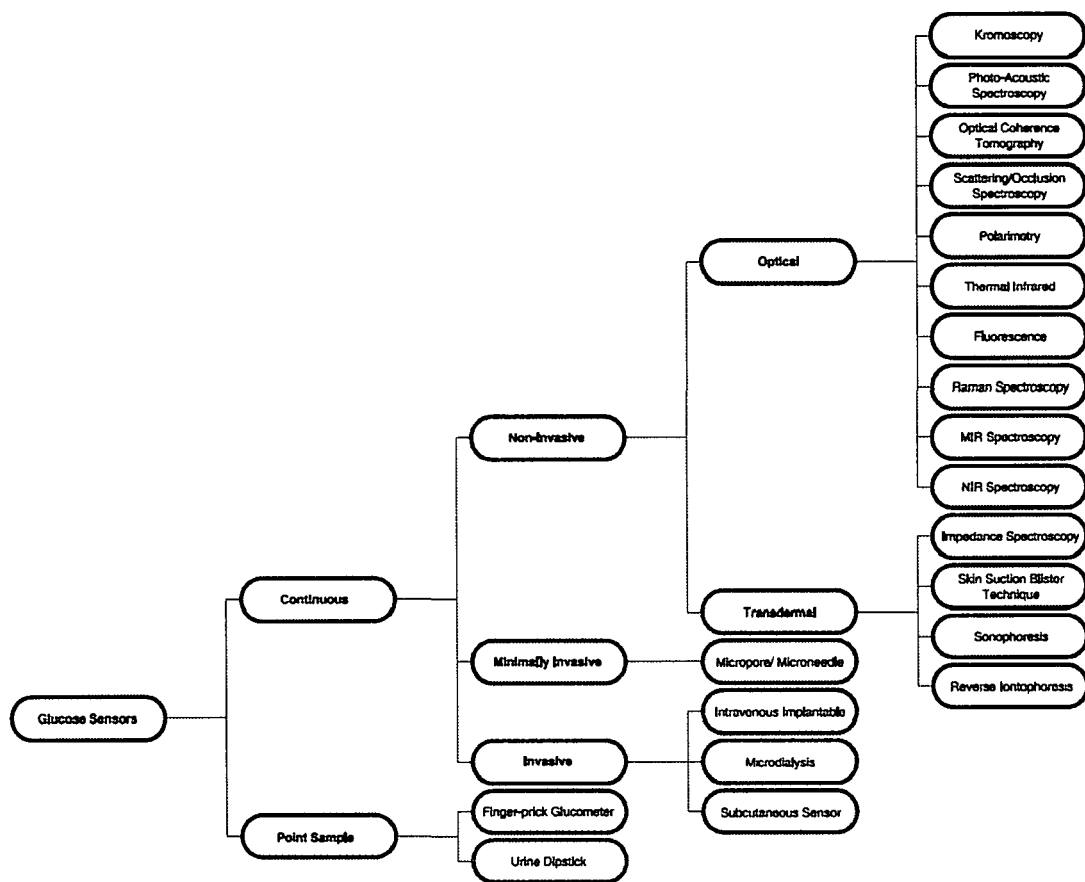
Fig-2.48: Technologies under development for glucose sensors: MIR - mid-infrared; NIR - near infrared [187].

To address these issues, we report on chapter-5 of this doctoral thesis development of a technique for rapid detection of glucose concentration in blood plasma using optical waveguide sensor and integrated with LOC. The microfluidic LOC device that we use is a commercially available microfluidic chip (*Product code: 15-1503-0168-02, microfluidic ChipShop GmbH, Stockholmer Str.20D-07747 Jena, Germany, dated: 05-03-2013*) of size 75.5mm x 25.5mm x 1.5 mm) [200]. The chip is specifically engineered and optimized for the generation of high quality plasma. It consists of chamber volume of 25 µl, a luer interface for blood loading, a support channel with a cross section of 300µm x 100µm for the transfer of the blood on top of a separation membrane. The ultimate goal of the work of this thesis is to integrate an entire optical

sensing system with LOC for separation of blood plasma from whole blood which is discussed in detail in chapter-5 of this thesis.

It is seen that many technologies are being pursued to develop novel glucose sensors (as shown in the Fig. 2.48), including non-invasive, continuous monitors etc.

2.6.2.4 Challenges of glucose sensors and motivation of planar waveguide sensor with Lab-on-chip for glucose concentration measurement

Major advances have been made to enhance functionality of measuring devices for glucose level detection. Despite the impressive advances, it is seen that there are still many challenges related to the achievement of stable and reliable glycemic monitoring. Desirable features of such a sensor system are accuracy, reliability, ultra sensitivity, fast response and of course low cost per test. Further, it is very much important that the sensor system is user-friendly and give very accurate results with high sensitivity with very minimal sample. This is one of the reasons that drive the thirst towards the development of integrated devices.

In US patent 6,497,845 [188] issued on behalf of Roche, in December of 2002, an invention is described including a storage container for holding analytical devices (an integrated device). This invention became a commercial product after a couple of years with the launch of Accu-Chek Compact Plus. This device is a blood glucose monitoring system based on reflectometric technology. The system consists of a meter and dry reagent test strips designed for capillary blood glucose testing by people with diabetes or by health care professionals. Compact Plus uses drums with 17 test strips, and the meter is automatically calibrated by inserting a new drum. An electronic check is performed automatically and a test strip is pushed forward when the meter is turned on with a button. The system requires a blood volume of 1.5 μL and provides a result within 5 seconds. The test principle of Compact Plus relies on the reaction of glucose oxidase with pyrroloquinolone quinone (PQQ). An indicator changes from yellow to blue by means of a mediator and a redox-process. The blue color is read reflectometrically. The meter has the capacity to store 300 results in memory. Accu-Chek Softclix Plus lancet pen is fastened to the Compact Plus meter. The lancet pen can be used either when fastened to the meter or it can be taken off the meter.

A method and apparatus for handling multiple sensors in a glucose monitoring instrument system is described in US patent 5,510,266 [189] issued in April of 1996, in favor of Bayer. The invention is generally related to a glucose monitoring system and, more particularly, to an improved device for handling multiple sensors that are used in analyzing blood glucose. This invention became a reality in 2003, with the launch of Ascenia Dex, which was the first blood glucose monitor to store multiple strips inside the meter. This device was very easy to use and its integration reduced incorrect results due to the human error. The integration of the test strips in the device was a major innovation, resulting in significant profit to the companies. This is one of the reasons that these patents became a subject of litigation between Roche and Bayer, since there is an apparent similarity between the drum and the disk that Accu-Chek Compact and Ascensia Dex have.

Another challenge that glucose sensors manufacturers had to face is the many manual operating steps in conventional lancet systems (lancet and lancing device), which is obviously disadvantageous to the user. In most of the systems that are available at present, the lancets for use in lancing devices are provided in a loose form and for each lancing process, the user manually removes a lancet from a pack and has to insert it into the lancet holder of the lancing device and fix it there. Numerous attempts to eliminate the above disadvantage have been described. In US patent 6,616,616 [190], issued in September 2003, Roche describes an invention concerning a lancet system comprising a plurality of essentially needle-shaped lancets, a drive unit which has a drive element in order to move the lancet from the resting position into the lancing position, a storage area to store the lancets, a withdrawal area to guide at least the tip of the lancet out of the system during the lancing process and a transport unit which can transport lancets from the storage area into the withdrawal area. The above invention became a reality in 2004, with the launch of the MultiClix. MultiClix is now one of the most popular lancing devices. It is the only one with a six-lancet drum, combining safety and convenience, since no handling of lancets is necessary. It also provides 11 penetration depth settings, letting the patient adjust the penetration according to his skin type, reducing by this way the pain by avoiding contact with deeper nerves.

Online monitoring of glucose level in diabetes management is certainly a major challenge in the field of clinical diagnostics. In this respect, researchers have demonstrated many techniques for glucose level detection. At the same time, it is seen that nowadays commercial blood glucose meters are also produced by many companies worldwide and the major players are Roche Diagnostics, LifeScan, Abbott and Bayer who mostly employ mediated amperometric biosensor technology. Other alternative include minimally invasive testing meters and continuous glucose monitoring. We see that as this field enters the area of intense research, the huge demand is creating the need for the development of new approaches with enhanced sensitivity. The trend towards the development of a sensor system with high sensitivity is expected to greatly improve the control and management of diabetes in the very near future. For accurate rapid online measurement of glucose concentration from blood plasma, it requires the followings:

- ❖ High sensitivity
- ❖ Minimal sample volume
- ❖ Accurate/online separation of blood plasma
- ❖ Low response time sensor
- ❖ Use of low cost material for fabrication of planar waveguide sensor
- ❖ Use of conventional IC process technology for fabrication in order to mass production

Keeping all these requirements in mind we have tried to use our proposed planar waveguide sensor (as mentioned in Chapter-3) for rapid measurement of glucose concentration from blood plasma (which can be transferred to waveguide sensor with capillary pressure obtained for Lab-On-Chip) and reported in Chapter-5.

2.7 Conclusion

In this chapter, a review study on optical sensors that use light to convert bio/chemical processes into a detectable signal has been done as demonstrated by different authors. We have shown how sensitivity is related to the limit of detection (LOD), which is defined as the minimum amount of concentration or mass of the biochemical substance that can be detected by the sensor over the background signal. A mathematical

description of wave propagation in planar waveguide using Maxwell's equation has been made to explain evanescent wave sensing phenomenon. For finding the propagation constant, a brief review on different numerical methods like Simple Effective Index Method (SEIM), Finite Element Method (FEM), Finite Difference Time Domain (FDTD) method and Beam Propagation Method (BPM) has also been done. Since, $SiO_2/SiON$ has been used as the waveguide material for fabricating the optical sensor, in this context a comparative study also has been done with other waveguide material such as SOI, $SiO_2/SiO_2\text{-}GeO_2$, Ti: $LiNbO_3$, GaAsInP/InP and polymeric materials. From the relevant literature survey done in this chapter, it is found that optical sensors based on planar waveguide platform offers the viable advantage of the better control of light path by the use of the optical waveguides, and a reduced size with high sensitivity compared to the conventional existing sensors. So, it is required to use optical waveguide sensors with larger sensor area and requirement of minimal sample volume and detection time. We have tried to propose and use waveguide sensors with the above characteristics for application of adulteration of petroleum products and glucose level detection in blood sample.

2.8 List of References

1. Lifante, G. *Integrated Photonics: Fundamentals*, John Wiley & Sons Ltd, England, 2003.

2. Lifante, G., et al. Planar Optical Waveguides Fabricated by Molecular Beam Epitaxy of Pd-Doped CaF2 Layers, *Applied Physics Letters* **70**, 2079–2081 1997.

3. Stoffer, R., et al. Numerical Studies of 2D Photonic Crystals: Waveguides, Coupling Between Waveguides and Filters, *Optical and Quantum Electronics* **32** (6-8), 947–961, 2000.

4. Snyder, A. W. & Love, J. D. *Optical Waveguide Theory*, Chapman & Hall, London and New York, 1983.

5. Marz, R. *Integrated Optics: Design and Modeling*, Artech House, Norwood, 1995.

6. Marcatili, E. A. J. Dielectric rectangular waveguide and directional coupler for integrated optics, *Bell Syst. Tech. J.* **48** (i7), 2071-2102, 1969.

7. Knox, R. M., & Toulios, P. P. Integrated circuits for the millimeter through optical frequency range in, *M.R.I. Symp. Submillimeter waves* (1970), Brooklyn, New York.

8. Nishihara, H., Haruna, M., & Suhara, T. *Optical Integrated Circuits*, McGraw-Hill, New York, 1989.

9. Rahman, B. A. M. & Davies, J. B. Finite element analysis of optical and microwave problems, *IEEE Trans. Microwave Theory Tech.* MTT-**32** (1), 20-28, 1983.

10. Koshiba, M., et al. Improved finite element formulation in terms of the magnetic fields vector for dielectric waveguides, *IEEE Trans. Microwave Theory Tech.* MTT-**33** (3), 227-233, 1985.

11. Lee, J. F., et al. Full wave analysis of dielectric waveguides using tangential finite elements, *IEEE Trans. Microwave Theory Tech.* MTT-**39** (8), 1262-1271, 1991.

12. Yee, K. S. Numerical solution of initial boundary value problems involving Maxwell's equations in isotropic media, *IEEE Trans. Antennas Prop.* AR-**14** (3), 302-307, 1966.

13. Taflov, A. *Computational Electrodynamics: The Finite Difference Time Domain Method*, Artech House, Norwood MA, 1995.

14. Ridder, R. M., et al. Silicon Oxynitride Planar Waveguiding Structures for Application in Optical Communication, *IEEE J. Sel Top. Quant. Elect.* **4** (6), 930-937, 1998.

15. Strang, G. On the construction and comparison of difference schemes, *SIAM J. Numerical Analysis* **5** (3), 506-517, 1968.

16. Shang, J. S. Characteristic based methods for the time-domain Maxwell equations, *IEEE Ant. Prop. Magazine*, **37** (3), 15-25, 1995.

17. Colella, P. & Woodward, P. R. The piecewise parabolic method (PPM) for gas dynamical simulations, *J. Comp. Phys.* **54** (1), 174-201, 1984.

18. Hadley, G. R. Transparent boundary condition for the beam propagation method, *J. Quantum Electron.* **28** (1), 363-370, 1992.

19. Feng, N. An Efficient Split-Step Time-Domain Beam-Propagation Method for Modeling of Optical Waveguide Devices, *Journal of Lightwave Tech.* **23** (6), 2186-2191, 2005.

20. Manoharan, K. *Design and analysis of high-Q, amorphous micro ring resonator sensor for gaseous and biological species detection*, M.S. Thesis, University of Ohio at Athens, USA, 2009.

21. Fossum, E. R. CMOS Image Sensors:Electronic Camera-On-A-Chip, *IEEE trans on Electron. Devices* **44** (10), 1689-1698, 1997.

22. Passaro, V.M.N., et al. Review Electromagnetic field photonic sensors; *Progress in Quantum Electronics* **30** (2-3), 45-47, 2006.

23. Krioukov, E., et al. Integrated optical microcavities for enhanced evanescent-wave spectroscopy, *Opt. Lett.* **27** (17), 1504-1506, 2002.

24. Campopiano, S., et al. Microfluidic sensor based on integrated optical hollow waveguides, *Opt. Lett.* **29** (16), 1894-1896, 2004.

25. Zhang, A. P. Advances in optical fiber Bragg grating sensor technologies, *Photonic Sensors* **2** (1), 1-13, 2012.

26. Passaro, V.M.N., & Dell''olio, F. Guided-wave optical biosensors, *Sensors* **7** (4), 508-536, 2007.

27. Yu, F. T. S., & Shizhuo, Y. *Fiber Optic Sensors*, Marcel Decker, Inc., New York, 2002.

28. Inaudi, D., & Glisic B. Overview of Fibre Optic Sensing Applications to Structural Health Monitoring in, *Symposium on Deformation Measurement and Analysis* (2008), Lisbon, Portugal.

29. Fidanboylu, K., & Efendioglu, H. S. Fiber Optic Sensors and Their Applications, *Proceedings of 5th International Advanced Technologies Symposium (IATS'09)*, Karabuk, Turkey, 13–15.

30. Yin, S.Z., Ruffin, P.B. & Yu, F.T.S. *Fiber Optic Sensors*, 2nd ed., CRC Press, Taylor & Francis Group: Boca Raton, FL, USA, 2008.

31. Xiangyang, L., et al. Fiber-Optical Sensors: Basics and Applications in Multiphase Reactors, *Sensors* **12**(9), 12519–12544, 2012.

32. Méndez, A. Overview of fiber optic sensors for NDT applications in Nondestructive Testing of Materials and Structures, Springer, Atlanta, GA, USA, 2013.

33. Jenny, R. Fundemantals of Fiber Optics: An Introduction for Beginners, Volpi Manufacturing USA Co., New York, 2000.

34. Casas J. R., & Paulo, J. S. Fiber Optic Sensors for Bridge Monitoring, *Journal of Bridge Engineering* **8** (6), 362-373, 2003.

35. Berthold, J. W. Historical Review of Microbend Fiber Optic Sensors, *Journal of Lightwave Technology* **13** (7), 1193-1199, 1995.

36. Udd, E., et al. Fiber Optic Sensors for Infrastructure Applications, http://ntl.bts.gov/lib/10000/10600/10640/fibop.pdf, 1998.

37. Krohn, D. A. *Fiber Optic Sensors: Fundamental and Applications*, Instrument Society of America, Research Triangle Park, North Carolina, 1988.

38. Johnson, L. M., et al. Integrated optical temperature sensor, *Appl. Phys. Lett.* **41** (2), 134-136, 1982.

39. Izutsu, M., et al. Optical-Waveguide micro-displacement Sensor, *Electron. Lett.* **18** (20), 867-868, 1982.

40. Kersten, R. Th. Integrated optics for sensors, *Optical Fiber Sensors,* Vol. 1, Artech House, Norwood, MA, 1988.

41. Parriaux, O. Integrated optics sensors, *Advances in Integrated Optics*, Springer, Plenum Press, New York, 1994.

42. Luff, B. J., et al. Integrated optical Mach-Zehnder biosensor, *J. Light. Technol.* **16** (4), 583-592, 1998.

43. Jimenez, D., et al. An integrated silicon ARROW Mach-Zehnder interferometer for sensing applications, *Opt. Commun.* **132** (5-6), 437-441, 1996.

44. Righini, G. C., Tajani, A. & Cutolo, A. *An Introduction to Optoelectro Sensors*, World Scientific Publishing, Singapore, 2009.

45. Hunsperger, R. G. *Integrated optics: theory and technology,* Springer Verlag, Berlin, 1982.

46. Lukosz, W., et al. Input and output grating couplers as integrated optical biosensors, *Sensors & Actuators A* **25** (1-3), 181-184, 1991.

47. Grattan, K. T. V. & Meggitt, B. T. *Optical Fiber Sensor Technology*, Vol.4, Kluwer academic publishers, Netherlands, 1999.

48. Baldini, F., et al. *Optical Chemical Sensors*, Springer, Netherlands, 2006.

49. Sanchis, P., et al. Design of Silicon-Based Slot Waveguide Configurations for Optimum Nonlinear Performance, *J. Lightwave Technol.* **25** (5), 1298-1305, 2007.

50. Pandraud, G., et al. Evanescent wave sensing: new features for detection I small volumes, *Sensors and Actuators A: Phys.* **85** (1-3), 158-162, 2000.

51. Kumar, P. S., et al. A fibre optic evanescent wave sensor used for the detection of trace nitrites in water, *Journal of Optics A: Pure and Applied Opt.* **4** (3), 247-250, 2002.

52. Helmers, H., et al. Performance of a compact, hybrid optical evanescent-wave sensor for chemical and biological applications, *Applied Optics* **35** (4), 676–680, 1996.

53. Kasap, S.O. *Optoelectronics and Photonics*, Prentice Hall, 2001.

54. Lukosz, W. Integrated optical chemical and direct biochemical sensors, *Sensors and Actuators B* **29** (1-3), 37-50, 1995.

55. Lambeck, P.V., et al. Three novel integrated optical sensing structures for the chemical domain, *Sensors & Actuators B* **113** (2), 718-729, 2006.

56. Homola, J., et al. Surface plasmon resonance sensors: review, *Sensors & Actuators B* **54** (1-2), 3-15, 1999.

57. Kretschmann, E. Die Bestimmung optischer Konstanten von Metallen durch Anregung von Oberflächenplasmaschwingungen, *Physik* **241** (4), 313-324, 1971.

58. Nylander, C., et al. Gas detection by means of surface plasmon resonance, B. Liedberg, T. Lind, *Sensors & Actuators* **3**, 79-88, 1982-1983.

59. Liedberg, B., et al. Surface plasmon resonance for gas detection and biosensing, *Sensors & Actuators* **4**, 299-304, 1983.

60. Sheridan, A.K., et al. Phase interrogation of an integrated optical SPR sensor, *Sensors & Actuators* **B 97** (1), 114-121, 2004.

61. Homola, J. *Surface Plasmon Resonance Based Sensors*, Springer, 2006.

62. Lukosz, W., & Tiefenthaler, K. Sensitivity of integrated optical grating and prism couplers as (bio)-chemical sensors, *Sensors and Actuators* **15** (3), 273-284, 1988.

63. Lukosz, W., & Tiefenthaler, K. Sensitivity of grating couplers as integrated optical chemical sensors, *J. Opt. Soc. Am. B* **6** (2), 209-220, 1989.

64. Lukosz, W. Principles and sensitivities of integrated optical and surface plasmon sensors for direct affinity- and immunosensing, *Biosensors Bioelectron.* **6** (3), 215-225, 1991.

65. Lukosz, W., & Tiefenthaler, K. Embossing technique for fabricating integrated optical components in hard inorganic wave guiding materials, *Optics Lett.* **8** (10), 537-539, 1983.

66. Heuberger, K., & Lukosz, W. Embossing technique for fabricating surface relief gratings on hard oxide waveguides, *Appl. Opt.* **25** (9) (1986) 1499 1504.

67. Lukosz, W., & Tiefenthaler, K. Directional switching in planar waveguides effected by adsorption desorption processes in, *2nd Eur. Conf. Integrated Optics* (1983), Florence, 152-155.

68. Tiefenthaler, K., & Lukosz, W. Integrated optical humidity and gas sensors in, *Intl Conf on Optical Fiber Sensors* (OFS'84), Stuttgart, Germany.

69. Tiefenthaler, K., & Lukosz, W. Grating couplers as integrated optical humidity and gas sensors, *Thin Solid Films* **126** (3-4), 205-211, 1985.

70. Tiet'enthaler, K., Embossed surface-relief gratings on planar waveguides as integrated optical switches and gas sensors, Ph.D. Thesis, University of ETH Zurich at Zurich, 1985.

71. Burke, C. S., et al. Development of an optical sensor probe for the detection of dissolved carbon dioxide, *Sensors and Actuators B: Chemical* **119**(1), 288-294, 2006.

72. Burke, C. S., et al. Planar Optical Sensors and Evanescent Wave Effects, *Optical Chemical Sensors*, Springer, Netherlands, 2006, 193-215.

73. Brandenburg A., et al. Ammonia Detection via Integrated Optical Evanescent Wave Sensors, *Mikrochim. Acta.* **121**, 95-105, 1995.

74. Pandraud G., et al. Evanescent wave sensing: new features for detection in small volumes, *Sensors and Actuators* **85** (1-3), 158-162, 2000.

75. Cunningham, B.T. Label-free optical biosensors: An Introduction in *Label-Free Biosensors: Techniques and Applications*, Cambridge University Press, 2007, 1-28.

76. D'Amico, A., & Natale, C. D. A Contribution on Some Definitions of Sensors Properties, *IEEE Sens. Jour.* 1 (3), 183-190, 2001.

77. Deka, B. *Design and Development of Compact Two Mode Interference and Multimode Interference Couplers for Photonic Integrated Devices*, Ph. D. Thesis Tezpur University, Napaam, Tezpur, 2013.

78. Wörhoff, K., et al. Silicon oxynitride-A versatile material for integrated optics applications, *Journal of the Electrochemical Society* 149 (8), F85-F91, 2002.

79. Offrein, B. J., et. al. Wavelength tunable optical Add after drop filter with flat pass band for WDM networks, *IEEE Photonics Tech. Lett.* 11 (2), 239-241, 1999.

80. Janz, F., et al. Bent waveguide couplers for Demultiplexing of arbitrary broadly separated wavelengths using two mode interference, *IEEE Photonics Tech. Lett.* 7 (9), 1037-1039, 1995.

81. Zappe, H. P., & Neyer, A. Integrated optical multichannel wavelength multiplexer for monomode system, *IEEE Electron. Lett.* 20, 744-746. 1984.

82. Papuchon, M., et al. Electrically active optical bifurcation: BOA, *Applied Physics Letter* 31 (4), 266-267, 1977.

83. Zappe, H. P. *Introduction to Semiconductor Integrated Optics*, Artech House, Boston, 1995.

84. Kashahara, R., et al. New structures of silica-based planar light wave circuits for low power thermo optic switch and its application to 8x8 optical matrix switch, *J. Light wave Tech.* 20 (6), 993-1000, 2002.

85. Takato, N., et al. Silica based Integrated Optic Mach Zehnder Multi/Demultiplexer family with channel spacing of 0.01-250 nm, *IEEE Selected Areas in Comm.* 8 (6), 1120-1127, 1990.

86. Yagi, M., et.al. Versatile multimodes interference photonic switches with partial index modulation regions, *IEEE Electron. Lett.* 36 (6), 533-534, 2000.

87. Darmawan, S., et al. A Rigorous Comparative Analysis of Directional Couplers and Multimode Interferometers Based on Ridge Waveguides, *IEEE J. of Sel. Topics of Quant. Electron.* **11** (2), 466-475, 2005.

88. Ma, Y., et al. Ultracompact Multimode Interference 3-dB Coupler with Strong Lateral Confinement by Deep Dry Etching, *IEEE Photonics Lett.* **12** (5), 492-494, 2000.

89. Leuthold, J., & Joyner, C. H. Multimode Interference couplers with tunable power splitting ratios, *IEEE J. of Lightwave Tech.* **19** (5), 700-707, 2001.

90. Offrein, B. J., et al. Adaptive gain equalizer in high index contrast SiON technology, *IEEE Photonics Technology Lett.* **12** (5), 504-506, 2000.

91. Kumar, D., & Singh, V. Theoretical modeling of a nonlinear asymmetric metal-clad planar waveguide based sensors, *Optik* **122** (20), 1872-1875, 2011.

92. Parriaux, O., & Dierauer, P. Normalized expressions for the optical sensitivity of evanescent wave sensors: erratum, *Optics Lett.* **19** (20), 1665-1665, 1994.

93. Taya, S.A., et al. Enhancement of sensitivity in optical waveguide sensors using left-handed materials, *Optik* **120** (10), 504-508, 2009.

94. Carlos, A. B., et al. Label-free optical biosensing with slot-waveguides, *Optics Lett.* **33** (7), 708-710, 2008.

95. Karasinski, P. Planar Optical Waveguide Sensor Structures with Grating Couplers, *Acta Physica Polonica A* **116**, 30-32, 2009.

96. Carlos, A.B. Optical Slot-Waveguide Based Biochemical Sensors, *Sensors* **9** (6), 4751-4765, 2009.

97. Densmore, A., et al. A Silicon-on-Insulator Photonic Wire Based Evanescent Field Sensor, *IEEE Photonic Tech. Lett.* **18** (23), 2520-2522, 2006.

98. Karasinski, P. Optical uniform/gradient waveguide sensor structure characterization, *Opto-Electronics Review* **19** (1), 01-09, 2011.

99. Sofyan, A.T., & Taher, M.E. A reverse symmetry optical waveguide sensor using a plasma substrate, *J. Opt.* **13**, 1-6, 2011.

100. Renling, Z., et al. The Sensing Structure Optimization of Planer Optical Waveguide with Fermi Refractive Index, *J. of Lightwave Tech.* **28** (23), 3439-3443, 2010.

101. Yimit, A., et al. Thin film composite optical waveguides for sensor applications: a review, *Talanta* **65** (25), 1102-1109, 2005.

102. Airoudj, A., et al. Design and Sensing Properties of an Integrated Optical Gas Sensor Based on a Multilayer Structure, *J. Anal. Chem.* **80** (23), 9188-9194, 2008.

103. Veldhuis, G.J., et al. Sensitivity Enhancement in Evanescent Optical Waveguide Sensors, *J. of Lightwave Tech.* **18** (5), 677-682, 2000.

104. Gupta, A. K., & Sharma, R. K. A New Method for Estimation of Automobile Fuel Adulteration, in *Air Pollution*, *Sciyo*, Rijeka, Croatia, 2010, 357-370.

105. Bhatnagar, V.P., An ultrasonic method to find liquid fuel adulteration, *Journal of Acoust. Soc. India* **9**, 19-23, 1981.

106. Bahari, M. S., et al. Determination of the adulteration of petrol with kerosene using rapid phase titration procedure, *Analyst* **115**, 417-419, 1990.

107. Bahari, M. S., et al., Spectrophotometric end-point phase-titration determination of the adulteration of petrol with kerosene, *Analaytical Proceeding* **28**, 14-16, 1991.

108. Srivastava, A., et al., Optical sensor for determining adulteration in petrol by kerosene, in International Conference On Fiber Optics and Photonics (1997), New Delhi, 989-991.

109. Sharma, R. K., & Gupta, A. K. Detection/ Estimation of Adulteration in Gasoline and Diesel using Ultrasonics, *International Conference on Industrial and Information Systems* (ICIIS' 2007), Penadeniya, 509-11.

110. Yadav, S. R., et al. Estimation of petrol and diesel adulteration with kerosene and assessment of usefulness of selected automobile fuel quality test parameters, *International Journal of Environmental Science & Technology* **1** (4), 253-255, 2005.

111. Roy, S. Fiber optic sensor for determining adulteration of petrol and diesel by kerosene, *Sensors & Actuators B* **55** (2-3), 212, 1999.

112. Biswas, D. Consequences of fuel adulteration.
http://cpcbenvis.nic.in/newsletter/fueladultration/ch60703.htm

113. Aziz al, R. A. *Identification of Automobile Petrol Adulteration By Using Optical Methods*, Ph. D. Thesis, College of Science, King Saud University, Riyadh, Kingdom of Saudi Arabia, 2008.

114. Gawande, A. P., & Kaware, J. P. Fuel Adulteration Consequences in India: A Review, *Sci. Revs. Chem. Commun.* **3** (3), 161-171, 2013.

115. Paulo, J. M., et al. A study of adulteration in gasoline samples using flame emission spectroscopy and chemometrics tools, *Analyst.* **137**, 5919-5924, 2012.

116. Tsubochi, M., et al. Determination of anionic surfactants by two-phase titration with tetrabromophenolphthalein ethyl ester as indicator, *Journal of the American Oil Chemists' Society* **56** (11), 921-923, 1979.

117. Suri, S. K. Analysis by phase-titration of three-component systems containing two mutually immiscible or partially miscible components, *Talanta* **19** (6), 804-7, 1972.

118. Chandy, R. P., et al. An optical fiber sensor for biofilm measurement using intensity modulation and image, *IEEE Journal of Selected Topics in Quantum Electronics,* **6** (5), 764-772, 2000.

119. Laguesse, M. An optical fibre refractometer for liquids using two measurement channels to reject optical attenuation, *J. Phys. E: Sci. Instrum* **21** (1), 64-67, 1988.

120. Wiedemann, L.S.M., et al. Adulteration detection of Brazilian gasoline samples by statistical analysis, *Fuel* **84** (4), 467-473, 2005.

121. Bali, L. M., et al. Optical sensor for determining adulteration in a liquid sample, *Opt. Eng.* **38** (10), 1715-1721, 1999.

122. Kishor, K., et al., Optical sensor for the determination of adulteration in petrol: design and development, in Novel Optical Systems Design and Optimization XIV (2011), San Diego, California, USA.

123. Bahari, M. S., et al. Spectrophotometric End-Point for the Phase-titration Determination of the Adulteration of Petrol with Kerosene, *Analytical Proceedings,* **28**, 14-16, 1991.

124. Mishra, V., et al. Fuel adulteration detection using long period fiber grating sensor technology, *Indian Journal of Pure & Applied Physics,* **46** (02), 106-110, 2008.

125. Patil, S. S. Refractometric Fiber Optic Adulteration Level Detector for Diesel, *International Journal of Advances in Engineering & Technology*, **1** (4), 195-203, 2011.

126. Lenshof A., et al. Acoustic Whole Blood Plasmapheresis Chip for Prostate Specific Antigen Microarray Diagnostics, *Anal. Chem.* **81** (15), 6030-6037, 2009.

127. Tachi T., et al. Simultaneous separation, metering, and dilution of plasma from human whole blood in a microfluidic system, *Anal. Chem.* **81** (8), 3194-8, 2009.

128. Haeberle S., et al. Centrifugal extraction of plasma from whole blood on a rotating disk, *Lab Chip* **6**, 776-781, 2006.

129. Dimov I. K., et al. Stand-alone self-powered integrated microfluidic blood analysis system (SIMBAS), *Lab Chip* **11**, 845-850, 2011.

130. Whitesides, G. M. The origins and the future of microfluidics, *Nature* **442**, 368-373, 2006.

131. Kuswandi, B., et al. Optical sensing systems for microfluidic devices: A review, *Anal. Chim. Acta* **601** (2), 141-155, 2007.

132. Mark, D., et al. Microfluidic lab-on-a-chip platforms: requirements, characteristics and application, *Chem. Soc. Rev.* **39** (3), 1153-1182, 2010.

133. Chou, C., et al. Noninvasive glucose monitoring in vivo with an optical heterodyne polarimeter, *Appl. Opt.* **37** (16), 3553-3557, 1998.

134. Malik, B. H. Real-time, closed-loop dual-wavelength optical polarimetry for glucose monitoring, *J. Biomed. Opt.* **15** (1), 017002, 2010.

135. Enejder, A. M., et al. Raman spectroscopy for noninvasive glucose measurements, *J. Biomed. Opt.* **10** (3), 031114, 2005.

136. Lambert, J. L., et al. Glucose determination in human aqueous humor with Raman spectroscopy, *J. Biomed. Opt.* **10** (3), 031110, 2005.

137. Marbach, R., et al. Noninvasive blood glucose assay by near-infrared diffuse reflectance spectroscopy of the human inner lip, *Appl. Spectrosc.* **47** (7), 875-881, 1993.

138. Maruo, K., et al. In vivo noninvasive measurement of blood glucose by nearinfrared diffuse-reflectance spectroscopy, *Appl. Spectrosc.* **57** (10), 1236-1244, 2003.

139. Vrancic, C., et al. Continuous glucose monitoring by means of mid-infrared transmission laser spectroscopy in vitro, *Analyst* **136** (6), 1192–1198, 2011.

140. Gabriely, I., et al. Transcutaneous glucose measurement using near-infrared spectroscopy during hypoglycemia, *Diabetes Care* **22** (12), 2026–2032, 1999.

141. Spanner, G., & Niessner, R. New concept for the non-invasive determination of physiological glucose concentrations using modulated laser diodes, *Fresenius J. Anal. Chem.* **354** (3), 306-310, 1996.

142. Malchoff, C. D., et al. A novel noninvasive blood glucose monitor, *Diabetes Care* **25**, 2268–2275, 2002.

143. Guo, X., et al. Wavelength-modulated differential laser photothermal radiometry for blood glucose measurements, *J. Phys. Conf. Ser.* **214** (1), 012025, 2010.

144. Ballerstadt, R., et al. In vivo performance evaluation of a transdermal near-infrared fluorescence resonance energy transfer affinity sensor for continuous glucose monitoring, *Diabetes Technol. Ther.* **8** (3), 296–311 (2006).

145. March, W., et al. Fluorescent measurement in the non-invasice contact lens glucose sensor, *Diabetes Technol. Ther.* **8** (3), 312–317 (2006).

146. Kottmann, J., et al. New photoacoustic cell design for studying aqueous solutions and gels, *Rev. Sci. Instrum.* **82**, 084903 (2011).

147. Spanner, G., & Niessner, R. Noninvasive determination of blood constituents using an array of modulated laser diodes and a photoacoustic sensor head, *Fresenius J. Anal. Chem.* **355** (3-4), 306–310 (1996).

148. Zhao, Z. *Pulsed photoacoustic techniques and glucose determination in human blood and tissue*, Ph.D. thesis, University of Oulu, 2002.

149. Heller, A., & Feldman, B. Electrochemical Glucose Sensors and Their Applications in Diabetes Management, *Chem. Rev.*, **108**, 2482–2505, 2008.

150. Tuchin, V. M, Commercial biosensors for diabetes, in *Handbook of Optical Sensing of Glucose in Biological Fluids and Tissues*, Fragkou, V., & Turner, A. P. F. ed. CRC Press, Boca Raton, Fla, 2009, pp. 41–64.

151. Klonoff, D. C., Continuous glucose monitoring: roadmap for 21st century diabetes therapy, *Diabetes Care* **28** (5), 1231–9, 2005.

152. Skyler, J. S. Continuous glucose monitoring: an overview of its development, *Diabetes Technol Ther*, **11** (Suppl. 1), S5–10, 2009.

153. Valdes, T. I., & Moussy, F. In vitro and in vivo degradation of glucose oxidase enzyme used for an implantable glucose biosensor, *Diabetes Technol. Ther.* **2** (3), 367–76, 2000.

154. Pickup, J. In vivo glucose sensing for diabetes management: progress towards non-invasive monitoring, *BMJ.* **319** (7220), 1289, 1999.

155. Pickup, J. C., et al. In vivo glucose monitoring: the clinical reality and the promise, *Biosens. Bioelectron.*, **20** (10), 1897–902, 2005.

156. Gerritsen, M., et al. Performance of subcutaneously implanted glucose sensors for continuous monitoring, *Neth J. Med.* **54** (4), 167–79, 1999.

157. Wickramasinghe, Y., et al. Current problems and potential techniques in in vivo glucose monitoring, *J. Fluoresc.* **14** (5), 513–20, 2004.

158. Newman, J. D., & Turner, A. P. Home blood glucose biosensors: a commercial perspective, *Biosens. Bioelectron.* **20** (12), 2435–53, 2005.

159. Brown, J. Q., et al. Encapsulation of glucose oxidase and an oxygen-quenched fluorophore in polyelectrolyte-coated calcium alginate microspheres as optical glucose sensor systems, *Biosens. Bioelectron.* **21** (1), 212–6, 2005.

160. Brown, J. Q., et al. Enzymatic fluorescent microsphere glucose sensors:evaluation of response under dynamic conditions, *Diabetes Technol. Ther.* **8** (3), 288–95, 2006.

161. Zhu, H., et al. Combined Physical and Chemical Immobilization of Glucose Oxidase in Alginate Microspheres Improves Stability of Encapsulation and Activity, *Bioconjugate Chem.* **16** (6), 1451–1458, 2005.

162. Zhu, H., & McShane, M. J. Macromolecule encapsulation in diazoresin-based hollow polyelectrolyte microcapsules, *Langmuir* **21** (1), 424–30, 2005.

163. Zhu, H., et al. Spontaneous Loading of Positively Charged Macromolecules into Alginate-Templated Polyelectrolyte Multilayer Microcapsules, *Biomacromolecules* **6** (4), 2221–8, 2005,

164. Stein, E. W., et al. Microscale Enzymatic Optical Biosensors Using Mass Transport Limiting Nanofilms. 1. Fabrication and Characterization Using Glucose as a Model Analyte, *Anal. Chem* **79** (4), 1339–48, 2007.

165. Schultz, J. S., & Sims, G. Affinity sensors for individual metabolites, *Biotechnol. Bioeng. Symp.* **9**, 65–71, 1979.

166. Schultz, J. S., et al. Affinity Sensor: A New Technique for Developing Implantable Sensors for Glucose and Other Metabolites, *Diabetes Care* **5**, 245–53, 1982.

167. Meadows, D. L., & Schultz, J. S. Design, manufacture and characterization of an optical fiber glucose affinity sensor based on an homogeneous fluorescence energy transfer assay system, *Anal. Chim. Acta* **280**, 21–30, 1993.

168. Mansouri, S., & Schultz, J. S. A Miniature Optical Glucose Sensor Based on Affinity Binding, *Nat. Biotechnol.* **2**, 885–90, 1984.

169. Ballerstadt, R., & Schultz, J. S. A Fluorescence Affinity Hollow Fiber Sensor for Continuous Transdermal Glucose Monitoring, *Anal. Chem.* **72** (17), 4185–92, 2000.

170. Ballerstadt, R., et al. In vitro long-term performance study of a near-infrared fluorescence affinity sensor for glucose monitoring, *Biosens. Bioelectron.* **19** (8), 905–14, 2004.

171. Chinnayelka, S., & McShane, M. J. Glucose-sensitive nanoassemblies comprising affinity-binding complexes trapped in fuzzy microshells, *J. Fluoresc.* **14** (5), 585-95, 2004.

172. Russell, R. J., et al. A Fluorescence-Based Glucose Biosensor Using Concanavalin A and Dextran Encapsulated in a Poly (ethylene glycol) Hydrogel, *Anal. Chem.* **71** (15), 3126–32, 1999.

173. Ballerstadt, R., et al. Fluorescence Resonance Energy Transfer-Based Near-Infrared Fluorescence Sensor for Glucose Monitoring, *Diabetes Technol. Ther.* **6** (2), 191–200, 2004.

174. Ballerstadt, R., et al. In Vivo Performance Evaluation of a Transdermal Near-Infrared Fluorescence Resonance Energy Transfer Affinity Sensor for Continuous Glucose Monitoring, *Diabetes Technol. Ther.* **8** (3), 296–311, 2006,
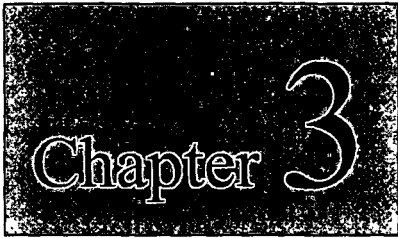
175. Ballerstadt, R., et al. Concanavalin A for in vivo glucose sensing: A biotoxicity review, *Biosens. Bioelectron.* **22** (2), 275–84, 2006.

176. Fang, H., et al. Progress in Boronic Acid-Based Fluorescent Glucose Sensors, *J. Fluoresc.* **14** (5), 481–9, 2004.

177. Kawanishi, T., et al. A Study of Boronic Acid Based Fluorescent Glucose Sensors *J. Fluoresc.* **14** (5), 499–512, 2004.

178. Phillips, M. D., & James, T. D. Boronic Acid Based Modular Fluorescent Sensors for Glucose, *J. Fluoresc.* **14**(5), 549–559, 2004.

179. Chaudhary, A., et al. Evaluation of glucose sensitive affinity binding assay entrapped in fluorescent dissolved-core alginate microspheres, *Biotechnol. Bioeng.* **104** (6), 1075–85, 2009.

180. Chaudhary, A., & Srivastava, R. Glucose Sensing Using Competitive Binding Assay Co-Encapsulated in Uniform Sized Alginate Microspheres, *Sens. Lett.* **6** (2), 253–60, 2008.

181. Chinnayelka, S., & McShane, M. J. Resonance Energy Transfer Nanobiosensors Based on Affinity Binding between Apo-Enzyme and Its Substrate, *Biomacromolecules* **5** (5), 1657–61, 2004.

182. Chinnayelka, S., & McShane, M. J. Microcapsule Biosensors Using Competitive Binding Resonance Energy Transfer Assays Based on Apoenzymes, *Anal. Chem.* **77** (17), 5501–11, 2005,

183. Chinnayelka, S., et al. Near-Infrared Resonance Energy Transfer Glucose Biosensors in Hybrid Microcapsule Carriers, *Journal of Sensors* 1–10, 2008.

184. D'Auria, S., et al. A Thermophilic Apoglucose Dehydrogenase as Nonconsuming Glucose Sensor, *Biochem. Biophys. Res. Commun.* **274** (3), 727-731, 2000.

185. Tolosa, L., et al. Glucose sensor for low-cost lifetime-based sensing using a genetically engineered protein, *Anal. Biochem.* **267** (1), 114–20, 1999.

186. Gärtner, C. microfluidic ChipShop. http://www.microfluidic-chipshop.eu/Download/Lab-on-a-Chip%20Catalogue_032014.pdf

187. Oliver, N. S., et al. Glucose sensors: a review of current and emerging technology, *Diabet. Med.* **26**(3), 197-210, 2009.

188. Sacherer, *Storage container for analytical devices*, **US Patent No. 6,497,845**, December 24, 2002

189. Bonner et al. *Method and apparatus of handling multiple sensors in a glucose monitoring instrument system*, **US Patent No. 5,510,266**, Apr. 23, 1996.

190. Fritz, et al. *Lancet system*, **US Patent No. 6,616,616**, September 9, 2003.

✳ ✳ ✳ ✳ ✳

It doesn't matter how beautiful your theory is, it doesn't matter how smart you are. If it doesn't agree with experiment, it's wrong.

- Richard P. Feynman

Theoretical Modeling, Design and Development of Integrated Planar Waveguide Optical Sensor

Outline of the Chapter:

3.1   Introduction
3.2   Proposed waveguide structure for sensor
      3.2.1   Solution of the wave equation for planar waveguide sensor
      3.2.2   Waveguide Sensitivity
      3.2.3   Power propagation in the structure
3.3   Design of the proposed sensor structure
      3.3.1   Estimation of sample volume
3.4   Fabrication of the designed sensor
      3.4.1   Fabrication processes
            3.4.1.1   Preparation of Wafer for Fabrication
            3.4.1.2   Deposition of Silica (SiO_2) Layer as Lower Cladding
            3.4.1.3   Deposition of Silicon Oxynitride (SiON) as Guiding Layer
            3.4.1.4   Preparation of Mask
            3.4.1.5   Annealing
            3.4.1.6   Transfer of Pattern on Guiding Layer
            3.4.1.7   Spin Coating of Photoresist
            3.4.1.8   Photolithography
            3.4.1.9   Mask cleaning
            3.4.1.10   Alignment and Exposure
            3.4.1.11   Development and Post Baking
            3.4.1.12   Metallization
            3.4.1.13   Lift-off Technique
            3.4.1.14   Reactive Ion Etching
            3.4.1.15   Wet Etching/RIE of Metallization (Cr) layer
3.5   Experimental set up for sensing application
      3.5.1   Measurements
      3.5.2   Results and Characterization
3.6   Conclusion
3.7   List of References

3.1 Introduction

As discussed in chapter-2, for enhancement of sensitivity and reduction of fabrication cost we need to propose a new planar waveguide sensor structure consisting of less number of layers and requiring minimal sample volume for sensing application and with high sensitivity. In this direction, although many researchers have reported a large number of waveguide sensors [1]-[4], it is seen that no waveguide sensor structure provides all these characteristics as stated in chapter-2.

Herein, this chapter we have tried to propose a new planar waveguide structure with theoretical modeling. Using its analytical model, we have tried to design the sensor structure and derive the analytical formula for waveguide sensitivity. After designing of the same, the proposed structure is fabricated with combination of Photolithography, Reactive Ion Etching (RIE) and Plasma Enhanced Chemical Vapour Deposition (PECVD) processes. We have made experimental setup for the planar waveguide sensor and then detect glucose concentration in saline water for experimental validation of sensor.

3.2 Proposed waveguide structure for sensor

In this section, we focus on the design of an optical waveguide sensor structure. The proposed waveguide sensor structure is relatively simple, in comparison with that of other integrated optical sensors. We introduce the rectangular coordinate system to have refractive index variation in the x-direction and the wave to be propagated in the z-direction. The medium is infinite in the y-direction (no refractive index variation). The refractive index profile is given by:

$$n(x) = \begin{cases} n_c & ; \quad 0 \le x \le x_1 \\ n_s & ; \quad x_1 < x \le x_2 \\ n_a & ; \quad x > x_2 \end{cases} \tag{3.1}$$

where x_1=half width of the core and x_2-x_1=sensing region width [as shown in Fig. 3.1 (b)]. Based on this phenomenon, starting from the wave equation that satisfies a TE mode propagating in a planar waveguide, as seen in Eq. (3.2), characterized by its propagation constant β, we consider an optical waveguide structure which consists of a guiding layer of Silicon Oxynitride (SiON) [core refractive index (R.I), n_c=1.46] deposited on silica-on-silicon substrate, sensing region of refractive index, n_s as a cladding and an outside medium (air) with refractive index n_a, lower than R.I of the core. Since the sensitivity of TE mode in planar waveguide sensor is more than that of TM mode, we consider the transverse electric (TE) modes, i.e. only the y-component of the electric field vector is nonzero. So the wave equation is obtained as:

$$\frac{d^2 E_y}{dx^2} + \left[k_0^2 n^2(x) - \beta^2\right] E_y(x) = 0 \tag{3.2}$$

This differential equation is the wave equation that satisfies the electric field amplitude $E_y(x)$ for TE propagation in planar structures, where $k_0=2\pi/\lambda_0$ and λ_0 is the wavelength of the light in free space, related to the angular frequency by $\omega=2\pi c/\lambda_0$. Since the wave Eq. (3.2) is a second-order differential equation, in order to resolve it for a planar waveguide structure, it is necessary to impose additional conditions. For three regions (region-I, II and III), the wave equations are written as

$$\frac{d^2 E_y(x)}{dx^2} + \alpha_1^2 E_y(x) = 0 \qquad ; 0 < x < x_1 \tag{3.3}$$

$$\frac{d^2 E_y(x)}{dx^2} - \gamma^2 E_y(x) = 0 \qquad ; x_1 < x < x_2 \tag{3.4}$$

$$\frac{d^2 E_y(x)}{dx^2} - \alpha_2^2 E_y(x) = 0 \qquad ; x > x_2 \tag{3.5}$$

Fig. 3.1(a) shows the three dimensional (3D) schematic view of planar waveguide sensor structure housed in a Plastic Cylindrical Enclosure (PCE). The xz plane view of waveguide based sensor is shown in Fig. 3.1(b), in which region-I represent the core region whereas region-II and region-III represents the sensing region (SR) and the outer surrounding medium of SR respectively. Although the fabricated waveguide is placed inside a PCE, the effect of surrounding region is very less as sensitivity through leaky quasi-modes depends mainly upon the refractive index of core and sensing region.
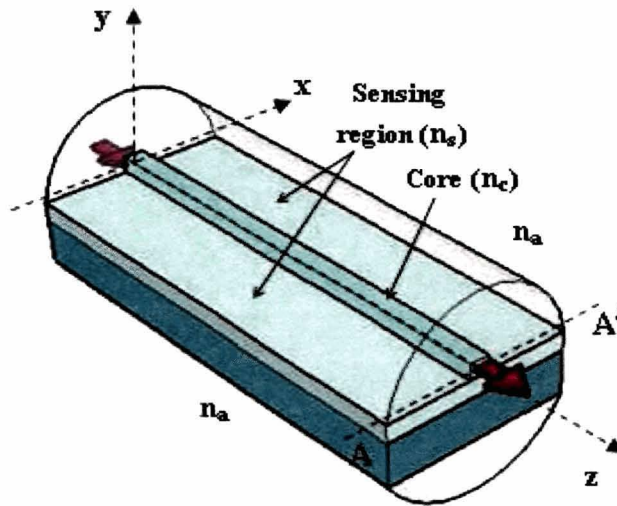
(a)
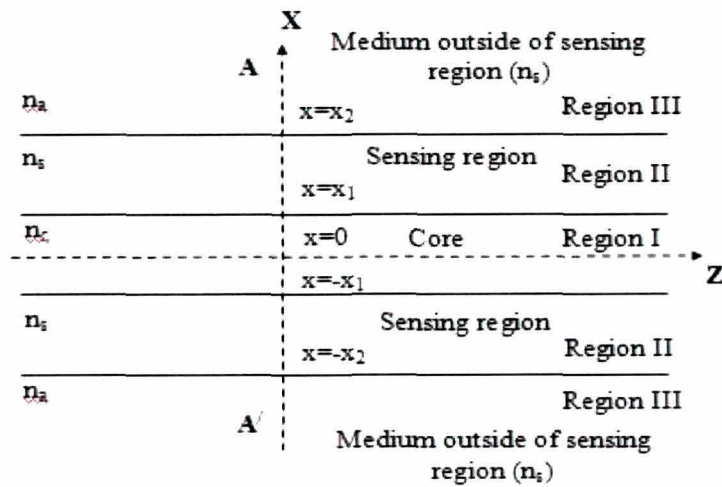
(b)

Fig- 3.1(a): Three-dimensional schematic view of planar optical waveguide sensor with sensing region (SR) placed on the top of silica on silicon substrate and **(b)** Cross sectional view of waveguide core along xz-plane AA'.

Fig. 3.2 shows the refractive index profile for the planar leaky optical waveguide structure,

$$n(x) = \begin{cases} n_c & ; \quad 0 < x < x_1 \\ n_s & ; \quad x_1 < x < x_2 \\ n_{air} & ; \quad x > x_2 \end{cases}$$
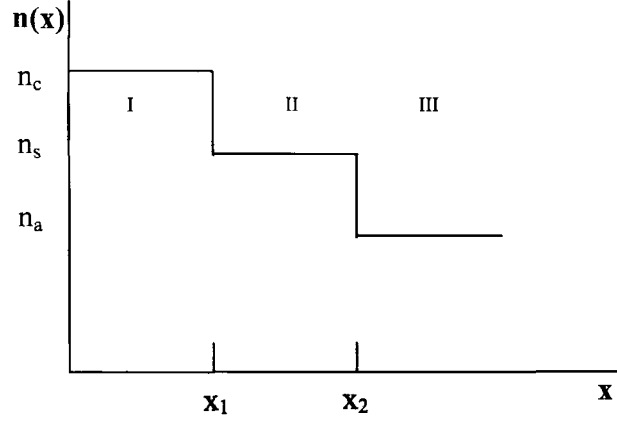

Fig- 3.2: Refractive index profile for the leaky structure.

3.2.1 Solution of the wave equation for planar waveguide sensor

We postulate solutions for the $E_y(x)$ component for the regions I, II and III in the form as:

$$\psi_I(x) = A_+ \sin\alpha_1 x \qquad ; (0 < x \leq x_1) \tag{3.6}$$

$$\psi_{II(x)} = B_+ e^{\gamma(x-x_1)} + B_- e^{-\gamma(x-x_1)} \quad ; (x_1 < x \leq x_2) \tag{3.7}$$

$$\psi_{III}(x) = C_- e^{-\alpha_2(x-x_2)} \qquad ; (x > x_2) \tag{3.8}$$

It is proved that expressions (3.6), (3.7) and (3.8) satisfy the wave equation (3.2) providing that the parameter α_1, α_2 and γ is given by:

$$\alpha_1 = \sqrt{k_0^2 n_c^2 - \beta^2}, \quad \gamma = \sqrt{\beta^2 - k_0^2 n_s^2}, \quad \alpha_2 = \sqrt{\beta^2 - k_0^2 n_a^2}$$

where β is the propagation constant. The solutions are in the form of oscillatory functions, while the behavior of the fields in the cover region is in the form of exponential decay. This situation corresponds to substrate radiation modes, where the light is not confined to the film region, but spreads out to the substrate. The electric fields in the cover are indeed evanescent waves, a particular case where the directions of

propagation and attenuation are perpendicular whose penetration is determined by γ. A dimensional parameter, called effective refractive index N, has been introduced which is directly related to the propagation constant β of the mode through the formula:

$$\beta \equiv k_0 N \tag{3.9}$$

Following this definition, the effective refractive index N represents the refractive index experienced by the mode propagating along the z-axis. Using the boundary conditions for TE modes and considering the continuity of tangential components of the fields and their first derivative at the interface of core-sensing region ($x=x_1$), outer medium of the sensing region ($x=x_2$), we obtain

$$B_+ = \frac{1}{2} A_+ \left[\sin \alpha_1 x_1 + \frac{\alpha_1}{\gamma} \cos \alpha_1 x_1 \right] \tag{3.10}$$

$$B_- = \frac{1}{2} A_+ \left[\sin \alpha_1 x_1 - \frac{\alpha_1}{\gamma} \cos \alpha_1 x_1 \right] \tag{3.11}$$

$$C_- = \frac{1}{2} B_+ (1 + \frac{\gamma}{\alpha_2}) e^{\gamma(x_2-x)_1} + \frac{1}{2} B_- (1 - \frac{\gamma}{\alpha_2}) e^{-\gamma(x_2-x)_1} \tag{3.12}$$

On solving the Eqs. (3.10)-(3.12), the following dispersion equation corresponding to the guided TE modes of the waveguide structure (as shown in Fig. 3.1) is obtained [5],

$$\alpha_1 x_1 = m\pi + Cot^{-1} \left(\frac{\cosh \gamma x_2 + \left(\frac{\gamma}{\alpha_2} \right) \sinh \gamma x_2}{\alpha_1 \left(\frac{1}{\gamma} - \frac{1}{\alpha_2} \right) \sinh \gamma x_2} \right) \tag{3.13}$$

Where, m =0, 1, 2....represent mode number. For the TM modes analysis is similar to the preceding of TE modes. Since H_y and E_z are continuous at the interfaces, however a square of the index ratio is additionally included in the eigen value equation:

$$\alpha_1 x_1 = m\pi + Cot^{-1} \left(\frac{n_c^2}{n_s^2} \frac{\cosh \gamma x_2 + \left(\frac{\gamma}{\alpha_2} \right) \sinh \gamma x_2}{\alpha_1 \left(\frac{1}{\gamma} - \frac{1}{\alpha_2} \right) \sinh \gamma x_2} \right) \tag{3.14}$$

A set of parameters, called normalized parameters have been introduced. This is defined as:

Normalised mode index, $V = k_0 T \sqrt{n_c^2 - n_s^2}$ (3.15)

Normalised mode index, $b_I = \dfrac{\left(N^2 - n_s^2\right)}{\left(n_c^2 - n_s^2\right)}$ (3.16)

Asymmetry measure, $a_E = \dfrac{\left(n_s^2 - n_c^2\right)}{\left(n_f^2 - n_s^2\right)}$ (3.17)

In terms of these normalised parameters, the transcendental relation as shown in Eq. (3.13) as function of the propagation constant β, is obtained as:

$$V \sqrt{1 - b_I} = (m + 1)\pi - \tan^{-1} \sqrt{\frac{1 - b_I}{b_I}} - \tan^{-1} \sqrt{\frac{1 - b_I}{b_I + a_E}} \qquad (3.18)$$

Normalized frequency V and the normalized guided index, b_I is defined as:

$$V = k_0 W \sqrt{N_1^2 - n_s^2} \qquad (3.19)$$

Also, $V \sqrt{1 - b_I} = (m + 1)\pi - 2\tan^{-1}\left(\dfrac{1 - b_I}{b_I}\right)$ (3.20)

Or, $V = \dfrac{(m + 1)\pi}{\sqrt{1 - b_I}} - \dfrac{2}{\sqrt{1 - b_{II}}} \tan^{-1}\left(\dfrac{1 - b_I}{b_I}\right)$ (3.21)

where $b_I = \dfrac{N^2 - n_s^2}{N_1^2 - n_s^2}$ (3.22)

and $N = \sqrt{b_I N_1^2 - n_s^2 (b_I - 1)}$ (3.23)

It is possible that a given structure has no solution for the transcendental Eq. (3.13), and in this case (for a particular working wavelength) the waveguide cannot support any guided mode.

Corresponding to different regions of the structure, the fields corresponding to the discrete guided mode can be written as [6],

$$\psi_g(x) = \begin{cases} A_g \sin\alpha_g x & ; \quad 0 < x \le x_1 \\ A_g \sin\alpha_g x_1 \, e^{-\gamma_g(x - x_1)} & ; \quad x_1 < x \le x_2 \\ A_g \sin\alpha_g x_1 e^{-\gamma_g(x - x_2)} & ; \quad x > x_2 \end{cases} \qquad (3.24)$$

where α_g is evaluated by determining the propagation constant of the discrete guided mode with Eq. (3.13) and the subscript 'g' refers to the quasi-guided modes.

Using the normalization condition, $\int_0^\infty |\psi_g(x)|^2\, dx = 1$, we normalize the guided

mode given by Eq. (3.24), such that,

$$\int_0^{x_1} |\psi_g(x)|^2\, dx + \int_{x_1}^{x_2} |\psi_g(x)|^2\, dx + \int_{x_2}^\infty |\psi_g(x)|^2\, dx = 1$$

$$\Rightarrow |A_g|^2 \int_0^{x_1} |\sin\alpha_g x|^2\, dx + \int_{x_1}^{x_2} |\sin\alpha_g x_1 e^{\gamma_g(x-x_1)}|^2\, dx + \int_{x_2}^\infty |\sin\alpha_g x_1 e^{\gamma_g(x-x_2)}|^2\, dx = 1$$

$$\Rightarrow |A_g|^2 [I_1 + I_2 + I_3] = 1 \tag{3.25}$$

On solving Eq. (3.25) for I_1, I_2 and I_3, we obtain

$$I_1 = \int_0^{x_1} |\sin\alpha_g x|^2\, dx = \frac{1}{2}\left[x_1 - \left.\frac{|\sin 2\alpha_g x|}{2\alpha_g}\right|_0^{x_1} \right] = \frac{1}{2}\left[x_1 - \frac{\sin 2\alpha_g x_1}{2\alpha_g} \right] \tag{3.26}$$

$$I_2 = \int_{x_1}^{x_2} |\sin\alpha_g x_1 e^{\gamma_g(x-x_1)}|^2\, dx$$

$$= \sin^2\alpha_g x_1 e^{-2\gamma_g x_1} \int_{x_1}^{x_2} \left[e^{2\gamma_g x} \right] dx = \sin^2\alpha_g x_1 \frac{e^{-2\gamma_g x_1}}{2\gamma_g}\left[e^{2\gamma_g x_2} - e^{-2\gamma_g x_1} \right]$$

$$= \frac{1}{2\gamma_g}\sin^2\alpha_g x_1 \left[e^{2\gamma_g(x_2-x_1)} - 1 \right] \tag{3.27}$$

$$I_3 = \int_{x_2}^\infty |\sin\alpha_g x_1 e^{\gamma_g(x-x_2)}|^2\, dx$$

$$= \sin^2\alpha_g x_1 e^{2\gamma_g x_2} \int_{x_2}^\infty e^{-2\gamma_g x}\, dx = \sin^2\alpha_g x_1 e^{2\gamma_g x_2}\left[\frac{e^{-2\gamma_g x}}{-2\gamma_g} \right]_{x_2}^\infty$$

$$= \frac{1}{2\gamma_g}\sin^2\alpha_g x_1 (1 - 2\gamma_g x_2) \tag{3.28}$$

Therefore, $|A_g|^2 [I_1 + I_2 + I_3] = 1$ becomes

$$|A_g|^2 \frac{1}{2}\left[x_1 - \frac{\sin 2\alpha_g x_1}{2\alpha_g} \right] + \frac{1}{2\gamma_g}\sin^2 \alpha_g x_1 \left[e^{2\gamma_g(x_2-x_1)} - 1 \right] + \frac{1}{2\gamma_g}\sin^2 \alpha_g x_1 \left(1 - 2\gamma_g x_2\right) = 1$$

$$\Rightarrow |A_g|^2 \begin{bmatrix} \frac{1}{2}x_1 - \frac{1}{4\alpha_g}\sin 2\alpha_g x_1 - \frac{1}{2\gamma_g}\sin^2 \alpha_g x_1 + \frac{1}{2\gamma_g}\sin^2 \alpha_g x_1 + \frac{1}{2\gamma_g}e^{2\gamma_g(x_2-x_1)}\sin^2 \alpha_g x_1 - \\ \frac{1}{2\gamma_g}\sin^2 \alpha_g x_1 e^{2\gamma_g x_2} + \frac{1}{2\gamma_g}\sin^2 \alpha_g x_1 e^{-2\gamma_g x_2} \end{bmatrix} = 1$$

$$\Rightarrow |A_g|^2 \left[\frac{1}{2}x_1 - \frac{1}{4\alpha_g}\sin 2\alpha_g x_1 + \frac{e^{-2\gamma_g x_1}}{2\gamma_g}\sin^2 \alpha_g x_1 \right] = 1$$

$$\Rightarrow \frac{|A_g|^2}{2}\left[x_1 - \frac{1}{2\alpha_g}\sin 2\alpha_g x_1 + \frac{e^{-2\gamma_g x_1}}{2\gamma_g}\sin^2 \alpha_g x_1 \right] = 1$$

$$\Rightarrow \frac{|A_g|^2}{2\alpha_g \gamma_g}\left[2\alpha_g \gamma_g x_1 - \gamma_g \sin 2\alpha_g x_1 + 2\alpha_g e^{-2\gamma_g x_1}\sin^2 \alpha_g x_1 \right] = 2$$

$$\Rightarrow |A_g|^2 = \left(\frac{4\alpha_g \gamma_g}{2\alpha_g \gamma_g x_1 - \gamma_g \sin\left(2\alpha_g x_1\right) + 2\alpha_g \sin^2 \alpha_g x_1 e^{2\gamma_g(x_2-x_1)}} \right)$$

$$\text{Or, } A_g = \left(\frac{4\alpha_g \gamma_g}{2\alpha_g \gamma_g x_1 - \gamma_g \sin\left(2\alpha_g x_1\right) + 2\alpha_g \sin^2 \alpha_g x_1 e^{2\gamma_g(x_2-x_1)}} \right)^{1/2} \qquad (3.29)$$

These are obviously the radiation modes of the waveguide that satisfies the orthonormality condition, $\int_0^\infty \psi_{\beta'}^*(x)\psi_\beta(x)dx = 0 \quad ; \quad (\beta \neq \beta')$

At z=0, the propagation of the beam has a field very close to Ψ_g which would excite the radiation modes of the structure [shown in Fig-3.1(a)], and the field was defined as,

$$\psi(x,z) = \int \psi_\beta(x)\varphi(\beta)\exp(i\beta z)d\beta \qquad (3.30)$$

We have considered only those values of β that are near to β_g, thus for region I and region II we get,

$$\psi_\beta(x) \approx \left(\frac{A_+}{A_g} \right)\psi_g(x) \qquad (3.31)$$

In order to evaluate A$_+$, we express it in terms of C$_-$. Hence, on substituting the value of B$_+$ and B$_-$ from Eq. (3.10) and Eq. (3.11) in Eq. (3.12) for C$_-$, we obtain:

$$C_- = \frac{1}{2} A_+ \left[\sin \alpha_g x_1 \left\{ \left(1 + \frac{\gamma_g}{\alpha_{2g}} \right) e^{\gamma_g (x_2 - x_1)} + \left(1 - \frac{\gamma_g}{\alpha_{2g}} \right) e^{-\gamma_g (x_2 - x_1)} \right\} \right] +$$

$$\frac{1}{2} A_+ \left[\left(\frac{\alpha_g}{\gamma} \right) \cos \alpha_g x_1 \left\{ \left(1 + \frac{\gamma_g}{\alpha_{2g}} \right) e^{\gamma_g (x_2 - x_1)} - \left(1 - \frac{\gamma_g}{\alpha_{2g}} \right) e^{-\gamma_g (x_2 - x_1)} \right\} \right]$$

(3.32)

For obtaining C$_-$, use has been made of the relations,

$$\left. \begin{array}{l} \sin \alpha_g x_1 = \dfrac{\alpha_g}{\delta} \\[2mm] \cos \alpha_1 x_1 = \dfrac{-\gamma_g}{\delta} \\[2mm] \delta^2 = \alpha_1^2 + \gamma_2^2 = k_0^2 \left(n_c^2 - n_s^2 \right) \end{array} \right\}$$

(3.33)

On substituting Eq. (3.33) in Eq. (3.32), C$_-$ is obtained as:

$$C_- = \frac{1}{4} |A_+| \frac{\delta \beta_g}{\gamma_g^2 \alpha_g} \left(1 + \gamma_g x_1 \right) \left| 1 + \frac{\gamma_g}{\alpha_{2g}} \right| e^{\gamma_g (x_2 - x_1)} \left(\beta - \beta_g \right) +$$

$$\frac{1}{4} |A_+| \frac{\delta \beta_g}{\gamma_g^2 \alpha_g} \left(1 + \gamma_g x_1 \right) \left| 1 - \frac{\gamma_g}{\alpha_{2g}} \right| e^{-\gamma_g (x_2 - x_1)} \left(\beta - \beta_g \right)$$

$$C_- \approx \frac{1}{4} |A_+| \frac{\delta \beta_g}{\gamma_g^2 \alpha_g^2} \left(1 + \gamma_g x_1 \right) e^{\gamma_g (x_2 - x_1)} \left[\left(\beta - \beta_g \right)^2 + \Gamma^2 \right]^{1/2}$$

(3.34)

For $\alpha_2 = \alpha_2'$, the integral for orthonormalization of radiation modes is considered as:

$$\int_0^\infty \psi_{\alpha_2'}^* (x) \, \psi_{\alpha_2} (x) dx = \int_0^{x_2} \psi_{\alpha_2'}^* (x) \, \psi_{\alpha_2} (x) dx + \int_{x_2}^\infty \psi_{\alpha_2'}^* (x) \, \psi_{\alpha_2} (x) dx$$

Now, $I = \displaystyle\int_0^\infty C_-^2 e^{-\left(\alpha_2 + \alpha_2' \right) \xi d\xi}$, where $\xi = x - x_2$

Using the condition, $C_- = C_-^*$, we obtain $\qquad C_- = \left(\dfrac{1}{2\alpha_{2g}} \right)^{1/2}$

(3.35)

From Eq. (3.34) and Eq. (3.35), taking the modulus and equating the R.H.S, we obtain,

$$\frac{1}{4}|A_+|\frac{\delta\beta_g}{\gamma_g^2\alpha_g^2}\left(1+\gamma_g x_1\right)e^{\gamma_g(x_2-x_1)}\left[(\beta-\beta_g)^2+\Gamma^2\right]^{1/2} = \left(\frac{1}{2\alpha_{2g}}\right)^{1/2}$$

$$A_+ = \frac{4\alpha_g^2\gamma_g^2 e^{-\gamma_g(x_2-x_1)}}{\beta_g\delta^2\sqrt{2\alpha_{2g}}\left(1+\gamma_g x_1\right)\left[(\beta-\beta_g)^2+\Gamma^2\right]} \qquad (3.36)$$

$$\text{where} \quad \Gamma = \frac{4\alpha_g^4\gamma_g^4 e^{-2\gamma_g(x_2-x_1)}}{\beta_g^2\delta^4\alpha_{2g}\left(1+\gamma_g x_1\right)}$$

Now, in region III ($x>x_2$), as Ψ_g has a negligible value, the contribution from region III to the integral in Eq. (3.30) is very less. So Eq. (3.30) can be expressed as,

$$\varphi_\beta = \left(\frac{A_+}{A_g}\right)\int_0^\alpha|\psi_g(x)|^2\,dx = \frac{A_+}{A_g} \qquad (3.37)$$

$$\text{where} \quad |A_+| = \frac{4\alpha_g^2\gamma_g^2 e^{-\gamma_g(x_2-x_1)}}{\beta_g\delta^2\sqrt{2\alpha_{2g}}\left(1+\gamma_g x_1\right)\left[(\beta-\beta_g)^2+\Gamma^2\right]^{1/2}} \qquad (3.38)$$

3.2.2 Waveguide Sensitivity

From the dispersion relation given by Eq. (3.13), the waveguide sensitivity S_w (i.e. the rate of change of effective refractive index N with respect to refractive index n_s of the sensing medium) is obtained as,

$$S_w = \frac{\delta\left(\beta/k_0\right)}{\delta n_s} \qquad (3.39)$$

where, β/k_0=effective refractive index and n_s is the sensing region refractive index.
The dispersion relation as obtained in Eq. (3.13) is:

$$Cot(\alpha_1 x_1 - m\pi) = \left(\frac{\cosh\gamma x_2 + \left(\frac{\gamma}{\alpha_2}\right)\sinh\gamma x_2}{\alpha_1\left(\frac{1}{\gamma}-\frac{1}{\alpha_2}\right)\sinh\gamma x_2}\right) \qquad (3.40)$$

where $\alpha_1 = \sqrt{k_0^2 n_c^2 - \beta^2}$; $\gamma = \sqrt{\beta^2 - k_0^2 n_s^2}$; $\alpha_2 = \sqrt{\beta^2 - k_0^2 n_a^2}$

Now, to find S_w, Eq. (3.40) is differentiated, such that

$$\frac{\partial}{\partial n_s} Cot(\alpha_1 x_1 - m\pi) = \frac{\partial}{\partial n_s}\left[\frac{\left(\cosh \not x_2 + \left(\frac{\gamma}{\alpha_2}\right)\sinh \not x_2 \right)}{\alpha_1\left(\frac{1}{\gamma} - \frac{1}{\alpha_2}\right)\sinh \not x_2} \right]$$ (3.41)

$$\Rightarrow -Cosec^2(\alpha_1 x_1 - m\pi)\frac{\partial}{\partial n_s}(\alpha_1 x_1 - m\pi)$$

$$= \left[\frac{\left(\sinh \not x_2 + \frac{\gamma}{\alpha_2}\cosh \not x_2\right)\frac{\partial}{\partial n_s} \not x_2 \alpha_1 \left(\frac{1}{\gamma} - \frac{1}{\alpha_2}\right)\sinh \not x_2 - \left(\cosh \not x_2 + \frac{\gamma}{\alpha_2}\sinh \not x_2\right)}{\alpha_1^2 \left(\frac{1}{\gamma} - \frac{1}{\alpha_2}\right)^2 \sin^2 h(\not x_2)} \frac{\partial}{\partial n_s}\left[\alpha_1\left(\frac{1}{\gamma} - \frac{1}{\alpha_2}\right)\sin^2 h \not x_2\right] \right]$$ (3.42)

For convenience, we denote the terms in Eq. (3.42) by:

$$\left(\sinh \not x_2 + \frac{\gamma}{\alpha_2}\cosh \not x_2\right) = A_2$$ (3.43)

$$\alpha_1\left(\frac{1}{\gamma} - \frac{1}{\alpha_2}\right)\sinh \not x_2 = A_3$$ (3.44)

$$\left(\cosh \not x_2 + \frac{\gamma}{\alpha_2}\sinh \not x_2\right) = A_4$$ (3.45)

$$\frac{\partial}{\partial n_s}\left[\alpha_1\left(\frac{1}{\gamma} - \frac{1}{\alpha_2}\right)\sin^2 h \not x_2\right] = A$$ (3.46)

$$\alpha_1^2\left(\frac{1}{\gamma} - \frac{1}{\alpha_2}\right)^2 \sin^2 h(\not x_2) = A_5$$ (3.47)

Let the L.H.S term,

$$-Co\sec^2(\alpha_1 x_1 - m\pi)\frac{\partial}{\partial n_s}(\alpha_1 x_1 - m\pi) = B$$ (3.48)

On solving Eq. (3.46) for A, we find

$$\Rightarrow \frac{\partial}{\partial n_s}\left[\alpha_1\left(\frac{1}{\gamma}-\frac{1}{\alpha_2}\right)\sin^2 h\gamma x_2\right]=\frac{k_0^2}{2\sqrt{k_0^2 n_c^2-\beta^2}}\left[-2\frac{\beta}{k_0}\frac{\partial}{\partial n_s}\left(\beta/k_0\right)\right]\left(\frac{1}{\gamma}-\frac{1}{\alpha_2}\right)\sinh \gamma x_2$$

$$-\frac{\alpha_1 k_0^2}{\beta^2-k_0^2 n_s^2}\left(2\frac{\beta}{k_0}\frac{\partial}{\partial n_s}\beta/k_0-2n_s\right)\sinh \gamma x_2 +\alpha_1\left(\frac{1}{\gamma}-\frac{1}{\alpha_2}\right)\cosh \gamma x_2$$

$$\left[\frac{k_0^2\left(2\frac{\beta}{k_0}\frac{\partial(\beta/k_0)-2n_s}{\partial n_s}\right)x_2}{2\sqrt{\beta^2-k_0^2 n_s^2}}+\gamma\frac{\partial}{\partial n_s}x_2\right]$$

$$\Rightarrow \frac{\partial}{\partial n_s}\left[\alpha_1\left(\frac{1}{\gamma}-\frac{1}{\alpha_2}\right)\sin^2 h\gamma x_2\right]=\frac{k_0^2}{2\sqrt{k_0^2 n_c^2-\beta^2}}\left[-2\frac{\beta}{k_0}\frac{\partial}{\partial n_s}\left(\beta/k_0\right)\right]\left(\frac{1}{\gamma}-\frac{1}{\alpha_2}\right)\sinh \gamma x_2$$

$$-\frac{\alpha_1 k_0^2}{\beta^2-k_0^2 n_s^2}\left(2\frac{\beta}{k_0}\frac{\partial}{\partial n_s}\beta/k_0-2n_s\right)\sinh \gamma x_2 +\alpha_1\left(\frac{1}{\gamma}-\frac{1}{\alpha_2}\right)\cosh \gamma x_2$$

$$\left[\frac{k_0^2\left(2\frac{\beta}{k_0}\frac{\partial(\beta/k_0)-2n_s}{\partial n_s}\right)x_2}{2\sqrt{\beta^2-k_0^2 n_s^2}}+\gamma\frac{\partial}{\partial n_s}x_2\right]$$

$$=\frac{\partial}{\partial n_s}\left(\beta/k_0\right)\left[\begin{array}{l}-\frac{k_0^2}{\alpha_1}\frac{\beta}{k_0}\left(\frac{1}{\gamma}-\frac{1}{\alpha_2}\right)\sinh \gamma x_2-\frac{\alpha_1 k_0^2}{\gamma^2}2\frac{\beta}{k_0}\sinh \gamma x_2 + \\ \alpha_1\left(\frac{1}{\gamma}-\frac{1}{\alpha_2}\right)\cosh \gamma x_2\frac{k_0^2 2\beta/k_0}{2\gamma}\end{array}\right]$$

$$+\left[\frac{2n_s\alpha_1 k_0^2}{\gamma^2}\sinh \gamma x_2-\frac{n_s\alpha_1\left(\frac{1}{\gamma}-\frac{1}{\alpha_2}\right)x_2\cosh \gamma x_2}{\gamma}+\gamma\frac{\partial x_2}{\partial n_s}\right]$$

(3.49)

In Eq. (3.49), let $\alpha_1\left(\frac{1}{\gamma}-\frac{1}{\alpha_2}\right)=A_7$.

Now, $\dfrac{\partial(\gamma x_2)}{\partial n_s}=\dfrac{k_0^2\left[2\beta/k_0\cdot\dfrac{\partial}{\partial n_s}\left(\beta/k_0\right)-2n_s\right]}{2\gamma}+\gamma\dfrac{\partial x_2}{\partial n_s}$

Since, $\beta^2 - k_0^2 n_s^2 = \gamma^2$, in the above equation we substitute for $\gamma = \sqrt{\beta^2 - k_0^2 n_s^2}$.

Next, we solve the L.H.S term.

$$-Co\sec^2(\alpha_1 x_1 - m\pi)\frac{\partial}{\partial n_s}(\alpha_1 x_1 - m\pi) =$$

$$-Co\sec^2(\alpha_1 x_1 - m\pi)\left[\left\{\frac{k_0^2\left(-2\beta/k_0\frac{\partial}{\partial n_s}(\beta/k_0)\right)}{2\alpha_1}\right\}x_1 + \alpha_1\frac{\partial x_1}{\partial n_s}\right] \qquad (3.50)$$

$$= \frac{x_1 k_0^2}{\alpha_1}Co\sec^2(\alpha_1 x_1 - m\pi)\frac{\beta}{k_0}\frac{\partial}{\partial n_s}\left(\frac{\beta}{k_0}\right) - \alpha_1\frac{\partial x_1}{\partial n_s}Co\sec^2(\alpha_1 x_1 - m\pi)$$

In Eq. (3.50), let $\alpha_1\frac{\partial x_1}{\partial n_s}Co\sec^2(\alpha_1 x_1 - m\pi) = A_1$

On substituting A_1 in Eq. (3.50), we get

$$-Co\sec^2(\alpha_1 x_1 - m\pi)\frac{\partial}{\partial n_s}(\alpha_1 x_1 - m\pi) = \frac{x_1 k_0^2}{\alpha_1}Co\sec^2(\alpha_1 x_1 - m\pi)\frac{\beta}{k_0}\frac{\partial}{\partial n_s}\left(\frac{\beta}{k_0}\right) - A_1$$

Now, putting all these substitutions in Eq. (3.49), we obtain:

$$\frac{x_1 k_0^2}{\alpha_1}Co\sec^2(\alpha_1 x_1 - m\pi)\frac{\beta}{k_0}\frac{\partial}{\partial n_s}\left(\frac{\beta}{k_0}\right) - A_1 = \frac{A_2\left[k_0^2\left\{2\frac{\beta}{k_0}\frac{\partial}{\partial n_s}\left(\frac{\beta}{k_0}\right) - 2n_s\right\}A_3 - A_4 A\right]}{A_5}$$

$$\Rightarrow \frac{\partial}{\partial n_s}\left(\frac{\beta}{k_0}\right)\left[\frac{x_1 k_0^2}{\alpha_1}Co\sec^2(\alpha_1 x_1 - m\pi)\frac{\beta}{k_0} - \frac{A_2}{A_5}k_0^2\frac{2\beta}{2k_0}\right] = A_1 - \frac{2n_s A_2 k_0^2}{A_5} + \gamma\frac{\partial x_2}{\partial n_s}\frac{A_3}{A_5} - A_4 A$$

$$\Rightarrow \frac{\partial}{\partial n_s}\left(\frac{\beta}{k_0}\right)\left[\begin{array}{l}\dfrac{x_1 k_0^2}{\alpha_1}Co\sec^2(\alpha_1 x_1 - m\pi)\dfrac{\beta}{k_0} - \dfrac{A_2}{A_5}\beta k_0 \\ + A_4\left\{\begin{array}{l}-\dfrac{k_0^2}{\alpha_1}\dfrac{\beta}{k_0}\left(\dfrac{1}{\gamma} - \dfrac{1}{\alpha_2}\right)\sinh \gamma x_2 \\ -\dfrac{\alpha_1 k_0^2}{\gamma^2}\dfrac{2\beta}{k_0}\sinh \gamma x_2 + \alpha_1\left(\dfrac{1}{\gamma} - \dfrac{1}{\alpha_2}\right)\cosh \gamma x_2\dfrac{k_0^2\dfrac{2\beta}{k_0}}{2\gamma}\end{array}\right\}\end{array}\right]$$

$$= A_1 - \frac{2n_s A_2 k_0^2}{A_5} + \gamma\frac{\partial x_2}{\partial n_s}\frac{A_3}{A_5} - A_4 A_6$$

Hence, $\dfrac{\partial}{\partial n_s}(\beta / k_0) = \dfrac{A_1 - 2n_s A_2 k_0^2 + \gamma \dfrac{\partial x_2}{\partial n_s} \dfrac{A_3}{A_5} - A_4 A_6}{\dfrac{x_1 k_0^2}{\alpha_1} Co\sec^2(\alpha_1 x_1 - m\pi) \dfrac{\beta}{k_0} - \dfrac{A_2}{A_5} \beta k_0}$ (3.51)

$$- A_4 \left\{ \dfrac{k_0^2}{\alpha_1^2} \dfrac{\beta}{k_0} \alpha_1 \left(\dfrac{1}{\gamma} - \dfrac{1}{\alpha_2} \right) \sinh \gamma x_2 - \dfrac{\alpha_1 k_0^2}{\gamma} \dfrac{2\beta}{k_0} \sinh \gamma x_2 \right\} +$$

$$\alpha_1 \left(\dfrac{1}{\gamma} - \dfrac{1}{\alpha_2} \right) \cosh \gamma x_2 \dfrac{k_0^2 2 \dfrac{\beta}{k_0}}{2\gamma}$$

$$= \dfrac{A_1 A_5 - 2n_s A_2 A_5 k_0^2 + \gamma A_3 \dfrac{\partial x_2}{\partial n_s} - A_4 A_5 A_6}{\left[\begin{array}{l} \dfrac{x_1 k_0 A_5}{\alpha_1^2} Co\sec^2(\alpha_1 x_1 - m\pi)\beta \alpha_1 - A_2 \beta k_0 - A_4 A_5 \left\{ \dfrac{k_0 \beta}{\alpha_1^2} A_7 \sinh \gamma x_2 - \dfrac{2\beta \alpha_1 k_0}{\gamma} \sinh \gamma x_2 \right\} + \\ A_7 \cosh \gamma x_2 \dfrac{k_0 \beta}{\gamma} \end{array} \right]}$$ (3.52)

On substituting, $\dfrac{k_0 \beta}{\alpha_1^2} = A_8$ in Eq. (3.52), the expression reduces to,

$$\dfrac{\partial}{\partial n_s}(\beta / k_0) = \dfrac{A_1 A_5 - 2n_s A_2 A_5 k_0^2 + \gamma A_3 \dfrac{\partial x_2}{\partial n_s} - A_4 A_5 A_6}{\alpha_1 x_1 A_8 A_5 \beta Co\sec^2(\alpha_1 x_1 - m\pi) - \beta k_0 A_2}$$ (3.53)

$$- A_4 A_5 \left\{ A_8 A_7 \sinh \gamma x_2 - \dfrac{k_0 \alpha_1}{\gamma} 2\beta \sinh \gamma x_2 \right\} + A_7 \cosh \gamma x_2 \dfrac{k_0 \beta}{\gamma}$$

In the above relation, we find that $\dfrac{\partial x_2}{\partial n_s} = 0$ and also $\dfrac{\partial x_1}{\partial n_s} = 0$, hence

$A_1 = 0$; $A_5 \rightarrow A_1$; $A_8 \rightarrow A_4$; $A_4 \rightarrow A_1$

On substituting, $A_4 A_5 \left\{ A_8 A_7 \sinh \gamma x_2 - \dfrac{k_0 \alpha_1}{\gamma} 2\beta \sinh \gamma x_2 \right\} + A_7 \cosh \gamma x_2 \dfrac{k_0 \beta}{\gamma} = Q$, the

expression for waveguide sensitivity in Eq (3.53) is obtained as:

$$S_w = \dfrac{\delta\left(\dfrac{\beta}{k_0}\right)}{\delta n_s} = \dfrac{-2n_s A_2 A_5 k_0^2 + A_1 A_5 A_6}{\alpha_1 x_1 A_4 A_5 \beta \cos ec^2(\alpha_1 x_1 - m\pi) - \beta k_0 A_2 - Q}$$ (3.54)

Fig. 3.3 shows the waveguide sensitivity versus core refractive index (n_c) with $(x_2-x_1)=475$ μm, $n_{sub}=1.45$ obtained by using Eq. (3.54) for the proposed three layer embedded waveguide structure. The dotted line indicates the waveguide sensitivity of rib waveguide sensor as demonstrated by previous authors [13] [14]. Although Si slot waveguides [15] [16] can exhibit sensitivity > 1 due to slotted waveguide structure as compared to the proposed device, but the waveguide sensitivity of the proposed structure is almost independent with core refractive index.
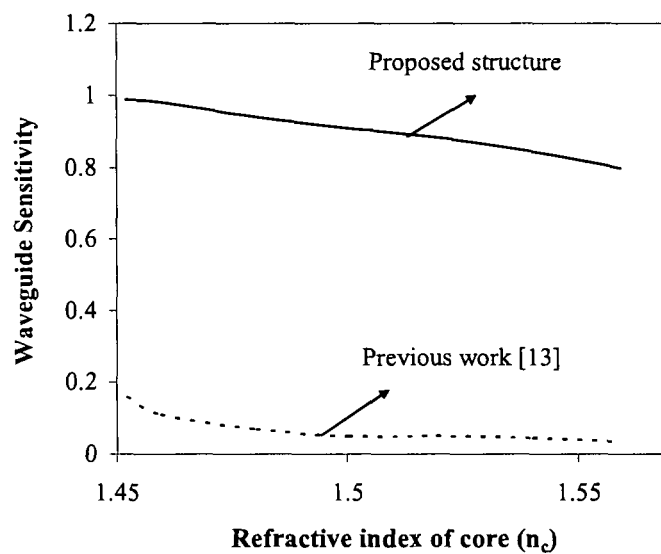

Fig- 3.3: Waveguide sensitivity versus n_c with $n_s=1.45$ and $x_2-x_1=475$ μm for proposed waveguide structure (solid line) and previous works [13] (dotted line).

3.2.3 Power propagation in the structure

A final quantity of interest is the fractional power flow in the core of the waveguide for a given mode. As illustrated in the Fig. 3.1(a) above, the electromagnetic field for a given mode does not go zero at the core-cladding interface, but changes from oscillating form in the core to an exponential decay in the cladding. Thus, the electromagnetic energy of a guided mode is carried partly in the core and partly in the cladding. With cutoff frequency, the signal of below cutoff wavelength will be confined. As cutoff is approached, the field penetrates further into the cladding region and a

greater percentage of the energy travels in the cladding. At cutoff the field no longer decays outside the core and the mode now becomes a fully radiating mode.

The fractional power W(z) that remains inside the core along z-axis can be expressed as,

$$W(z) = \left| \int_0^\alpha \psi_\beta^*(x,0)\psi(x,z)dx \right|^2 \approx \left| \int |\phi(\beta)|^2 e^{i\beta z} d\beta \right|^2 \tag{3.55}$$

where $\quad |\phi(\beta)|^2 = \left| \dfrac{A_+}{A_g} \right|^2$.

Therefore, Eq. (3.55) becomes $W(z) = \left| K \int_{-\infty}^\infty \dfrac{e^{i\beta z}}{(\beta - \beta_g)^2 + \Gamma^2} \right|$

Considering $\beta - \beta_g = \xi$, we have

$$W(z) = \left| K \int_{-\infty}^\infty \dfrac{e^{i\beta z}}{[(\beta - \beta_g)^2 + \Gamma^2]} \right|^2 = \left| K \int_{-\infty}^\infty \dfrac{e^{i\xi z}}{[(\xi + i\Gamma)(\xi - i\Gamma)]} \right|^2 \tag{3.56}$$

where $\quad \Gamma = \dfrac{4\alpha_g^4 \gamma_g^4 e^{-2\gamma_g (x_2 - x_1)}}{\beta_g^2 \delta^4 \alpha_{2g} (1 + \gamma_g x_1)}$

The above integral in Eq. (3.56) has been evaluated using complex variable techniques and Jordan's lemma.

Let $F(z) = \dfrac{e^{i\xi z}}{\xi^2 + \Gamma^2}$ has simple poles at $\xi = i\Gamma$. A contour in the complex ξ-plane consisting of the real axis and a semi-circle in the upper half plane was chosen where the integral vanishes, such that

$$\int_{-R}^R F(x)dx + \int_{C_R} F(z)dz = 2\pi i \; res\,(F, i\Gamma) \tag{3.57}$$

But $res\,(i\Gamma) = \lim_{\xi \to i\Gamma}(\xi - i\Gamma)\dfrac{e^{i\xi z}}{(\xi + i\Gamma)(\xi - i\Gamma)} = \dfrac{e^{-\Gamma z}}{2i\Gamma}$

On substituting the value of $res\,(i\Gamma)$ in Eq. (3.48A) we obtain:

$$\int_{-R}^R F(x)dx + \int_{C_R} F(z)dz = 2\pi i \; res\,(F, i\Gamma) = \dfrac{\pi e^{-\Gamma z}}{\Gamma}$$

Therefore, substituting this in Eq. (3.48) we get,

$$W(z) = \left| K \int_{-\infty}^{\infty} \frac{e^{i\xi z}}{[(\xi + i\Gamma)(\xi - i\Gamma)]} \right| = \frac{K^2 \times \pi^2 e^{-2\Gamma z}}{\Gamma^2}$$

Or, $W(z) = W'(0)e^{-2\Gamma z}$ (3.58)

where $W'(0) = \left(\dfrac{0.0018}{n_s - 1.3315} \right) W(0)$; $W(0) = \dfrac{k^2 \pi^2}{\Gamma^2}$.

3.3 Design of the proposed sensor structure

The propagation constant (β) have been determined using Effective Index Method (EIM) in which three dimensional (3D) waveguide geometry [as shown in Fig. 3.1(a)] has been approximated as two 2-dimensional waveguides for calculating the effective refractive index: waveguide-1 along the x-direction and waveguide-2 along y-direction with light confinement in the z-direction as shown in the Fig. 3.4. The core refractive index, N_I of waveguide-2 is basically effective index of waveguide-1 obtained by using Eq. (3.30).
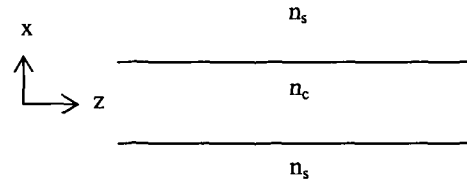
(a) Waveguide-1
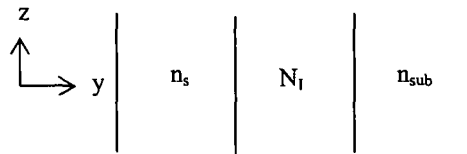
(b) Waveguide-2

Fig- 3.4: Effective index model of waveguide as shown in Fig. 1 [N_I = effective index of two dimensional Waveguide–1 and n_{sub} = refractive index (RI) of substrate].

Since the fundamental mode carries most of the power propagated in the waveguide [8] [9], using Simple Effective Index Method (SEIM) [10], we have

estimated β/k_0 versus x_1 for fundamental mode of the waveguide with n_c=1.46 and (x_2-x_1)=475 µm as shown in Fig. 3.5, where the solid line and dotted curve represents TE mode and TM mode obtained by using Eq. (3.13) and Eq. (3.14) respectively as encircled by 1. The curves encircled as 1 of β/k_0 for TE mode was found to be almost close to that of TM mode and hence it has been proved that the structure shown in Fig. 3.1(a) is polarization independent. The curve encircled as 2 shows β/k_0 versus x_1 for cylindrical structure reported by previous authors [11] [12] for comparison with the proposed sensor. It is seen that β/k_0 of the cylindrical structure almost saturates with same value of the proposed structure at x_1=25 µm.
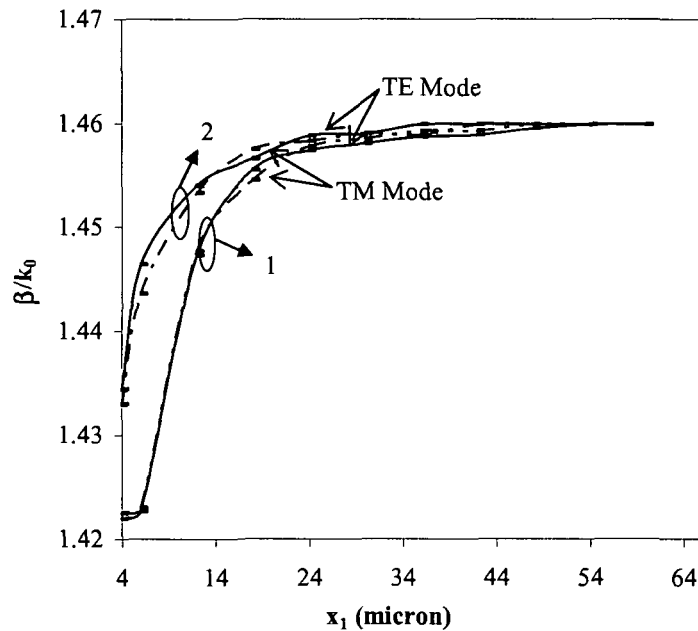

Fig- 3.5: β/k_0 versus core thickness of proposed waveguide sensor and cylindrical structures for TE mode and TM mode with n_{sub} =1.45 and n_c = 1.46 and x_2-x_1=475 µm respectively.

Further, it is found that as core thickness increases, β/k_0 rises and saturates at x_1=25 µm which gives core width of $2x_1$=50 µm.

It is of major interest to see that the waveguide sensitivity of the proposed embedded waveguide structure is ~10 times more than that of the previous works [17]

[18] and ~5 times more (not shown in the figure) than that of asymmetrical waveguide structure as reported by previous authors [8] [9]. Although the sensitivity is found to be close to that of reverse symmetry waveguide structure with plasma substrate [19], it is practically difficult to use as a sensor. As it is found that the sensitivity of the proposed waveguide sensor remains almost constant up to $n_c=1.46$, we have chosen $n_c=1.46$ to obtain waveguide of higher core width which is considered to be $2x_1=50$ μm.

3.3.1 Estimation of sample volume

The sample volume of the sensor is calculated using the relation,

Sample volume = inside volume of PCE volume of waveguide sensor

where volume of waveguide sensor = volume of waveguide core and volume for wafer and lower cladding and silicon substrate. Hence,

$$\text{Sample volume} \approx \pi r_{PCE}^2 L_{PCE} - W^2 L_{PCE} - W_{substrate \ width} \times L_{substrate} \times T_{substrate} \qquad (3.59)$$

where $T_{substrate} = 310$ μm [300 μm (Si) + 10 μm (SiO₂)]

$L_{substrate} = L_{PCE} = 100,000$ μm

$W_{substrate \ width} = 1000$ μm

$r_{PCE} = 1000$ μm

W = core area = 50 μm (since $x_1 = 25$ μm, therefore $2x_1 = 50$ μm)

Substituting these values in Eq. (3.59), we get

Sample volume = 282.995 x 10^{-9} x 10^3 liter

= 0.28 ml

3.4 Fabrication of the designed sensor

Although different technologies are being employed for producing integrated optic waveguide-based sensors which depend on the application, the SiON technology includes large range of wavelengths from visible to near-infrared. We have used silicon oxynitride (SiON) as the waveguide core material for realizing the designed device leading to high sensor sensitivity. The modeling and designing part of the presented study have been completed here at Tezpur University whereas the fabrication of the designed structures was carried out with the help of Dr. Bidyut Deka at the Center for

Excellence in NanoScience and Nanoelectronics (CENSE), Indian Institute of Science (IISc.), Bangalore under Indian NanoScience User Program (INUP) at IISc. which have been sponsored by DIT, MCIT, Government of India. In the following sub section we will first present the fabrication process of SiON waveguide and finally next its application to an optical waveguide sensor.

3.4.1 Fabrication processes

The process of fabrication begins with the deposition of lower (cladding) layer of SiO_2, grown by high-pressure thermal oxidization, Dry-Wet-Dry Oxidization, and Plasma Enhanced Chemical Vapor Deposition (PECVD) process. The detail deposition process is discussed later in this section.

The silicon oxynitride (SiON) film as a core layer is deposited using silane (SiH_4) and nitrous oxide (N_2O) precursor gases in the PECVD reactor. Because of the high refractive index difference ($n=2$ for Si_3N_4, vs $n=1.45$ for SiO_2), the core layer need to be relatively thin to ensure single-mode operation. Thermal oxidation is performed using a quartz-tube electric furnace to heat Si wafers in a flowing oxygen atmosphere [20]-[22]. To grow a thick SiO_2 layer, the oxidation rate is enhanced by using steam or steam-added oxygen atmospheres (Wet oxidation). The refractive index of the SiO_2 layer exhibits slight dependence on the atmosphere. The thickness of the underlying oxide buffer layer is large enough to ensure that the optical mode remains well confined in the core (Silicon Oxynitride) layers and does not leak into the high-index silicon substrate. The refractive index and the thickness of the films were measured using Ellipsometer and Profilometer. To understand the material behavior of deposited films, composition analysis has also been carried out using high resolution FTIR spectroscopy. The detail of each fabrication process steps and experimental results are discussed in the proceeding sections.

3.4.1.1 Preparation of Wafer for Fabrication

Wafer specifications : Si wafer

Type   : P-type

Orientation   : <100>

Thickness	: 525 ± 0.25 μm
Diameter	: 100 mm
Resistivity	: 1-15 ohms-cm
Surface	: one side polished

Wafer Cleaning Process: The RCA clean is a standard set of wafer cleaning steps which need to be performed before high temp processing steps (such as oxidation, diffusion, CVD etc.) of silicon wafers in fabrication process. Werner Kern developed the basic procedure in 1965 while working for RCA, the *Radio Corporation of America*. It involves the following:

1. Removal of the organic contaminants (Organic Clean)
2. Removal of thin oxide layer (Oxide Strip)
3. Removal of ionic contamination (Ionic Clean)

The wafers are prepared by soaking them in DI water. The first step RCA-1 (also called SC-1, where SC stands for Standard Clean) is performed with a 1:1:5 solution of NH_4OH (ammonium hydroxide) + H_2O_2 (hydrogen peroxide) + H_2O (water) at 75 or 80 °C typically for 10 minutes. This treatment results in the formation of a thin silicon dioxide layer (about 10 Angstrom) on the silicon surface, along with a certain degree of metallic contamination (notably Iron) that shall be removed in subsequent steps. This is followed by transferring the wafers into a DI water bath.

The second step is a short immersion in a 1:50 solution of HF + H_2O at 25 °C, in order to remove the thin oxide layer and some fraction of ionic contaminants.

The third and last step RCA-2 (also called SC-2) is performed with a 1:1:6 solutions of HCl + H_2O_2 + H_2O at 75 °C or 80 °C. This treatment effectively removes the remaining traces of metallic (ionic) contaminants. The details cleaning process steps approached are as follows:

The cleaning processes are carried out in the Chemical Wet bench as shown in Fig. 3.8.

RCA (WET BENCH)

The RCA (Radio Corporation of America) have 2 process steps as discussed above: **RCA-1 and RCA-2.**

RCA-1: (DI water: H_2O_2: $NH_4OH=5:1:1$)

        DI water $=200$ ml

        $H_2O_2 = 40$ ml

        $NH_4OH =40$ ml

Instead of Ammonium Hydroxide, ammonium solution can also be used.

- Temperature of the solution $=75\text{-}80^\circ$ C
- RCA-1 function : Remove organic residues
- Quartz beaker is mandatory.
- Magnetic stirrer: rotate uniformly and mix the solution and the temperature to be maintained at $75\text{-}80^\circ$ C.
- Wafer holder: used to hold the wafer.

Exhaust to be on, while performing RCA Cleaning.
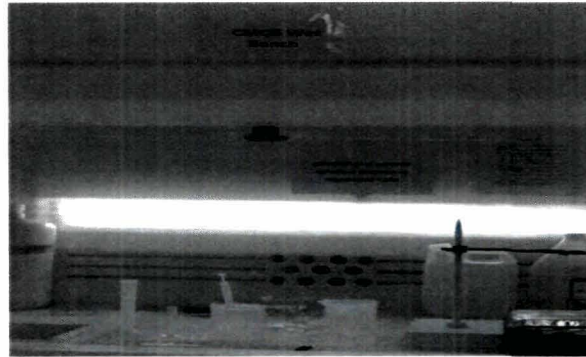
Fig-3.6: Chemical Wet Bench
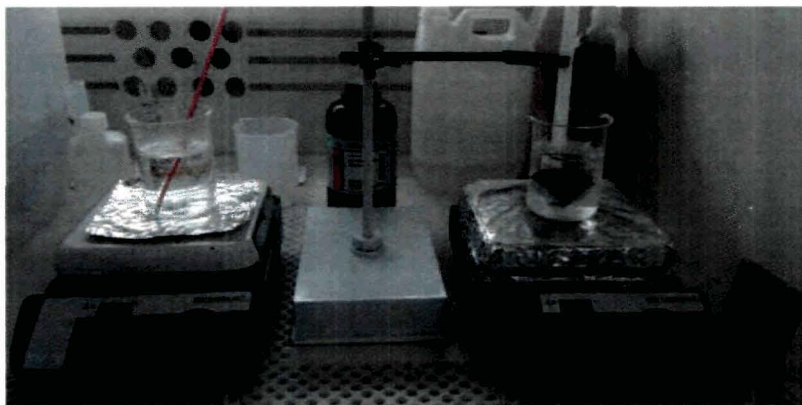
Fig-3.7: RCA-1 Cleaning Process

RCA-1 Cleaning Procedure:

RCA-1 cleaning removes the surface contaminants like dust, grease etc. The process steps are:

Step-1: We take 200 ml DI water into quartz beaker then add 40 ml H_2O_2 and 40 ml NH_4OH to DI water. Once the solution is prepared, it is kept on a hot plate and set the temperature to 250° C. The temperature of the solution is maintained at 75- 80° C.

Step-2: A magnetic Stirrer is put in the solution so that it uniformly rotates and mix the solution.

Step-3: Once solution gets heated up to 80° C, load silicon wafer into wafer holder and immerse into heated RAC-1 solution for 10 minutes. After 10 minutes of cleaning we take out wafers from the solution and rinse with DI water thoroughly for 1 minute, so that it can be cool down.

Step-4: After doing RCA-1, all beakers should be washed with DI water. Acid waste and DI water to be disposed in drain.

RCA-2: (DI water: H_2O_2: HCL=6:1:1)

DI =240 ml

H_2O_2 = 40 ml

HCL =40 ml

- Temperature of the solution = 75-80° C
- RCA-2 function : Remove metallic residues
- Quartz beaker is mandatory.
- Magnetic stirrer: rotate uniformly and mix the solution and the temperature is maintained at 75-80° C.
- Wafer holder: used to hold the wafers.
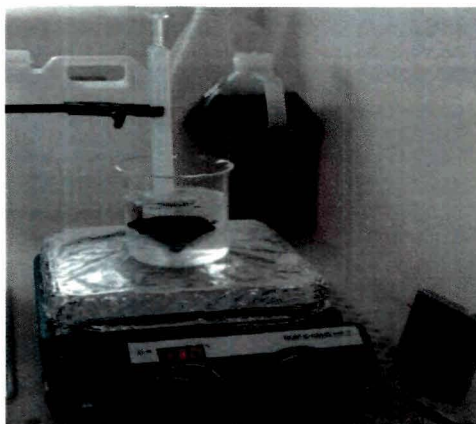- Exhaust to be on, while performing RCA Cleaning.

Fig-3.8: RCA-2 Cleaning Process

RCA-2 Cleaning Procedure:

The RCA-2 cleaning removes the metallic contaminants from the wafer. The cleaning process steps are:

Step-1: We take 240 ml DI water into quartz beaker. Next we add 40 ml H_2O_2 and 40 ml HCl to DI water. Once the solution is prepared, it is kept on a hot plate and set the temperature to 250° C. The solution is needed to be heated at 75- 80° C.

Step-2: Magnetic Stirrer is put in the solution so that it uniformly rotates and mix the solution.

Step-3: Once solution gets heated up to 80° C, we load silicon wafer into wafer holder and immerse it into heated RAC-2 solution for 10 minutes. After 10 minutes of cleaning we take out wafers from the solution and then rinse with DI water thoroughly for 1 minute, so that it can be cooled down.

Step-4: After doing RCA-2, all beakers should be washed with DI water. Acid waste and DI water to be disposed in drain.

After RCA-1 and RCA-2 cleaning process, next process step is:

HF (hydrofluoric acid solution) DIP: (DI water: HF=10:1)

DI water = 100 ml

HF= 1 ml

- This process takes about 5 to 7 minutes to get it complete.
- We should avoid using glass beaker with HF since HF attacks glass. It is always advised to use plastic beaker.
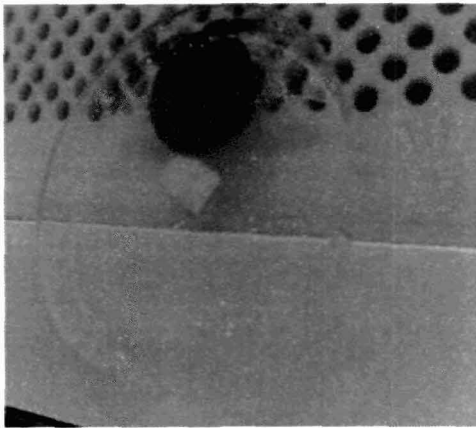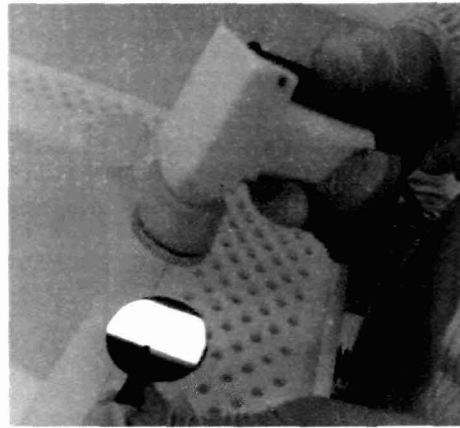
Procedure:

Fig-3.9: (a) HF solution dipped Wafer   **Fig-3.9 (b):** Blow dry with Nitrogen

We take 100 ml of DI water using measuring cylinder and pour into polypropylene beaker and then add 1 ml of HF in a polypropylene measuring cylinder and add to DI water and mix thoroughly using Teflon rod. Then dip RCA-2 cleaned silicon wafer into dilute HF solution for 15 seconds and finally rinse with DI water for 1 min. Wafers should be blown dry with Nitrogen and store in a wafer box. Now the wafers are ready for thermal wet oxidation process.

3.4.1.2   Deposition of Silica (SiO₂) Layer as Lower Cladding

In thermal oxidation, silicon wafers are oxidized in furnaces at about 1000^0 C. The furnaces consist of a quartz tube in which the wafers are placed on a carrier made of quartz glass. For heating there are several heating zones and for chemical supply

multiple pipes. Quartz glass has a very high melting point (above 1500^0 C) and thus is applicable for high temperature processes. To avoid cracks or warping, the quartz tube is heated slowly (e.g. $+10^0$ C per minute). The tempering of the tube can be done very accurate via individual heating zones. Depending on the gases different oxidations occur (a thermal oxidation has to take place on a bare silicon surface). Fig. 3.10 shows the schematic diagram of Wet Oxidation Furnance/Tempress Furnance used for dry-wet-dry oxidation.
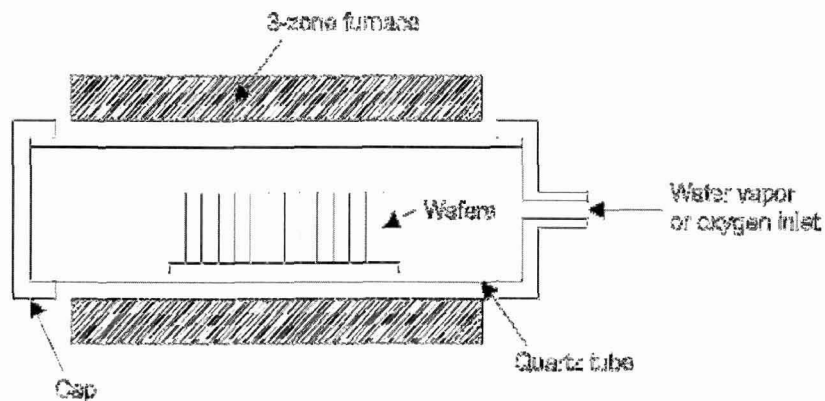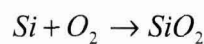

Fig.-3.10: Schematic diagram of an oxidation furnace

The thermal oxidation can be divided into the dry and wet oxidation:

The dry oxidation takes place under pure oxygen atmosphere. The silicon and oxide reacts to form silicon dioxide (SiO_2):

$$Si + O_2 \rightarrow SiO_2$$

In wet thermal oxidation, the oxygen is led through a bubbler vessel filled with heated water (about $\sim95^0$ C), so that in addition to oxygen water is present in the quartz tube as steam. The oxidation is given by:

$$Si + 2H_2O \rightarrow SiO_2 + 2H_2$$
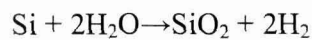
This process is done by 90^0 C to 1000^0 C. The characteristics of wet thermal oxidation are:

i. Fast growth rate even on low temperatures
ii. Less quality than dry oxides

This dry process is done at 1000^0 C to 1200^0 C actually. To create a very thin and stable oxide the process can be done at even lower temperatures of about 800^0 C. Characteristic of the dry oxidation:

    i. Slow growth of oxide

    ii. High density

    iii. High breakdown voltage

In the beginning, the oxygen and silicon react to form silicon dioxide. Now the oxide layer at the surface has to be surpassed by other oxygen atoms which have to diffuse through the dioxide layer to react with the silicon crystal beneath. For this reason the growth rate primarily depends on the reaction time of oxygen and silicon, while at a certain thickness the oxidation rate is mainly determined by the velocity of diffusion of the oxygen through the silicon dioxide. With increasing thickness of the dioxide the growth rate decreases. Since the layer is amorphous, not all bonds in the silicon dioxide are intact. Partial there are dangling bonds (free electrons and holes) at the interface of silicon and SiO_2, and therefore there is a slightly positively charged zone at the interface. Since these charges affect the integrated circuit in a negative manner, therefore in general these charges are reduced with a higher temperature during oxidation or by using the wet oxidation which causes only a light charge.

Details Oxidation Procedure:

A. Growth of SiO_2 of 1 μm thickness: Dry-Wet-Dry

    Material: SiO_2

    Thickness: 2-3 μm (for >1 μm PECVD is preferred)
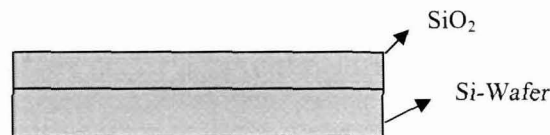
At the first, the mains of thermal wet oxidation furnace are switched-on to grow 1 μm oxide layer on the top of the cleaned silicon wafer. Through Digital temperature controller the furnace is ramp up and the temperature is executed.

Fig-3.11: Digital temperature controller

1	Display mode
2	Program mode
3	Execute mode

Thermal oxidation is carried out for growing SiO_2 layer on the cleaned Si surfaces. SiO_2 layer of thickness~1 μm is grown in the first step of oxidation using dry-wet- dry oxidation sequence.
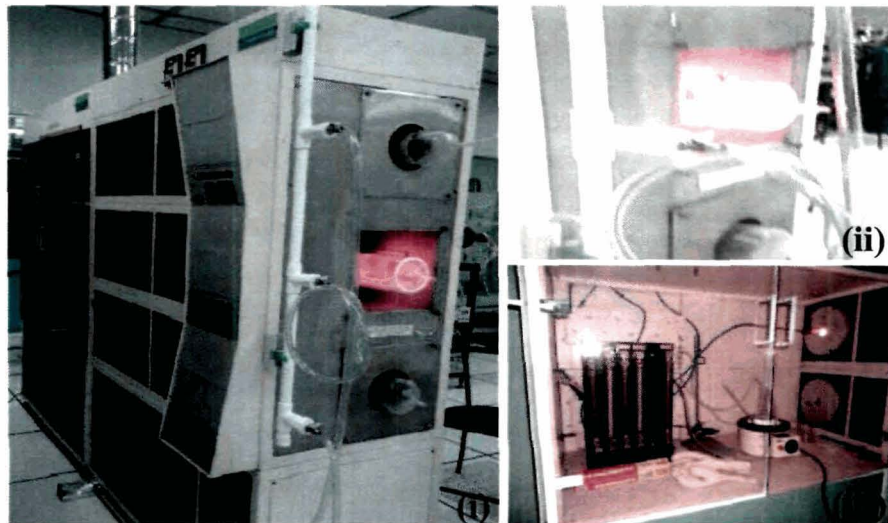

Fig-3.12: (i) Oxidation Furnace, (ii) Front view of the furnace chamber (iii) Back view along with bubbler and gas (Installed at CeNSE, IISc.)

The steps for thermal oxidation are as follows:

Step-A: The oxidation furnace temperature is set to 1100^0 C and purges the furnace with pure N_2 gas.

N_2 Flow rate -1 liter/min for 15 min.

Step-B: Wafers are loaded in oxidation furnace in a N_2 ambient (N_2 is used only during loading and unloading of wafers in oxidation furnace).

Step-C: Dry oxidation carried out for 10 min. O_2 is driven into the furnace. Dry oxidation is to get the uniform layer of thickness and good interface between Si and Oxide.

       O_2 Flow rate -1 liter/min.

Step-D: Wet oxidation to be carried out for 3 hours. The water is heated up to 97° C and connects to the furnace. The O_2 is passed through bubbler. The oxygen carries water vapours along with it to the wafer surface enabling wet oxidation to take place.

Fig.-3.13: Bubbler

Step-E: Dry oxidation to be carried out for 10 min.

       Hence a 1 μm of SiO_2 is grown by the above process. At the end of this duration, the ambient gas is again switched to N_2 and wafers are unloaded.

Colour of 1 μm oxide - green violet.
The dry-wet-dry sequence used in the process helps achieve a good quality Si-SiO_2 interface (enabled by dry oxidation) and at the same time a faster oxidation rate is achieved (due to wet oxidation).
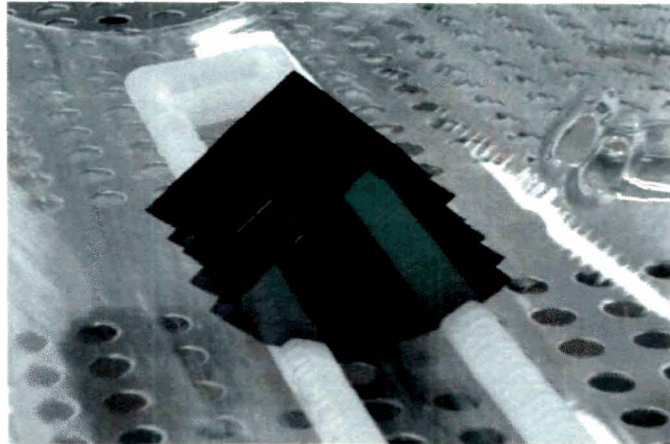
Fig.-3.14: Unloaded Si-wafer after oxidation

Note: Initially 25-35 min will take to set the furnace temperature 1100^0 C and water heater to 97^0 C.

Timings: Loading of wafers: 1: 10 p.m

Dry oxidation: 1:20 p.m to 1:30 p.m

Wet Oxidation: 1:30 p.m to 5:10 p.m

Dry Oxidation: 5:10 p.m to 5:20 p.m

Unloading of wafers: 5:40 p.m

Thickness Measurement of Deposited SiO$_2$ Layer:

The thickness of the growth SiO$_2$ layer on the top of a Si-wafer by using thermal oxidation technique is measured with the help of Ellipsometer Thickness Measurement System (Model: XLS100 from J. A. Woollam Co. Inc). Fig. 3.15 (a) shows the photograph of the system whereas Fig. 3.15 (b) shows the schematic diagram. The measured result indicating the thickness of deposited SiO$_2$ lower cladding layer of ~1 μm (10455.19 A^0) is shown in Fig. 3.16.

Further on the top of thermally grown SiO$_2$ layer of thickness ~1 μm, another layer of SiO$_2$ of thickness ~2 μm is deposited using Plasma Enhanced Chemical Vapor Deposition (PECVD) technique.
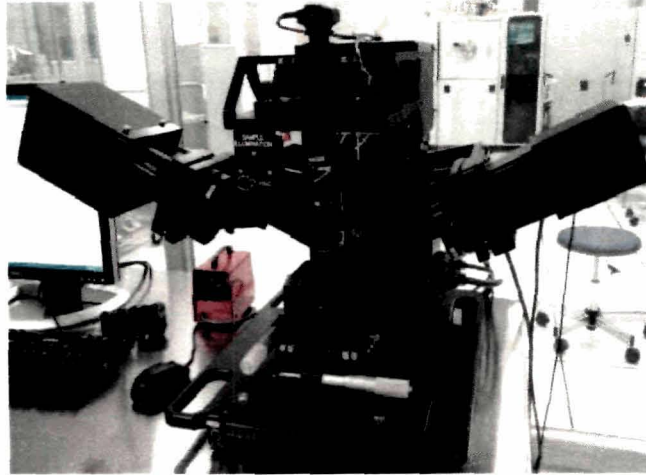
Fig.-3.15(a): Ellipsometer Measurement System (Model: XLS100)
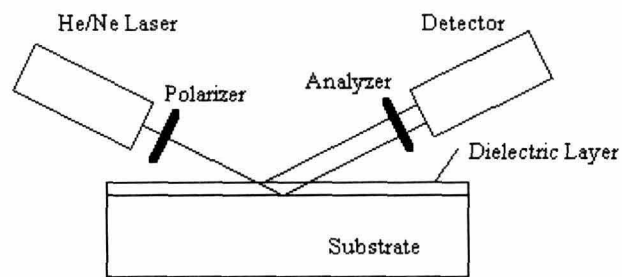(Installed at CeNSE, IISc., Bangalore)

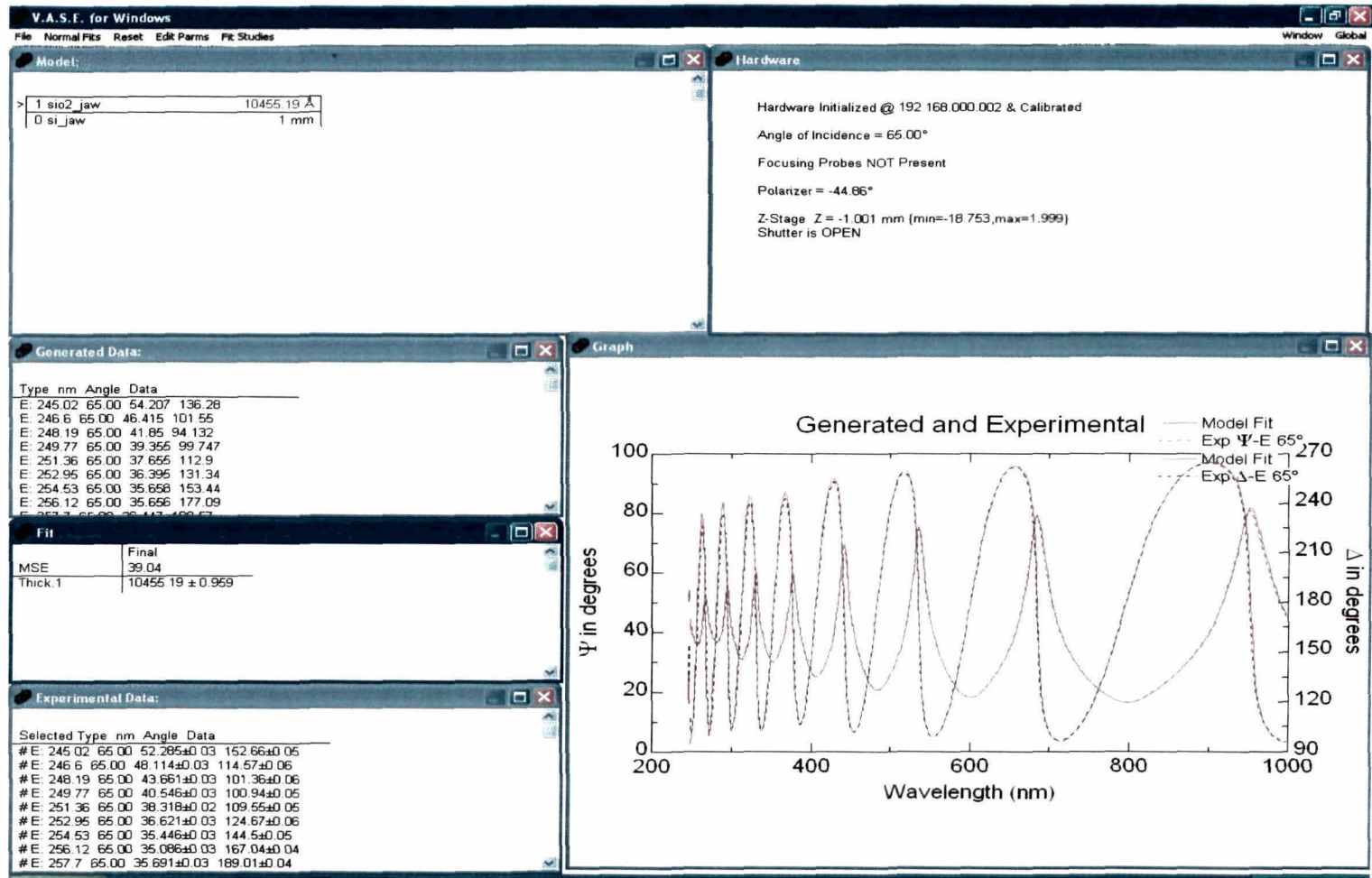**Fig.-3.15(b):** Schematic of Ellipsometer

Fig.-3.16: Measured thickness of SiO₂ layer ~1 μm deposited using thermal oxidation

B. Deposition of Silica (SiO$_2$) Layer using PECVD Method

The basic reaction for the formation of the silica (SiO$_2$) using SiH$_4$ and N$_2$O precursor gases in PECVD is as follows:

$$SiH_4 \text{ (gas)} + 4\ N_2O = SiO_2 \text{ (solid)} + 2\ H_2O \text{ (gas)} + 4\ N_2 \text{ (gas)}$$
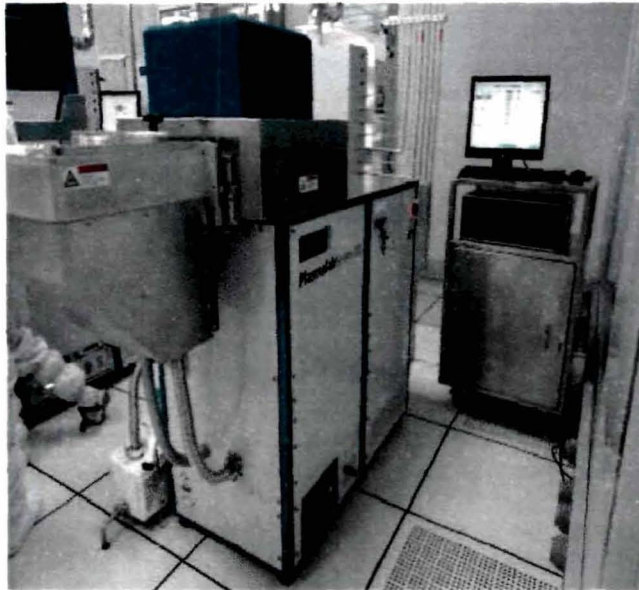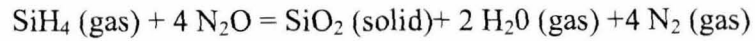

Fig.-3.17: PECVD system (Oxford PlasmaLabSystem100)

(Installed at CeNSE, IISc.)

Fig. 3.17 shows the schematic view of the PECVD system (PlasmaLabSystem100) from Oxford Instrument System which is used for deposition of SiO$_2$ lower cladding layer of thickness ~2 μm with the following process parameters.

Process parameters used:

RF power @ 13.56 MHz	: 20 W
Pump pressure	: 1000 mTorr
Silane (SiH$_4$) flow rate	: 8.5 sccm
N$_2$O flow rate	: 710 sccm
N$_2$ flow rate	: 161 sccm
Substrate temperature	: 350^0 C
Deposition rate	: 1 μm/25 min

The details of PECVD system is discussed in the proceeding section-3.6.1.3. The thickness and refractive index of the deposited SiO_2 layer is measured using ellipsometer. Fig. 3.18 shows the process parameters of SiO_2 deposition using PECVD system whereas the measured thickness of SiO_2 layer (~3 μm) is shown in Fig. 3.19.
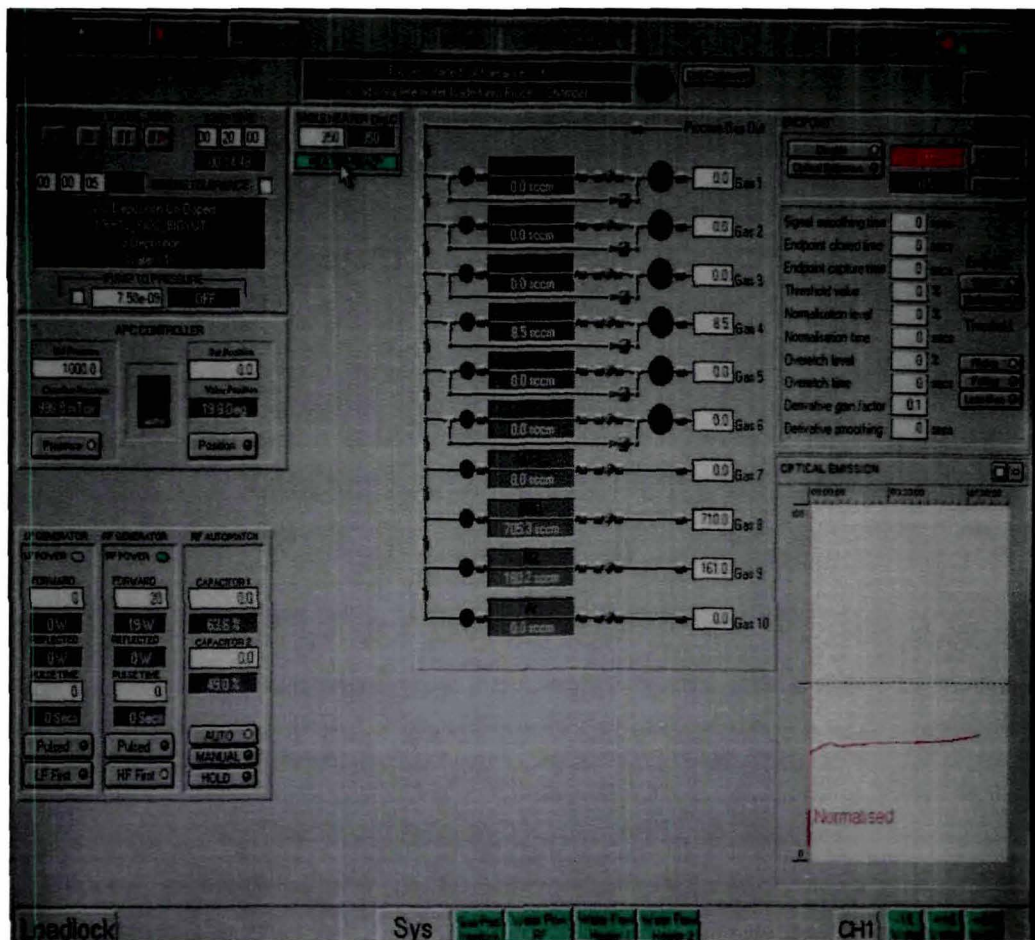

Fig.-3.18: Process parameters for deposition of SiO_2 layer using PECVD
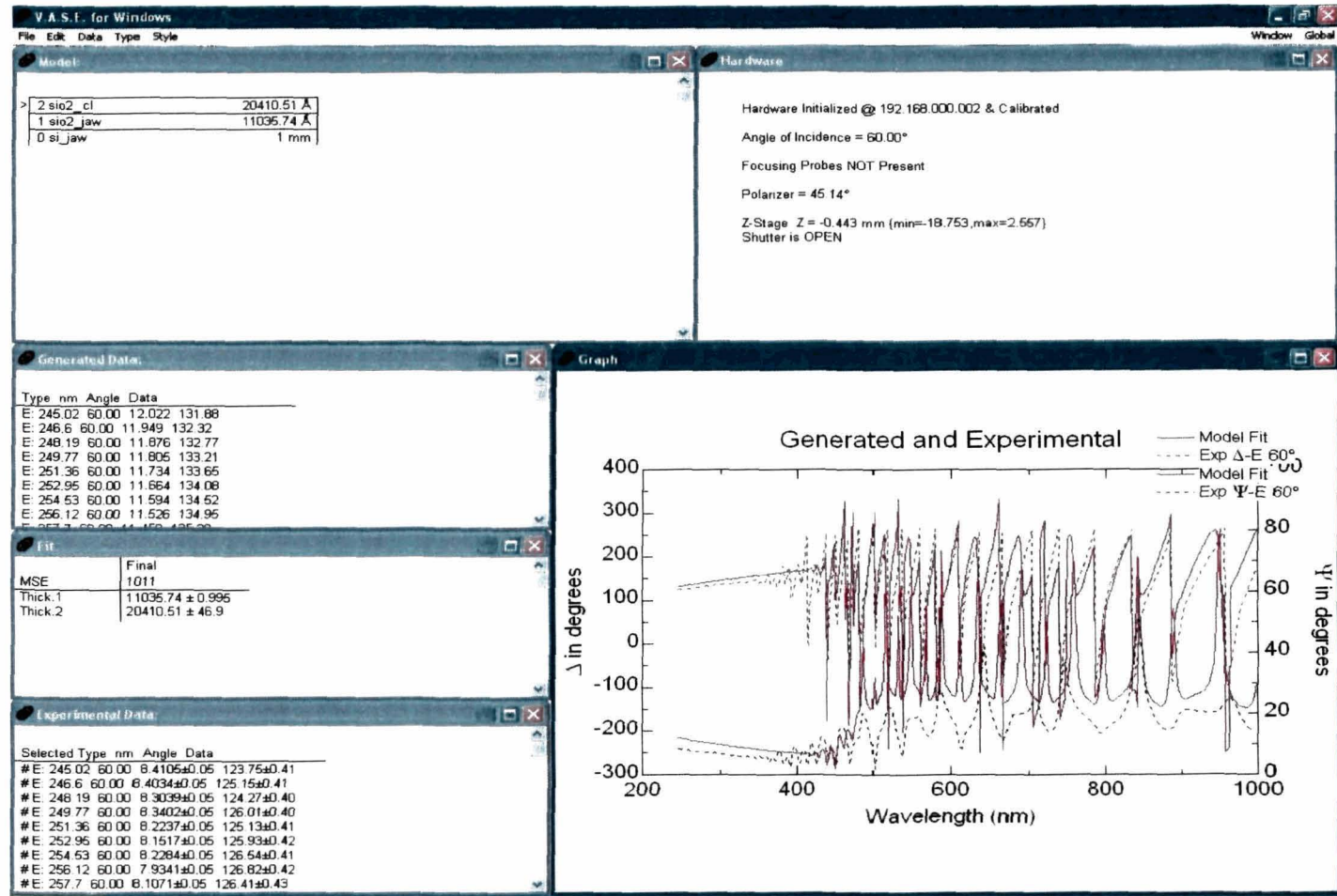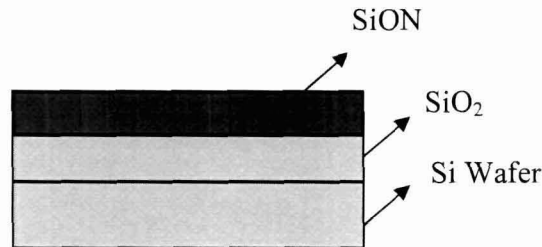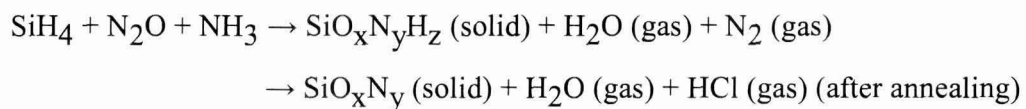
Fig.-3.19: Measured thickness of SiO$_2$ layer ~2 μm deposited using PECVD

3.4.1.3 Deposition of Silicon Oxynitride (SiON) as Guiding Layer

Material   : SiON

Thickness   : 1.5 μm

Among the variety of techniques available for silicon oxynitride production, plasma enhanced chemical vapour deposition (PECVD) technique is one of the most widely utilized due to the relative high deposition rates and low deposition temperatures [23][24]. On the other hand, for optical applications, besides the tunability of the refractive index of the materials involved, thick films (3–5 μm) with lower internal stress are essential. Plasma Enhanced Chemical Vapor Deposition (PECVD) for silicon oxynitride (SiON) layers results in a flexible material for optical waveguides. Deposition of silicon oxide and oxynitride by PECVD is identified as quite attractive technology for development of compact optical devices as films fabricated by this process easily matches the refractive index profile by changing the process parameters. In the PECVD process, the precursors used and the deposition parameters strongly influence the optical properties and quality of the deposited films. For the most part of PECVD processes for waveguide fabrication, nitrous oxide (N_2O) and silane (SiH_4) are used as main precursors for fabrication of pure silica. The basic reaction for the formation of SiON is given below,

$$SiH_4 + N_2O + NH_3 \rightarrow SiO_xN_yH_z \text{ (solid)} + H_2O \text{ (gas)} + N_2 \text{ (gas)}$$

$$\rightarrow SiO_xN_y \text{ (solid)} + H_2O \text{ (gas)} + HCl \text{ (gas) (after annealing)}$$

Process Parameters used:

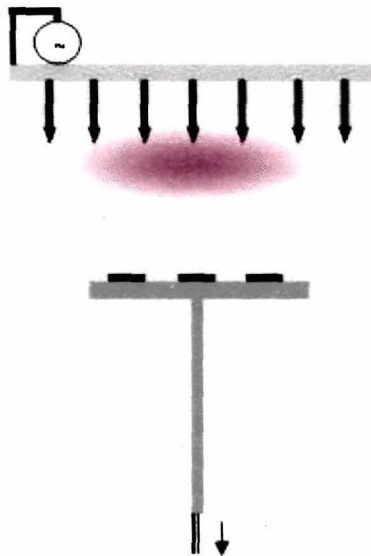|	
Si-Substrate temperature	: 350^0 C
RF power @ 13.56MHz	: 20 W
Pressure	: 1000 mTorr
SiH_4 flow rate	: 10 sccm
NH_3 flow rate	: 10 sccm
N_2O flow rate	: 200 sccm
N_2 flow rate	: 500 sccm
Deposition rate	: 1 μm/20 min

Fig.-3.20: PECVD technology (courtesy: Oxford Instrument System)

The silicon oxynitride films are deposited by using plasma enhanced chemical vapor deposition (PECVD) system (PlasmaLabSystem100) of Oxford Instruments System as shown in Fig. 3.17 and Fig. 3.20. The precursor gases are fed through a shower head which evenly distributes the gas mixture over the substrate holder; exhaust gases are pumped out from the bottom of the reactor. The plasma is created between the shower head and the substrate holder and hence the substrate is in direct contact with the plasma. This system can be operated at two different frequencies: 13.56 MHz and 100 kHz. The system can be programmed to switch back and forth between the two

frequencies automatically during a deposition run. Fig. 3.21 shows the process parameters with precursor gases used for SiON deposition by PECVD whereas the measured thickness of SiON layer obtained by using Ellipsometer is shown in Fig.-3.27. The refractive index and thickness of the deposited films were measured using a Model 2010 prism coupler from Metricon Corporation and Ellipsometer respectively. It uses a 632.8 nm He-Ne laser with a rutile prism to couple the beam into the film. All the measurements were done at TE polarization mode using a single film on substrate algorithm.
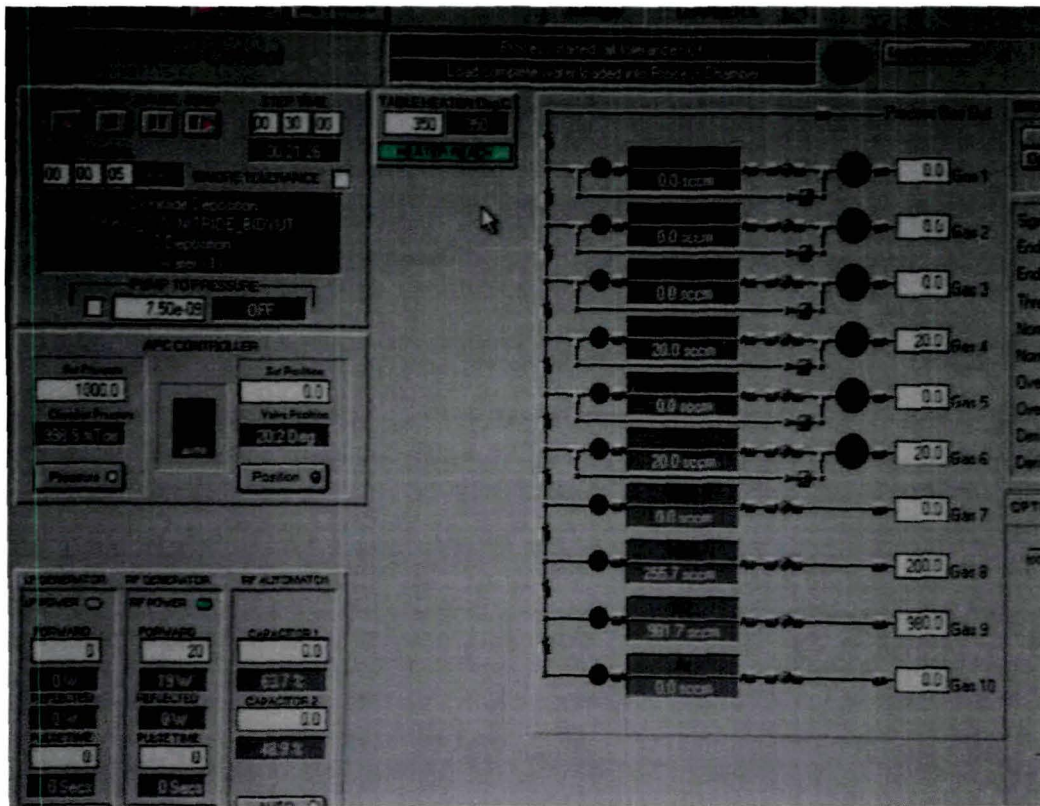

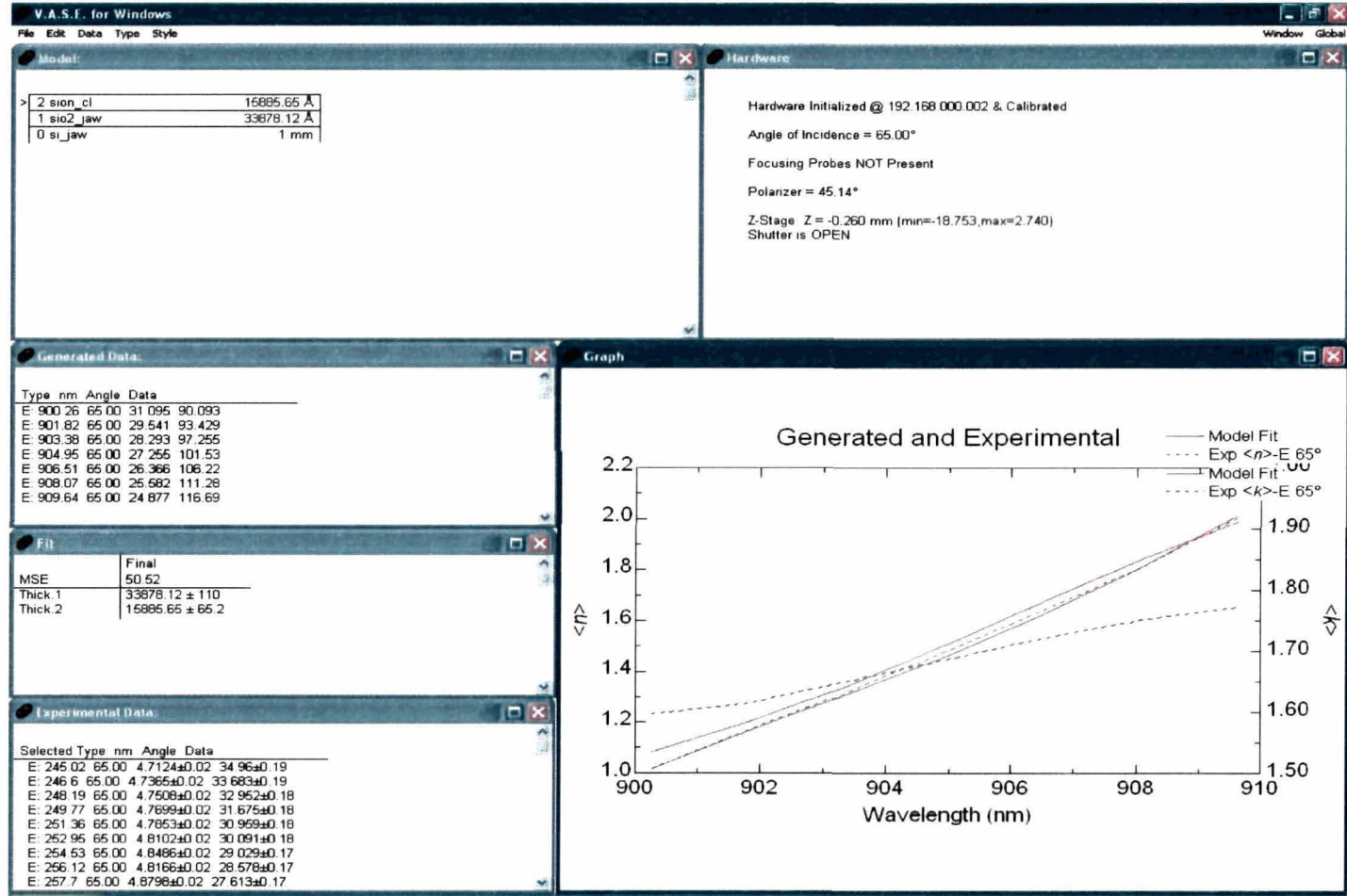**Fig-3.21:** Process parameters for deposition of SiON layer using PECVD

Fig.-3.22: Measured thickness of SiON layer ~1.5 μm deposited using PECVD
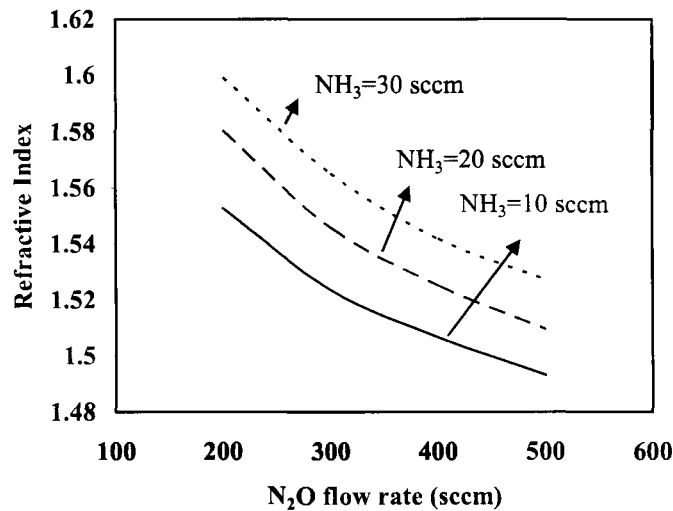
Fig.-3.23: Refractive index variation of SiON films as a function of N₂O and NH₃.

It is seen that different factors such as flow rates of gases, pressure, power, temperature etc. affect both the deposition rates and refractive index of the deposited SiON films. Fig. 3.23 shows the refractive index variation with the N_2O gas flow rates for 3 different NH_3 gas flow rate with the same environments and parameters. The refractive index of deposited SiON films can be modified successively between 1.55 and 1.495, which is the range of interest for waveguide application. Higher refractive indices up to 1.912 are probable by exploiting a lower N_2O/SiH_4 ratio or using a greater NH_3 flow rate. But high refractive index is not suitable to waveguide application. A common tendency discovered is that the refractive index decreases when flow rate of N_2O increases owing to nitrogen's weaker chemical reactivity compared to oxygen [20], [25]. This occurs because oxygen atoms are more reactive than nitrogen atoms and large amount of oxygen with small amount of nitrogen will be incorporated into the silicon oxynitride film, resulting in refractive index closer to that of stoichiometric SiO_2. At lower N_2O flow rate and in the absence of ammonia, a large index film was produced because of the higher silicon abundance (silicon rich films). Besides, as the flow rate of ammonia gas was increased, the refractive index was enhanced due to the increase in nitrogen as well as hydrogen contents.

3.4.1.4   Preparation of Mask

The LaserWriter System is a useful tool for transfer of designed patterns on a Cr mask plate or directly on the substrate. The system transforms a laser beam into a controlled writing tool for photolithographic mask fabrication or for direct in-situ processing on planar substrates.
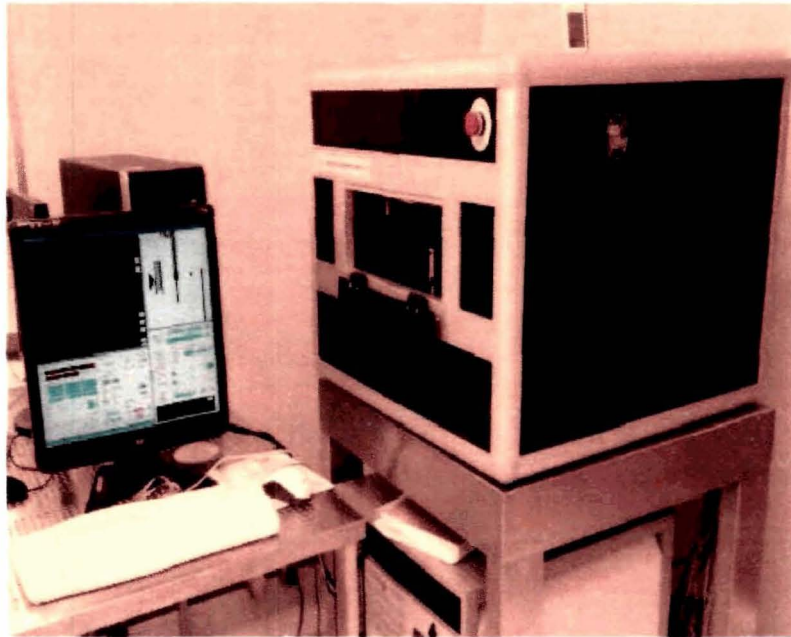

Fig.-3.24: Microtech LW 405A Laser Writer used for Mask Preparation
(Installed at CeNSE, IISc.)

The Laser Writer [Model: Microtech LW 405A] is used for preparation of 4 inch Cr-Mask plate. The mask layout of the design patterns is prepared using L-Edit software and optiBPM software before writing to the mask plate. The LaserWriter is driven by a MICROTECH proprietary data format-LDF, LaserDraw Format-obtained by automatic translation from a number of industry standard languages accepted by the LaserWriter, such as CIF, DXF, and GDSII. Fig. 3.25 shows the photograph of prepared mask.

Fig.-3.25: Patterned Mask for Photolithography

3.4.1.5 Annealing

The PECVD deposited SiON layer contains certain amount of O-H bonds, N-H bonds, and Si-H bonds that are known to be main cause of optical absorption at 1.38 μm, 1.48 μm and 1.51 μm respectively. In order to eliminate these bonds, the deposited SiON layer has been annealed at 800^0 C - 1000^0 C for 3 hrs with N_2 ambient using the First Nano drive-in furnace. For higher annealing temperatures (>1000^0 C), a large number of cracks occurred in the deposited SiON film. Fig. 3.26 shows the First Nano's EasyTube® 6000 Horizontal Furnace System installed at CeNSE, IISc., Bangalore. The Fourier Transform Infrared (FTIR) spectroscopy of SiON deposited film after annealing and before annealing is carried out which is shown in Fig. 3.27. This FTIR spectroscopy is carried out at Sophisticated Analytical Instrumentation Facility (SAIF), Tezpur University.

Fig.-3.26: First Nano Drive-in Furnace (Installed at CeNSE, IISc.)
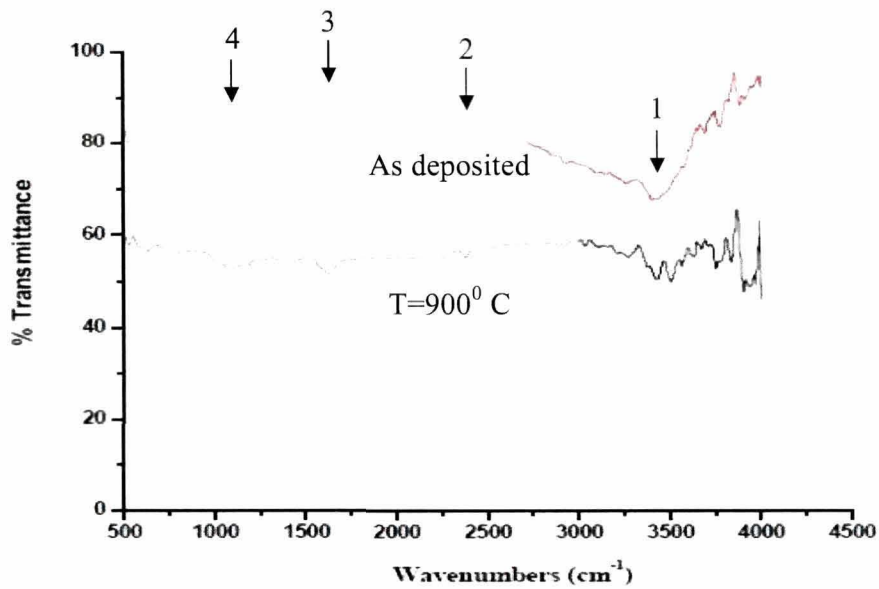
Fig.-3.27: FTIR analysis of SiON layer (**1**: Si-O-H, **2**: -Si-H, **3**: -N-H$_2$ and **4**: Si-O-H, -Si-H bonds respectively)

3.4.1.6 Transfer of Pattern on Guiding Layer

After cleaning the mask plate (prepared using Laser Writer as discussed in section-3.4.1.4) using acetone and IPA, the standard photolithography is performed for the

transfer of designed patterns on the top of SiON core layer using EVG 620 double sided mask aligner set-up. The details process steps are discussed as follows:

3.4.1.7   Spin Coating of Photoresist

Process Parameters:

Positive Photoresist (PR)	: AZ315B
Developer	: MF26A
Thickness of photo resist	: 1-1.2 μm (4000 RPM)
Exposure	: 85 mJ/cm2
Standard NUV	: 350-450 nm
Lamp power	: 350 W-500 W

The positive photoresist (AZ315B) is coated on sample with spinner coater at 4000 rpm for 40 second. An exposure with UV light is given for 1.5 sec, after pre-baking of sample at 125^0 C for 1 min. The photoresist (PR) is developed in developer for 60 sec and then the sample is kept in oven for post baking at 125^0 C for 1 min in order to make further hardening of the exposed portion of photoresist.
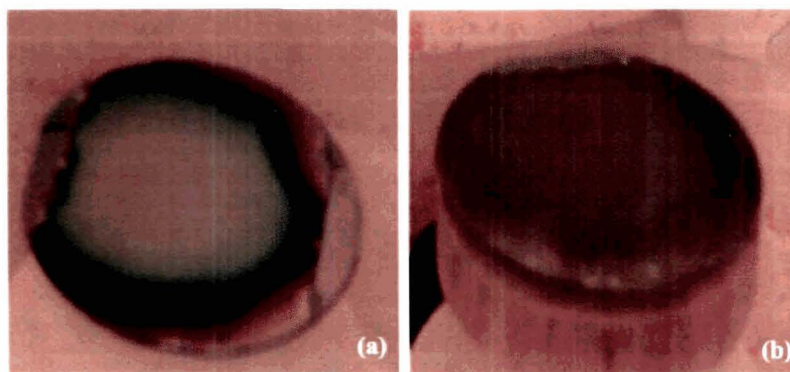

Fig-3.28: Photoresist on the sample (a) before spinning (b) after spinning

Fig-3.29: Wet Bench and Spin coater (Installed at CeNSE, IISc.)

3.4.1.8 Photolithography

Photolithography is the standard process to transfer a pattern that has been designed with computer-aided-engineering (CAE) software packages, on to a certain material (mask plate). The process steps involved in photolithography are resist coating, exposure, development, lift-off and etching etc. In the photolithographic process, a photoresist layer is spin-coated on to the material to be patterned. Next, the photoresist layer is exposed to ultraviolet (UV) light through the mask. This step is done in a mask aligner, in which mask and wafer are aligned with each other before the subsequent exposure step is performed. A mask with the desired pattern is created which is a glass plate with a patterned opaque layer (typically chromium) on the surface. Resist is coated on the waveguide substrate by a spinner. It is essential that the resist film coating is thin and as uniform and as free of pinholes as possible. The baking of the resist films has been done in an oven after coating to vaporize the solvent completely and to enhance adhesion to the substrate. Depending on the mask aligner generation, mask and substrate are brought in contact or close proximity (contact and proximity printing) or the image of the mask is projected (projection printing) on to the photoresist-coated substrate. Fig. 3.30 shows the photograph of EVG Mask Aligner Photolithography Set-up installed at CeNSE, IISc., which is used for transfer of patterns to sample.
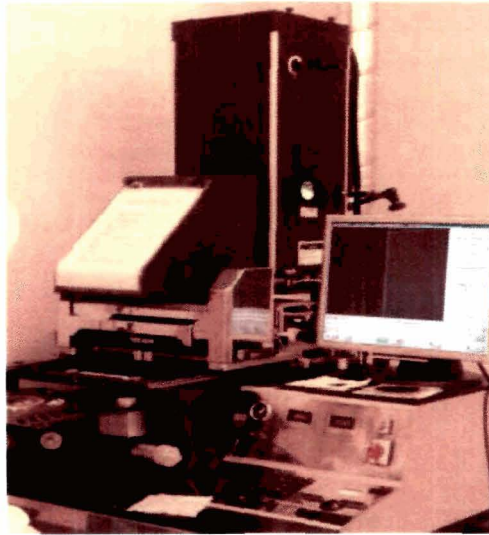
Fig-3.30: EVG 620 Mask Aligner Photolithography Set-up (CeNSE, IISc.)

Fig. 3.31 shows the basic steps of photolithography (positive) whereas the basic differences of positive and negative photolithography are shown in Fig. 3.32(a) and Fig. 3.32(b) respectively.
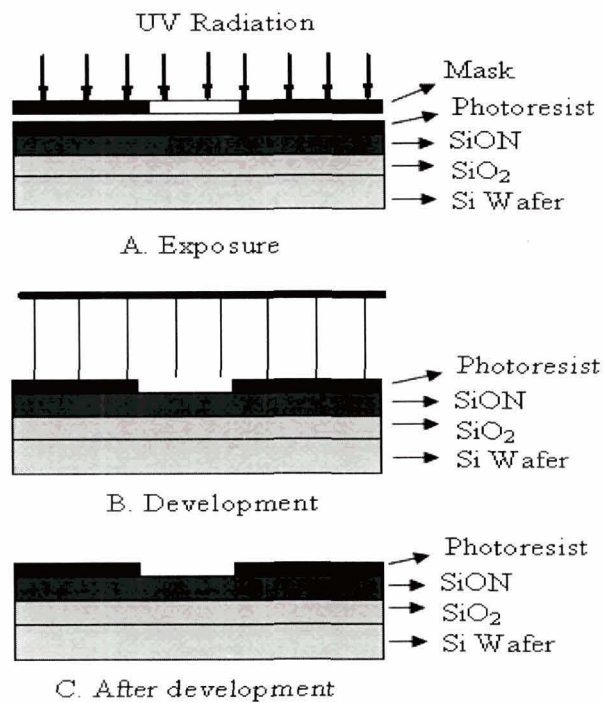

Fig.-3.31: Photolithography steps

Depending on whether positive or negative photoresist was used, the exposed or the unexposed photoresist areas, respectively, are removed during the resist development process. The remaining photoresist acts as a protective mask during the subsequent etching process, which transfers the pattern onto the underlying material. Alternatively, the patterned photoresist can be used as a mask for a subsequent ion implantation. After the etching or ion implantation step, the remaining photoresist is removed, and the next layer can be deposited and patterned.
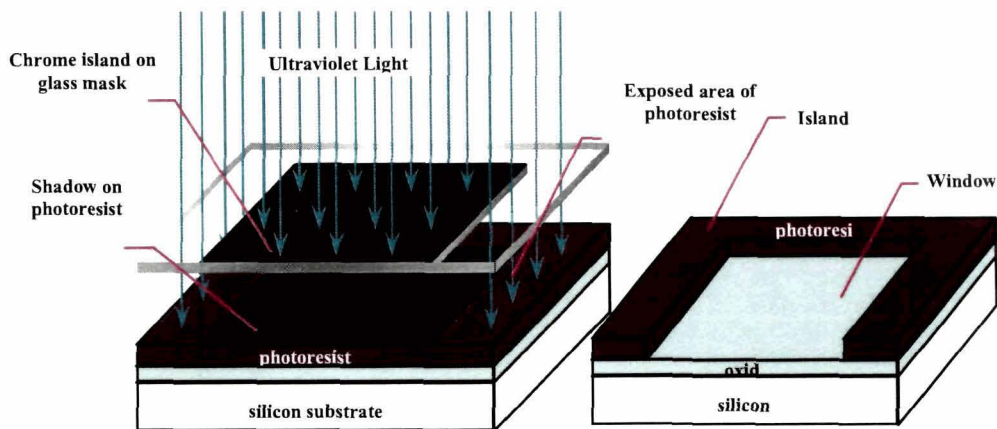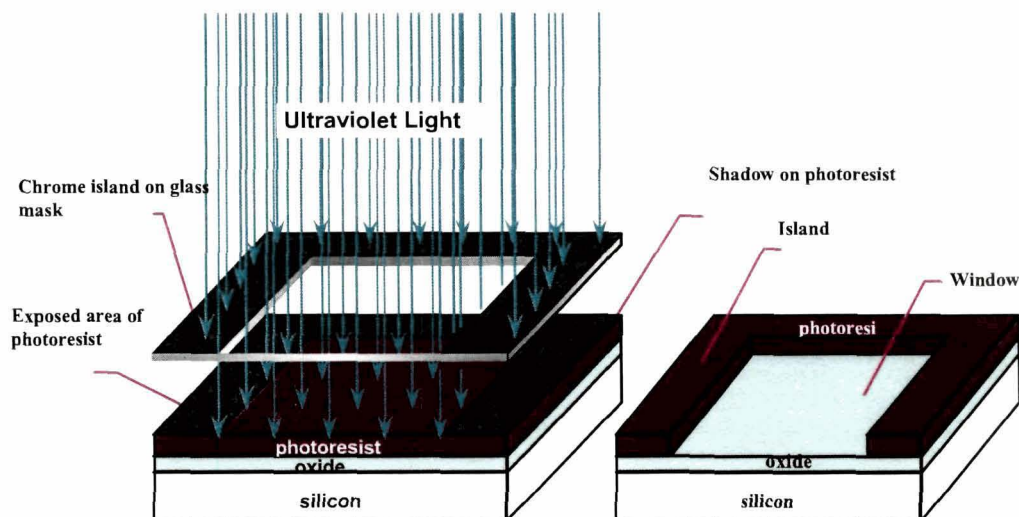

Fig.-3.32(a): Negative Photolithography

Fig.-3.32(b): Positive Photolithography (www.me.ccny.cuny.edu)

3.4.1.9 Mask cleaning

The mask pattern made on the chromium (Cr) plate is cleaned using piranha solution (a mixer of H_2O_2 + H_2SO_4) before used in mask aligner system.

3.4.1.10 Alignment and Exposure

Before giving the exposure to the sample, proper alignment should be taken care off for the well matching of the alignment marks at the mask plate. The mask pattern was aligned upon wafer before transfer of the same using EVG-620 alignment set up as shown in Fig. 3.32. After soft baking (at 125^0 C for 30 sec), the mask pattern is transferred on wafer via exposure of UV light where they were aligned on the mask. The exposure time is optimized, during the experiment (~1.5 seconds) after the several iterations were made. Proper UV exposure time is essential to deliver light with the proper intensity, directionality, spectral characteristics and uniformity across the wafer.

3.4.1.11 Development and Post Baking

The photoresist (AZ315B) is developed in developer solution (MF26A) for 60 sec and then the sample is kept in oven for post baking at 125^0 C for 1 min in order to make further hardening of the exposed portion of photoresist.

3.4.1.12 Metallization

    Material   : Chrome (Cr) metal

    Thickness : 150 nm-200 nm

    Method   : RF Sputtering/Thermal evaporation vacuum coating unit

Metallization
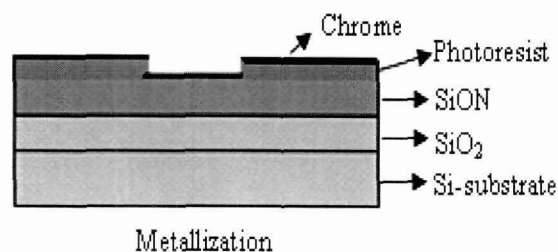
Process Parameters: RF power   : 100 W

                             Ar flow rate   : 200 sccm

                             O_2 flow rate : 20 sccm

The so-called lift-off technique is used to structure a thin-film material, which would be difficult to etch. Here, the thin-film material is deposited on top of the patterned photoresist layer. In order to avoid a continuous film, the thickness of the deposited film must be less than the resist thickness. In this regards, a chromium (Cr) metal layer of 150 nm thicknesses is deposited over the patterned wafer with the guiding layer using RF Sputtering unit. The total time taken for the deposition of chrome layer (thickness 150 nm) is ~2-3 hrs, whereas deposition rate is 1.25 nm/sec. The photograph of RF sputtering unit is shown in Fig. 3.33 whereas Fig. 3.34 shows the window of process parameters respectively.

Fig.-3.33: RF sputtering unit (Installed at CeNSE, IISc.)
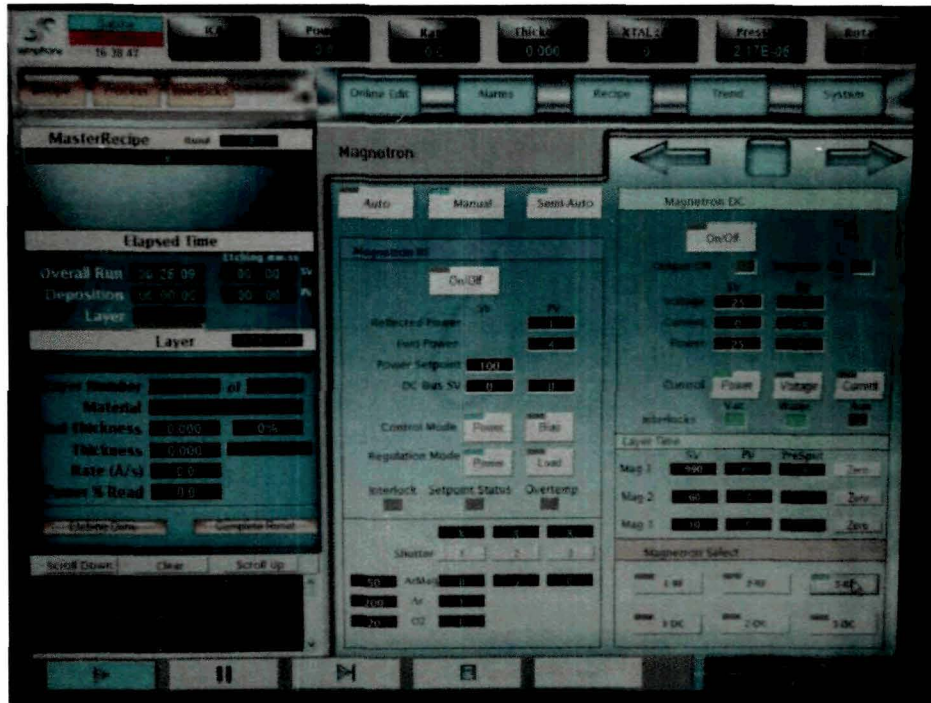
Fig-3.34: Process parameters used for Cr metallization

3.4.1.13 Lift-off Technique

The lift off technique is widely used for the patterning of relatively thin waveguide cores. After metal deposition on photoresist content surface of the wafer, it was kept in boiled acetone for 3 minutes. The metal was lift from the places where the photo resist was present because photo resist is soluble in acetone. By removing the underneath photoresist, the thin-film material on top is also removed by 'lifting it off', leaving a structured thin film on the substrate.
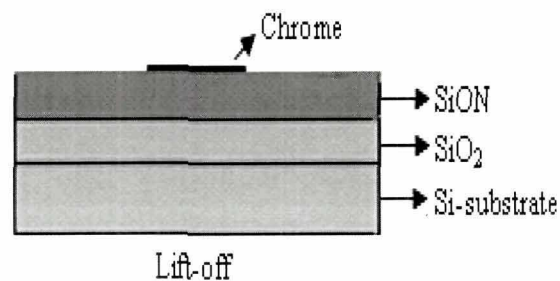
Lift-off

After the lift-off, the structures are verified with the help of optical microscope (shown in Fig. 3.35) before approaching to the further fabrication process.

**Fig-3.35:** Optical Microscope (Model: Leika DFC290 at CeNSE, IISc.)

3.4.1.14 Reactive Ion Etching

Reactive Ion Etching (RIE) is a dry etching technique which is used to selectively etch thin films in various device structures. The etching characteristic-selectivity, etch profile, etch rate, uniformity, reproducibility- can be controlled very precisely in the reactive ion etching. It involves a combination of both Physical Etching as well as Chemical Etching. Selection of an appropriate recipe (combination) of gases is an important issue. Typically the etch rates are slow and can be controlled by regulating parameters like the Electrode Bias, applied RF Power, Chamber pressure and flow rate of gases chosen in the recipe. RIE is capable of providing highly anisotropic profiles with reasonable selectivity. It is also possible to add custom recipes to etch new materials which are extremely useful for research purposes.

Reactive Ion Etching of SiON
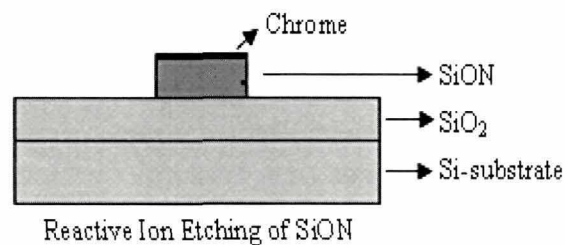
Material to be etch   : SiON

Thickness   : 1-2 μm

Method   : F –based

Process Parameters:

RF power   : 50 W (Lower electrode)

ICP power   : 2500 W (Top)

Chamber Pressure   : 5 mTorr

SF_6 flow rate   : 9 sccm

CHF_3 flow rate   : 40 sccm

Etch rate   : 366 nm/min

Etch duration   : 6 minutes (for depth 2.2 μm)

For the RIE process, the etch rates of the SiO_xN_y films were determined first. The films were first etched separately and the etch rate of each film was determined. Following this, the patterned wafers were etched with an assigned time for the correct depth. Several issues were important for the etching processes: the side-wall anisotropy, side-wall roughness and grass formation. For the side-wall anisotropy, a mixture of tri-fluoromethane (CHF_3) and argon (Ar) were used as the process gas. With the above parameter specifications, the anisotropy and roughness were found to be within the limits of tolerance. In an RIE system, reactive ions are generated in plasma and are accelerated towards the surface to be etched, thus providing directional etching characteristics. The basic reaction for the RIE of SiON can be written:

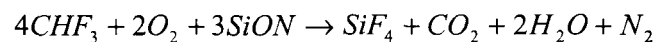$$4CHF_3 + 2O_2 + 3SiON \rightarrow SiF_4 + CO_2 + 2H_2O + N_2$$

.

Fig. 3.36 shows the photograph of RIE system whereas the etch depth measurement result is shown in Fig. 3.38 obtained by using Dektak Set-up which is shown in Fig. 3.37 respectively.

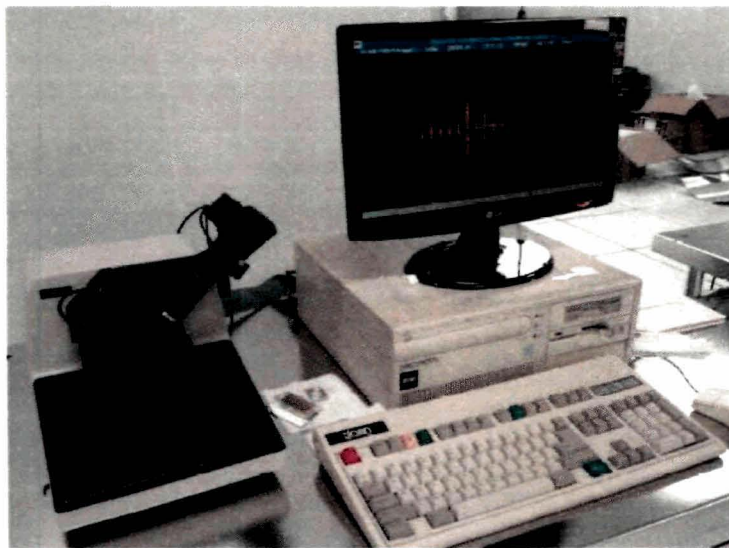**Fig-3.36:** RIE Set-up, F based (PlasmaLabSys-Oxford Instrument System), CeNSE

Fig.-3.37: Dektak Set-up for step height measurement (CeNSE, IISc.)
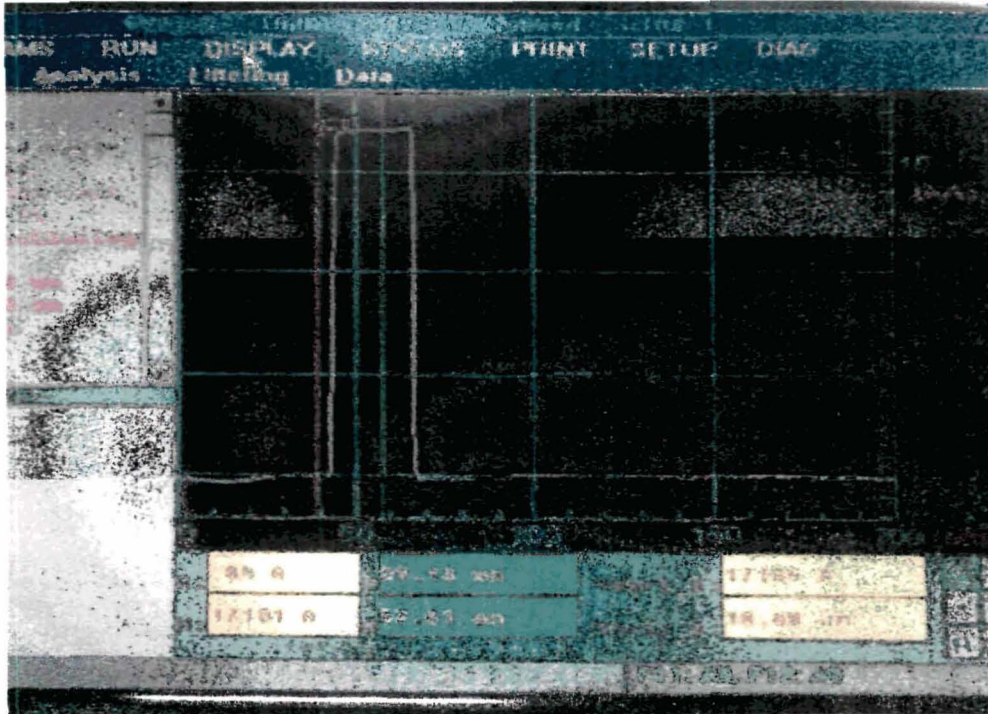
Fig-3.38: Step height measurement after RIE of SiON layer using Dektak system (depth~1.71 μm)

3.4.1.15 Wet Etching/RIE of Metallization (Cr) layer

A list of available etchants for wet etching is shown in the Table-3.1.

Table-3.1: List of available etchants for wet etching

Concentrations	Etchants	Rate
2:3:12	$KMnO_4$: $NaOH$:H_2O	
3:1	H_2O:H_2O_2	
Concentrated and dilute	HCl	
3:1	HCl:H_2O_2	
2:1	FeCl: HCl	
	Cyantek CR-7s (Perchloric based)	7 min/μm
1:1	HCl: glycerine	12 min/μm after depassivation
1:3	[50g $NaOH$+100 ml H_2O]: [30g $K_3Fe(CN)_6$+100 ml H_2O]	

Material to be etched : Cr

Thickness : *150 nm*

Etchant used : $H_2O:H_2O_2$

Fig.-3.39 shows the SEM images of the fabricated waveguide based optical sensor.

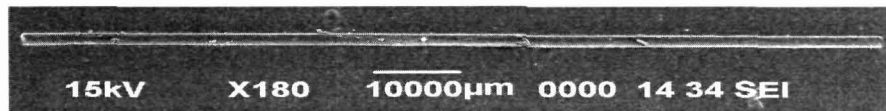**15kV   X180   10000μm   0000 14 34 SEI**

Fig-3.39: SEM image of fabricated sensor

3.5   Experimental set up for sensing application

After the fabrication of the designed planar waveguide sensor with silicon oxynitride as the waveguide core material, the optical power loss measurement is executed for performance evaluation of the developed sensor device.

3.5.1   Measurements

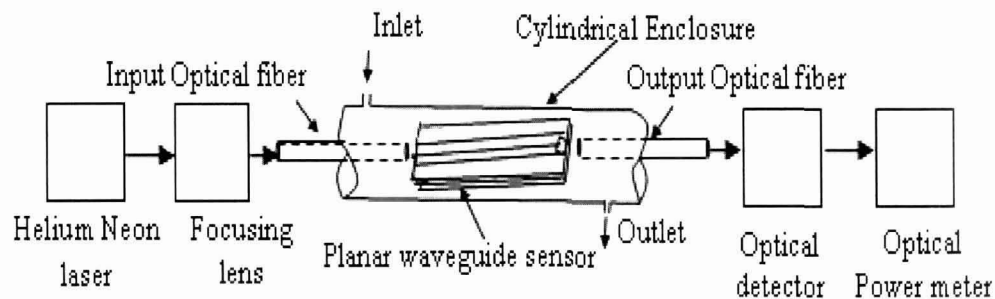**Fig-3.40:** Schematic block diagram of a power measurement set-up for use of the planar waveguide based sensor

Fig. 3.40 shows the schematic block representation of the experimental set-up that is used for measurement of power loss whereas the photograph of the developed measurement set-up in the laboratory is shown in Fig. 3.41 Helium Neon (He-Ne) laser beam of wavelength 0.6328 μm and power 1 mW was used as the source of light and

launched to the optical fiber using focusing lens for light input into the waveguide sensor. The transmitted light through the testing devices to the other end is measured using power sensor (Ge doped/Model: FieldMax II-VIS from Cohernt Inc.) attached to the Powermeter (Model: FieldMax II-TOP from Cohernt Inc.). The complete set-up is kept on the top of vibration free optical bread board of size (1 m x 1 m x 1 m). The output power of the sensor was coupled to another optical fiber for detection of the same, using a movable germanium p-i-n detector placed at the other end.
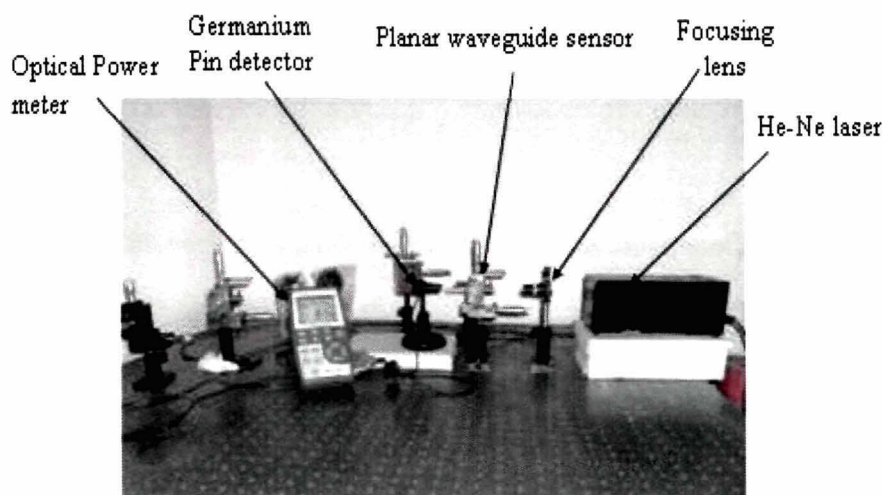

Fig-3.41: Power measurement set-up for use of three layer planar waveguide as sensor for measurement of glucose concentration

3.5.2 Results and Characterization

The characteristics of the designed waveguide sensor have been validated injecting distilled water inside the cylindrical enclosure having planar waveguide inside. The normalized power ~0.9996, 0.9994 and 0.9993 as measured by the power meter (indicated by cross signs as shown in Fig. 3.42) using waveguide sensor of length ~100,000 μm, 120,000 μm and 150,000 μm respectively are in good agreement with the theoretical curves. Using the experimental set up (shown in Fig. 3.41), the waveguide sensor have been used for sensing glucose concentration (C) (with C varying from 0.1 gm/100 ml to 0.8 gm/100 ml) in aqueous solution by measuring the normalized powers $W(z)/W(0)$ (where $W(0)$ is measured with distilled water in the sensing region).
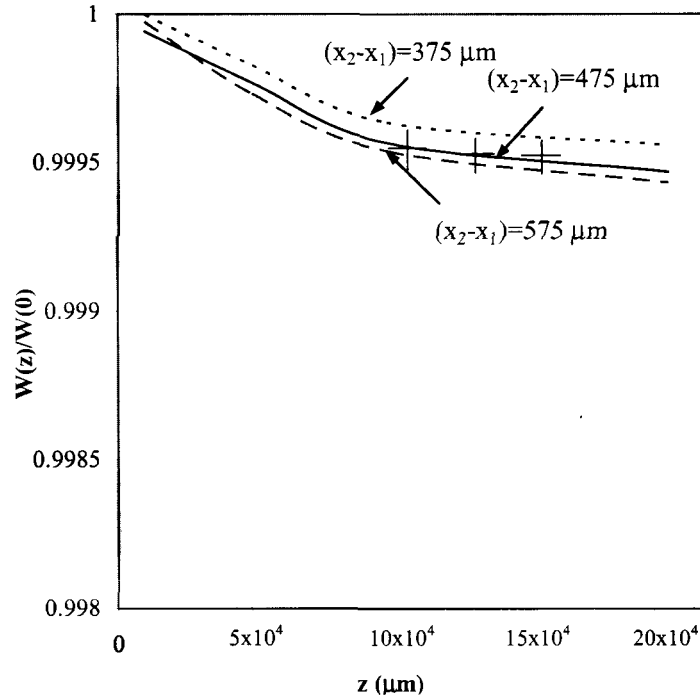
Fig-3.42: Normalized power versus length of the wave guide along z direction for different (x_2-x_1) ~375μm, 475 μm and 575 μm with n_{sub}=1.45, n_s=1.33 and n_c=1.46. The cross sign indicates experimental point for x_2-x_1=475 μm.

Fig. 3.42 shows the normalized power W(z)/W(0) versus z of the waveguide along the z direction for different thickness of the cladding layer (x_2-x_1)=375 μm, 475 μm and 575 μm respectively. From the Fig. it is found that, W(z)/W(0) decreases with increase of z and this variation saturates at z=100,000 μm for the mentioned (x_2-x_1) values. For z<100,000 μm, the rate of decrease of W(z)/W(0) for x_2-x_1=475 μm was found to be more than that for x_2-x_1=375 μm but for x_2-x_1=475 μm, it is almost close to that for x_2-x_1=575 μm. The cross signs indicates the values of experimental results. So we have chosen x_2-x_1=475 μm. We have estimated W(0) with pure distilled water (refractive index ~1.333) in the sensing region surrounded with waveguide and determined the variation of W(z)/W(0) with change of refractive index of sensing region (n_s) for n_s ranging from 1.33363 to 1.33453 by using Eq. (3.58), as shown in Fig. 3.43. The inset figure shows the variation of refractive index with change in glucose concentration (C)

with C varying from 0.1 gm/100 ml to 0.8 gm/100 ml. From the Fig. 3.43, it is found that $W(z)/W(0)$ decreases with increase of n_s Furthermore, the curves are almost close to each other for all z values mentioned in the figure. The cross signs indicating the experimental results, obtained by sensing glucose aqueous solution with varying concentration as the cladding/sensing layer.
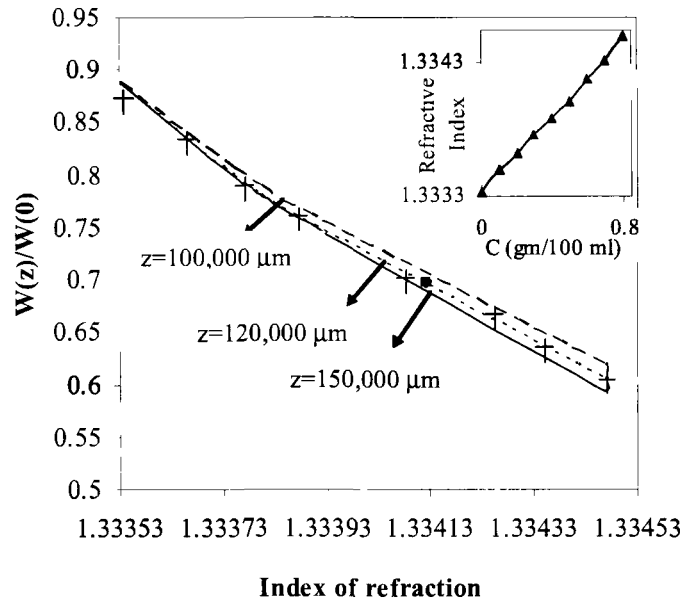
Fig-3.43: Normalized power versus refractive index for waveguide sensor with z=100,000 μm, 120,000 μm and 150,000 μm with n_c=1.46 and $2x_1$=50 μm. (The cross points represent experimental results of glucose solution as sensing region). The black dot corresponds to power $W(z)$=0.56 mW and $W(0)$=0.8 mW, corresponding to refractive index ~ 1.3341 at measured glucose concentration.

The operating principle of the proposed device (i.e. the waveguide sensor) is based on evanescent wave sensing mechanism. The variation of refractive index with C is measured by Abbe Refractrometer at ambient temperature of 25^0 C is shown in Fig. 3.43. As shown in the Fig. 3.43, it is seen that refractive index does not increase with change of glucose concentration but the change of power occurs due to more evanescent decay at the cladding region with large sensing area of the proposed structure. $W(z)$ is basically the signal power confined in the core of the waveguide sensor whereas $W(0)$ is

the power coupled to the sensor waveguide (z=0). The black dot corresponds to power W(z)=0.56 mW and W(0)=0.8 mW, corresponding to refractive index ~1.33413 at measured glucose concentration. The comparison study of theoretical results with experimental results shows that there may be ~ ± 3% deviation in measurement uncertainty.

It is found that as the concentration of glucose aqueous solution increases, R.I (as measured by Abbe Refractometer) increases; thus the confinement of light wave in the waveguide core reduces with more leakage of power through leaky quasi-modes. Hence, more absorption takes place for increasing concentration of glucose solution in the sensing region. The measured values of the normalized power as indicated by the cross signs in Fig. 3.41 are in good agreement with the theoretical curves. It is seen that the signal at the output of the sensor is independent of refractive index of the sensing region for $n_s \geq n_c$, as the signal will no longer be confined in the core region. So, the Limit of Detection (LOD) of our sensor will be restricted up to core refractive index and for our experimental set up, LOD is ~1.333–1.46 which is found to be more than the earlier reported works [26]-[28].

Fig.-3.44: Abbe Refractometer

3.6 Conclusion

In this chapter an optical sensor incorporating composite planar waveguide geometry have been designed and developed on SiO_2-Si wafer with a view to implement sensor

platform. Using a mathematical model based on quasi-guided modes the dispersion relations are derived for estimating the propagation constants of TE and TM modes. The proposed fabricated waveguide of length 100,000 µm and core width ~50 µm, housed within a PCE of diameter ~1000 µm was adapted for sensing glucose concentration in aqueous solution as an evidence of the design and development. The sensitivity of the waveguide sensor is derived from the dispersion relations. It is found that the sensitivity of the proposed waveguide is 0.95 which is ~10 times more than that of the existing planar waveguide sensors [14] [15] and 5 times more than that of asymmetric waveguide structure [7] [8]. It is seen that the proposed waveguide sensor is polarization independent. The experimental results of normalized power are in good agreement with the result obtained theoretically. Furthermore, this optical sensor requires very minimal sample volume for its detection and has the great potential to realize for rapid detection of blood glucose level, which is discussed in chapter 5. We have studied rapid detection of adulteration of petroleum products as mentioned in chapter 4.

3.7 List of References

1. Vijayan, M. V., et al. Fuke, R. N. Karekar, and R. C. Aiyer, Planar Optical Waveguide CO_2 Evanescent Wave Sensor Based on a Clad of Alstonia Scholaris Leaf Extract, *IEEE Sensors Journal* 9 (1), 13-19, 2009.

2. Barrios, C. A. Optical Slot-Waveguide Based Biochemical Sensors, *Sensors*, 9 (6), 4751-4765, 2009.

3. Liu, Y., et al. An Integrated Optical Sensor for Measuring Glucose Concentration, *Appl. Phys. B* 54, 18-23, 1992.

4. Mukundan, H., et al. Planar optical waveguide-based biosensor for the quantitative detection of tumor markers, *Sensors and Actuators B* 138 (2), 453-460, 2009.

5. Lifante, G. *Integrated Photonics: Fundamentals*, John Wiley & Sons Ltd, England, 2003.

6. Dutta, A. et al. Modeling and fabrication of evanescent waveguide-based optical sensor for sensitivity enhancement using silicon oxynitride technology, *Optic. Eng.* 52, 077101-6, 2013.
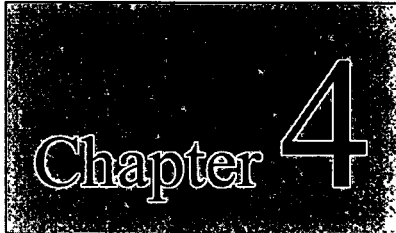
7. Ghatak, A. K., & Thyagarajan, K. Leaky modes in optical waveguides, in *Optical Electronics*: Cambridge University Press, New York, 2004, 347-358.

8. Taya, S. A., et al. Theoretical Analysis of TM nonlinear asymmetrical waveguide optical sensors, *Sensors and Actuators A: Phys.* **147**, 137-141, 2008.

9. Taya, S. A., et al. Nonlinear planar asymmetrical optical waveguides for sensing applications, *Optik* **121** (9), 860-865, 2010.

10. Deka, B. & Sahu, P. P. Transformation relationship of directional coupler with multimode interference coupler and two mode interference coupler, *Journal of Opt.* **38** (2), 75-87, 2009.

11. Snyder, A. W. & Love, J. D. Circular fibers, in *Optical Waveguide Theory*: Kluwer Academic Publishers, USA, 2000, 301-335.

12. Gloge, D. Weakly Guiding Fibers, *Applied Optics* **10**(10), 2252-2258, 1971.

13. V. M. N. Passaro, F. Dell'Olio, B. Casamassima and F. De Leonardis, Guided-Wave Optical Biosensors, *Sensors* 7(4), 508-536 (2007).

14. Dell'Olio, F., et al. Sensitivity Analysis of Rib Waveguides for Integrated Optical Sensors, in International Workshop on Advances in Sensors and Interface (IWASI'2007), Bari, Italy.

15. Passaro, V. M. N., et al. Efficient Chemical Sensing by Coupled Slot SOI Waveguides, *Sensors* **9** (2), 1012-1032, 2009.

16. Dell'Olio, F., & Passaro, V. M. N. Optical sensing by optimized silicon slot waveguides, *Optic Express* **15**(8), 4977-4993, 2007.

17. Veldhuis, G. J., et al. Sensitivity Enhancement in Evanescent Optical Waveguide Sensors, *IEEE Journal of Lightwave Tech.* **18**(5), 677-682, 2000.

18. Jamid, H. A. Multilayer ARROW channel waveguide for evanescent field enhancement in low-index media, *Applied Opt.* **41**(7), 1385-1390, 2002.

19. Taya, S. A. & El-Agez, T. M. A reverse symmetry optical waveguide sensor using a plasma substrate, *Journal of Opt.* **13**(7), 1-6, 2011.

20. Naskar, S. *Deposition and Characterisation of Silicon Oxynitride material for the Fabrication of Optical Waveguides*, Ph. D. thesis, University of Case Western Reserve at Cleveland, Ohio, USA, 2006.

21. Nishihara, H., Haruna, M., & Suhara, T. *Optical Integrated Circuits*, McGraw-

Hill, New York, 1989.

22. Gandhi, S. K. *VLSI Fabrication Principles: Silicon and Gallium Arsenide*, Willey-India, New Delhi, 2008.

23. Worhoff, K., et al. Design, tolerance analysis and fabrication of silicon oxynitride based planar optical waveguides for communication devices, *J. of Lightwave Tech.* **17** (8), 1401-1407, 1999.

24. Bona, G. L. et al. SiON high refractive-index waveguide and planar lightwave circuit, *IBM J. Res. & Dev.* **47** (2.3), 239-249, 2003. ·

25. Hussein, M.G., et al. Stability of low refractive index PECVD silicon oxynitride layers in, Symposium IEEE/LEOS Benelux Chapter 2003, 77-80.

26. Nunes, P. S., et al. Refractive Index Sensor Based on a 1D Photonic Crystal in a Microfluidic Channel, *Sensors* **10** (3), 2348-2358, 2010.

27. Heideman, R.G., & Lambeck, P.V. Remote opto-chemical sensing with extreme sensitivity: design, fabrication and performance of a pigtailed integrated optical phase-modulated Mach–Zehnder interferometer system, *Sensors and Actuators B Chemical* **61**(1-3), 100–127, 1999.

28. Lambeck, P. V. Integrated optical sensors for the chemical domain, *Measurement Science and Technology* **17**(8), R93–R116, 2006.

✳ ✳ ✳ ✳ ✳

Chapter 4

Integrated Optic Sensor for detecting adulteration in petroleum based products

Outline of the Chapter:

Chapter 4

4.1 Introduction

In the recent years although extended research on the effects of fuel properties been performed worldwide, but we find that adulteration of petroleum product especially petrol, kerosene and diesel (high speed diesel (HSD)), has become a serious problem. Skyrocketing prices of petroleum product is the only worry that the consumers are facing with the issue of purity. Even after paying a good price for them, the rampant practise of adulteration of petroleum product has overwhelmed the market. Further, it is seen that the metropolitan growth is too associated with rising number of automobiles to meet chiefly public conveyance and goods transport. Adulteration differs from contamination in that; people deliberately add cheaper products like kerosene [1]-[2] to pure petroleum products like petrol or diesel in an endeavor to lift profit margins. This in turn lowers the octane number [3] of the fuel. The price differential in the market of various petroleum products is the main driving force for this malpractice of adulteration and hence, it motivates for the illegal mixing of a cheaper fuel with a more expensive fuel. [4] [5]. The adulteration of petrol by diesel and that of diesel by kerosene is difficult to detect [6]-[12]. Further, it has been found that mixing kerosene with diesel does not lead to an increase in tailpipe emission, but contributes to air pollution indirectly. All engines are designed and manufactured to run on specified fuel. They emit substantially more pollutants if the fuel specification is changed and poorly maintained. Often, but not always the adulterated fuel lessen the life of engine components and also reduces performance of the engine. And as a result, these practices lead to losses in several areas, which include some damaging of the engines and deterioration in air quality through increased emissions. In the recent years we find that, due to the high demand and good price of petrol, it is very much prone to adulteration.

As described in chapter-3, the designed optical sensor with the embedded planar

waveguide geometry was developed using the Silicon Oxynitride (SiON)/SiO$_2$ waveguide technology and has been adapted for detecting adulterated petroleum products such as petrol, kerosene and diesel. This chapter discusses in detail an adulteration detection technique, using evanescent wave sensing principle.

4.2 Design of the waveguide sensor for adulteration applications

We consider a waveguide structure as depicted in Fig. 4.1, consisting of a guiding (core) layer of Silicon Oxynitride (SiON) [Refractive Index (R.I), $n_c=1.46$], deposited on silica-on-silicon substrate and sensing region of refractive index, n_s as a cladding and an outside medium (air) with refractive index n_a that is less than R.I of core. The dispersion equation of waveguide sensor structure is derived in chapter 3 as:

$$\alpha_1 x_1 = m\pi + Cot^{-1} \left(\frac{\cosh \gamma x_2 + \left(\frac{\gamma(C)}{\alpha_2} \right) \sinh \gamma x_2}{\alpha_1 \left(\frac{1}{\gamma(C)} - \frac{1}{\alpha_2} \right) \sinh \gamma x_2} \right) \tag{4.1}$$

$$\text{where } \gamma(C) = \sqrt{\beta^2 - k_0^2 n_s^2(C)} \tag{4.2}$$

and $n_s(C)$ is the refractive index of sensing region depending on concentration (C) of the adulterant.
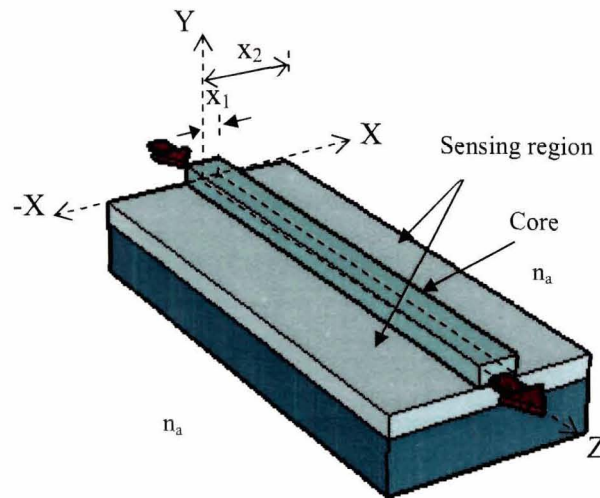

Fig-4.1: 3D view of the planar optical waveguide sensor with sensing region placed on the top of silica on silicon substrate.

The most important quantity when speaking about optical sensing is the power flow inside the different layer of the optical waveguide. The sensitivity of the sensor is dependent on the fraction of total power propagating inside the core of the waveguide. From the dispersion relation, given by Eq. (4.1) as discussed in detail in section 3.2.1 of chapter 3, the following expression for the estimation of normalized power along the z-axis of waveguide core is obtained as:

$$W(z) = W'(0)e^{-2\Gamma(C)z} \tag{4.3}$$

where $\qquad W'(0) = \left(\dfrac{0.0018}{n_s(C) - 1.3315} \right) W(0)$; $\quad W(0) = \dfrac{k^2\pi^2}{\left[\Gamma(C)^2 \right]}$

$$\Gamma(C) = \frac{4\alpha_g^4 \gamma_g^4 e^{-2\gamma_g(x_2 - x_1)}}{\beta_g^2 \delta(C)^4 \alpha_{2g}(1 + \gamma_g x_1)}, \quad \delta(C) = \sqrt{\alpha_1^2 + \gamma(C)^2} \; ;$$

$$\alpha_g = \sqrt{k_0^2 n_c^2 - \beta_g^2}, \quad \gamma_g = \sqrt{\beta_g^2 - k_0^2 n_s^2(C)}, \quad \beta_g = \sqrt{k_0^2 n_c^2 - \alpha_g^2}$$
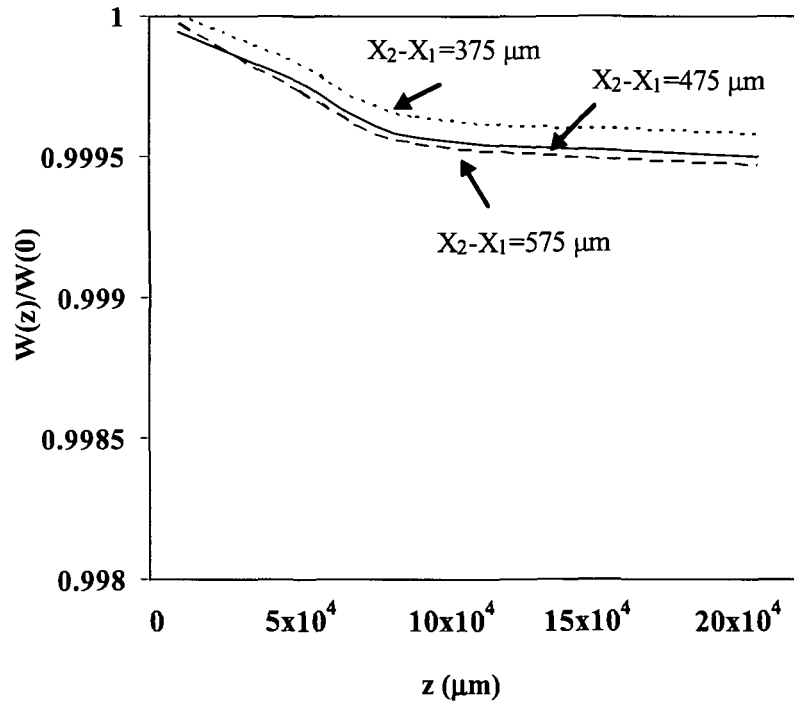
Fig-4.2: Normalized power versus length of the waveguide along z-direction for different $(x_2 - x_1) \sim 375$ μm, 475 μm and 575 μm with $n_{sub} = 1.45$ and $n_c = 1.46$ respectively.

Fig. 4.2 shows the normalized power $W(z)/W(0)$ versus z of the waveguide along the z-direction for different thicknesses of the cladding layer $(x_2-x_1)=375$ μm, 475 μm and 575 μm respectively. From the figure it is seen that $W(z)/W(0)$ decreases with increase of z and this variation saturates at z=90,000 μm for the mentioned (x_2-x_1) values. For z<90,000 μm the rate of decrease of $W(z)/W(0)$ for $x_2-x_1=475$ μm was found to be more than that for $x_2-x_1=375$ μm but for $x_2-x_1=475$ μm, it is close to that for $x_2-x_1=575$ μm. So, we have chosen $x_2-x_1=475$ μm and length of waveguide as 90,000 μm.

4.2.1 Sensitivity response

The sensitivity of the sensor is dependent on the fraction of total power propagating inside the core of the waveguide. From the dispersion relation given by Eq. (4.1), the waveguide sensitivity S_w (i.e. the rate of change of effective refractive index N with respect to refractive index n_s of the sensing medium) is obtained as:

$$S_w = \frac{\delta\left(\beta/k_0\right)}{\delta n_s(C)}$$ (4.4)

where β is the propagation constant, $k_0 = \frac{2\pi}{\lambda}$, $n_s(C)$ is the refractive index of sensing region depending on concentration (C) of the adulterant. The sensitivity of the proposed planar waveguide sensor is then analyzed for detection of adulteration in petroleum product. For detecting such petroleum adulteration, adulterated petroleum product was used as a sensing material which acted as the cladding layer of the planar waveguide sensor and was put inside the cylindrical enclosure (CE).

Fig. 4.3 shows the sensitivity of the waveguide sensor versus core refractive index $(n_c=1.45)$ with $x_2-x_1=475$ μm for different core width $(2x_1)$ of the waveguide. It is observed that sensitivity increases slightly with increase of n_c and independent of waveguide core thickness. This is because the sensing area does not increase with increase of n_c and x_1.
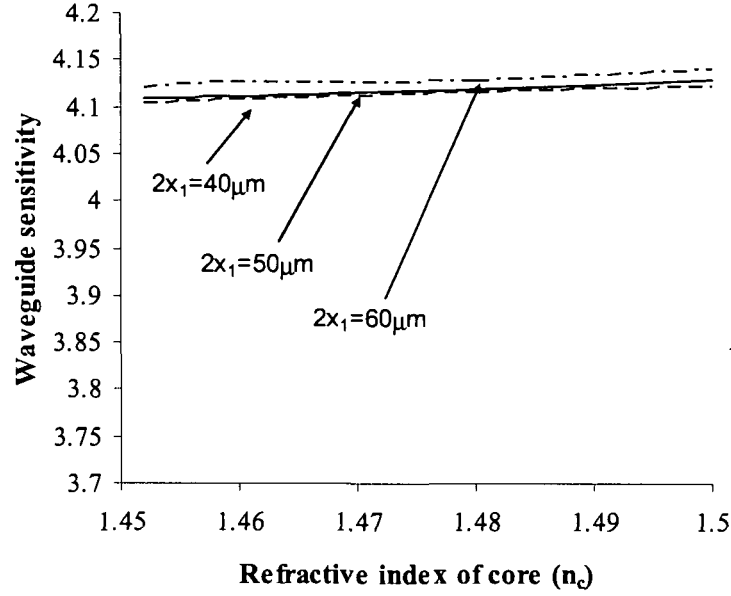
Fig-4.3: Waveguide sensitivity versus n_c of the proposed waveguide structure with different core width ($2x_1$).

4.2.2 Limit of Detection (LOD)

In the proposed waveguide sensor for adulteration detection, we find that the signal at the output of the sensor is independent of refractive index of the sensing region for $n_s \geq n_c$, as the signal will no longer be confined in the core region. So, the limit of detection (LOD) of our sensor will be restricted up to core refractive index and for our experimental setup as shown in Fig. 4.4, Limit of Detection (LOD) is, 1.333-1.46.

4.2.3 Estimation of sample volume

The sample volume of the sensor was set at 0.25 ml. This is calculated using the relation,

$$Sample\ Volume = Inside Volume\ of\ PCE - Volume\ of\ Waveguide\ Sensor \qquad (4.5)$$

where, volume of waveguide sensor = volume of waveguide core and volume for wafer and lower cladding on silicon substrate.

Thus,

$$Sample\ Volume = \pi r_{PCE}^2 L_{PCE} - W^2 L_{PCE} - W_{substrate\ width} \times L_{substrate} \times T_{substrate} \approx 0.25\ ml$$

where $T_{substrate} = 310\ \mu m$; $L_{substrate} = L_{PCE} = 90,000\ \mu m$; $W_{substrate\ width} = 1000\ \mu m$, and

---

r_{PCE} = 1000 µm; W = core area = 50 µm respectively.

4.2.4 Estimation of detection time

The total detection time of the sensor is obtained, using the relation:

$$T_{tot} = T_{refill} + T_{response}$$

and $T_{response}$= detector response time ~800 ps [13] which is very small in comparison to T_{refill}. And so, detection time $(\tau_D) \approx T_{refill}$ and is obtained as:

$$Detection\ Time\ (\tau_D) = \frac{\pi r_{PCE}^2 L_{PCE}}{v}$$

$$= \frac{0.25}{1}\ ml/mlsec^{-1} \tag{4.6}$$

$$= 0.25\ sec$$

where v= flow rate of sample ~1 ml/sec, r_{PCE} is the radius of the cylindrical enclosure and L_{PCE} is the length of the cylindrical enclosure that holds the planar waveguide sensor inside. We have seen in experimental set up that beyond this value of detection time, the experimental set up is unstable. Detection time is the sum of filling up time of sample and response time. The response time is 800 ps which is very small in comparison to filling up time of sample.

4.2.5 Material and methods

4.2.5.1 Procurement of petroleum product samples

Pure petrol, diesel and kerosene were procured from Indian Oil Corporation (IOC), Assam Oil Division (AOD), Digboi, Assam, India.

4.2.5.2 Preparation of samples

The adulteration for these samples has been made using the relation:

$$Concentration\ of\ diesel = \frac{x}{x+y} \times 100\% \tag{4.7}$$

where x =volume of diesel and y= volume of petrol.

4.2.5.3 Design parameters

Table 4.1 shows the design parameters used for the proposed planar waveguide optical sensor.

Table 4.1: Design parameters

Design parameters	Values
Length of the sensor (L)	90000 µm
Width of the sensor	1000 µm
Refractive index of core (n_c)	1.46
Length of substrate ($L_{substrate}$)	90000 µm
Radius of PCE(r_{PCE})	1000 µm
Core area (W)	50 µm
Sensing area width (x_2-x_1)	475 µm
Lower cladding	310 µm
LOD	1.333-1.46
Sample volume	0.25 ml
Sensitivity	4.1
Detection time	0.25 secs

4.3 Experimental results and Discussion

As discussed earlier in section-3.4.1 of chapter-3, the waveguide sensor structure was fabricated on thermally oxidized <100> Si wafers. The embedded SiON waveguide core of width~50 µm was deposited by plasma enhanced chemical vapour deposition (PECVD) and the refractive index was tailored by controlling different gas concentrations (SiH_4, N_2O and NH_3). The waveguide patterns are transferred by standard photolithography, developed and etched by Reactive Ion Etching (RIE) using CF_4 and O_2. The designed and fabricated waveguide sensor using SiON technology with core refractive index 1.46 was housed within a cylindrical enclosure (CE) as shown in Fig. 4.4, with efficient butt couplings between the input fiber to waveguide sensor and waveguide to output coupling fiber to reduce the fiber/waveguide coupling losses during our experimental work.
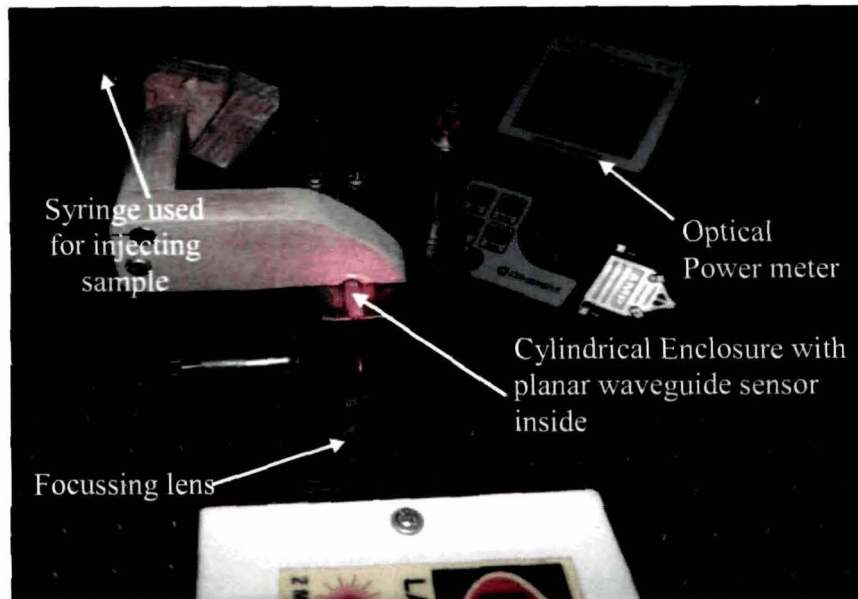
Fig-4.4: Photograph of the experimental set up for adulteration detection using planar waveguide optical sensor
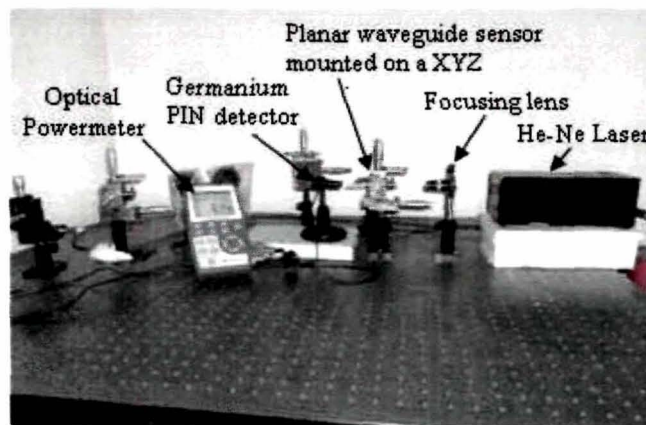
Fig-4.5: Block diagram of the experimental set up for use of the planar waveguide based sensor for adulteration detection.

In the experiment, He-Ne laser of wavelength 632.8 nm is taken as the light source. At first for validating its waveguide characteristics, we have measured the normalized power using distilled (DI) water as reference solution with the designed sensor placed inside the cylindrical enclosure (CE). Then the variation of the detected power with

change of adulterant concentration in petrol, kerosene and diesel has been measured using an optical power meter. The normalized powers $W(z)/W(0)$ for detecting the adulteration have been measured using the experimental set up as shown in Fig. 4.5, where $W(0)$ is measured with distilled water in the sensing region.
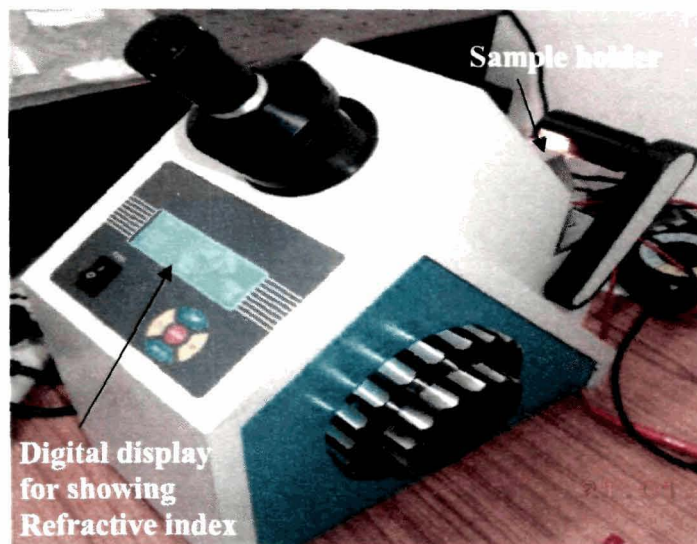

Fig-4.6: Photograph of the Abbe Refractometer (Model: CAR-02 Make: Contech) for Refractive Index Measurement

Even if there are minute variations, the variations in the normalized output power with adulteration would pursue an analogous trend. Since the sensor operates with reference to a reference sample, so by appropriately choosing the right reference adulteration is determined as the variation in the normalized output power would be due to adulteration only.

All experiments were conducted at room temperature 23^0C. The effect of temperature has also to be ascertained to make the sensor to be useful in practice. The variation of the refractive indices with adulterant (for petrol, diesel and kerosene) has also been measured by using an Abbe refractometer (as shown in Fig. 4.6). The refractive indices of petrol, kerosene and diesel as measured using an Abbe refractometer (Model: CAR-02 Make: Contech) are found to be 1.419, 1.436 and 1.461 respectively. It is very much mandatory to find whether there are variations in the refractive indices of petrol, kerosene and diesel after adulterating.

Fig. 4.7 shows the variation of refractive index (RI) versus concentration of kerosene mixed with pure petrol. It is found that the RI value increases with increasing concentration of adulterant (here kerosene is used as the adulterant). Whereas, in Fig. 4.8 we see that there is a decreasing trend of RI variation with increasing concentration of kerosene mixed with diesel. Fig. 4.9 shows the variation of RI versus increasing concentration of kerosene for both petrol and diesel.
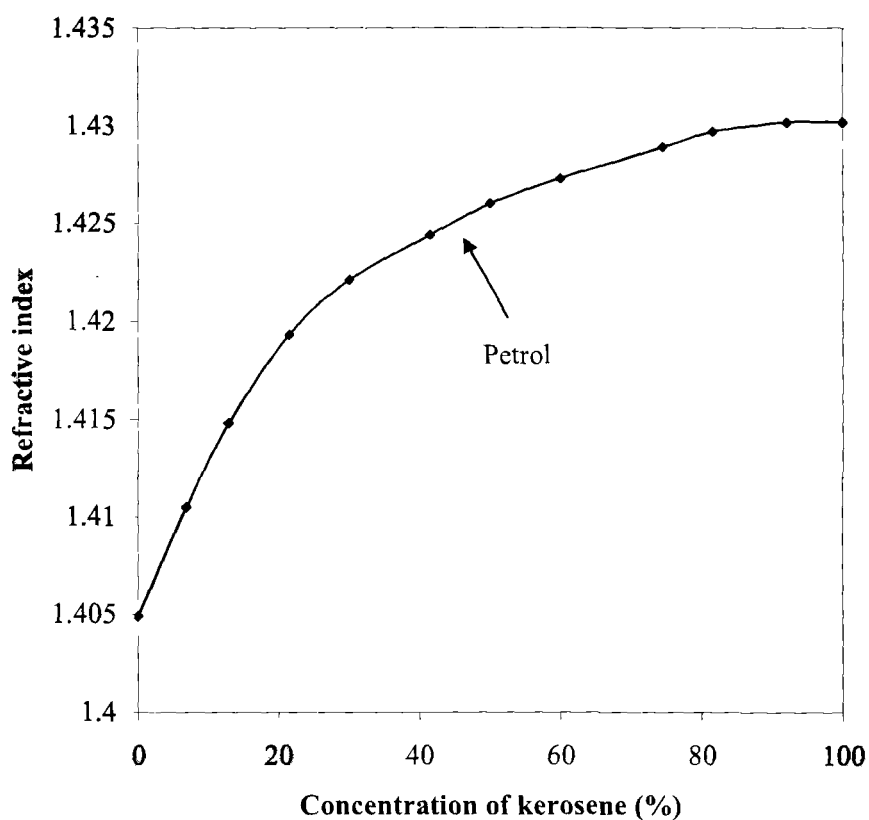

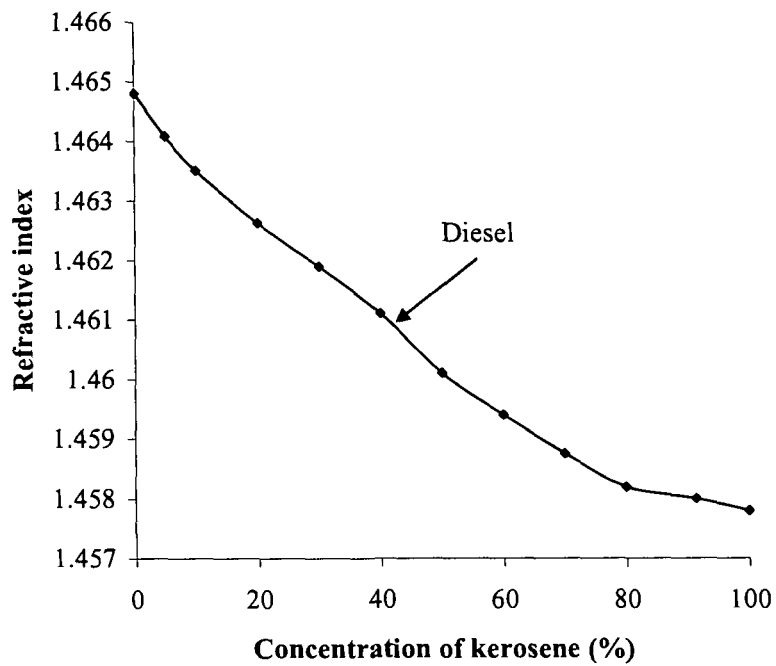Fig-4.7: Refractive index versus kerosene concentration.

Fig-4.8: Refractive index versus kerosene concentration.
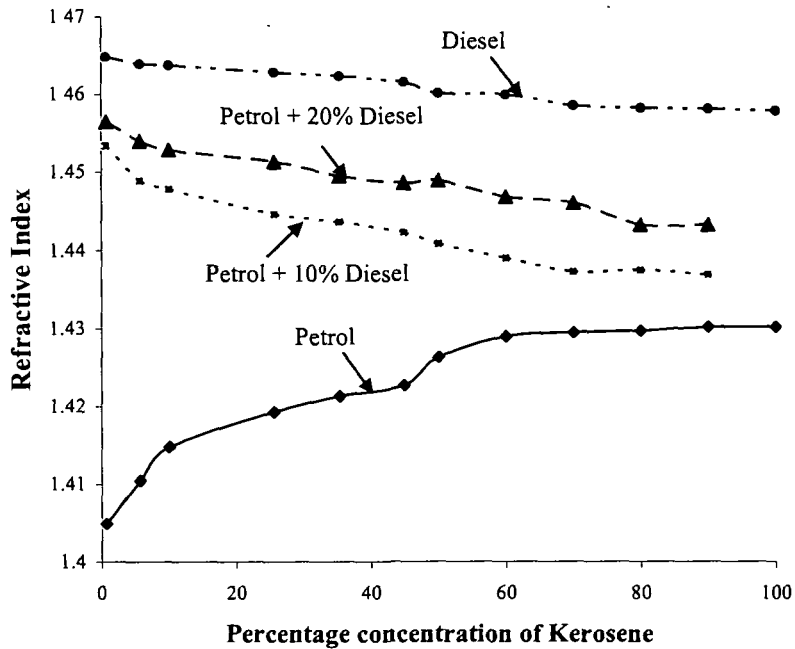
Fig-4.9: Refractive index versus kerosene concentration.

Fig. 4.10(a) shows the measured normalized power W(z)/W(0) versus measured diesel concentration for petrol with diesel, where W(0) is the incident power coupled to the sensor using experimental set up (as shown in Fig. 4.4). It is seen that the normalized power decreases with increase of diesel concentration. This is due to the fact that the refractive index (measured by Abbe refractometer) increases with increase of diesel concentration (as shown in the inset of the figure) as the number of light rays confined in waveguide sensor decreases. The similar type of behaviour is obtained in the case of W(z)/W(0) versus concentration of kerosene for kerosene mixed with petrol. The rate of of decrease of W(z)/W(0) in case of kerosene mixed with petrol is slightly more than that in case of diesel mixed with petrol.
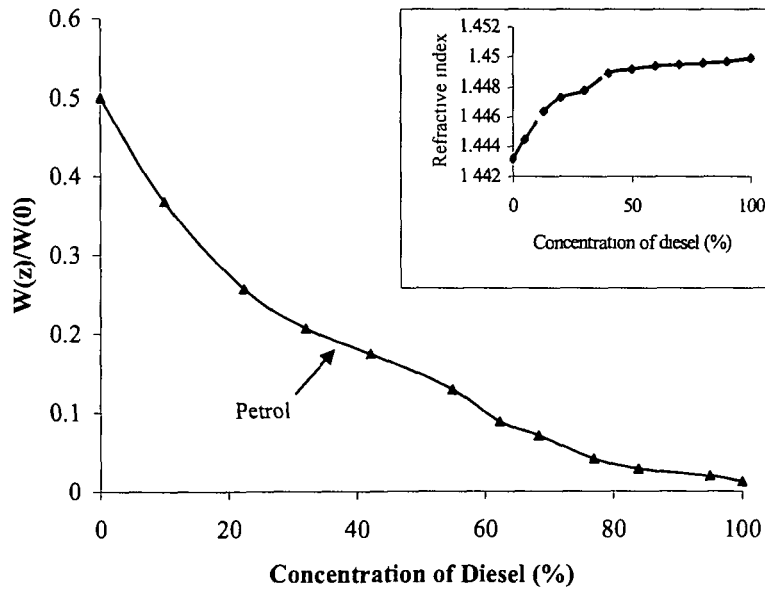
Fig-4.10(a): Normalized power versus diesel concentration.

We have also studied W(z)/w(0) versus diesel concentration for diesel mixed with petrol as shown in Fig. 4.10 (c). It is seen that the rate of decrease of W(z)/W(0) with respect to diesel concentration is slightly more than those for petrol with kerosene and petrol with diesel.
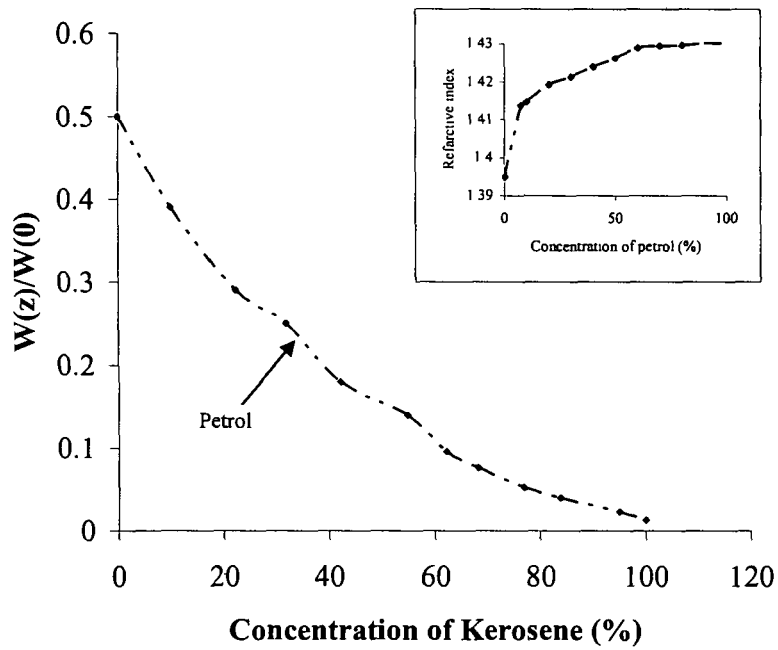
Fig-4.10(b): Normalized power versus kerosene concentration
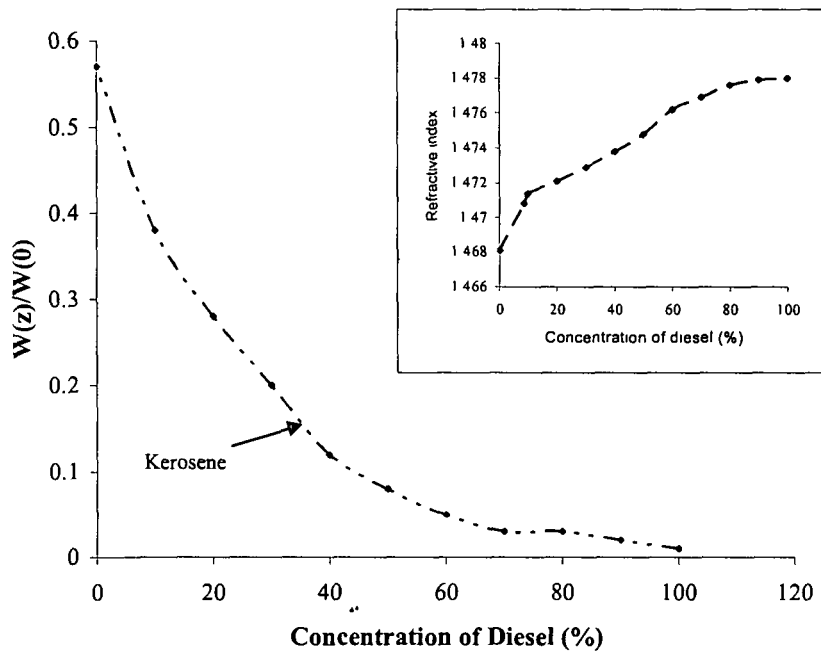
Fig-4.10 (c): Normalized power versus diesel concentration
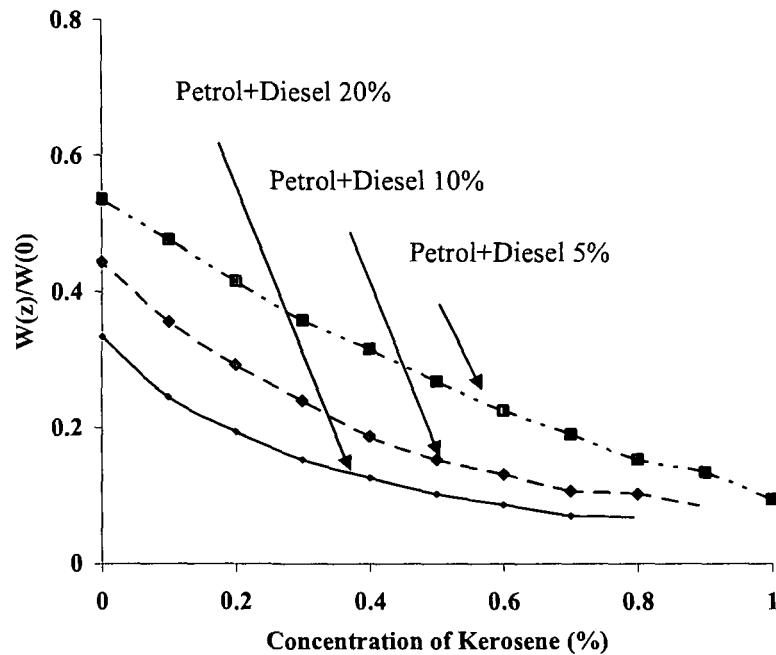
Fig-4.10(d): Normalized power versus kerosene concentration for petrol+diesel (5%), petrol+diesel (10 %) and petrol+diesel (20 %).

Fig. 4.10(d) shows the measured Normalized power (W(z)/w(0)) versus kerosene concentration for petrol+diesel (5%), petrol+diesel (10%) and petrol+diesel (20%) respectively. It is seen that the measured normalized power decreases with the increase in kerosene (used as the adulterant).

4.4 Performance comparison

Table 4.2 shows the comparison of the performance of our experimental set up with other existing experimental set ups of sensor. It is seen that in our proposed optical waveguide sensor the sample volume required for testing of adulteration of petroleum products is 0.25 ml which is 160 times less than that required for fiber optic sensor, reported by S. Roy [12]. Further, we find that the waveguide sensitivity of our planar waveguide sensor is 4.1 which is quite higher in comparison to other works because of having large sensing region of our proposed sensor. The limit of detection (LOD) of our waveguide sensor is 1.33-1.46 which is higher than the previous work [4]. Finally, it is seen that the detection time of this proposed waveguide based optical sensor is ~ 0.25.

Table 4.2: Performance comparison with other existing systems

Parameters	Previous work [4]	Previous Work [12]	Our proposed work
Sensitivity	0.14 NM/ %	-	4.1
LOD	3.57×10^{-4} RI	-	1.333-1.46
Sample volume	-	80 ml	0.25 ml
Detection time	-	-	0.25 secs

4.5 Conclusion

In this chapter, an optical waveguide sensor of length 90,000 μm and core width ~50 μm incorporating composite planar waveguide geometry (as described in Chapter-3) have been adapted for rapid detection of adulterant traces in pure petroleum products such as petrol, kerosene and diesel. The sensor sensitivity has been analyzed for detecting the adulterant traces in pure petroleum products, procured from Indian Oil Corporation Limited (IOCL), Assam Oil Division (AOD) Digboi, Assam. We find that the sensitivity of the sensor is dependent on the fraction of total power propagating inside the core of the waveguide. The waveguide sensitivity is obtained as ~4.1 which is ~40 times more than that of the existing planar waveguide sensors [14] and ~20 times more than that of asymmetric waveguide structure [15]. The technique allows spot determination of adulteration in pure petroleum products without involving the use of chemicals. Further, this approach preserves the miniature dimensions of the sensor and simplifies the instrumental design requiring only very minimal sample volume for its sensing purpose. Advantages include high sensitivity, easy fabrication and more importantly, requirement of very minimal sample volume for detecting adulteration.

4.6 List of References

1. Lawal, Y. O. Kerosene Adulteration in Nigeria: Causes and Effects, *American Journal of Social and Management Sciences* 2 (4), 371-376, 2011.
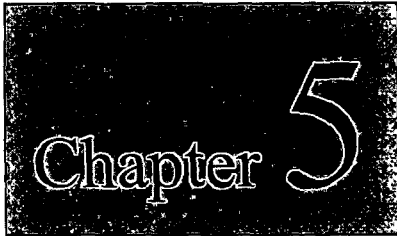
2. Osueke, C. O., & Ofondu, I. O. Fuel Adulteration in Nigeria and its Consequences, *International Journal of Mechanical & Mechatronics Engineering* **11** (4), 32-35, 2011.

3. Al-Ghoutia, M. A., et al. Determination of motor gasoline adulteration using FTIR spectroscopy and multivariate calibration, *Talanta* **76** (5), 1105-1112, 2008.

4. Mishra, V., et al. Fuel adulteration detection using long period fiber grating sensor technology, *Indian Journal of Pure & Applied Physics* **46** (2), 106-110, 2008.

5. Kardamakis, A. A., & Pasadakis, N. Autoregressive modeling of near-IR spectra and MLR to predict RON values of gasolines, *Anal. Chim. Acta* **89** (1), 158-161, 2006.

6. Bhatnagar, V.P. An ultrasonic method to find liquid fuel adulteration, *Journal of Acoust. Soc. India* **9**, 19-23, 1981.

7. Bahari, M. S., et al. Determination of the adulteration of petrol with kerosene using rapid phase titration procedure, *Analyst* **115**, 417-419, 1990.

8. Bahari, M. S., et al. Spectrophotometric End-Point for the Phase-titration Determination of the Adulteration of Petrol with Kerosene, *Analytical Proceedings.* **28**, 14-16.1991.

9. Srivastava, A., et al. Optical sensor for determining adulteration in petrol by kerosene in, International Conference On Fiber Optics and Photonics (1997), New Delhi, 989-991.

10. Sharma, R. K., & Gupta, A. K. Detection/ Estimation of Adulteration in Gasoline and Diesel using Ultrasonics in, International Conference on Industrial and Information Systems (ICIIS' 2007), Penadeniya, 509-11.

11. Yadav, S. R., et al. Estimation of petrol and diesel adulteration with kerosene and assessment of usefulness of selected automobile fuel quality test parameters, *International Journal of Environmental Science & Technology* **1** (4), 253-255, 2005.

12. Roy, S. Fiber optic sensor for determining adulteration of petrol and diesel by kerosene, *Sensors & Actuators B* **55** (2-3), 212, 1999.

13. Masini, G., et al., High-Performance p-i-n Ge on Si Photodetectors for the Near Infrared: From Model to Demonstration, *IEEE Trans. On Electr. Dev.* **48** (6), 1092-1096, 2001.

14. Passaro, V.M.N., & Dell'olio, F. Guided-wave optical biosensors, *Sensors* **7** (4), 508-536, 2007.

15. Taya, S. A., et al. Theoretical Analysis of TM nonlinear asymmetrical waveguide optical sensors, *Sensors and Actuators A: Phys.* **147** (1), 137-141, 2008.

✻ ✻ ✻ ✻ ✻

Chapter 5

Integrated Optical Waveguide Sensor with Lab-on-a-Chip Device Platform for Detecting Glucose Concentration in Blood Plasma

Outline of the Chapter:

5.1 Introduction

In the recent years, the assessment of accurate glucose level variation in fluid samples like blood plasma is a major challenge in the field of clinical diagnostics. We see that conventional way of measuring glucose level however, at present causes delays between sampling and analysis by analyzing samples at a clinical laboratory. Addressing to this matter, in this chapter we have developed a new miniaturized technique for detection of glucose concentration in blood plasma using Poiseuille's equation of viscous flow and light propagation through the optical waveguide. The technique is safe and capable of providing accurate result in terms of enhanced sensitivity. It is found that although tremendous investigation has been expanded in the development of wide range of accurate optical sensors in numerous applications including bio-sensing [1][2] and chemical detection [3], there is an immense need for an accurate sensor with fast detection which can provide patients with highly useful information of glucose concentration throughout the day. In spite, of the fact that researchers have demonstrated many techniques for glucose level detection using tools such as auto analyzer based on centrifuge system [4] and homecare glucose meter [5] but it is seen that the glucose meters vary in accuracy depending on multiple factors including patient's technique in trying and finger cleanliness, and the chemistry and cross-reactivity with interfering substances. When selecting the optimal glucose meter, not only much aspects from the patient's lifestyle and other health treatment be taken into account, but also the glucose meter systems must also be assessed in detail to ensure the minimum risk of interference [6]. Further, auto analyzer entail more time (order of few minutes) [4]. This chapter explores that the integration of an optical planar waveguide based sensor platform with LOC promises enhanced functionality and

performance such as high sensitivity, compactness and lower manufacturing expenses by the realization of such structures with silicon based material systems.

5.2 Sensing Concept and Design

In the proposed design of detecting glucose concentration, the blood samples were obtained from the eye-vein of rat and collected in the heparanized tube which acts as the reservoir and then it is pushed into the LOC using a syringe pump. Fig. 5.1 illustrates the proposed concept of rapid diabetes detection technique using optical waveguide sensor housed in a Plastic Cylindrical Enclosure (PCE). Using microfluidic LOC device the separated plasma from alloxan-induced diabetic rat blood is incorporated into the PCE through an interfacing tube between LOC and PCE. The LOC is installed within a fluidic network that includes interfacing capillary tube connected between LOC and optical waveguide sensor.
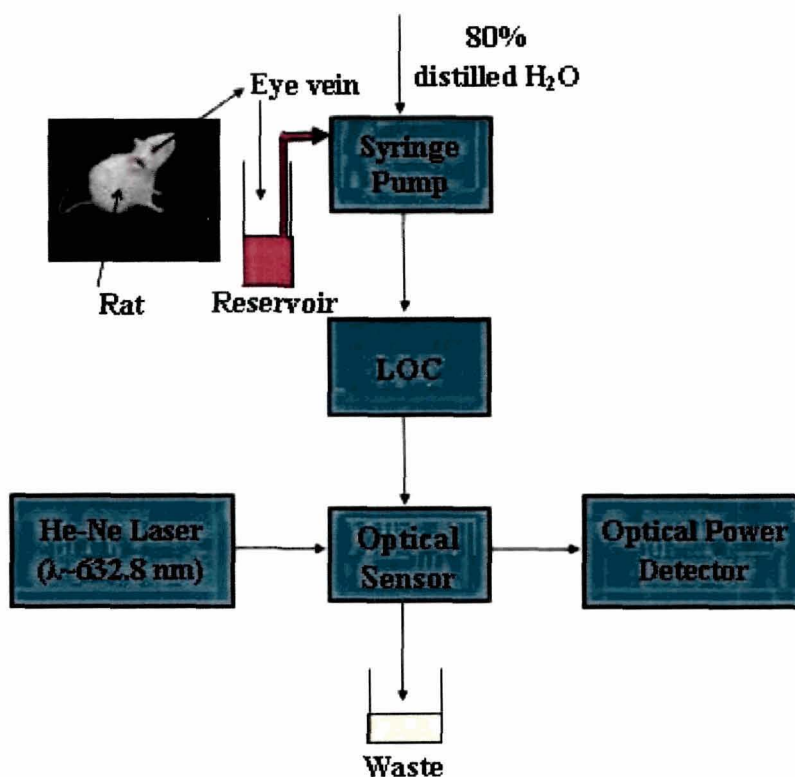
Fig-5.1: Block diagram showing the proposed concept of rapid diabetes detection using optical waveguide sensor.

In this technique, on-chip plasma separation is targeted to replace the classical bench top centrifugation. Fig. 5.2 shows the complete photograph of the experimental arrangement with LOC mounted on the specially developed optical set up along with micrometer adjustment for alignments.
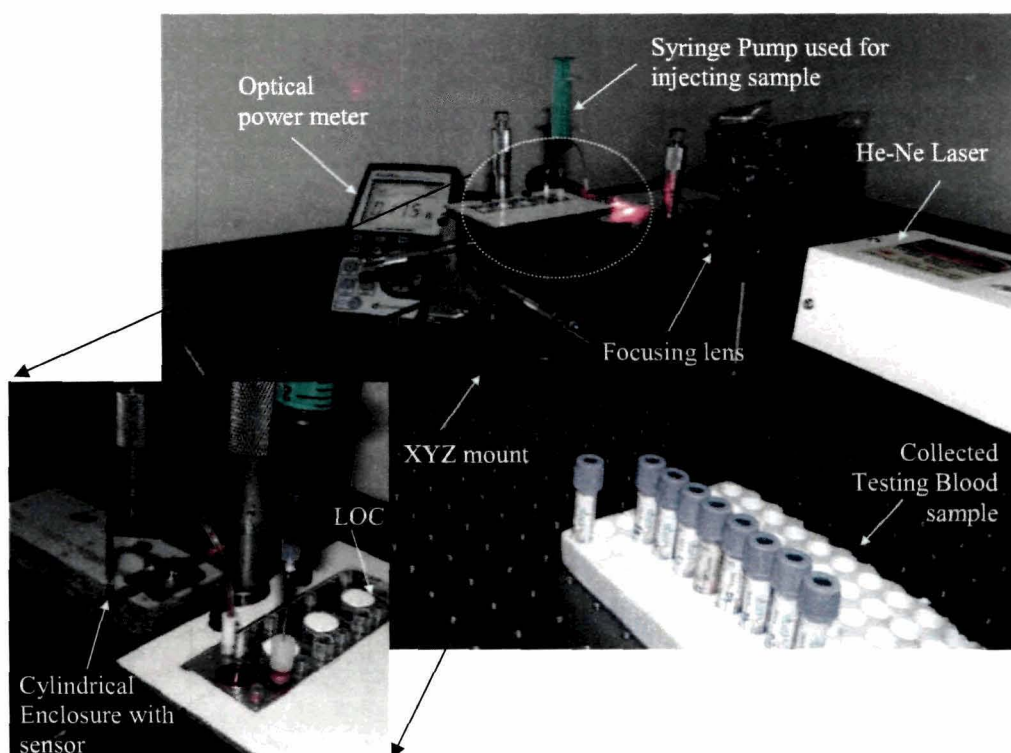
Fig-5.2: Photograph of the experimental set up.

5.2.1 Lab-on-a-Chip

The two main factors that take part in the choice of detection method for a lab-on-a-chip (LOC) application are sensitivity and scalability to smaller dimensions, especially with the increasing demands placed on sensors/detectors as volumes decrease. LOC is a commercially available microfluidic chip (*Product code: 15-1503-0168-02, microfluidic ChipShop GmbH, Stockholmer Str.20D-07747 Jena, Germany, dated: 05-03-2013*) of size 75.5 mm x 25.5 mm x 1.5 mm). It consists of chamber volume of 25 µl, a luer interface for blood loading, a support channel with a cross section of 300 µm x 100 µm for the transfer of the blood on top of a separation membrane [7]. An integrated

plasma/serum generation chip for development of a sensor system is shown Fig 5.3 (a). Whereas, Fig. 5.3 (b) shows the close-up of one plasma/serum generation unit.
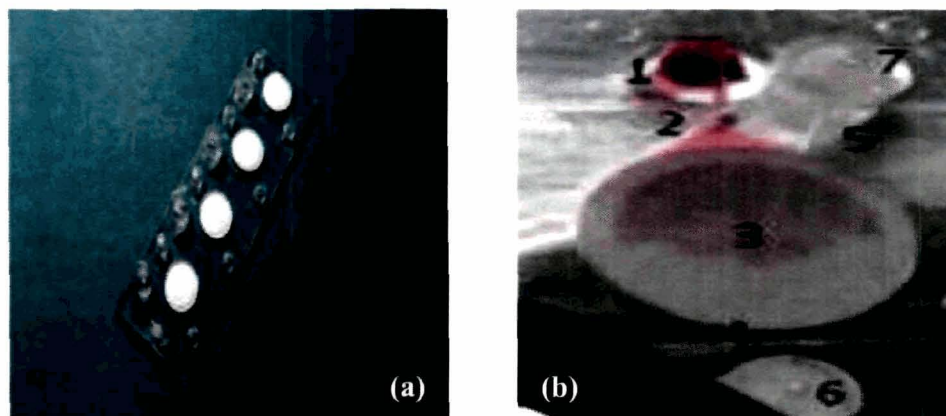
Fig-5.3: **(a)** Integrated plasma/serum generation chip for development of sensor system. (*Product code: 15-1503-0168-02, microfluidic ChipShop GmbH, StockholmerStr.20D-07747 Jena, Germany)* and **(b)** Close-up of one plasma/serum generation unit

5.2.2 Design of sensor with interfacing capillary tube
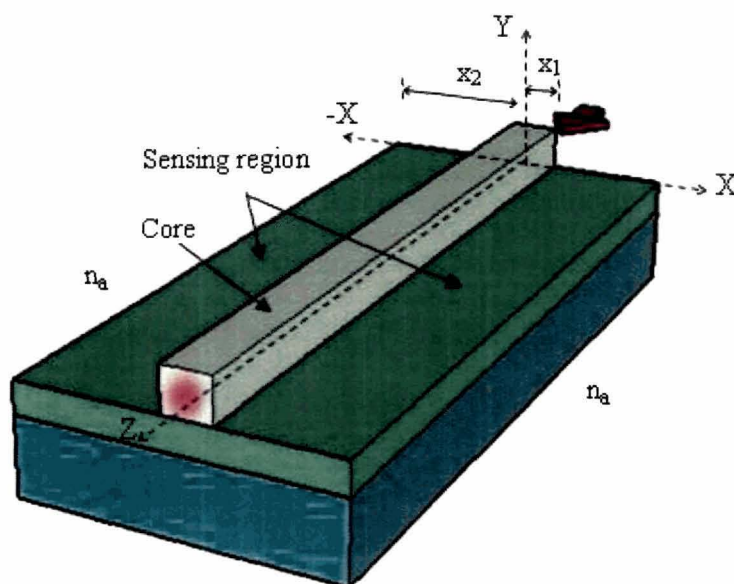
Fig-5.4: Schematic of the planar waveguide sensor structure

For the design of the sensor, an optical planar waveguide sensor structure is considered as depicted in Fig. 5.4. As discussed earlier in chapter 3, the structure consists of a guiding (core) layer of Silicon Oxynitride (SiON) [Refractive Index (R.I), $n_c=1.46$]. This is deposited on silica-on-silicon substrate and sensing region of refractive index, n_s as a cladding and an outside medium (air) with refractive index n_a that is less than R.I of core. As observed earlier in chapter-3 and chapter-4 respectively, the change of the refractive index of the sensing layer results in the change in effective refractive index of the modes propagating in the planar waveguide sensor structure. Based on the Simple Effective Index Method (SEIM) [8], as discussed in detail in section chapter-2, and using the boundary conditions for Transverse Electric (TE) modes, the fractional power $W(z)$ that remains inside the core along z-axis is obtained as [9],

$$W(z) = W'(0)e^{-2\Gamma z} \tag{5.1}$$

where $W'(0) = \left(\dfrac{0.0018}{n_s - 1.3315}\right)W(0)$, $W(0) = \dfrac{k^2\pi^2}{\Gamma^2}$, $k = \dfrac{2\pi}{\chi}$ and Γ is a function of waveguide

parameters and λ = wavelength. The normalized power $W(z)/W(0)$ versus length of the waveguide (z) is shown in Fig. 5.5. Although the design is being done for different cladding layer thickness $(x_2-x_1)\sim850$ μm, 950 μm and 1050 μm, it is seen that, $W(z)/W(0)$ decreases with increase of z and becomes almost constant for $z>50,000$ μm. Further, we find that the variation of $W(z)/W(0)$ for $(x_2-x_1)=950$ μm is almost close to that for $(x_2-x_1)=1050$ μm. So we have chosen (x_2-x_1) =950 μm and z= 50,000 μm respectively.

In this technique the accurate length of the optical waveguide sensor and designing of the interfacing tube is an essential part because we need to maintain the input pressure that generates inside the interfacing capillary tube for flowing of the blood plasma and filling up of the PCE which is illustrated in the next section. The blood plasma which gets collected in the PCE (via the interfacing tube) acts as the sensing layer (or, cladding layer) of the optical waveguide sensor for detection of plasma glucose level.
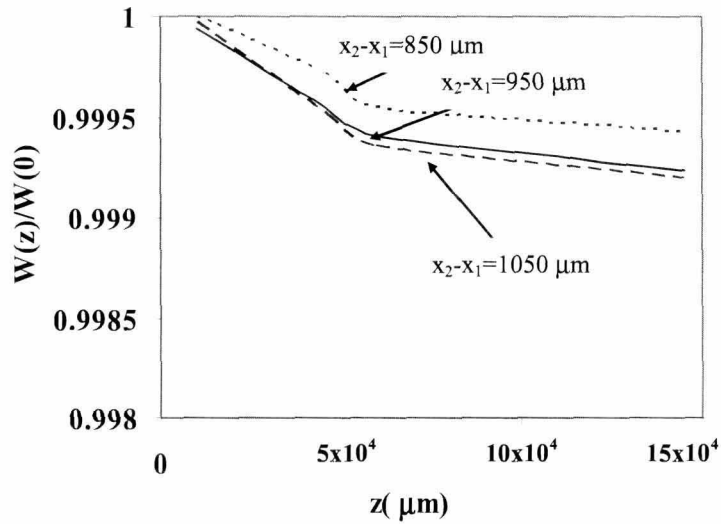
Fig-5.5: Normalized power versus length of the wave guide along z direction for different $(x_2\text{-}x_1) \sim 850$ μm, 950 μm and 1050 μm with $n_{sub}=1.45$, $n_s=1.329$ and $n_c=1.46$ respectively.

Fig. 5.6 shows the capillary interfacing tube of length $L_{interface}$ connected with LOC and PCE. The blood plasma is flowing through the tube under a constant pressure with the principle of *Newton's law of viscous flow*, following the Poiseuille's equation.
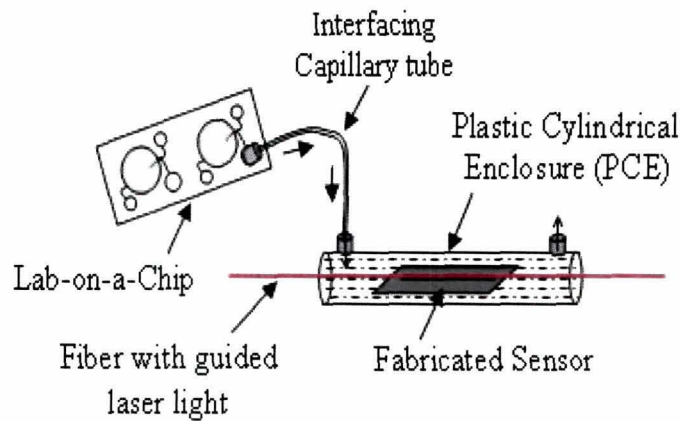
Fig-5.6: Schematic diagram of the capillary interfacing tube connected with LOC.

The input pressure P_{in} required to inject the blood into LOC is determined as $P_{in} \sim 25000$ Pa, for maintaining the velocity (v) of blood plasma flowing at all points inside LOC to be 2×10^{-6} liter/sec as specified by microfluidic ChipShop [7].

For designing the interfacing tube, at first we have taken the viscosity ($\sim 3.35 \times 10^{-3}$ Pa.s) of human blood, as the viscosity of blood plasma of human is almost constant with glucose level (90 mg/dl- 400 mg/dl). We have also measured viscosity of blood plasma of rat having glucose level varied from 90 mg/dl to 400 mg/dl by using a conventional viscometer (Viscometer labtech, LT 730) and plotted which confirms almost constant variation with glucose level as shown in Fig. 5.7. It is found that viscosity of human blood plasma is three times more than that of rat blood and therefore difficult to separate the plasma effectively from pure blood of rat [10]. We have mixed 80% distilled water with pure blood of rat to make the viscosity of blood of rat equivalent to that of human blood.
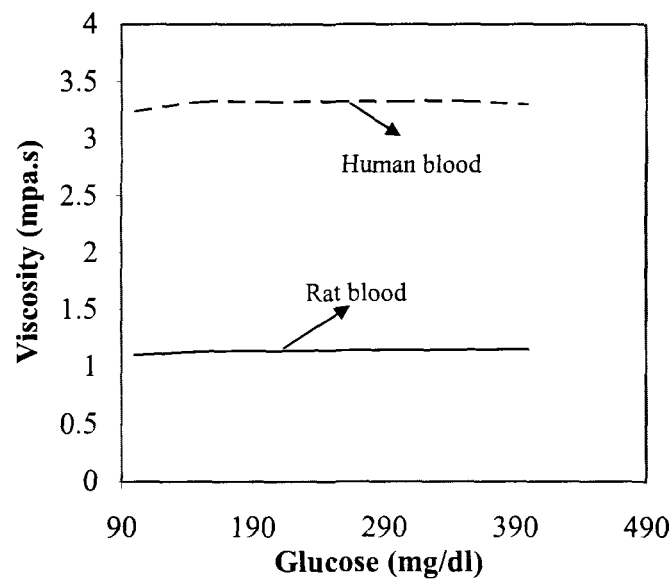
Fig-5.7: Viscosity versus glucose level for blood of rat and human blood as measured by a conventional viscometer.

For determining the pressure on LOC (P_{Lab}) and sensor input pressure ($P_{inputsensor}$), we assume a cylindrical layer of liquid of radius x, flowing through a capillary tube of

radius r, the velocity of flow at all points on this cylindrical layer is taken to be same. The schematic of the plasma flowing inside the interfacing capillary tube of length $L_{interface}$ is shown in Fig. 5.8 (a).The velocity distribution profile is shown in Fig. 5.8 (b).

Parabolic velocity profile

(a)

$$\frac{dv}{dx} = 0$$

(b)
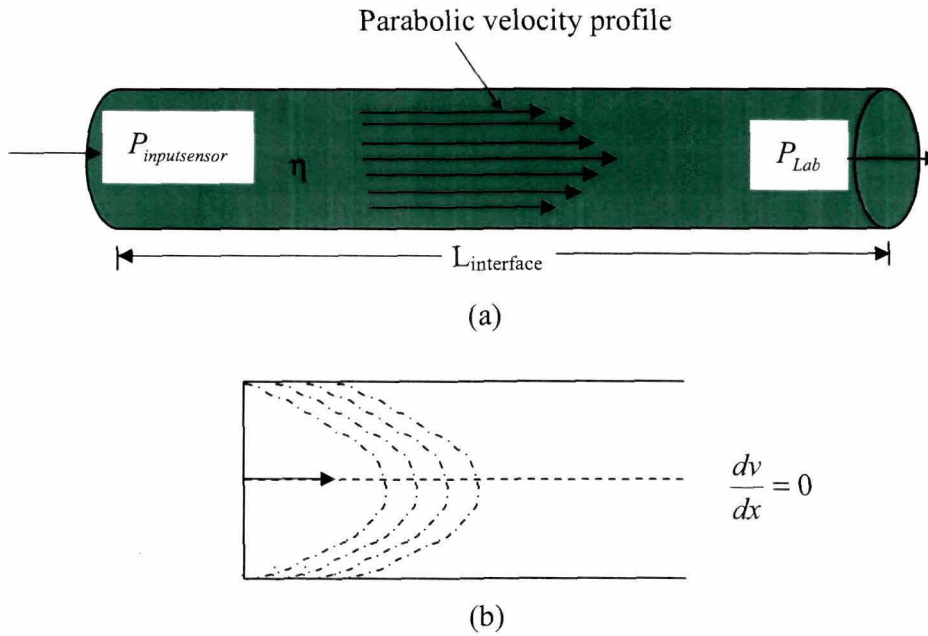
Fig-5.8:(a) Schematic of the plasma fluid flow inside the interfacing capillary tube of length $L_{interface}$ and (b) Velocity distribution curve.

If v is the velocity, as the velocity of the layers in contact with the walls of the tube is zero and goes on increasing towards the axis, it is obvious that the liquid inside the imaginary cylinder is moving faster than outside it and the backward tangential force due to the outer slower, moving liquid on the inner faster moving liquid is in accordance with the relation I, given by

$$\eta . 2\pi x . L_{int\ erface} \cdot \frac{dv}{dx} \tag{5.2}$$

where η is the coefficient of viscosity of the liquid, surface area (A) of the cylindrical shell of radius x is equal to $2\pi x.l$, $L_{interface}$ is the length of the capillary tube interfacing with the sensor and dv/dx is the velocity gradient, as shown in Fig. 5.8 (b). We consider

the pressure difference at the two ends of the capillary tube be $P_{input\,sensor}$ and P_{lab}. Then the forward force on the cylindrical shell in the direction of flow is:

$$\left(P_{input\,sensor} - P_{lab}\right) \times \pi x^2$$

This tends to accelerate the motion of the liquid. Therefore, if the motion of the liquid is steady, following Poisseule Equation [11] we obtain:

$$\eta.2\pi x.L_{int\,erface}\frac{dv}{dx} = -\left(P_{input\,sensor} - P_{lab}\right) \times \pi x^2$$

The negative sign indicates that the two forces are in opposite direction. On integrating for v, we obtain:

$$v = \frac{-\left(P_{input\,sensor} - P_{lab}\right)x^2 + C_1}{4\eta l} \tag{5.3}$$

where C_1 is a constant of integration.

Now when v=0, x=r because the layer in contact with the sides of the tube are stationary.

$$\text{Therefore, } C_1 = \frac{\left(P_{input\,sensor} - P_{lab}\right)r^2 + C_1}{4\eta L_{int\,erface}} \tag{5.4}$$

$$\text{Hence, } v = \frac{\left(P_{input\,sensor} - P_{lab}\right)\left(r^2 - x^2\right)}{4\eta L_{int\,erface}} \tag{5.5}$$

This is the velocity of flow of the liquid at a distance x from the axis of the tube.

$$\text{Volume of the interfacing capillary tube is} = \pi r_{int\,erface}^2 L_{int\,erface} v \tag{5.6}$$

where $r_{interface}$ is the radius of the capillary tube to be fitted with outlet of LOC. In order to determine the pressure on LOC (P_{Lab}) and Sensor input pressure ($P_{inputsensor}$), we assume another co-axial cylindrical shell of the liquid, of radius $(x+dx)$. The cross sectional area between the two shells is $2\pi x dx$. Since, v is the velocity of flow of the liquid in between the two shells, the volume of the liquid flowing per second through the cross sectional area is $dv = 2\pi x.dx.v$. If we imagine the whole of the tube to be made of such like cylindrical shells, the volume v of liquid flowing through the capillary tube in unit time is obtained by integrating Eq. (5.5) for v between x=0 and x=r and is obtained as:

$$v = \int_0^r 2\pi x . dx . v = \pi \frac{\left(P_{input\,sensor} - P_{lab}\right)r^4}{8\eta L_{int\,erface}} \tag{5.7}$$

$$\text{Or, } \left(P_{input\,sensor} - P_{lab}\right) = \frac{8\eta v L_{int\,erface}}{\pi r^4} \tag{5.8}$$

Therefore, the input pressure of the sensor generated by the interfacing capillary tube with perpendicular radii of curvature r is calculated with the Poiseuille's equation and is obtained as:

$$P_{input\,sensor} = P_{Lab} + \frac{8\eta v L_{int\,erface}}{\pi r^4_{int\,erface}} \tag{5.9}$$

Now following Hagen-Poiseuille law [11] which states, the flow rate is proportional to the pressure difference $\left(\Delta P = P_{inputsensor} - P_{Lab}\right)$ between the ends of the capillary tube and the fourth power of its chip radius, r_{chip} we find,

$$P_{Lab} = P_{in} - \frac{8\eta v L_{chip}}{\pi r^4_{chip}} \tag{5.10}$$

But P_{in} is the input pressure required to inject the fluid into the LOC ~250 mbar as specified by Microfluidic chipShopp [7], η is the coefficient of viscosity, $L_{interface}$ is the length of the interfacing capillary tube, L_{chip}, length of channel carrying blood plasma in chip, r_{chip} is the radius of chip. The velocity (V) of plasma flow in microfluidic chip is 2×10^{-9} m^3/sec.

Now, volume of channel carrying blood plasma in chip is $= \pi r^2_{chip} L_{chip} . v$ (5.11)
For evaluating $L_{interface}$, it follows from Eq. (5.6) and Eq. (5.11), that the length of the interfacing capillary tube can be expressed as:

$$L_{int\,erface} = \frac{r^2_{chip}}{r^2_{int\,erface}} L_{chip} \tag{5.12}$$

For r_{chip} = 0.26 mm, $r_{interface}$ = 0.075 mm and L_{chip} = 9 mm, from Eq. (5.12), the length of the capillary tube that interfaces with LOC is obtained as, $L_{interface}$ =115 mm to maintain the flow rate as same as that in the channel of LOC. Further, substituting in Eq. (5.10) for η=0.00035 Pa.s; v=2 x 10^{-9} m^3/sec, the pressure on the Lab-on-a-chip is obtained as, P_{Lab}=24999.916 Pa. From Eq. (5.9), substituting for $r_{interface}$=0.075 mm to be fitted with outlet of LOC. We get the input pressure that is maintained inside the capillary tube to

cause the blood plasma flow into PCE is derived using Poiselle's equation and obtained as:

$$P_{inputsensor} = P_{Lab} + \frac{8\eta v L_{int\,erface}}{\pi r^4_{int\,erface}} \sim 25001.71362\,\text{Pa} \qquad (5.13)$$

For evaluating the length of the PCE, it follows from Eq. (5.6) that the volume (v) of liquid flowing through the capillary tube in unit time is obtained by integrating Eq. (5.7) for v and obtained as:

$$v = \pi \frac{\left(P_{input\,sensor} - P_{lab}\right)r^4}{8\eta L_{int\,erface}} \qquad (5.14)$$

Now if r_{sensor} is the radius of PCE (that holds the waveguide sensor inside) and P_{atm} is the atmospheric pressure we get:

$$\frac{\pi\left(P_{inputsensor} - P_{Lab}\right)r^4_{sensor}}{8\eta L_{int\,erface}} = \frac{\pi\left(P_{inputsensor} + P_{atmos}\right)r^4_{int\,erface}}{8\eta l_2} \qquad (5.15)$$

Here, r_{sensor} the radius of PCE is designed for $\sim 1000 \times 10^{-6}$ m by considering waveguide propagation characteristics which is discussed later. Atmospheric pressure (P_{atm}) is negligible, as a result from the above expression (5.15), the length of the plastic cylindrical enclosure (PCE) is obtained as,

$$l_2 = \frac{L_{int\,erface}\left(P_{inputsensor} + P_{atmos}\right)r^4_{int\,erface}}{\left(P_{inputsensor} - P_{Lab}\right)r^4_{sensor}} \sim 50000\,\mu m \qquad (5.16)$$

5.2.3 Sensitivity

As we see that for sensor performance, sensitivity is an important factor for determining the actual accuracy of the sensing system. As described in detail in chapter 3, the condition for maximum sensitivity to changes in the cover/sensing(cladding) layer also known as the waveguide sensitivity S_w (i.e. the rate of change of effective refractive index N with respect to refractive index n_s of the sensing medium) is expressed as,

$$S_w = \frac{\delta\left(\beta/k_0\right)}{\delta n_s} \qquad (5.17)$$

where, β/k_0=effective refractive index and n_s is the sensing region refractive index.

Fig. 5.9 shows the waveguide sensitivity versus core refractive index (n_c) with n_s=1.45 and x_2-x_1=950 μm for proposed waveguide structure (solid line) and previous works [18] (dotted line). It is found that the waveguide sensitivity of the proposed structure is almost independent with core RI. The high waveguide sensitivity of the ~ 4.1 compared to the earlier reported is ~40 times more than that of the previous works as reported by previous authors [18].
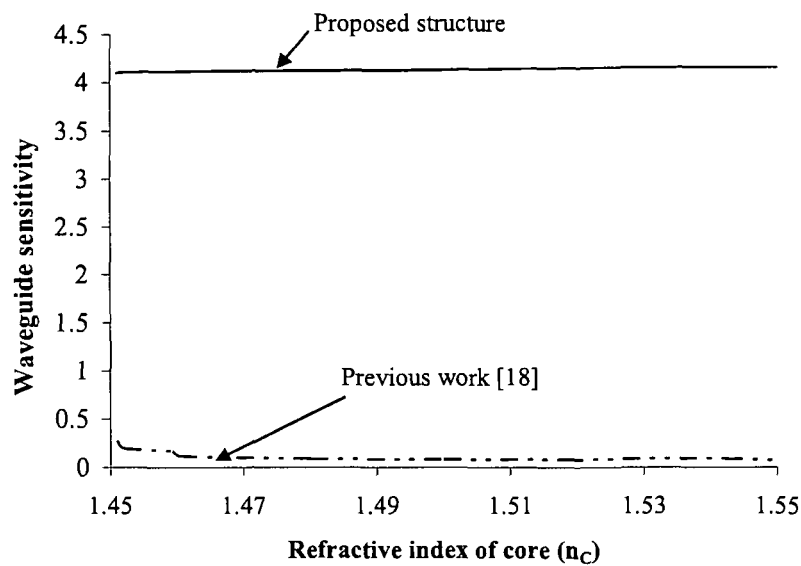
Fig- 5.9: Waveguide sensitivity versus n_c with n_s=1.45 and x_2-x_1=950 μm for proposed waveguide structure (solid line) and previous works [18] (dotted line).

5.2.4 Limit of Detection (LOD)

Sensitivity is related to the limit of detection (LOD), which is defined as the minimum amount of concentration or mass of the biochemical substance that can be detected by the sensor over the background signal. Limit of detection depends on the resolution of the sensor. In the proposed technique of glucose level detection, we see that the measured values of the normalized power (W(z)/W(0)) versus glucose level for three group of rats A_1, A_2 and A_3 (having almost same body weight) as discussed in section 5.5.1 are in good agreement with the theoretical result. It is seen that the signal at the output of the sensor is independent of RI of the SR for $n_s \geq n_c$, as the signal will no

longer be confined in the core region. So, the limit of detection (LOD) of our sensor will be restricted up to core RI and for our experimental setup as shown in Fig. 5.3, Limit of Detection (LOD) is 1.333-1.46 which is found to be more than the earlier reported works [12].

5.2.5 Estimation of detection time

The detection time (τ_D) is an important parameter for detecting the concentration of glucose in blood plasma. In the proposed technique τ_D comprises of separation time, t_{sep}, propagation time, t_p, refilling time, t_r, and the time required by the detector to give the response. As such, τ_D can be written as:

$$\tau_D = \text{Separation time } (t_{sep}) + \text{Propagation time } (t_p)$$

$$+ \text{Refilling time } (t_r) + \text{Detector response } (t_{response}^d) \tag{5.18}$$

where, $t_{sep} = 20 \sec$ [7] and

$$t_p = \frac{channel\ length}{velocity\ of\ plasma\ in\ channel} \tag{5.19}$$

Also we find that the rate of flow of plasma in channel depends upon the radius of the chip (r_{chip}) and the velocity (V) of plasma flow. Therefore, we may put this as:

$$\text{Velocity of plasma in channel is} = \frac{V}{\pi\ r_{chip}^2}$$

$$= \frac{2 \times 10^{-9}\ m^3 / \sec}{(0.26)^2 \times 3.14 \times 10^{-6}}$$

$$= 9.421\ mm/sec \tag{5.20}$$

After substitution of (5.20) in (5.19), t_p is found to be ~ 0.95 seconds.
Thus,

$$\text{Refilling time, } t_r = \frac{\pi r_2^{PCE}\ l}{V}$$

$$= \frac{3.14 \times (250 \times 10^{-6})^2 \times 5 \times 10^{-2}}{2 \times 10^{-9}}$$

$$= 4.2\ sec$$

And $\left(t^{d}_{response}\right)$ is very much negligible ~ 800 ps [12].

Therefore, the total time required by the sensor for its detection is found to be ~25.85 seconds.

5.2.6 Estimation of sample volume

The sample volume of the sensor was set at 0.141 ml. Its volume is calculated using the relation,

Sample volume = Inside volume of PCE – Volume of waveguide sensor

where volume of waveguide sensor = volume of waveguide core and volume for wafer and lower cladding on silicon substrate. Hence,

$$\text{Sample volume} \approx \pi r^{2}_{PCE} L_{PCE} - W^{2} L_{PCE} - W_{substrate\ width} \times L_{substrate} \times T_{substrate} \quad (5.21)$$

where $T_{substrate}$ = 310 μm [300 μm (Si) + 10 μm (SiO_2)]

$L_{substrate} = L_{PCE}$ = 50, 000 μm

$W_{substrate\ width}$ = 1000 μm

r_{PCE} = 1000 μm

W = core area = 50 μm (since x_1 = 25 μm, therefore $2x_1$ = 50 μm)

Substituting these values in Eq. (5.21), we get

Sample volume = 141.375 x 10^{-9} x 10^{3} liter

= 0.000141375 liter

= 0.141 ml

In the proposed sensor, we find that the simplicity of its construction and the high precision of this planar waveguide optical glucose sensor make it an alternative to previously reported commercially available glucose sensors. Especially the sample volume of 0.141 ml and the 25.85 sec measurement time are the highest specifications for its sensing purpose compared to the currently available glucose sensors. Table 5.1 shows the design parameters for integrating the waveguide sensor with LOC.

Table 5.1: Design parameters used for the proposed planar waveguide optical sensor

Design parameters	Values
L_{sensor}	50000 μm
Core width (2x$_1$)	50 μm
Cladding width (x$_2$-x$_1$)	950 μm
Substrate refractive index (n$_{sub}$)	1.45
Sensing region refractive index (n$_s$)	1.329
Refractive index of core (n$_c$)	1.46
Viscosity (η)	0.00035 Pa.s
P_{in}	250 mbar
V	2×10^{-9} m^3/sec
r_{chip}	260 μm
$r_{interface}$	75 μm
L_{chip}	9000 μm
P_{Lab}	24999.916 Pa
$P_{inputsensor}$	25001.71362 Pa
r_{sensor}	1000 μm

5.3 Fabrication of waveguide sensor

Although different technologies are being employed for producing integrated optic waveguide-based sensors which depend on the application but application of SiON has been mainly motivated by its excellent optical properties, such as low absorption losses in the visible and near infrared wavelength range as mentioned in chapter-2. The sensor planar waveguide of length 50,000 μm was fabricated using SiON as the waveguide core material. Fig. 5.10 shows the SEM image of the waveguide sensor. The fabrication process is described in detail in chapter 3. The embedded SiON waveguide core of width 50 μm has been deposited by plasma enhanced chemical vapor deposition and the RI has been tailored by controlling different gas concentrations (SiH$_4$, N$_2$O, and NH$_3$).

Patterns are transferred by standard photolithography and have been developed and etched by RIE using CF_4 and O_2.

Fig-5.10: SEM image of the waveguide sensor

5.4   Experiment for the diabetic study

5.4.1   Preparation of the rat model

Adult both male and female Wistar rats 5-6 months, weighing 200-250 gm were housed in groups of six with ad libitum access to food and water. Animals were maintained in a temperature-controlled room with 12 hour alternating light and dark cycles. Experiments were performed during the light period of the cycle and were conducted in accordance with the "Principles of Laboratory Animal care" (National Institute of Health, USA publication 85-23, revised 1985) and were approved by institutional animal ethical committee.

5.4.1.1 Induction of Experimental Diabetes

Total 36 rats were fasted for 72 hours before drug administration. The next morning animals were anesthetized with Phenobarbital sodium at a dose level of 40 mg/kg body weight before injecting alloxan monohydrate. A single intraperitoneal injection of alloxan in fixed dose in freshly prepared 10×10^{-3} mol/l sodium citrate [13], (pH 4.5) was delivered through the eye to induce diabetes.

5.4.1.2 Fixation of doses for induction of diabetes

Different timing and doses of Alloxan administration were made to develop an efficacious drug dosage. Fig. 5.11(a) and Fig. 5.11(b) show the chemical structure and IUPAC nomenclature of Alloxan. Specifically, different doses (60 mg/kg, 90 mg/kg, and 110 mg/kg) had different effects on diabetes. In the proposed experiment for diabetic study, rats were routinely treated daily (Monday through Friday).
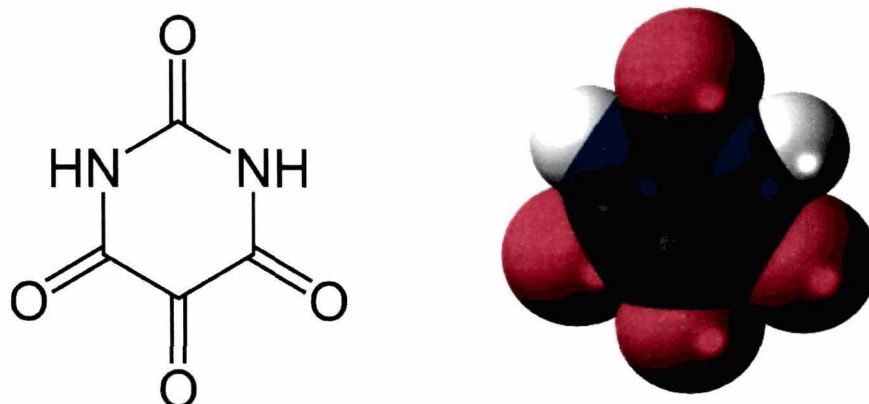
Fig-5.11: (a) Chemical structure of Alloxan and **(b)** IUPAC nomenclature.

5.4.2 Assessment of Diabetes and Hyperglycemia

Rats were considered diabetic and included in the study if they had plasma glucose levels >170 mg/dl [14]. After confirmation of the development of diabetes by measuring the fasting plasma glucose concentration, the animals were returned to their home cages. In addition, the fasting plasma glucose concentration was determined after 72 hours to confirm that hyperglycemia was maintained during this period. The plasma glucose level was estimated for every 3rd day, 5th day, 8th and 11th day. The plasma glucose estimation was also done orally in the pathological laboratory (Tezpur University Health Centre). The development of diabetes was verified with results obtained by the state of the art device used in the Tezpur University Centre, the Siemens Dimension ® clinical chemistry system.

5.5   Measurement Setup

After the fabrication of the designed planar waveguide sensor, as discussed above and verification of diabetes the optical power measurement is executed for detection of glucose level using the developed sensor device in the proposed experimental setup as shown in Fig. 5.3 above. A stabilized Helium Neon laser beam of wavelength 0.6328 µm and power 1 mW was launched to the optical fiber (which is butt-coupled to waveguide sensor inside PCE) by aligning with the focusing lens for light input into the

11 days. In case of A_2 rats with dose 90 mg/kg body weight the measured power varies from zero day to 11 days as glucose level increase with number of days as shown in Table-5.2. In case of A_3 rats with dose 110 mg/kg body weight, the glucose level increases from 108 mg/dl to 823 mg/dl (which is severe diabetic) within 3 days and because of that the measured power is reduced to 40 % with respect to input power.
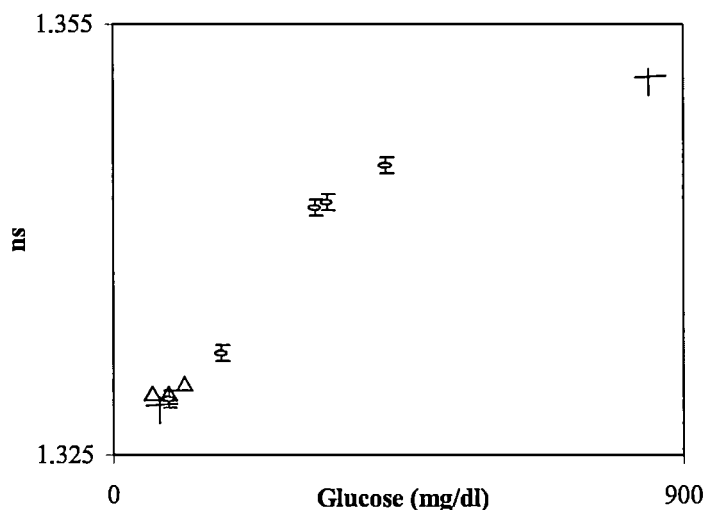
Fig-5.13: Refractive index (n_s) of blood plasma versus glucose level (as measured by Abbe Refractometer) for all three groups of rats A_1, A_2 and A_3

Table 5.2: Effect of Alloxan on glucose level of rats for different days

Number of days	A_1 rat with alloxan dose 60 mg/ kg body weight glucose level	A_2 rat with alloxan dose 90 mg/ kg body weight glucose level	A_3 rat with alloxan dose 110 mg/ kg body weight glucose level
0	98	105	105
3	100	176	823
5	108	295	-
8	117	385	-
11	115	420	-

Table 5.3: Detection performance comparison for different blood glucose concentration measurement system.

S.L No.	Authors/ (Year)	Technique/ process used	Detection time	Sample volume	Sensitivity	Limit of Detection (LOD)	Accuracy	Capability of measuring glucose samples concentration(C)
1.	Lin, J. F. et al./(2009) [18]	Electro-optically modulated circular polariscope	-	-	-	-	-	as low as 0.2 gm dl-1
2.	Suhandy, D. et al./(2012) [19]	ATR-THz spectroscopy	-	300 μL	-	-	-	-
3.	Cubuk, S. et al./ (2013) [20]	Boronic acid based fluorescence sensor	-	-	-	over a concentration of 0.1 ppm–0.7 ppm	-	-
4.	Yasin, M. et al./(2010)[21]	Intensity modulated fiber optic	-	50 ml	0.0103mV/(%)	-	-	-
5.	Pockevicius, V. et al./(2013)[22]	Using Inter-digital Electrodes	-	-	-	-	Error does not exceed 10 %	-
6.	Tura, A. et al./(2010) [23]	Electromagnetic sensor	-	-	~0.22 mV/(mg/dL)	(~78–5,000 mg/dL)	-	-
7.	Lin, Y. H. et al./(2013)[24	a solid-state sensor, micro-pump, and micro-valve integrated into a microfluidic device		200 μl	49.16 mV pH^{-1}			
8.	Worsley, G.J. et al./(2008)[25]	Phenylboronic-based sensor		40 μl	-	-	-	-
9.	V, A., Kumar, N./(2013)[26]	Wavelet Transform and Neural Networks	-	20 μl	-	-	-	-
10.	Our proposed technique	Based on integrated waveguide sensing technology and integrated with LOC	25.85 secs	0.141 ml	4.1	0-850 mg/dl		

Interdigital Electrodes [19], phenylboronic-based sensor [22], Wavelet Transform and Neural Networks [23] but obtaining accurate measurements is a key concern. Very recently, in ref [24] we find that although the author has developed a sensor for blood glucose estimation using inter digital electrodes which eliminate finger pricking and any possible risk of infection but the sensor lacks from accuracy compared to our proposed sensor structure. Table 5.3 shows the detection performance comparison for different blood glucose concentration measurement system. From the reported work in ref [21], we see that for measurement of glucose concentration the author has made use of microfluidic chip integrated with an electrolyte-insulator-semiconductor sensor. But it is important to note that in this existing technique the amount of sample consumption is more, around ~200 µl compared to our sample volume ~0.141 ml for its sensing application.

5.7 Conclusion

In this chapter, the study and design of a rapid diabetic detection technique using integrated optical waveguide sensor with Lab-on-a-chip device platform was carried out using Poiseuille's of viscous flow and light propagation through optical waveguide. The technique developed was implemented for detection of glucose level in alloxan-induced rat blood with administration of different doses of Alloxan. It is found that the intra peritoneal injection of alloxan dose 90 mg/kg body weight induces the diabetes starting from normal glucose level (110 mg/dl) in zero days to 420 mg/dl in 11 days. The integrated approach developed requires very minimal sample volume of ~0.141 ml which is less than the work found in the recent reported literature [24]. The concept presented in this work promises low cost online diagnostic technique for detection of glucose level in the near future.

5.8 List of References

1. Cooper, M. A. Optical biosensors in drug discovery, *Nat. Rev. Drug Discovery*, **1** (7), 515–528, 2002.

2. Vollmer, F., et al. Protein detection by optical shift of a resonant microcavity, *Appl. Phys. Lett.* **80** (21), 4057–4059, 2002.

3. Vahala, K. J. Optical microcavities, *Nature* **424** (6950), 839–846, 2003.

4. Bush, V. & and Cohen, R. The Evolution of Evacuated Blood Collection Tubes, *Lab. Med.* **34** (4), 304–310, 2003.

5. Lin, F. C., et al. Cellular sedimentation and barrier formation under centrifugal force in blood collection tubes, *Lab Med.* **32**, 588-594, 2001.

6. Bode, B. W. The Accuracy and Interferences in Self-monitoring of Blood Glucose. http://www.touchendocrinology.com/articles/accuracy-and-interferences-self-monitoring-blood-glucose.

7. Gartner, C. Microfluidic ChipShop Lab-on-Chip Catalogue. http://www.microfluidic-chipshop.com/index.php?pre_cat_open=209&id=214&.

8. Deka, B., & Sahu, P. P. Transformation relationship of directional coupler with multimode interference coupler and two mode interference coupler, *Journal of Opt.* **38** (2), 75-87, 2009.

9. Dutta, A. et al. Modeling and fabrication of evanescent waveguide-based optical sensor for sensitivity enhancement using silicon oxynitride technology, *Optic.* Eng. **52**, 077101-6, 2013.

10. Abdelhalim, M. A. K., & Mady, M. M. Rheological Parameters Assessment in Serum, Plasma and Whole Blood of Rats after Administration of Gold Nanoparticles of Different Sizes: In vivo, *J. Nanomed. Nanotechol.* **3** (6), 1-5, 2012.

11. Mathur, D. S. Elements of Properties of Matter, 11th Ed. Shyamlal Charitable Trust, New Delhi, 1996.

12. Masini, G., et al., High-Performance p-i-n Ge on Si Photodetectors for the Near Infrared: From Model to Demonstration, *IEEE Trans. On Electr. Dev.* **48** (6), 1092-1096, 2001.

If we knew what it was we were doing, it would not be
called research, would it?

-Albert Einstein

Chapter 6

Conclusion & Future Scope

6.1 Conclusion

In this thesis, effort have been made for a systematic and comprehensive study of a planar waveguide optical sensor that include design and development of a theoretical model using Simple Effective Index Method (SEIM) for the sensor structure and its application for adulteration testing of petroleum products and glucose level detection in blood plasma. At first, a detail survey on design and development of optical sensors and its appliance reported by earlier authors in the existing literature has been reviewed. A thorough study has been done on the available waveguide materials such as Silicon-On-Insulator (SOI) (silicon core), SiO_2/SiO_2-GeO_2 (Core) and $SiO_2/Silicon$ Oxynitride (SiON core) etc. as stated in chapter-2 for fabricating the designed waveguide sensor device and then compared. Since SiO_xN_y waveguides permit strong confinement of light with moderately low propagation losses, high index contrast, polarization sensitiveness, chemical inertness, low material cost and its compatibility with well known conventional silicon based IC technology; we have chosen $SiO_2/SiON$ as the waveguide material for fabricating the designed planar waveguide based optical sensor.

In these studies, at first starting from Maxwell's equation a theoretical analysis has been carried out for wave propagation in planar waveguide sensor with Silicon Oxynitride (SiON) as the waveguide material. Using boundary condition of the proposed structure on the solution of wave equation, the dispersion relation from the wave equation of the structure has been derived for estimating the propagation constants of the modes propagated in the planar waveguide structure. Simple Effective Index method (SEIM) has been used for the modal analysis of the three dimensional (3D) planar waveguide sensors. In addition, the result obtained from simulation has shown that the measured normalized power reduces with increase in length (L) of the waveguide and this decrease slowly with length (L) for L>10 cm. The normalized

obtained from the wave equation of the designed waveguide sensor structure, the sensitivity of the proposed planar waveguide sensor has been analyzed for detection of adulteration in petroleum product. For detecting the petroleum adulteration, adulterated petroleum product was used as a sensing material which acted as the cladding layer of the planar waveguide sensor and was put inside the cylindrical enclosure (CE). It is seen that the sensor sensitivity increases slightly with increase of core refractive index (n_c) and independent of waveguide core thickness. This is because the sensing area does not increase with increase of n_c and width of the core (x_1). The waveguide sensitivity is obtained as ~4.1 which is ~40 times more than that of the existing planar waveguide sensors and ~20 times more than that of asymmetric waveguide structure. The adulteration detection technique developed allows spot determination of adulteration in pure petroleum products without involving the use of chemicals

In this work, an effort has also been made to develop a technique for rapid detection of glucose concentration in blood plasma in support of diabetes management. In the proposed technique, Lab-on-a-Chip (LOC) device platform has been integrated with plastic enclosure having optical waveguide sensor, using Poiseuille's equation of viscous flow. The technique developed has been implemented for detection of glucose level in blood plasma of alloxan-induced diabetic rat. At first, we have designed the interfacing capillary tube using the viscous flow equation, for flowing of the blood plasma into the cylindrical enclosure (CE) that holds the planar waveguide sensor inside. Using this same principle, the cylindrical length has also been designed to make the viscous force push the blood plasma to get the CE filled with it. It is seen from the theoretical results, that for different waveguide core thickness the measured normalized power decreases with increase of the waveguide length and this becomes almost constant at length (L)~50,000 μm which is same as that obtained from interfacing tube design. So the waveguide of core width 50 μm and length~50,000 μm have been fabricated for the use in detection of glucose concentration in blood plasma. The detection time (τ_D) has been estimated that comprises of separation time (t_{sep}), propagation time, t_p, refilling time, t_r, and the time required by the detector to give the response. It is found that the detection time is ~25.85 seconds. The sample volume of the sensor was set at 0.141 ml. This has been calculated using inside volume of PCE,

6.2 Future Prospect

As future prospects an attempt can be made to apply the fabricated integrated optical planar waveguide sensor for online monitoring of adulterated petroleum products in refinery during the fractional distillation process. Such a sensor which requires very minimal sample volume ~ 0.25 ml for its adulteration detection and does not involve other chemicals for its adulteration detection would help to ensure the purity of the product yielding better accuracy. This technique can be used as an online diagnostic tool for detecting glucose level in blood plasma due to its rapid detection capability, and requirement of minimal sample volume. Also, as future scope, this sensor can be extended for rapid testing of bacteria colony, detection of arsenic content in water owing to high sensitivity, high accuracy and rapid detection capability.

✳✳✳✳✳